



# VCU

Virginia Commonwealth University  
VCU Scholars Compass

---

Theses and Dissertations

Graduate School

---

2013

## Principled Variance Reduction Techniques for Real Time Patient-Specific Monte Carlo Applications within Brachytherapy and Cone-Beam Computed Tomography

Andrew Sampson  
*Virginia Commonwealth University*

Follow this and additional works at: <https://scholarscompass.vcu.edu/etd>



Part of the [Health and Medical Physics Commons](#)

© The Author

---

Downloaded from

<https://scholarscompass.vcu.edu/etd/3063>

This Dissertation is brought to you for free and open access by the Graduate School at VCU Scholars Compass. It has been accepted for inclusion in Theses and Dissertations by an authorized administrator of VCU Scholars Compass. For more information, please contact [libcompass@vcu.edu](mailto:libcompass@vcu.edu).

# Principled Variance Reduction Techniques for Real Time Patient-Specific Monte Carlo Applications within Brachytherapy and Cone-Beam Computed Tomography

A dissertation presented to the School of Medicine at Virginia Commonwealth University in  
partial fulfillment of the requirements for the degree of

DOCTOR OF PHILOSOPHY

by

Andrew Joseph Sampson

Director: Dr. Jeffrey Williamson  
Professor, Department of Radiation Oncology, Division of Medical Physics

Virginia Commonwealth University  
Richmond, VA  
April, 2013



## Acknowledgement

There are just too many people for me to thank for helping me complete this dissertation. First and foremost, my must thank my Father in Heaven for providing the needed spiritual strength to overcome life's challenges that have molded me into who I am today.

Following Him, my deepest appreciation and love is given to my wife. I truly believe that she has the more difficult job keeping our family in order. Next, I must thank my children for being so patient for so many years with numerous nights without their father to safely tuck them in and read them a story and as their closest friends move away year after year.

I owe great gratitude to my advisor, Dr. Jeffrey Williamson for his support and treasured guidance throughout the course of this research. He has provided needed council and direction. Without him, this dissertation would never have come to fruition.

Lastly, I thank my advisory committee, Drs. Jeffrey Siebers, Dorin Todor, Chet Ford, and Randy Baker. I'm especially grateful for Randy since he had to put up with my incessant questions and lack of understanding.

# Table of Contents

Abstract.....	viii
1. Introduction .....	1
1.1 The Boltzmann transport equation (BTE).....	1
1.2 Variance reduction .....	3
1.3 Brachytherapy dosimetry in heterogeneous media .....	4
1.3.1 Effects of tissue heterogeneities on low-energy brachytherapy dose distributions ..	4
1.3.2 Current Understanding of the Dose Response Relationship in Low-energy brachytherapy.....	6
1.3.3 Solutions to overcome TG-43 deficiencies.....	8
1.3.4 Correlated sampling .....	10
1.4 Cone Beam Computed Tomography .....	11
1.4.1 CBCT scatter effects on reconstructed image quality.....	12
1.4.2 CBCT scatter mitigation strategies .....	13
1.4.3 Importance Sampling through Weight Windowing.....	14
1.5 Research Aims and Organization.....	16
2. Correlated Monte Carlo.....	0
2.1 Introduction.....	0
2.2 Correlated Monte Carlo .....	0
2.3 PTRAN Implementation .....	3

2.4	Case Studies .....	3
2.5	Accuracy of Correlated Monte Carlo.....	5
2.6	Correlated Monte Carlo Efficiency.....	6
2.6.1	Choice of Homogeneous medium for Breast Implants.....	10
2.6.2	Phase Space Model .....	12
2.6.3	Programming Memory Management.....	13
2.7	Discussion .....	15
2.8	Conclusion .....	16
3.	Interpolated Correlated Monte Carlo .....	18
3.1	Introduction.....	18
3.2	Interpolated Correlated Monte Carlo .....	18
3.3	Simulation Cases.....	20
3.4	Efficiency.....	22
3.5	ICMC Accuracy .....	24
3.5.1	ICMC Total Error .....	24
3.5.2	Inverse Square Law Gradient Effect.....	28
3.5.3	Cross-Section Gradient Effect .....	32
3.5.4	Local Absorption Gradient Effect.....	36
3.6	Discussion .....	40
3.7	Conclusion .....	43

4. Adjoint Biased Forward Monte Carlo .....	44
4.1 Introduction.....	44
4.2 Theory .....	44
4.2.1 Weight Windows .....	44
4.2.2 The Forward and Adjoint Boltzmann Transport Equation .....	45
4.2.3 Optimal Weight Window Target Value.....	47
4.2.4 Importance Sampling Revisited.....	48
4.2.5 Consistent adjoint-driven importance sampling (CADIS).....	49
4.2.6 Forward Adjoint Importance Generator.....	50
4.3 CADIS Implementation .....	51
4.3.1 Multigroup Approximation.....	51
4.3.2 Choice of Forward Source Function.....	53
4.3.3 Detector Response Function .....	56
4.3.4 PARTISN Implementation.....	56
4.3.5 PTRAN Modifications .....	59
4.4 ABFMC Performance Assessment .....	59
4.4.1 Assessing Accuracy .....	59
4.4.2 Efficiency Assessment.....	61
4.4.3 ABFMC Candidate Comparison.....	61
4.4.4 PTRAN Simulation Environment.....	62

4.5	Discussion .....	74
4.6	Conclusion .....	77
5.	Discussion .....	78
5.1	Correlated Monte Carlo .....	78
5.2	Adjoint Biased Forward Monte Carlo.....	80
5.3	Conclusion .....	81
6.	Contributions .....	82
6.1	Correlated Monte Carlo .....	82
6.2	Interpolated Correlated Monte Carlo.....	82
6.3	Adjoint Biased Forward Monte Carlo.....	83
7.	References .....	85
	Appendices.....	92



## Abstract

### PRINCIPLED VARIANCE REDUCTION TECHNIQUES FOR REAL TIME PATIENT-SPECIFIC MONTE CARLO APPLICATIONS WITHIN BRACHYTHERAPY AND CONE-BEAM COMPUTED TOMOGRAPHY

By Andrew Joseph Sampson, B.S.

A dissertation submitted in patient fulfillment of the requirements for the degree of Doctor of Philosophy at Virginia Commonwealth University.

Virginia Commonwealth University, 2013

Major Director: Dr. Jeffrey Williamson  
Professor, Department of Radiation Oncology, Division of Medical Physics

This dissertation describes the application of two principled variance reduction strategies to increase the efficiency for two applications within medical physics. The first, called correlated Monte Carlo (CMC) applies to patient-specific, permanent-seed brachytherapy (PSB) dose calculations. The second, called adjoint-biased forward Monte Carlo (ABFMC), is used to compute cone-beam computed tomography (CBCT) scatter projections. CMC was applied for two PSB cases: a clinical post-implant prostate, and a breast with a simulated lumpectomy cavity. CMC computes the dose difference,  $\Delta D$ , between the highly correlated dose computing homogeneous and heterogeneous geometries. The particle transport in the heterogeneous geometry assumed a purely homogeneous environment, and altered particle weights accounted for bias. Average gains of 37 to 60 are reported from using CMC, relative to un-correlated Monte Carlo (UMC) calculations, for the prostate and breast CTV's, respectively. To further increase

the efficiency up to 1500 fold above UMC, an approximation called interpolated correlated Monte Carlo (ICMC) was applied. ICMC computes  $\Delta D$  using CMC on a low-resolution (LR) spatial grid followed by interpolation to a high-resolution (HR) voxel grid followed. The interpolated, HR  $\Delta D$  is then summed with a HR, pre-computed, homogeneous dose map. ICMC computes an approximate, but accurate, HR heterogeneous dose distribution from LR MC calculations achieving an average 2% standard deviation within the prostate and breast CTV's in 1.1 sec and 0.39 sec, respectively. Accuracy for 80% of the voxels using ICMC is within 3% for anatomically realistic geometries. Second, for CBCT scatter projections, ABFMC was implemented via weight windowing using a solution to the adjoint Boltzmann transport equation computed either via the discrete ordinates method (DOM), or a MC implemented forward-adjoint importance generator (FAIG). ABFMC, implemented via DOM or FAIG, was tested for a single elliptical water cylinder using a primary point source (PPS) and a phase-space source (PSS). The best gains were found by using the PSS yielding average efficiency gains of 250 relative to non-weight windowed MC utilizing the PPS. Furthermore, computing 360 projections on a  $40 \times 30$  pixel grid requires only 48 min on a single CPU core allowing clinical use via parallel processing techniques.

# 1. Introduction

Towards the end of the Second World War the ENIAC, the world's first electronic multi-purpose computer, was created and opened the door to scientific computing. It was immediately applied to computing particle flux from thermo-nuclear reactions through a process known as statistical sampling, the name "Monte Carlo" (MC) being coined shortly thereafter<sup>1</sup>. Following over a decade of use for particle physics transport, Berger published his seminal paper on the condensed history technique for coupled electron-photon transport in 1963<sup>2</sup>. This technique substantially increased the efficiency of the coupled electron-photon transport calculations and paved the way for MC radiation transport to be adapted for medical applications. Today, MC is used extensively in all subfields within medical physics and is the current gold standard for all radiation transport simulations for quantities of interest to the field.

This dissertation focusses on increasing the efficiency of MC solutions to two different low-energy photon transport problems within medical physics. First, the time required for MC computed patient-specific brachytherapy dose calculations is too great for clinical application. Likewise, MC simulated cone-beam computed tomography (CBCT) scatter projections are too time intensive for clinical adoption within scatter mitigation strategies. The remaining sections of this chapter present the major concepts, background, and rationale for this study. The final section then summarizes the aims and novelty of the remaining chapters.

## 1.1 The Boltzmann transport equation (BTE)

To begin, the time independent Boltzmann transport equation is presented:

$$\begin{aligned} \mathbf{\Omega} \cdot \nabla [\Phi(\mathbf{r}, E, \mathbf{\Omega})] + \mu(\mathbf{r}, E) \Phi(\mathbf{r}, E, \mathbf{\Omega}) = \dots \\ S(\mathbf{r}, E, \mathbf{\Omega}) + \iint \Phi(\mathbf{r}, E', \mathbf{\Omega}') \hat{\mu}(E', \mathbf{\Omega}' \rightarrow E, \mathbf{\Omega} | \mathbf{r}) dE' d\mathbf{\Omega}' \end{aligned} \quad (1.1.1)$$

where  $\Phi$  represents the fluence of particles, and  $\mathbf{r}$ ,  $E$ , and  $\mathbf{\Omega}$  represent position, energy and particle trajectory respectively. Furthermore,  $\mu$  represents the linear attenuation coefficient, and  $\hat{\mu}$  represents the total cross section for all interactions that produce a scattered photon. The first term,  $\mathbf{\Omega} \cdot \nabla [\Phi(\mathbf{r}, E, \mathbf{\Omega})]$ , is called the streaming operator, and represents the net number of particles having energy  $E$  and trajectory  $\mathbf{\Omega}$  leaving volume  $dV$ , centered about  $\mathbf{r}$ . The second term,  $\mu(\mathbf{r}, E) \Phi(\mathbf{r}, E, \mathbf{\Omega})$ , represents the loss of particles with energy and trajectory,  $(E, \mathbf{\Omega})$ , that change that change phase-space position within  $dV$  due to collision.  $S(\mathbf{r}, E, \mathbf{\Omega})$  is a general source term giving rise to particles in  $dV$  with energy  $E$  and trajectory  $\mathbf{\Omega}$  due to fixed, primary-particle sources. The final term,  $\iint \Phi(\mathbf{r}, E', \mathbf{\Omega}') \hat{\mu}(E', \mathbf{\Omega}' \rightarrow E, \mathbf{\Omega} | \mathbf{r}) dE' d\mathbf{\Omega}'$ , can be viewed as a “collision source” where particles within  $dV$  having energy  $E'$  and trajectory  $\mathbf{\Omega}'$  change phase-space positions due to collision to energy  $E$  and trajectory  $\mathbf{\Omega}$ . The integral form of this equation is solved via the Monte Carlo (MC) method for some scoring quantity of interest, such as absorbed dose or scatter photon signal in a detector.

The BTE can be solved both in the forward sense, running from  $E', \mathbf{\Omega}' \rightarrow E, \mathbf{\Omega}$  - higher energy states to lower energy states, or in the adjoint sense, and running from  $E, \mathbf{\Omega} \rightarrow E', \mathbf{\Omega}'$  - lower energy states to higher energy states. Instead of the particle flux, the adjoint version of the BTE describes for the adjoint flux or function,  $\Phi^*(\mathbf{r}, E, \mathbf{\Omega})$ ; its relevance will be discussed in later sections of this chapter and is a major topic in Chapter 5.

The BTE can be solved numerically through deterministic or stochastic methods. The most common deterministic approach is called the discrete ordinate method (DOM). Unlike statistical

methods such as Monte Carlo, DOM calculations solve the BTE directly and numerically by discretizing the phase space: energy, spatial position, and solid angle. DOM does not solve the BTE exactly, due to the discretization of the phase space  $(\mathbf{r}, \mathbf{\Omega}, E)$ , introducing a level of systematic error. On the other hand, the Monte Carlo stochastic method for solving the BTE does not discretize phase space, but produces an accurate, non-biased solution with a level of statistical, or random uncertainty. The Monte Carlo method is considered the gold standard for radiation transport simulations, as mentioned previously, but has historically required long computational run-times to converge to a solution with little statistical uncertainty.

## 1.2 Variance reduction

Though unbiased, a drawback of MC simulations, as stated previously, is that it provides a statistically inexact solution: there is a level of uncertainty or variance (square of standard deviation,  $\sigma$ ) associated with the final score due to averaging the total contribution from each successive photon history. Two generally used unbiased methods to reduce score variance are increasing the number of simulated histories and employing variance reduction (VR) strategies. The former is usually undesirable since variance is inversely proportional to the number of histories simulated leading to high CPU times for precise solutions. The latter technique, VR, uses clever methods to reduce the CPU time to reach a desired level of uncertainty. Though not VR, another method routinely used to reduce CPU time is through approximations to the physics transport model. Though this method can be quite effective, great care must be taken to not introduce unwanted systematic bias. Actual VR strategies can be classified into two groups. First, enhanced scoring or estimation techniques are designed to increase the number of scores to a detector using the same number of histories. An example would be the expected track-length estimator that provides a score to every detector along a photon trajectory instead of only at

interaction sites. Second, biased sampling schemes are available that alter the transport of photons so that CPU time is better focused on simulating events that have high “importance” to the final score. A by-product of many VR methods is the necessity of particle weight manipulation to remove any systematic error induced by sampling from biased probability density functions (PDF's).

### **1.3 Brachytherapy dosimetry in heterogeneous media**

#### **1.3.1 Effects of tissue heterogeneities on low-energy brachytherapy dose distributions**

The current standard of practice for brachytherapy dose calculation is the AAPM Task Group 43 protocol (TG-43)<sup>3</sup>, which assumes a patient composed of liquid water and ignores seed-to-seed attenuation and other applicator-shielding effects. Several studies have documented that tissue heterogeneities and inter-seed attenuation significantly influence traditional low-energy (<sup>125</sup>I or <sup>103</sup>Pd) permanent seed implants.

In prostate permanent seed brachytherapy (PSB) treatments, for example, the combined effect of modeling tissue heterogeneities and inter-seed attenuation in post-implant dosimetry is to decrease average  $D_{90}$  (dose delivered to 90% of the treatment volume, CTV) by 7% to 13%<sup>4-9</sup>, depending on the density of seeds within the implant. Carrier *et al*<sup>4</sup> showed a 5-7% decrease in the  $V_{200}$  (volume that receives a minimum of 200% of the prescribed dose) from taking into account tissue heterogeneities alone assuming a purely homogeneous prostate tissue environment. Using more realistic anatomical models show that TG-43 overestimates  $D_{90}$  by as much as 9%. Chibani *et al* showed that 1%-5% mass fractions of calcifications in the prostate volume can decrease  $D_{100}$  (dose delivered to 100% of the CTV) by as much as 58%<sup>6</sup>.

Even larger errors have been observed for  $^{103}\text{Pd}$  PSB implants following a lumpectomy for early stage breast cancer. Furstoss *et al*<sup>10</sup> studied the combined effects from inter-seed attenuation and tissue composition for PSB breast implants on the delivered dose distribution and found a decrease in  $D_{90}$  of 10.3% in conjunction with an associated increase in the number of “cold spots.” In our own studies, we have confirmed the decrease in  $D_{90}$  for breast and have shown an increase in dose outside the CTV by as much as 80-90%. Figure 1.1 demonstrates this effect by looking at the ratio of dose between accounting for tissue heterogeneities and not by utilizing TG-43 for a high resolution, tissue segmented, breast-dedicated cone-beam CT (BD-CBCT) image. These differences are largely due to the increased fractional volume of adipose tissue in the breast, up to 85%<sup>11</sup>, which has a lower linear attenuation coefficient than water at these energies by as much as 65%.

Looking at higher energies, a recent Monte Carlo study on the effects of tandem applicator shielding on dose distributions for gynecological intracavitary  $^{137}\text{Cs}$  brachytherapy found TG-43 overestimated dose by 33% in the region superior to the applicator<sup>12</sup>.

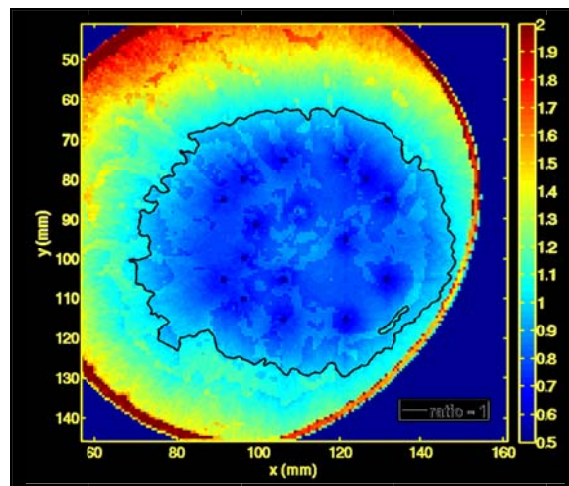


Figure 1.1: Ratio of MC heterogeneous dose and TG-43 for PSB breast brachytherapy using  $^{103}\text{Pd}$  seeds. The black contour represents unit. *BD-CBCT image courtesy of John Boone, UC-Davis.*

Noting the deficiencies of TG-43, Carrier *et al* concluded that a heterogeneous dose-calculation engine is needed to improve understanding of the dose-outcome relationship to further improve patient outcomes<sup>5</sup>.

Furthermore, Maughan *et al* studied the mass-energy absorption coefficients for various chemically assayed tumors, noting the percentage difference between the mass-energy absorption coefficient for tumor and water varied from 5% to 17% at 30 keV<sup>13</sup>. In the external beam energy range, these differences were limited to less than 3%. The higher percentage of local absorption differences between water and the tumor samples at lower energies is due to the increased cross-section for photoelectric absorption. The photoelectric effect is strongly dependent on material atomic composition, highlighting the need for accurate modeling of anatomical geometries. Unfortunately, ICRU<sup>14</sup> and ICRP<sup>15</sup> recommended tissue compositions and densities are based upon very sparse tissue sample measurements that exhibit substantial sample-to-sample variability<sup>16-18</sup>. As an example of sparseness, the weight fraction of water for prostate as recommended by ICRP 89 was derived from a single specimen taken from a 14 year old boy in 1935<sup>19</sup>. As an example of variability, Hammerstein performed a chemical analysis on mastectomy specimens revealing 8% to 10% variations in glandular and adipose tissue compositions by weight of carbon and oxygen. These variations translate into 8% to 15% uncertainties in the linear attenuation coefficient at 20 keV<sup>20</sup>.

### **1.3.2 Current Understanding of the Dose Response Relationship in Low-energy brachytherapy**

In a large retrospective study on patient outcome for PSB prostate implants, Stone *et al*<sup>21</sup> found a correlation between biochemical relapse-free survival (bRFS) rates and the D<sub>90</sub>, especially for intermediate and high risk patients. Another study<sup>22</sup> found local failure to be associated with a



low  $D_{90}$  among other dose-response descriptors. This all would suggest that delivering a higher  $D_{90}$  would significantly increase bRFS. Unfortunately, in another large retrospective study of over 5000 PSB prostate patients<sup>23</sup>, it was found that 54.5% of all patients experienced one or more of the following types of treatment complications: urinary, bowel, and erectile. Of these, 14.7% required further invasive procedures. Still additional studies have correlated toxicities to hot spots (increased  $V_{150}$  and  $V_{200}$ ), and a higher  $D_{90}$ . These studies suggest that a consistent increase to  $D_{90}$  to achieve better bRFS rates would also increase the incidence of toxicities observed in patient outcomes.

Since breast-PSB is still in its infancy, very limited outcome data is available. One study by Keller *et al*<sup>24</sup> reported the relationship between maximum skin dose and corresponding toxicities for a total of 95 patients that were treated between 2004 and 2011. Because of the large variability in the maximum skin dose among patients, no correlation was found between the maximum skin dose and related toxicities.

Neglecting tissue heterogeneities introduces potentially large delivery errors, having both systematic and random components which give rise to suboptimal clinical dose prescriptions in different ways. The systematic component is characterized by a mean offset (nominal vs. actual) over the entire patient population, represented by a translational shift in the dose-response curve. The random component, on the other hand, results in the patient-to-patient variability of the error, thereby reducing the slope of the dose-response curve.

Figure 1.1 shows an example of a systematic error in breast PSB that arises from computing dose to medium that is primarily adipose tissue instead of water. There is a stark contrast in the particle fluence distribution between the anatomical-breast environment and water because of the

decreased linear attenuation coefficient of adipose tissue relative to that of water. As stated previously, this difference causes the region outside the PTV to have an increased dose while the region within the PTV receives a decreased dose relative to TG-43 calculations. This behavior will be similar for all breast patients because of the larger fraction, on average, of adipose tissue over fibro-glandular resulting in a systematic shift in the dose-response curve for all patients. Another example of a systematic shift is the difference in the dose distributions observed between electronic and  $^{192}\text{Ir}$  HDR brachytherapy, creating difficulties when comparing their dose outcomes. Even when dwarfed by random errors, systematic shifts are always important since they result in shifts of the average dose in an entire patient population which may already be receiving doses close to normal tissue tolerances<sup>25</sup>.

Random errors on the other hand are best described by the patient-to-patient variability in tissue composition, and anatomical differences for both the breast and prostate treatment sites. The decreased slope of the dose-response curve causes local control to be reduced while simultaneously increasing toxicities.

The systematic and random errors may or may not need to be corrected for, but they first must be characterized through the use of model based dose calculation algorithms (MBDCA's) that incorporate tissue heterogeneities and compared with other sources of error such as organ motion, and seed placement accuracy.

### **1.3.3 Solutions to overcome TG-43 deficiencies**

Primarily, three classes of dose calculation algorithms have been proposed to clinically realize the potential of MBDCA's: first, collapsed-cone superposition convolution (CCSC)<sup>26,27</sup>; second, discrete-ordinate methods (DOM)<sup>28</sup>; and third, Monte Carlo simulation (MC). Carlsson-Tedgren

*et al*<sup>29</sup> has shown the efficacy of using CCSC for accurate sub-minute brachytherapy dose calculations, but to date their studies have been limited to simple applicator scatter corrections and not applied to patient-specific treatment planning. Recently, Varian Medical Systems released BrachyVision Acuros<sup>30</sup> that utilizes a radiation therapy specific rewrite of the DOM code ATTILA<sup>28</sup> and can compute most HDR dose-distributions in under 10 min. Deterministic solutions offer substantial speed enhancements, but are subject to systematic errors, e.g., ray-effects, due to overly coarse discretizations of the radiation transport phase space. Zourari *et al*<sup>30</sup> showed that for a single <sup>192</sup>Ir source in homogeneous medium, most differences between Acuros and MC were within 1%. These were systematic differences between Acuros and MC near the longitudinal axis of the source including a general over-estimation of the radial dose function by 1% and an oscillatory pattern exhibited along the radial dose function due to spatial discretization and ray effects. However, max errors between Acuros and MC were less than 2% and represent strong agreement with Monte Carlo simulations. DOM parameters are, however, often tuned to produce good results for a certain problem domain<sup>31</sup>.

CT-based MC methods, on the other hand, can be deployed in both applicator-attenuation and tissue-heterogeneity settings so to completely avoid systematic bias, for both low and high energy brachytherapy. However, the CPU time-intensiveness of MC transport solutions has limited its use in the clinical setting. For example, using Geant4 Carrier *et al*<sup>5</sup> reported post-implant Monte Carlo dose calculations run times of 4 hrs on a cluster of 8 Intel Xenon 2.4 GHz CPU's to give a statistical uncertainty of 0.1% in the  $V_{200}$  for  $1.3 \times 1.3 \times 2.5 \text{ mm}^3$  voxels. This is neither realistic for pretreatment planning nor for intraoperative plan adjustment. Optimization for treatment planning purposes is even a concern for accelerated codes<sup>5,6,8</sup> that employ various variance reduction techniques<sup>32</sup>. For example, PTRAN\_CT requires 15 min to achieve an

average 2% uncertainty within the CTV for 1 mm<sup>3</sup> voxels on a single 3.8 GHz processor<sup>33</sup>. One approach to overcome this limitation is to employ additional sophisticated variance reduction techniques to reduce the CPU time for a clinically acceptable uncertainty to be achieved on cost effective equipment. Due to the limitations imposed by current DOM and MC solutions, there is still a need for an efficient, robust, and accurate general purpose brachytherapy dose-calculation engine that overcomes the deficiencies of TG-43.

#### 1.3.4 Correlated sampling

Correlated Monte Carlo (CMC) was first proposed for accelerating MC brachytherapy dose calculations by Hedtj rn *et al* who demonstrated the potential for order-of-magnitude efficiency gains in simple two-dimensional geometries. Rather than computing absorbed dose directly, CMC estimates the dose difference between heterogeneous and homogeneous geometries on a voxel-by-voxel basis using photon histories sampled from the collision and transport kernels associated with the homogeneous environment. Any bias introduced into the heterogeneous dose from this biased sampling process is removed by applying an appropriate photon weight correction factor.

For a simple cylinder geometry, Hedtj rn *et al* show that CMC achieved efficiency gains as large as 10<sup>4</sup> with efficiency losses confined to regions that had a dose delivered to heterogeneous media 50% of the dose delivered to a corresponding homogeneous environment. Le *et al* further extended the application of CMC to CT-based Monte Carlo representations<sup>34</sup>. Via the VCU code, PTRAN\_CT, they were able to compute delivered patient dose within the CTV in less than 5.4 min with an average percent standard deviation of 2% in a 1×1×1 mm<sup>3</sup> grid<sup>35</sup>. I have made further enhancements to the code structure to allow streamlined simulation and reduced this time down to less than 40 sec under the same conditions. Some of these enhancements include

altering the way large arrays were stored and accessed in physical memory, and improved ray-tracing through combined analytical and CT voxelized geometries<sup>33</sup>.

Correlated sampling was chosen specifically for the brachytherapy heterogeneity problem because there are no high contrast structures in the CTV or OARs, excluding calcifications. Because of its nature, correlated sampling loses efficiency if a large volume of voxels within the region of interest exhibit large differences in the radiological properties between the heterogeneous and homogeneous environments.

#### 1.4 Cone Beam Computed Tomography

Cone-beam computed tomography (CBCT) has received widespread reception in radiotherapy and diagnostic imaging over the past decade. For radiotherapy, CBCT is an important tool for patient boney alignment, and in more recent years, CBCT has also gained more reception in operating rooms, for breast-dedicated CBCT<sup>36,37</sup>, and for dental imaging<sup>38,39</sup>.

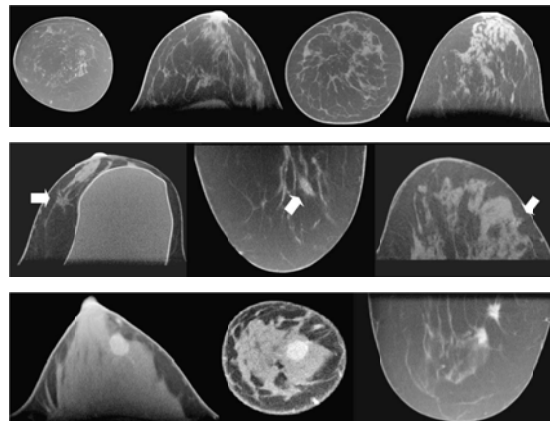


Figure 1.2: Demonstrating the cupping artifact from detector patient scatter: *top* - BD-CBCT sample images taken of a normal breast; *middle* - BD-CBCT detected lesions later found to be pathologically positive. The large uniform area of left image is breast implant; *bottom* - BD-CBCT images with use of Iodine contrast agent. The lower lesion in the right image was not detected by conventional mammography.

### 1.4.1 CBCT scatter effects on reconstructed image quality

Detected patient scatter radiation is defined as the detector array signal arising from scattered photons that are produced from primary beam interactions within the patient. Scatter induces artifacts such as loss of contrast, cupping, and streaking between high contrast materials. Typical scatter-to-primary ratios (SPR) in CBCT range from 0.5-0.95<sup>36,40</sup>, compared to 0.01<sup>41</sup> in 3<sup>rd</sup> generation fan-beam CT (FBCT) detector geometries. FBCT only acquires a very thin slice at a time limiting the field of view (FOV) while CBCT has a vastly larger scattering volume due to using a flat panel detector that sweeps over a large longitudinal FOV in a single circular orbit. These unwanted but detected scatter photons degrade image quality, giving rise to cupping artifacts, streaking artifacts, reduced contrast, and reconstructed Hounsfield unit (HU) inaccuracies<sup>42</sup>. The cupping artifact is characterized by lower HU toward the center of the reconstructed image than the edge (see Figure 1.2) and prevents proper rendering of the image with window/level settings.

Contrast also is degraded by an increase in SPR. Siewerdsen *et al* showed, for a simple phantom, that contrast falls from 5% to 2.2% when the SPR increases from 10% to 120%<sup>43</sup>. Accurate and uniform HU are needed to support computed aided detection (CAD), tissue classification<sup>44</sup>, and accurate quantitative assessment of vascular kinetics using injected contrast agents. Zhu *et al* showed that for a small homogeneous ROI within the Catphan©600, CBCT cupping artifacts will cause the HU to be underestimated by roughly 100 with a mean variation of  $\pm 50$ <sup>45</sup> whereas  $\pm 3-5$  HU is typical for FBCT. Furthermore for breast-dedicated CBCT (BD-CBCT), Altunbas *et al* found a similar underestimated HU shift with a standard deviation  $\pm 20$  HU for a medium sized breast before correction. For a large mastectomy specimen, the underestimated HU shift was found to be  $\sim 170 \pm 65$  HU<sup>46</sup>. Additionally, the overall image blurring and inaccurate HU's from

detected scatter reduces low-contrast detectability, thus reducing the clinical effectiveness of BD-CBCT. In radiotherapy, the decreased image quality associated with non-scatter corrected CBCT images has been shown to increase the variability of physician contouring relative to CBCT, thus diminishing the potential effectiveness of CBCT guided radiotherapy<sup>47</sup>. Image quality for CBCT could conceivably be improved if effective scatter and noise mitigation strategies could be applied<sup>48</sup>.

### 1.4.2 CBCT scatter mitigation strategies

While many methods have been proposed for mitigating scatter-related artifacts, no corrective technique exists that is simultaneously clinically practical, efficient, and clearly effective in improving CBCT image quality. The use of anti-scatter grids is a common technique that has varying results that depend on scan acquisition parameters. Siewerdsen *et al* showed that anti-scatter grids in CBCT increase the contrast-to-noise ratio (CNR) only for large reconstruction voxel sizes or for very high SPR conditions characteristic of pelvic or thoracic imaging<sup>49</sup>. He further showed that anti-scatter grids offer no benefits for high-resolution CBCT imaging such as BD-CBCT, a conclusion confirmed by Kyriakou<sup>50</sup>. A more successful and recent study has shown that using a primary beam modulator allows one to separate the scatter from the total signal<sup>51</sup>. Unfortunately, like all scatter subtraction methods, this technique leaves behind the scatter noise component in the remaining projection image thus reducing the contrast-to-noise ratio and should be corrected for separately to further improve image quality.

Proposed methods for mitigating scatter effects fail for one of the three following reasons: (a) use highly approximate or inaccurate scatter estimates that diminish image quality<sup>46,52-55</sup>; (b) require too much CPU time to be clinically feasible<sup>48,56,57</sup> even when accurate and robust; or (c) require multiple scans thereby increasing patient dose or scanning time and have been shown to

be extremely effective<sup>45,58</sup>. All proposed solutions in types (b) and (c) and most in (a) include some approach to separate the scatter signal from the primary. While the increased doses implied by type (c) solutions may be acceptable in radiotherapy applications, other applications require minimal patient doses, such as BD-CBCT where dose is constrained to that of two-view mammography<sup>37</sup>. The most accurate and robust solution is subtraction of scatter estimates derived from patient-specific MC simulations that use an approximate reconstructed image as input geometry. Using such a method, Lazos *et al*<sup>48</sup> was able to recover lost contrast to match that of images reconstructed from primary photon projections only. Unfortunately, all the MC solutions advanced to date for scatter subtraction require too much CPU time to compute to be clinically practical. For the 500-660 projections used in CBCT, the method proposed by Kyriakou *et al* would require 4 to 5.5 hours of CPU time<sup>57</sup>. Mainegra-Hing *et al* proposed a series of VR techniques to overcome the time limitation of MC scatter subtraction but were still unsuccessful in realizing acceptable CPU time intervals on clinically available systems<sup>59</sup>. Instead of using VR techniques, a more recent approach to increase computation efficiency involves adaptation of the Monte Carlo approach for graphics processing units (GPU)<sup>60,61</sup>. Though significant gains from utilizing the GPU of have been reported for CBCT dose calculations<sup>62</sup>, efficiency gains for MC CBCT scatter projection using a GPU have not been published.

### 1.4.3 Importance Sampling through Weight Windowing

Instead of relying on brute force Monte Carlo, we take the approach of principled Variance Reduction. The following sub-Aims outline the background of a powerful technique to drastically reduce the amount of CPU time required for Monte Carlo computed CBCT scatter projections.



### 1.4.3.1 Importance sampling

Importance sampling is a powerful MC VR tool. As previously shown, simulating MC particles can be fully described by a multi-dimensional phase space,  $\beta$ . For the description of importance sampling, we will let  $\mathbf{P} = (\mathbf{r}, \boldsymbol{\Omega}, E)$  specify the phase space parameters of a particle leaving a collision. Importance sampling is a particle sampling procedure (a method of randomly selecting  $(\mathbf{P}_i, W_i)$  from its preceding particle state  $i-1$ ) in which systematically biased probability distributions are used to drive simulated particles into phase-space regions of greater importance to the problem solution. For example, in CBCT simulations employing purely analog sampling techniques, many low-energy photons are absorbed in the bow-tie filter or patient tissues and never strike the detector. These photons are of little importance because they do not contribute to the score at the detector. It would be more efficient instead to bias the simulation by making unimportant photon trajectories unlikely and focusing valuable CPU time on photons that do contribute to the detector score.

### 1.4.3.2 Relationship between importance sampling and the weight windowing VR technique

Systematic splitting/rouletteing is an alternate implementation of importance sampling that avoids explicitly drawing random samples from biased PDFs<sup>63,64</sup>. A variant of the splitting/roulette technique is called weight windowing (WW) in which a photon's weight in  $\mathbf{P}$  is constrained to be within a certain interval or "window" centered about a desired target value. An illustration of WW is found in Figure 3 of the MCNP manual<sup>65</sup>. WW is especially useful when an additional VR technique causes particle weights to inflate or to become too variable, which can result in decreased efficiency. An example of such a phenomenon is the correlated Monte Carlo method<sup>33,66,67</sup>.

In general the process of picking the proper WW parameters can be a tedious task that requires skill and experience<sup>64</sup>. The adjoint function,  $\Phi^*(\mathbf{r}, E, \Omega)$ , has long been recognized to have physical interpretation as the importance of a region in phase space  $\mathbf{P}$  and can be associated with a zero variance Monte Carlo solution<sup>68</sup>. The MCNP weight window generator produces a forward computed adjoint function as the expected contribution from particles in a region about  $\mathbf{P}$  to the detector score from itself and all its possible progeny<sup>69</sup>. Other methods use a deterministically computed  $\Phi^*(\mathbf{r}, E, \Omega)$  as the importance function. In the nuclear engineering field, use of  $\Phi^*(\mathbf{r}, E, \Omega)$  for importance sampling is called adjoint-biased, forward Monte Carlo (ABFMC)<sup>70</sup>.

## 1.5 Research Aims and Organization

The use of patient specific Monte Carlo solutions for brachytherapy dose calculations and CBCT scatter projections can lead to improved patient outcomes. Accurate, individually-optimized brachytherapy treatments can increase local control while simultaneously reduce toxicities as a more accurate characterization of the dose-response relationship for both breast and prostate low-energy PSB is obtained. Additionally, the use of an accurate and efficient scatter subtraction correction for CBCT projections coupled with a scatter noise mitigation strategy will improve CBCT image quality, providing more accurate diagnoses and the capability for quantitative imaging techniques such as more accurate contouring in radiotherapy. These clinical applications have been widely studied, but the barrier of Monte Carlo efficiency still remains.

To address the problem of efficiency in patient-specific brachytherapy dose calculations, Chapter 2 discusses the application of the CMC algorithm to the PTRAN code family<sup>48,71-75</sup>. The accuracy and efficiency of the algorithm are presented relative to uncorrelated Monte Carlo for

two PSB patient geometries: a post-implant prostate evaluation and a simulated breast treatment. Chapter 3 is an extension to correlated Monte Carlo that introduces a method called interpolated correlated Monte Carlo (ICMC) as an approximation to further improve the efficiency of CMC calculations with little loss in accuracy. Similar to Chapter 2, the accuracy and efficiency of ICMC relative to uncorrelated Monte Carlo is presented.

To address the lack of efficiency in computing CBCT scatter projections, Chapter 4 contains the application of WW and ABFMC to the PTRAN code family. Each method is presented, including theory and background, for different scatter geometries.

Chapter 5 discusses the potential clinical benefit gained from application of the principles introduced in the previous chapters.

This dissertation is designed to supplement 3 papers that have been written for publication. For the reader's convenience, the published versions or current drafts of these appears are contained as Appendices A-C to supplement Chapters 2 and 4. Appendices A and B supplement Chapter 2, while Appendix C supplements Chapter 4. Additional Appendices D and E are given as supplementary material for Chapter 4. For readability, selected findings from each paper will be re-presented in its corresponding chapter while also inviting the reader to refer to the articles for more detail.

For all calculations within this dissertation: the same compilation flags were used with the intel "ifort" compiler suite version 12, were completed on an AMD Phenom X6 1090T Black Edition processor, and utilized only a single CPU core (non-hyperthreaded). Furthermore, all CPU times included in this dissertation are only for the radiation transport and do not include the CPU time

to setup the simulation geometry, though it is a critical factor in the total clinical time. The reason for this decision is given in each research chapter's discussion section.

## 2. Correlated Monte Carlo

### 2.1 Introduction

Model based dose calculation algorithms (MBDCA) for patient-specific dosimetry in low-energy brachytherapy have become increasingly utilized in recent years. Unfortunately, as referenced in Chapter 1, most MBDCA's presented to date require considerable CPU time for full clinical utilization. Correlated sampling, or correlated Monte Carlo (CMC), is well suited to increase the efficiency of Monte Carlo (MC) brachytherapy dose calculations.

### 2.2 Correlated Monte Carlo

Since the theory of CMC has been extensively described previously<sup>67</sup>, only a brief description will be included here. A similar explanation is given in Section II.A of Appendix B. CMC deviates from traditional uncorrelated Monte Carlo (UMC) by aiming to compute the dose difference between heterogeneous and homogeneous geometries, as opposed to absorbed dose in either geometry separately. Conceptually, deviations from a homogeneous water environment (including applicators, seeds, and tissue heterogeneities) are treated as perturbations.

First, a phase space vector, for the  $m^{\text{th}}$  history and  $n^{\text{th}}$  interaction,  $\beta_{m,n}^{\text{hom}}$ , is randomly sampled from a probability density function (PDF) that corresponds to a purely homogeneous geometry.

$\beta_{m,n}^{\text{hom}}$  is defined as,

$$\beta_{m,n}^{\text{hom}} = (\mathbf{r}_{m,n}, E_{m,n}, \Omega_{m,n}, W_{m,n}^{\text{hom}}) \quad (2.2.1)$$

where  $\mathbf{r}_{m,n}$  describes the location of the interaction,  $E_{m,n}$  is the photon's energy as it exits  $\mathbf{r}_{m,n}$ ,  $\boldsymbol{\Omega}_{m,n}$  describes the photon trajectory leaving  $\mathbf{r}_{m,n}$ , and  $W_{m,n}^{\text{hom}}$  represents the photon weight as it exits  $\mathbf{r}_{m,n}$ . Second, another phase space vector,  ${}^*\boldsymbol{\beta}_{m,n}^{\text{het}}$ , representing a point in phase space randomly selected from the unbiased probability distribution function (PDF) corresponding to the heterogeneous geometry, is generated using the same components of  $\boldsymbol{\beta}_{m,n}^{\text{hom}}$  with an additional correction factor on  $W_{m,n}^{\text{hom}}$  reflecting the presence of heterogeneities. Under this description,  ${}^*\boldsymbol{\beta}_{m,n}^{\text{het}}$  is defined as:

$${}^*\boldsymbol{\beta}_{m,n}^{\text{het}} = (\mathbf{r}_{m,n}, E_{m,n}, \boldsymbol{\Omega}_{m,n}, W_{m,n}^{\text{het}}) \quad (2.2.2)$$

The  $W_{m,n}^{\text{het}}$  quantity is the product between  $W_{m,n}^{\text{hom}}$  and the ratio between the unbiased and biased PDF's for sampling points in phase space,

$$W_{m,n}^{\text{het}} = W_{m,n}^{\text{hom}} \times \frac{P_{\text{het}}(\boldsymbol{\beta}_{0,0}^{\text{hom}}, \dots, \boldsymbol{\beta}_{m,n}^{\text{hom}})}{P_{\text{hom}}(\boldsymbol{\beta}_{0,0}^{\text{hom}}, \dots, \boldsymbol{\beta}_{m,n}^{\text{hom}})} \quad (2.2.3)$$

where  $P_{\alpha}(\boldsymbol{\beta}_{0,0}^{\text{hom}}, \dots, \boldsymbol{\beta}_{m,n}^{\text{hom}})$  represents the probability of selecting  $\boldsymbol{\beta}_{0,0}^{\text{hom}}, \dots, \boldsymbol{\beta}_{m,n}^{\text{hom}}$  in  $\alpha$  geometry. This weight correction factor removes the obvious bias arising from scoring heterogeneous dose using histories sampled from PDF's corresponding to a homogeneous medium. Calculation of  $W_{m,n}^{\text{het}}$  is facilitated by assuming a free electron scattering model that neglects characteristic x-ray emission and coherent scattering. Complete electron absorption following photoelectric interactions and Klein-Nishina scattering is also assumed. These two previous approximations have been shown to be accurate for low-energy brachytherapy dosimetry<sup>76</sup>. Because  ${}^*\boldsymbol{\beta}_{m,n}^{\text{het}}$  and  $\boldsymbol{\beta}_{m,n}^{\text{hom}}$  use the same sequence of collisions to score dose, their respective dose tallies are

frequently tightly correlated. In practice, this correlation is exploited by scoring the dose difference,

$$\Delta d_{ijk,m,n}^c = f_{ijk}^{\text{het}} (*\beta_{m,n}^{\text{het}}) - f_{ijk}^{\text{het}}(\beta_{m,n}^{\text{hom}}) \quad (2.2.4)$$

In this expression,  $ijk$  refers to a specific scoring voxel,  $f$  represents the scoring estimator, and  $\Delta d_{ijk,m,n}^c$  represents the CMC dose difference. The  $m$  and  $n$  subscripts denote the  $m^{\text{th}}$  history and  $n^{\text{th}}$  interaction. The final sample mean, signified by an over-line, is computed by summing together each random sample,  $\Delta d_{ijk,m,n}^c$  over the *interactions* and averaging over the *histories*,

$$\overline{\Delta D}_{ijk}^c = \frac{1}{N} \sum_{m=1}^N \sum_{n=1}^{M_m} \Delta d_{ijk,m,n}^c \quad (2.2.5)$$

The CMC estimate of the true  $D_{ijk}^{\text{het}}$ , (the expectation value of heterogeneous geometry sample mean over all possible sets of histories) is given by,

$$\overline{D}_{ijk}^{\text{het,c}} = D_{ijk}^{\text{hom}} \cdot \overline{HCF}_{ijk}^c, \text{ where } \overline{HCF}_{ijk}^c = 1 + \overline{\Delta D}_{ijk}^c / D_{ijk}^{\text{hom}} \approx 1 + \overline{\Delta D}_{ijk}^c / D_{ijk}^{\text{TG43}} \quad (2.2.6)$$

In this expression,  $HCF$  stands for the heterogeneity correction factor and  $\overline{HCF}_{ijk}^c$  is an unbiased estimate of its true value,  $HCF_{ijk} = D_{ijk}^{\text{het}} / D_{ijk}^{\text{hom}}$ .  $\overline{D}_{ijk}^{\text{het}}$  represents the computed heterogeneous dose using traditional, uncorrelated MC (UMC) methodology and is also an unbiased estimate of  $D_{ijk}^{\text{het}}$ .

In practice, exact  $D_{ijk}^{\text{hom}}$  computation requires additional Monte Carlo resources and would contribute to an overall loss in efficiency compared to UMC methods. Fortunately,  $D_{ijk}^{\text{hom}}$  can be well approximated using fast deterministic methods such as the TG-43 methodology<sup>3</sup>,  $D_{ijk}^{\text{hom}} \approx D_{ijk}^{\text{TG43}}$  as illustrated in eq. (2.2.6). Since  $D_{ijk}^{\text{TG43}}$  can be known with negligible statistical uncertainty, the only uncertainty in eq. (2.2.6) is due to  $\overline{\Delta D}_{ijk}^c$ . For tightly correlated

\*  $\beta_n^{\text{het}}$  and  $\beta_n^{\text{hom}}$  pairs, it can be shown<sup>67</sup> that for the variance,  $V$ ,

$$V(\overline{D}_{ijk}^{\text{het,c}}) = V(\overline{\Delta D}_{ijk}^c) \ll V(\overline{D}_{ijk}^{\text{het}}) \quad (2.2.7)$$

However, a positive covariance cannot be guaranteed<sup>67,77</sup> thus implying that efficiency could decrease in regions where local cross-sections and absorption properties deviate substantially from liquid water.

### 2.3 PTRAN Implementation

The correlated sampling technique described above, was implemented as an option within the more general MBDCA MC code family, PTRAN<sup>33,48,67,71-75,78</sup>. An extensive review of the capabilities of PTRAN can be found in Section II.B of Appendix B. Notably, in addition to PTRAN's capability to model various volume sources, a general brachytherapy phase-space source model was also implemented, and used for all PTRAN calculations completed for this study. More about the phase space source model can be read in Section 2.6.2.

Although correlated Monte Carlo had previously been implemented within PTRAN for both analytic and CT-based geometries by Drs. Williamson and Yi Le [Hedtjarn 2000 and Yi Abstract], they lacked robustness and generality for general brachytherapy applications. For this reason, I completely restructured the CMC code allowing general use for all source types within any combination of analytic and CT geometries and ensuring consolidating the multiple PTRAN libraries into a single library that supports all members of the PTRAN family.

### 2.4 Case Studies

Two brachytherapy patient cases were utilized to compare CMC relative to UMC for accuracy and efficiency. A detailed description is given in Appendix B section II.C, but each case is given a brief description here:

1. A post-implant CT of a permanent seed brachytherapy (PSB) prostate cancer patient with an 82 mL gland was implanted with 78 Model-6711 <sup>125</sup>I seeds with air-kerma



strengths  $0.636 \text{ U/seed}$  ( $1 \text{ U} = 1 \mu\text{Gy}\cdot\text{m}^2 / \text{h}$ ) and a prescribed  $D_{100}$  of 145 Gy. Using a ramp function, utilized by our clinic, a modified version of CTCREATE (ctcreate input file included as Appendix F), taken from the DOSXYZnrc<sup>79</sup> code family, and was used to assign each voxel of a single-energy CT to one of 55 different voxel-specific tissue compositions and density assignments. Assignment was made based on each voxel's Hounsfield unit (HU) intensity. Three different voxel grid sizes were studied:  $1\times 1\times 1 \text{ mm}^3$ ,  $2\times 2\times 2 \text{ mm}^3$ , and  $1\times 3\times 3 \text{ mm}^3$ .

2. A segmented breast CT image set, acquired on a breast-dedicated cone-beam CT imaging system<sup>36,44,80</sup>, was used to create a simulated  $^{103}\text{Pd}$  PSB post-lumpectomy implant. Following recommendations given by Pignol *et al*<sup>81</sup> a commercial treatment planning system<sup>1</sup> was used to generate an implant consisting of 87 Model 200 seeds with air-kerma strengths of 1.590 U. The implant was designed to deliver a prescribed  $D_{100}$  dose of 90 Gy to the CTV. The 44.6 mL CTV was defined to be a 1 cm expansion of a simulated spherical lumpectomy cavity with diameter of 2.4 cm. To minimize de-correlation between the homogeneous and heterogeneous geometry photon histories, an average breast composition<sup>11</sup> consisting of 85% adipose and 15% fibro-glandular tissue was used to compute  $D_{ijk}^{\text{hom}}$ . This change to the  $D_{\text{hom}}$  media increased the correlation between the homogeneous and heterogeneous photon histories and its effect on efficiency will be explored later in Section 2.6.1. Only one voxel grid was investigated:  $0.67\times 0.67\times 0.67 \text{ mm}^3$ .

<sup>1</sup> Varian VeriSeed 8.0

## 2.5 Accuracy of Correlated Monte Carlo

Accuracy of  $\bar{D}_{ijk}^{\text{het,c}}$  relative to  $\bar{D}_{ijk}^{\text{het}}$  was quantitatively evaluated using a method taken from Kawrakow *et al*<sup>82</sup>. The distribution of dose differences at each voxel  $ijk$  receiving more than 50% of the prescribed dose was evaluated and expressed as multiples of the combined statistical uncertainty,

$$z_{ijk} = \left( \left( \bar{D}_{ijk}^{\text{het,c}} - \bar{D}_{ijk}^{\text{het}} \right) / \sqrt{\sigma_{\bar{D}_{ijk}^{\text{het,c}}}^2 + \sigma_{\bar{D}_{ijk}^{\text{het}}}^2} \right) \quad (2.5.1)$$

The quantity  $z_{ijk}$  is defined as the difference between  $\bar{D}_{ijk}^{\text{het,c}}$  and  $\bar{D}_{ijk}^{\text{het}}$  expressed in multiples of standard deviations about the mean. In the absence of any systematic error or bias, the distribution of  $z_{ijk}$  would exhibit Gaussian form with a mean of zero and standard deviation of 1,

$$f(z) = \frac{1}{\sqrt{2\pi}} e^{-z^2/2} \quad (2.5.2)$$

To separate the random and systematic components of the CMC error, the  $z_{ijk}$  frequency histogram was fit to a function proposed by Kawrakow *et al*<sup>82</sup>,

$$f(z) = \frac{1}{\sqrt{2\pi}} \left[ \alpha_1 e^{-\frac{(z-\beta_1)^2}{2}} + \alpha_2 e^{-\frac{(z-\beta_2)^2}{2}} + (1-\alpha_1-\alpha_2) e^{-\frac{z^2}{2}} \right] \quad (2.5.3)$$

Eq. (2.5.3) can account for two normally distributed systematic errors, represented by the first two terms, with mean  $\beta_i$  with probability of occurrence,  $\alpha_i$ , where  $i=1,2$ . The remaining errors are purely statistical and represented by the final term.

Our investigation of CMC accuracy relative to UMC, using an unbiased MC solution for  $D_{ijk}^{\text{hom}}$ , is well documented in Appendix B, section III. Figure 2.1 is taken from Appendix B and displays

the frequency histograms of  $z_{ijk}$  for both prostate and breast with their corresponding fits to eq. (2.5.3). The best fit parameters with corresponding error interpretations are listed in Appendix B, Table II. Our analysis of CMC accuracy shows that CMC accurately reproduces UMC results with negligible systematic discrepancies. The largest difference was a 0.5% overestimation in less than 0.1% of the prostate voxels.

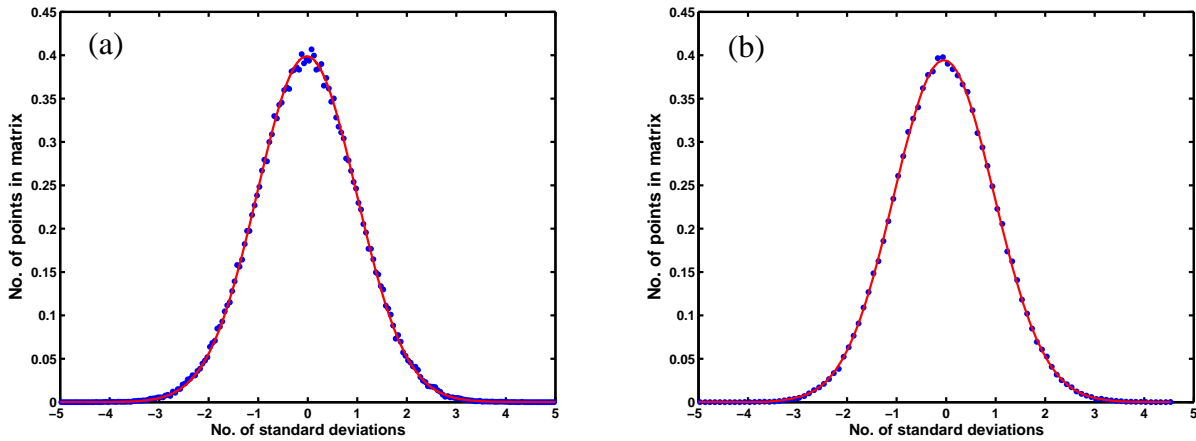


Figure 2.1: Frequency histogram of  $z_{ijk}$  (dots) for (a) prostate and (b) breast with their corresponding fits to  $f(z)$ .

## 2.6 Correlated Monte Carlo Efficiency

The efficiency of a Monte Carlo radiation transport calculation is often referred to as the “figure of merit” (FOM). It is defined as the inverse of the product between the final variance of the MC solution,  $\sigma^2$ , and the CPU time,  $t$ ,

$$FOM = \frac{1}{\sigma^2 \cdot t} \quad (2.6.1)$$

The efficiency gain for a voxel  $ijk$ ,  $G_{ijk}$ , is simply the ratio of FOM’s for the two simulations being compared,

$$G_{ijk} = \frac{FOM_{ijk}^{CMC}}{FOM_{ijk}^{UMC}} \quad (2.6.2)$$

Using eq. (2.6.2),  $G_{ijk}$  was computed for every  $ijk$  voxel for various anatomical regions within each patient case. For the breast case, the average  $G_{ijk}$  value was computed for the simulated lumpectomy cavity, and the CTV. Similarly, for the prostate case, the average  $G_{ijk}$  value was computed for the prostate (CTV), bladder, rectum, seminal vesicles, and urethra. For each anatomical region, the CPU time required to reach an average 2% statistical uncertainty about the mean was computed, as well, for both UMC and CMC methods. Additionally for both patient cases, the average value for  $G_{ijk}$  was also computed for the region that receives 50% of the prescribed dose.

Table IV in Appendix B reports substantial increases in the efficiency of Monte Carlo calculations for the prostate and breast geometries investigated. Most notably, of the regions that receive more than 50% of the prescribed dose, greater than 99.7% of the voxels for all prostate voxel grids enjoys a more than 25 fold increase in efficiency. For the breast, 100% of the voxels receiving more than 50% of the prescribed dose experience an average 55-fold efficiency gain relative to UMC.

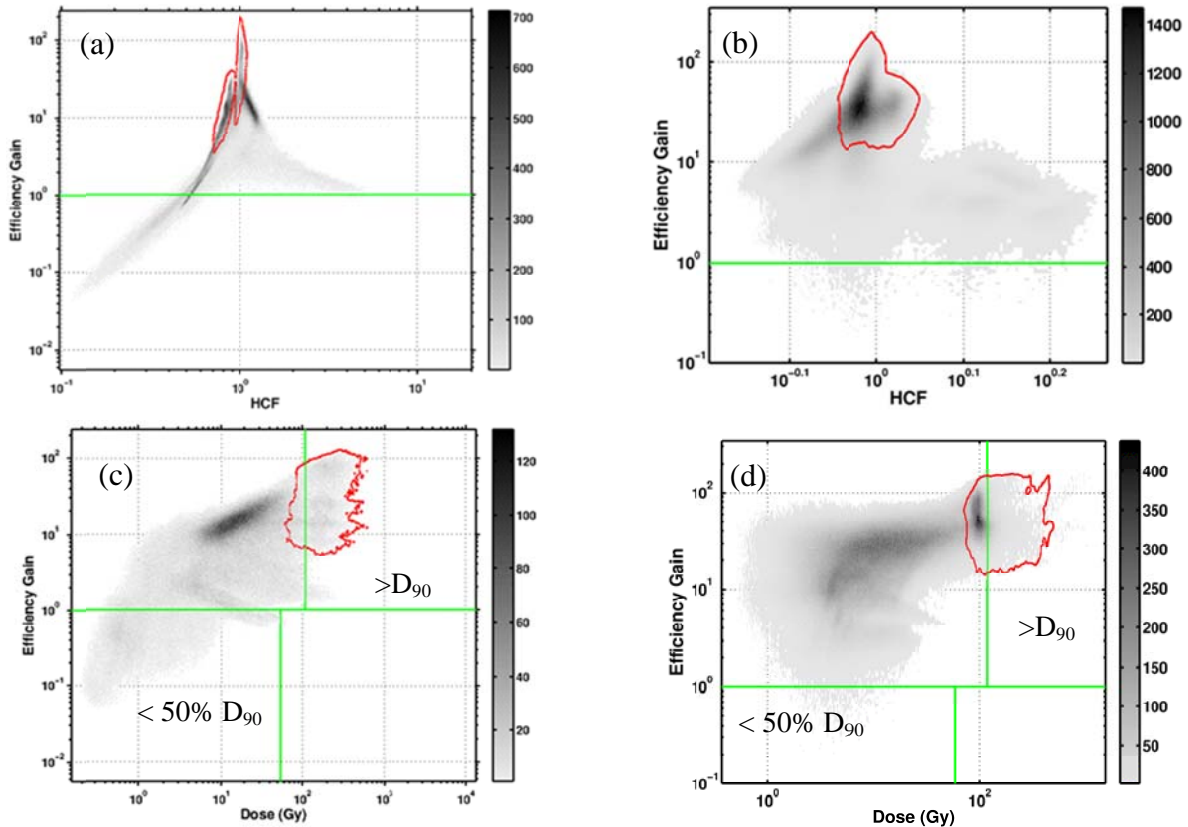


Figure 2.2: Scatter plot of the efficiency gain vs. the HCF for all voxels in the prostate (a) and breast (b) geometries; scatter plot of the efficiency gain vs. the delivered dose (Gy) for all voxels in the prostate (c) and breast (d) geometries. The area outlined in red circumscribes the voxels originating from the CTV.

Table 2-I: Average efficiency gain for the breast and prostate plans for various ROI's along with the estimated time required to compute Monte Carlo dose to achieve an average 2% percent standard deviations about the mean. Percentages within parentheses are the percentage of voxels within the corresponding structure that experience an efficiency gain greater than unity.

<b>Breast</b>		Time to achieve mean %SDM of 2%			Average Efficiency Gain		
	MC Type	(0.67 mm) <sup>3</sup>			(0.67 mm) <sup>3</sup>		
Lumpectomy	UMC	16.9 min			55.7 (100%)		
Cavity.	CMC	20.2 sec					
CTV	UMC	18.7 min			59.8 (>99.9%)		
	CMC	21.1 sec					
<b>Prostate</b>		Time to achieve mean %SDM of 2%			Average Efficiency Gain		
	MC Type	(1.0 mm) <sup>3</sup>	(2.0 mm) <sup>3</sup>	(3.0 mm) <sup>3</sup>	(1.0 mm) <sup>3</sup>	(2.0 mm) <sup>3</sup>	(3.0 mm) <sup>3</sup>
Prostate	UMC	15.3 min	1.59 min	30.9 sec	37.1 (100%)	44.7 (100%)	41.6 (100%)
(CTV)	CMC	38.6 sec	3.3 sec	1.1 sec			
Bladder	UMC	113 min	12.0 min	4.0 min	12.3 (99.3%)	13.5 (99.0%)	12.7 (97.5%)
	CMC	16.5 min	1.63 min	38.9 sec			
Rectum	UMC	45.2 min	4.55 min	1.44 min	14.0 (99.7%)	14.9 (99.1%)	14.3 (98.7%)
	CMC	4.7 min	27.4 sec	8.9 sec			
Seminal	UMC	29.1 min	3.02 min	56.9 sec	12.6 (99.4%)	14.0 (99.8%)	13.3 (99.3%)
Vesicles.	CMC	3.5 min	17.9 sec	6.23 sec			
Urethra	UMC	18.0 min	1.90 min	36.4 sec	43.2 (100%)	54.0 (100%)	54.1 (100%)
	CMC	38.9 sec	3.49 sec	1.13 sec			

Figure 2.2 shows the dependence of the efficiency gain on HCF and dose delivered. This figure shows that efficiency losses are localized to areas of lower dose, specifically, lower than 50% of the  $D_{90}$ . Additionally, for the prostate case, the losses were pronounced in regions where the HCF is less than unity. The breast geometry did not show this behavior, due to the decreased HCF range resulting from choosing average breast medium to estimate  $D_{ijk}^{hom}$ .

Table 2-I lists the average efficiency gains for the various anatomical regions listed above for both prostate and breast, demonstrating substantial gains over the already-optimized PTRAN UMC simulations.

Table 2-I also lists the time required for UMC and CMC to achieve an average 2% standard deviation about the mean. All times reported are for radiation transport, and not the time required to read in and set up the simulation geometry. CMC requires single-processor CPU times of only 38.6 sec, 3.3 sec, and 1.1 sec to achieve an average 2% standard deviation within the prostate using  $1 \times 1 \times 1 \text{mm}^3$ ,  $2 \times 2 \times 2 \text{mm}^3$ , and  $3 \times 3 \times 3 \text{mm}^3$  voxels, respectively. For the breast, only 21.1 sec is needed to achieve the average 2% standard deviation within the simulated CTV compared to 19 min for UMC. CMC increases efficiency for the breast implant on average by 59 fold with practically 100% of the voxels enjoying an efficiency gain. Similarly, 100% of the voxels within the prostate CTV experienced an improvement of more than 37 times over UMC for all three voxel sizes.

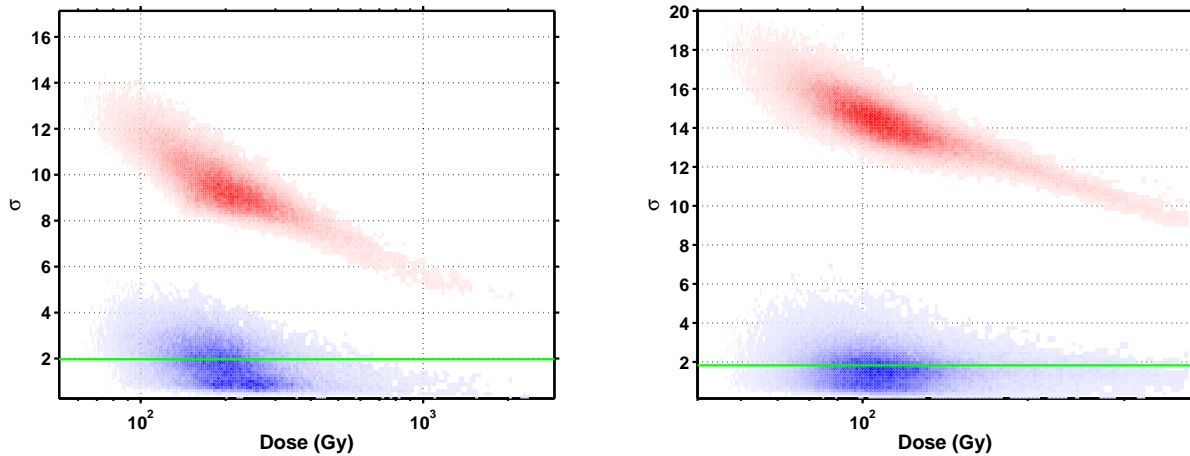


Figure 2.3: Scatter plot of percent standard deviation about the mean vs. dose for each individual voxel within the (a) prostate and (b) breast CTV for correlated (lower) and uncorrelated Monte Carlo (upper). The average percent standard deviation about the mean value for correlated Monte Carlo is plotted as a green line. Run-times were 39 sec and 21 sec for prostate and breast, respectively.

Figure 2.3 presents a scatter plot of the percent standard deviation about the mean vs. dose for each individual voxel within the prostate and breast following CPU run-times of 39 sec and 21 sec, respectively. Even though some voxels experience an efficiency loss, these voxels generally have a CMC uncertainty well below the average UMC uncertainty, showing CMC is globally advantageous despite the few voxels that exhibit increased statistical uncertainty. In other words, in all cases investigated to date, CMC always reduces maximum uncertainty in 3D arrays of voxel detectors.

### 2.6.1 Choice of Homogeneous medium for Breast Implants

Our CMC simulation for breast PSB used an average breast tissue in place of the homogeneous water medium to compute an estimate to  $D_{ijk}^{\text{hom}}$ . As shown in eq. (2.2.7), the variance of  $\bar{D}_{ijk}^{\text{het,c}}$  is substantially less than that of  $\bar{D}_{ijk}^{\text{het}}$ , but only in circumstances that maintain positive correlation between  $^* \beta_{m,n}^{\text{het}}$  and  $\beta_{m,n}^{\text{hom}}$  scores. Because  $^* \beta_{m,n}^{\text{het}}$  uses the same phase-space components as  $\beta_{m,n}^{\text{hom}}$ , the only differences between them are their respective particle weight values. From eq. (2.2.3),

as long as the HCF is close to unity, then the correlation remains very high. The breast geometry does not maintain a high correlation when using a homogeneous water medium to estimate  $D_{ijk}^{\text{hom}}$  because the breast contains a large fraction of adipose tissue which has a linear attenuation coefficient only 65% of that of water at 20 keV.

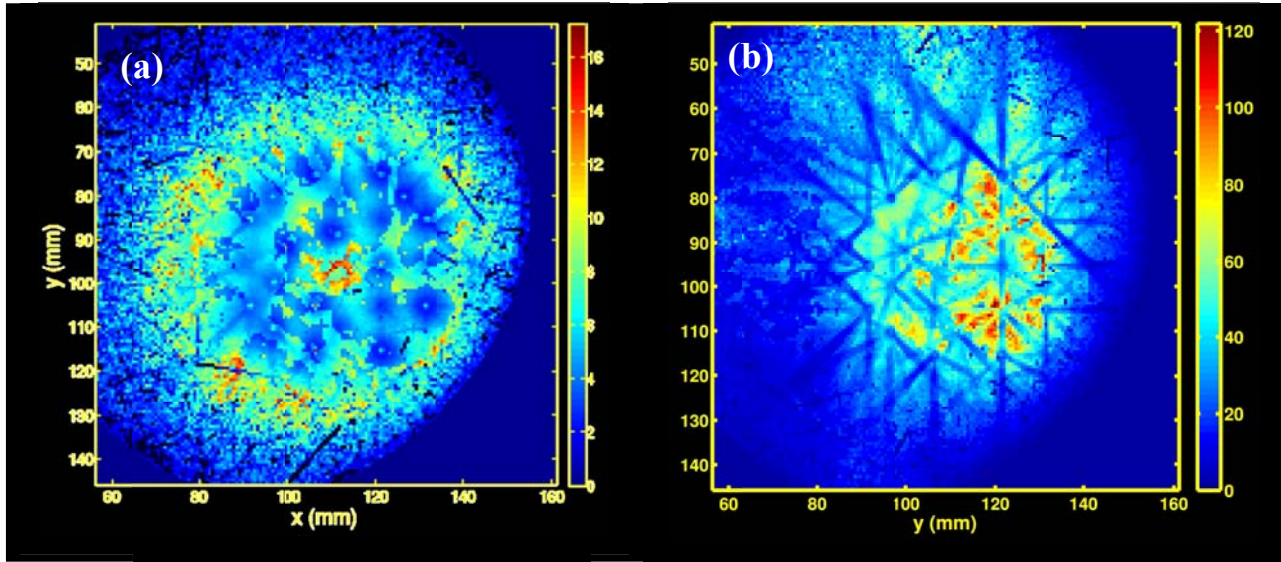


Figure 2.4: Central slice through breast simulated implant showing efficiency gain using (a) liquid water and (b) average breast medium to compute homogeneous dose.

Figure 2.4 shows a central slice through the simulated breast implant using liquid water as the homogeneous medium. Looking closely, the adipose and glandular tissue boundaries are visible, showing larger efficiencies in the glandular regions. Within the adipose regions, smaller 2 to 8 fold efficiency gains are observed. The visible streaks were found to be due to successive interactions within the adipose tissue, causing de-correlation between  $\beta_{m,n}^{\text{het}}$  and  $\beta_{m,n}^{\text{hom}}$ . Changing the homogeneous medium composition from liquid water to average breast medium44 recovered substantial correlation between  $\beta_{m,n}^{\text{het}}$  and  $\beta_{m,n}^{\text{hom}}$ , subsequently achieving the gains reported in this dissertation. Interestingly enough, streaks still remain following the homogeneous medium change, as seen in Figure 2.4(b). These streaks still correspond to a loss of correlation between



\* $\beta_{m,n}^{\text{het}}$  and  $\beta_{m,n}^{\text{hom}}$ , due to inter-seed attenuation effects. The Theragenics model 200 source contains a lead marker, as pictured in Figure 2.5, taken from the AAPM TG-43 update report<sup>3</sup>. As a primary photon emerges from a seed and interacts within the lead marker of a neighboring seed, the correlation between \* $\beta_{m,n}^{\text{het}}$  and  $\beta_{m,n}^{\text{hom}}$  brakes down, reducing efficiency gains along the lines connecting neighboring seeds. Although these remaining streaks inhibit potential efficiency gains, they do not cause efficiency losses. Referring again to Table 2-I, practically 100% of the breast CTV voxels report an improvement in efficiency relative to UMC.

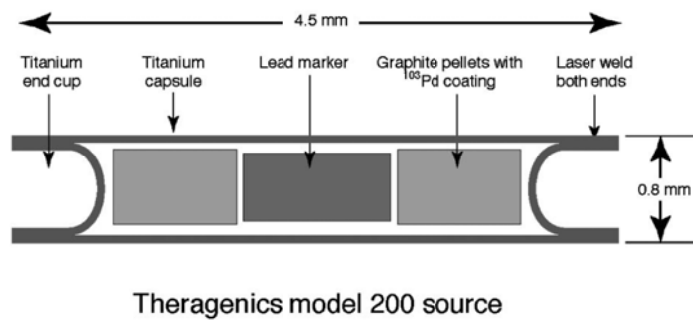


Figure 2.5: picture representation of the model 200 <sup>103</sup>Pd source from Theragenics.

## 2.6.2 Phase Space Model

A phase space source model is a list of phase space coordinates describing particles that have crossed a threshold of some sort. For the simulation of brachytherapy seeds, the outer seed encapsulation acts as the threshold: when a particle crosses the seed encapsulation, the particle is tallied and its phase space parameters are added to the phase space file. When utilizing a phase space source, instead of randomly selecting the phase space parameters of a primary particle from probability density functions, a particle is read from the previously generated file in consecutive order and transported as a primary particle. Use of a phase space source in and of

itself can be a powerful variance reduction technique (source biasing) when the geometry upstream of the threshold remains constant for various simulation environments. The phase space source model allows for the inclusion of atomic relaxation, characteristic x-ray emission, and electron binding for interactions occurring within the source. None of these effects are modeled in correlated sampling due to the weight correction factor found in eq. (2.2.3). Many brachytherapy seed designs incorporate high Z materials, as radio-opaque markers, that add significant number of characteristic x-rays to the fluence exiting the seed encapsulation. Since the phase-space source incorporates the full physics model, CMC utilizing a phase-space source can accurately reproduce UMC dose maps, as shown by Figure 2.1. As a side note, when employing a phase-space source, the user must ensure the file read time is not a detriment to the potential efficiency gains desired.

Use of the phase-space source model also increases the correlation between  $\beta_{m,n}^{*het}$  and  $\beta_{m,n}^{hom}$ , thus increasing the CMC efficiency. Since the phase-space model includes self-attenuation of the source for computation of the homogeneous dose distribution, the difference between the homogeneous and heterogeneous dose is reduced. This reduction increases the likelihood that a single heterogeneity found in the geometry can be treated as a perturbation. Figure 1 in Appendix A illustrates this principle, shown in the decreased values of the HCF for the prostate relative to those found in Figure 2.2(a).

### 2.6.3 Programming Memory Management

Tables 1 and 2 and Tables III and IV in Appendices A and B, respectively contain the same efficiency metrics, but report different values. In fact, the values reported in Appendix B are improved by a factor of 5 over those in Appendix A. This raises the following question: If they

report the same efficiency metrics, then why are they so different? To answer this question it is necessary to highlight the differences between the two simulations that produced the data: (1) Appendix B used more modern computer resources, and (2) a major modification to memory management was made for the simulations in Appendix B. The first difference has no bearing in the improvement of the efficiency gains reported in either study because the gains were relative to non-correlated simulations on the same computer architecture.

All Monte Carlo algorithms are statistical in nature and have a measure of uncertainty associated with the final estimated value. In 2001, Sempau *et al*<sup>83</sup> introduced a very fast and simple method to compute this uncertainty for radiation transport applications. With the aim of computing the homogeneous or heterogeneous dose, this method requires the storage and accessibility of five large arrays that are indexed to match the voxel grid: mean dose to voxel per history (for both primary and scatter separately), mean squared dose to voxel per history (for both primary and scatter separately), and the history index of the last photon that contributed to the voxel of interest. In the case of CMC, where the heterogeneous dose, homogeneous dose, and their difference are all tracked, fifteen 3-D arrays are required. Up to nine of these arrays are accessed each time a collision is scored. When utilizing 3-D grid optimized scoring routines, such as the expected track-length estimator<sup>74</sup>, then each array is accessed for multiple voxels every scoring event.

FORTTRAN assigns memory addresses according to what is called “column major.” This means that for a 2-D array, successive elements in memory follow the column. For example, given an array,  $\Omega$ , of size  $[3 \times 3]$ , column order means that consecutive memory addresses are given the following values in the following order:

$$[\Omega(1,1), \Omega(2,1), \Omega(3,1), \Omega(1,2), \Omega(2,2), \Omega(3,2), \Omega(1,3), \Omega(2,3), \Omega(3,3)]$$

If there is a third dimension, then that index would change next. Since fifteen 3-D arrays must be accessed consecutively for the same 3-D indices,  $ijk$ , there was a considerable amount of computational overhead spent jumping between widely separated memory locations.

To resolve this issue, I rewrote how the CMC uncertainty arrays were mapped into memory. Instead of being 3-D arrays, they became 1-D arrays with the following mapping from the 3-D  $ijk$  indices to a single 1-dimensional index,

$$\text{index}_{1-D} = n_z n_y (k-1) + n_x (j-1) + i \quad (2.6.3)$$

where  $n_x$ ,  $n_y$ , and  $n_z$  represents the number of voxels in the x, y and z dimensions. All fifteen 1-D arrays were then joined together to form one large 2-D array with dimensions of  $[15 \times (n_x n_y n_z)]$ .

For each scoring event, the updated values for each voxel index in the array are now adjacent to one another in memory because the columns now index array identity and have consecutive memory locations. Following this change, the 5-fold increase in efficiency from the data presented in Appendix A to Appendix B was realized.

Without this change, we would have erroneously concluded that CMC only modestly improved efficiency. When programming variance reduction strategies or other algorithms intended to increase the efficiency, it is imperative that memory management be optimized as well, so that increases in memory access time do not overshadow efficiency gains.

## 2.7 Discussion

Under many circumstances, CMC reduces the MC variance relative to UMC calculations.

However, regions with low dose or large dose differences between  $D_{ijk}^{\text{hom}}$  and  $D_{ijk}^{\text{het}}$  due to tissue

heterogeneities can experience diminished gains or even efficiency losses. Specifically, diminished gains were evident in Figure 2.4(b) caused by inter-seed attenuation effects due to the lead marker enclosed within the seed. On the other hand, both cases investigated by our study demonstrated reduction of the maximum and mean dose-uncertainty in anatomical regions of clinical relevance. We have shown that CMC is globally advantageous notwithstanding the small number of voxels that exhibit increased statistical uncertainty relative to UMC.

In comparison with other optimized codes, Yegin *et al*<sup>84</sup> reported full prostate dose calculations with 5 min run-times using BrachyDose, based on EGSnrc<sup>85</sup>. In addition, Thomson *et al*<sup>86</sup> reported 30 sec run-times using BrachyDose for  $2 \times 2 \times 2$  mm<sup>3</sup> voxels. Chibani *et al*<sup>6</sup> similarly reported run times in under 1 min for a  $2 \times 2 \times 2$  mm<sup>3</sup> voxel mesh. In contrast, PTRAN\_CT CMC computes dose under these same conditions in 3.3 sec.

Fast dose-computation execution is not the only barrier to clinical acceptance of model based dose calculation algorithms. For low-energy brachytherapy, the task of correctly assigning tissue cross sections to organs or individual voxels is an important unsolved problem<sup>87-89</sup>. Potentially, this issue could be addressed through quantitative imaging techniques such as dual-energy CT<sup>88,90-92</sup>.

## 2.8 Conclusion

Correlated Monte Carlo (CMC) was implemented and was shown to be a powerful and accurate tool for the post-implant analysis/treatment planning of permanent seed brachytherapy. CMC can be used confidently and efficiently, able to provide accurate dose maps in seconds, for patient-specific dose calculations. Barriers to full implementation include a user-friendly interface and accurate characterization of patient tissues for low keV applications.



# 3. Interpolated Correlated Monte Carlo

## 3.1 Introduction

The previous chapter introduced the correlated Monte Carlo (CMC) method for increasing the efficiency of brachytherapy dose calculations as a step towards implementing patient-specific model based dose calculation algorithms (MBDCA's) in the clinical setting. CMC provided an efficiency increase of over 30 to 40 fold relative to optimized un-correlated Monte Carlo (UMC) allowing single, high-resolution, dose distributions to be computed in under a minute. While CMC provides a reasonable framework for post-implant dosimetry, an additional increase in efficiency would be useful in applications that require multiple dose maps to be computed iteratively. For example, treatment planning optimization requires hundreds of dose maps to be computed for convergence<sup>93-97</sup>. If CMC were applied in conjunction with a genetic algorithm, like the one proposed by Lee et al<sup>93</sup>, with 1000 iterations for a  $1 \times 1 \times 1 \text{mm}^3$  voxel volume, then 11 hrs are required for the Monte Carlo (MC) calculations alone. Additional improvement in efficiency of these calculations is therefore needed for clinical application. This chapter focuses on a method used in conjunction with CMC that takes advantage of a fundamental difference between CMC and uncorrelated, standard Monte Carlo (UMC). We call this method interpolated correlated Monte Carlo (ICMC).

## 3.2 Interpolated Correlated Monte Carlo

Typically, a small voxel volume of  $1 \times 1 \times 1 \text{mm}^3$  or lower is desirable in brachytherapy to reduce volume averaging errors. Unfortunately, smaller voxels require more computation time since MC efficiency scales linearly with voxel volume. The voxel averaging error arises from averaging

over the high brachytherapy dose gradients from inverse square law effects. The inverse square law could be substantially restrained by subtracting  $\bar{D}_{ijk}^{\text{hom}}$  from  $\bar{D}_{ijk}^{\text{het}}$ , potentially leaving  $\overline{\Delta D}_{ijk}^{\text{CMC}}$  free from high gradients. This suggests that a high resolution approximation to  $D_{ijk}^{\text{het}}$  could be recovered by interpolating a low resolution (LR)  $\overline{\Delta D}_{ijk}^{\text{CMC}}$  to a high resolution (HR) grid, followed by summation with a HR solution to  $D_{ijk}^{\text{hom}}$ . We hypothesize that interpolation and partial volume errors in this composite solution are much lower than interpolating a LR  $\bar{D}_{ijk}^{\text{het}}$  to a HR grid. To test this hypothesis, we introduce the Interpolated Correlated Monte Carlo (ICMC) technique for computing high resolution (HR) dose maps from low resolution  $\overline{\Delta D}_{ijk}^{\text{CMC}}$  Monte Carlo calculations. To clarify, we hypothesize that ICMC can compute brachytherapy dose maps with accuracy comparable to HR-UMC in the same amount of time as a LR-CMC solution.

This process is described by Figure 3.1. First, a fast deterministic HR approximation to  $D_{ijk}^{\text{hom}}$ ,  $D_{ijk,\text{HR}}^{\text{TG43}}$ , is computed using the TG-43 protocol. Simultaneously, CMC is used to compute  $\overline{\Delta D}_{ijk,\text{LR}}^{\text{CMC}}$  on a LR voxel grid which is then interpolated onto the HR grid, yielding  $\Delta D_{ijk,\text{HR}}^{\text{ICMC}}$ . Finally, the  $\Delta D_{ijk,\text{HR}}^{\text{ICMC}}$  and  $D_{ijk,\text{HR}}^{\text{TG43}}$  arrays are added together voxel-by-voxel, yielding  $D_{ijk,\text{HR}}^{\text{ICMC}}$ , which approximates the true value of  $D_{ijk}^{\text{het}}$  as computed directly on the HR grid.



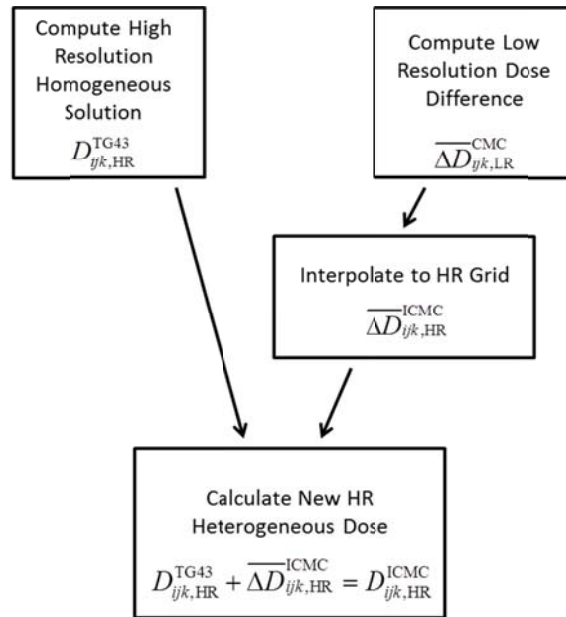


Figure 3.1: Flow chart describing the interpolated correlated Monte Carlo (ICMC) method.

For comparison purposes with ICMC, another method, called interpolated Monte Carlo (IMC) is also explored. IMC involves computing  $\overline{D}_{ijk}^{het}$  on a LR grid, using standard UMC, followed by interpolation to the HR grid to yield  $D_{ijk,HR}^{IMC}$ .

### 3.3 Simulation Cases

The same two patient cases described in Chapter 2 were used in this study along with an additional case:

A post-implant CT of a permanent seed brachytherapy (PSB) prostate cancer patient with an 82 mL gland was implanted with 78 Model-6711  $^{125}\text{I}$  seeds with air-kerma strengths 0.636 U/seed (1 U = 1  $\mu\text{Gy}\cdot\text{m}^2/\text{h}$ ) and a prescribed  $D_{100}$  of 145 Gy. Using CTCREATE from the DOSXYZnrc<sup>79</sup> code family, each voxel of a single-energy CT was assigned one of 55 voxel-specific tissue compositions and densities based on Hounsfield unit (HU) intensity. This prostate geometry will be referred to as the “custom ramp prostate.”

A segmented breast CT image set, acquired on a breast-dedicated cone-beam CT imaging system<sup>36,44,80</sup>, was used to create a simulated <sup>103</sup>Pd permanent seed brachytherapy (PSB) post-lumpectomy breast implant following the PSB partial breast irradiation recommendations given by Pignol *et al*<sup>81</sup>. Using a commercial treatment planning system<sup>2</sup> the 44.6mL CTV was defined to be a 1 cm expansion of a simulated spherical lumpectomy cavity with diameter of 2.4 cm. An implant consisting of 87 Model 200 seeds with air-kerma strengths of 1.590 U was designed to deliver a prescribed D<sub>100</sub> dose of 90 Gy to the CTV. Because of the high fraction of adipose tissue in the breast, rather than using liquid water for the computation of  $D_{\text{hom}}$  via the TG-43 method, a homogeneous average breast composition<sup>11</sup> medium consisting of 85% adipose and 15% fibroglandular tissue was used to reduce the range of HCF values. This change to the  $D_{\text{hom}}$  media increased the correlation between the homogeneous and heterogeneous photon histories as explained in Chapter 2.

The post-implant prostate CT used for the custom ramp prostate was mapped to 4 different ICRU tissues using the example, default material ramp in CTCREATE: air, lung, muscle, and bone. For the “default ramp prostate,” the prostate CTV was further segmented into simulated transitional, central and peripheral zones given media assignments picked from a muscle-like media list utilized by our clinic. Tissue compositions are listed in Table 3-I.

---

<sup>2</sup> Varian VeriSeed 8.0

Table 3-I: Tissue compositions for default ramp prostate geometry. Values are presented as percentage weight.

Region	Tissue Elemental Composition
peripheral	H: 10.8%; C: 36.6%; N: 2.1%; O: 49.9%; Na: 0.1%; P: 0.15%; S: 0.18%; Cl: 0.1%; K: 0.15%
transitional	H: 10.0%; C: 31.5%; N: 2.4%; O: 54.7%; Na: 0.1%; P: 0.20%; S: 0.20%; Cl: 0.1%; K: 0.20%
central	H: 10.9%; C: 41.6%; N: 1.9%; O: 45.1%; Na: 0.1%; P: 0.10%; S: 0.15%; Cl: 0.1%; K: 0.10%

All UMC Simulations were performed on a HR  $1 \times 1 \times 1 \text{ mm}^3$  (1 mm) voxel grid while IMC and ICMC calculations were initially executed on the LR  $2 \times 2 \times 2 \text{ mm}^3$  and  $3 \times 3 \times 3 \text{ mm}^3$  (2 mm and 3 mm respectively) voxel grids before interpolation. Additionally, the interaction cross-sections and mass-energy absorption coefficients for the LR voxels were assigned average values over the corresponding HR voxel volume.

### 3.4 Efficiency

The main benefit from ICMC is the efficiency gain granted by computing the Monte Carlo contribution to  $D_{ijk,HR}^{ICMC}$  for voxels with larger volumes. As stated in the previous chapter, the efficiency of a Monte Carlo radiation transport calculation is often referred to as the “figure of merit” (FOM). It is defined as the inverse of the product between the variance,  $\sigma^2$ , and the corresponding CPU time,  $t$ :

$$FOM = \frac{1}{\sigma^2 \cdot t} \quad (3.4.1)$$

The efficiency gain of ICMC relative to UMC at voxel  $ijk$  is simply the ratio of FOM's :

$$G_{ijk} = \frac{FOM_{ijk}^{ICMC}}{FOM_{ijk}^{UMC}} \quad (3.4.2)$$

Table 3-II tabulates the average value for  $G_{ijk}$  achieved through the various methods discussed: IMC, CMC, ICMC along with the expected CPU time required for the CTV to reach an average 2% standard deviation about the mean. The IMC and ICMC efficiencies are specified relative to the corresponding 1 mm voxel UMC simulation while the average CMC efficiency gain is specifically relative to the UMC calculation on the same grid size. Note that the CPU times for ICMC and CMC on the 2.0 mm and 3.0 mm voxels are the same due to their using the same calculation for each method. In other words, the 2.0 mm and 3.0 mm CMC calculations are compared against a UMC 2.0 mm and 3.0 mm solution respectively. ICMC results, on the other hand, are compared to a 1.0 mm UMC solution because, ICMC estimates dose on the HR, 1.0 mm grid, even though the Monte Carlo simulation is performed on LR voxels.

Table 3-II not only highlights the strength of the CMC variance reduction technique, showing 37-68 fold increases in efficiency on the HR grid, but also shows the additional power of ICMC relative to UMC calculations. Both the prostate and breast showed efficiency increases up to three orders of magnitude relative to UMC, suggesting CPU times of 1 sec or below to reach an average 2% standard deviation about the mean for the CTV volumes. Specifically, the breast 2 mm and 3 mm showed gains of 452 and 1507 fold respectively for HR 1 mm voxels. For the 3 mm ICMC calculation, this corresponds to an anticipated run time of 0.39 sec to reach an average 2% uncertainty in the 1 mm CTV voxels. Furthermore, the prostate shows efficiency gains of 523 and 1460 for the 2 mm and 3 mm grid respectively with corresponding run times of 3.3 and 1.1 sec. These times represent significant improvements over previously published methods. The clinical impact of these results is discussed in Section 3.6.

Table 3-II: Average efficiency gain for the breast and prostate cases with the estimated time required to compute Monte Carlo dose to achieve 2% standard deviation about the mean (for IMC and CMC this is for 1 mm voxels). All gains are relative to uncorrelated Monte Carlo. The CMC gains reported are relative to a UMC simulation using the same voxel size. The ICMC and IMC gains are relative to the corresponding (1.0 mm)<sup>3</sup> voxel UMC simulations, whereas CMC gains are relative to UMC for same voxel size.

MC Type		Time to achieve mean %SDM of 2%			Average Efficiency Gain		
		1.0 mm	2.0 mm	3.0 mm	1.0 mm	2.0 mm	3.0 mm
Breast		1.0 mm	2.0 mm	3.0 mm	1.0 mm	2.0 mm	3.0 mm
CTV	UMC	9.8 min	1.0 min	23.7 s	N/A	N/A	N/A
	IMC	N/A	1.0 min	23.7 s	N/A	9.8	24.8
	CMC	9.8 s	1.3 s	0.39 s	68.0	55.5	66.1
	ICMC	N/A	1.3 s	0.39 s	N/A	452	1507
Prostate		1.0 mm	2.0 mm	3.0 mm	1.0 mm	2.0 mm	3.0 mm
CTV	UMC	15.3 min	1.6 min	30.9 s	N/A	N/A	N/A
	IMC	N/A	1.6 min	30.9 s	N/A	9.6	29.7
	CMC	38.6 s	3.3 s	1.1 s	37.1	44.7	41.6
	ICMC	N/A	3.3 s	1.1 s	N/A	523	1460

### 3.5 ICMC Accuracy

To quantify the errors associated with the ICMC approximation relative to HR UMC, the

individual voxel error,  $\left( \frac{D_{ijk}^{ICMC}}{\overline{D}_{ijk}^{het}} - 1 \right) \times 100$ , and differences in the  $D_{90}$  and  $V_{200}$  DVH metric were

evaluated. A significant effort was made to separately quantify three sources of error associated with the ICMC methodology: the inverse square law gradient effect (ISGE), cross-section gradient effect (CSGE), and the local absorption gradient effect (LAGE).

#### 3.5.1 ICMC Total Error

Before I present each individual error source, the total ICMC error and its effect on the dose distribution and the DVH metrics relative to the UMC 1 mm voxel case are evaluated. Figure 3.2 shows the total percentage error distribution for the ICMC and IMC methods, and Table 3-III contains the corresponding quantitative metrics. The metrics contained in Table 3-III were computed by converting the distribution of errors to a cumulative probability density function. Figure 3.2 and Table 3-III do not clearly demonstrate a general improvement with accuracy from ICMC relative to IMC for all three geometries. The only case with substantial improvement in

accuracy is in the breast case where the mean error and standard deviation were reduced to .01% and by 3 fold, respectively, for both LR grids. On the other hand, improvement for both prostate cases was marginal.

Table 3-IV contains the comparisons for the DVH metrics  $D_{90}$  and  $V_{200}$  for all three geometries. Viewing the ICMC error in terms of DVH metrics instead of voxel-to-voxel ratios, as in Figure 3.2, the accuracy advantage of ICMC over IMC becomes apparent. Compared to IMC, ICMC increases  $D_{90}$  accuracy twofold to within 2% of the HR-UMC value for both LR grids while a four-fold accuracy increase is observed for the  $V_{200}$  where the inverse square law has greatest effect on the dose distribution. To highlight this, Figure 3.3(a) shows an overlay of the isodose curves for both the UMC and 3.0 mm ICMC. All three cases show barely distinguishable features between the UMC and ICMC calculations with a few localized isodose curve displacements of 2-3 mm or less.

Table 3-III: Quantitative metrics describing the total percent error distributions for the ICMC and IMC simulation relative to the corresponding UMC calculations. MPV stands for most probable value.

Custom Ramp Prostate	Mean	Std. Deviation	20 <sup>th</sup> Percentile	80 <sup>th</sup> Percentile	MPV
IMC (2.0 mm)	0.43	11.7	-5.78	8.98	-0.03
IMC (3.0 mm)	0.79	14.01	-6.13	10.33	1.48
ICMC (2.0 mm)	-0.86	10.96	-6.98	7.18	0.88
ICMC (3.0 mm)	-1.37	12.69	-8.08	7.83	4.73
<b>Breast</b>					
IMC (2.0 mm)	2.08	6.60	-0.28	5.43	1.58
IMC (3.0 mm)	2.83	10.34	-0.68	8.53	4.33
ICMC (2.0 mm)	0.01	2.88	-1.88	2.03	-0.18
ICMC (3.0 mm)	0.01	3.38	-2.48	2.58	-0.28
<b>Default Ramp Prostate</b>					
IMC (2.0 mm)	-0.48	9.31	-1.18	3.43	0.48
IMC (3.0 mm)	1.18	10.8	-1.18	5.13	0.38
ICMC (2.0 mm)	-0.69	8.55	-2.03	1.43	0.38
ICMC (3.0 mm)	-0.79	9.38	-2.58	1.58	-0.48

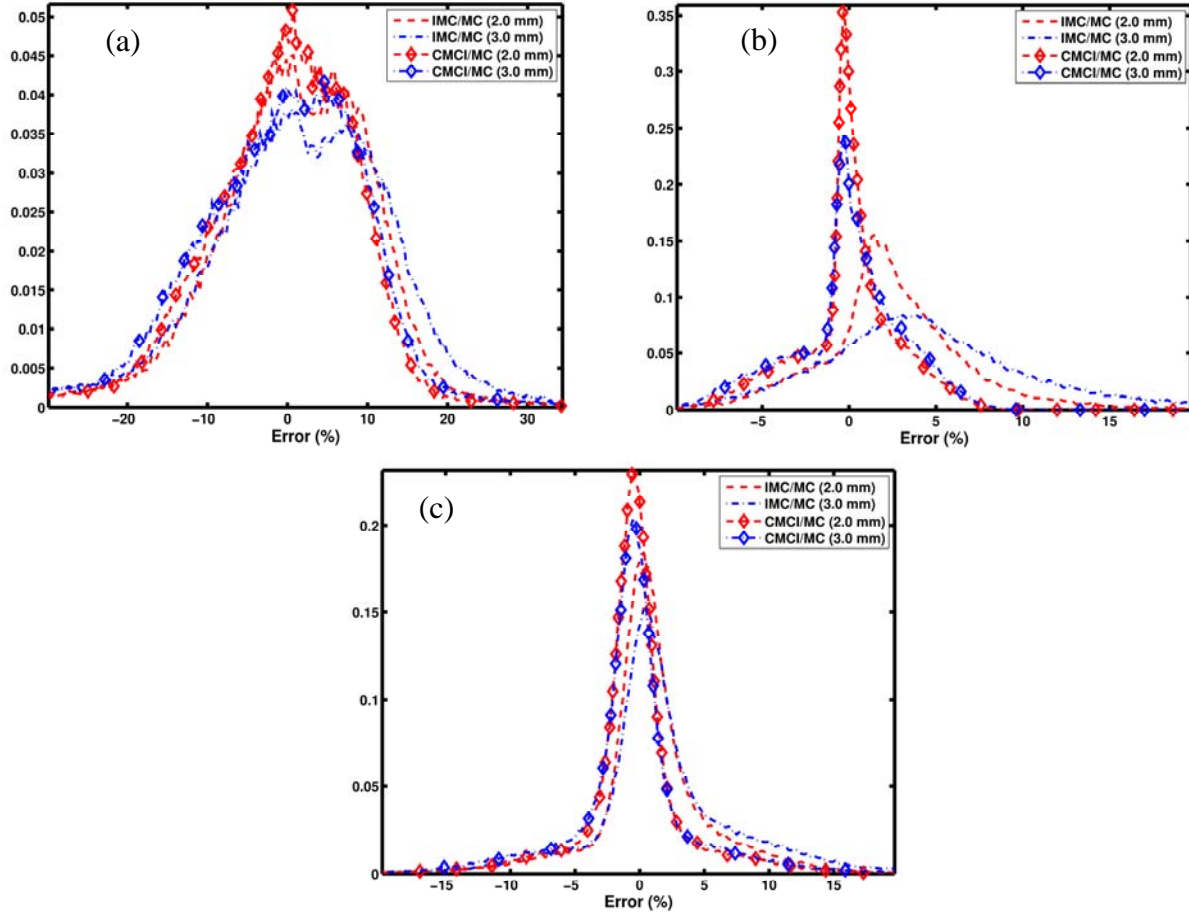


Figure 3.2: Frequency histogram of voxel-by-voxel relative percent total errors relative to UMC 1 mm voxel simulation from IMC (dashed) and ICMC (dashed-diamond) relative to regular HR MC. The prostate custom ramp, breast, and prostate default ramp cases are shown in (a), (b), and (c), respectively. Red and blue lines denote the error distributions for 2 mm and 3 mm IMC/ICMC, respectively.

Table 3-IV: DVH metrics for ICMC, IMC, and UMC for all three cases studied.

Custom Ramp Prostate	$D_{90}$ (Gy)	$D_{90}$ Error (%)	$D_{90}$ Error (Gy)	$V_{200}$ (cc)	$V_{200}$ Error (%)	$V_{200}$ Error (cc)
HR MC	100.6	N/A	N/A	8.29	N/A	N/A
IMC 2.0 mm		2.58	2.66		15.61	1.53
IMC 3.0 mm		3.26	3.39		18.01	1.82
ICMC 2.0 mm		1.65	1.69		-3.70	-0.30
ICMC 3.0 mm		1.42	1.45		-4.61	-0.37
Breast						
HR MC	86.0	N/A	N/A	2.35	N/A	N/A
IMC 2.0 mm		2.55	2.25		3.08	0.075
IMC 3.0 mm		4.02	3.60		-74.60	-1.01
ICMC 2.0 mm		0.69	0.60		-0.28	$-6.69 \times 10^{-3}$
ICMC 3.0 mm		0.69	0.60		-0.057	$-1.34 \times 10^{-3}$
Default Ramp Prostate						
HR MC	96.0	N/A	N/A	5.95	N/A	N/A
IMC 2.0 mm		3.41	3.39		18.68	1.37
IMC 3.0 mm		4.34	4.35		15.95	1.13
ICMC 2.0 mm		2.46	2.42		-2.75	-0.16
ICMC 3.0 mm		2.46	2.42		-1.48	-0.087

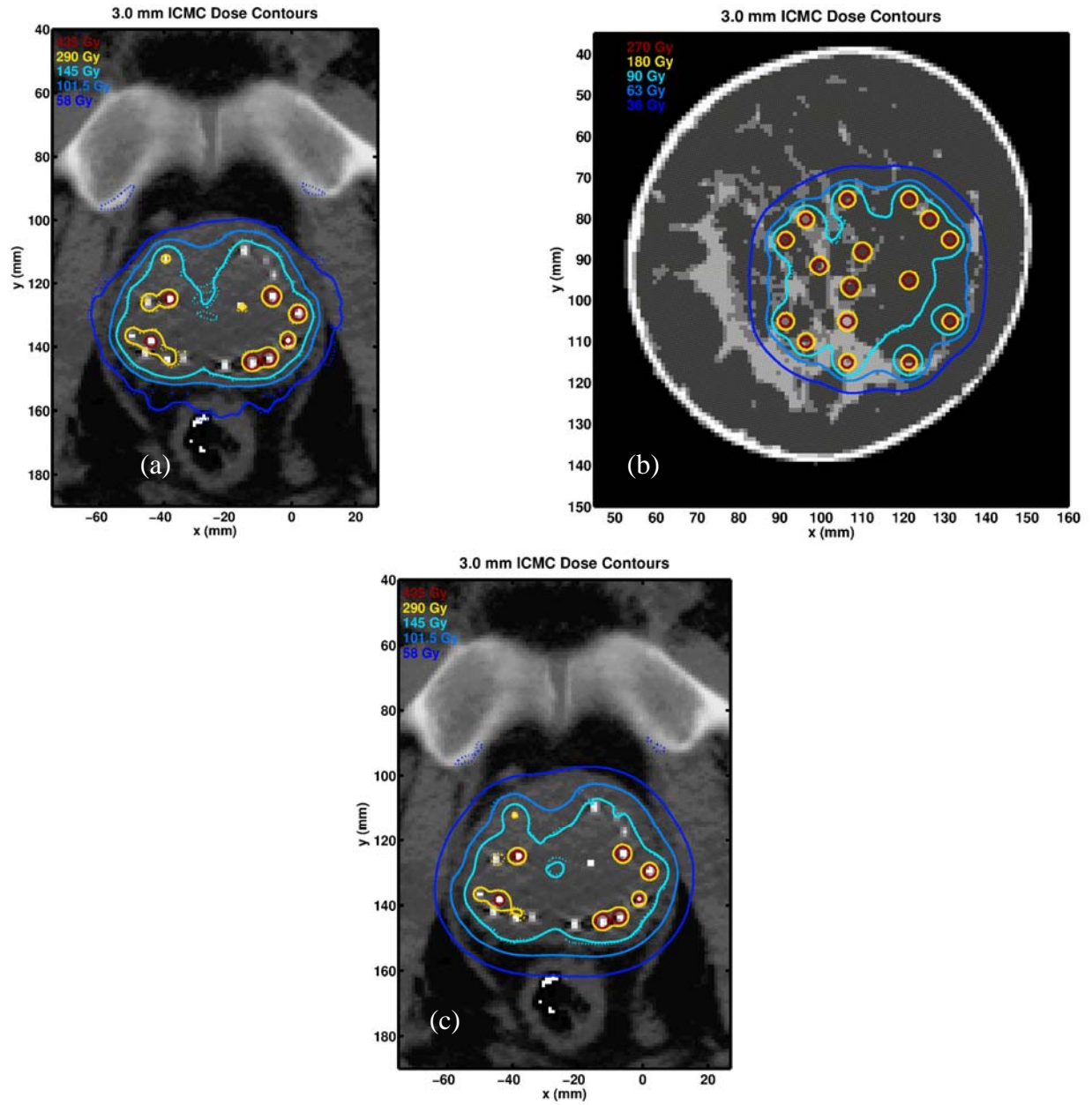


Figure 3.3: Isodose contours for ICMC (solid lines) overlaid on the corresponding UMC isodoses (dashed dot lines) The correlated sampling part of the ICMC calculation was performed on a 3.0 mm voxel size. The custom-ramp prostate, breast, and default ramp prostate cases are shown in (a), (b), and (c), respectively.



### 3.5.2 Inverse Square Law Gradient Effect

ISGE error is a combination of two separate effects: voxel averaging from scoring  $\overline{\Delta D}_{ijk}^{\text{CMC}}$  over a larger voxel volume and error from linearly interpolating  $\overline{\Delta D}_{ijk,\text{LR}}^{\text{CMC}}$  to  $\overline{\Delta D}_{ijk,\text{HR}}^{\text{ICMC}}$ . To quantitatively evaluate ISGE, a series of UMC and ICMC simulations were completed in homogeneous non-water media. This removes any error associated with voxel-to-voxel variations in cross-sections and local absorption properties while the non-water media result in a  $\overline{\Delta D}_{ijk}^{\text{CMC}}$  that differs significantly from zero. Simulations were completed using adipose and adult muscle tissues for the prostate case and adipose and glandular tissues for the breast case.

Figure 3.4 shows the percent error distributions and Table 3-V contains corresponding quantitative metrics for the prostate adipose and muscle ISGE simulations. Table 3-VI presents the DVH metric comparison. From this data, the following observations can be made:

1. All IMC simulations over-estimate  $D_{ijk}^{\text{het}}$ . This result is expected because of the effects from averaging the high dose gradients, with positive concavity, over a larger volume and then interpolating to regain the high resolution map. This process will naturally yield a general over-estimation of dose.
2. As expected, in all circumstances, ISGE error is less for the 2 mm LR grid than the 3 mm LR grid.
3. There are fewer ISGE errors for the muscle tissue than there are for the adipose tissue: less than 0.5% for both 2 mm and 3 mm grids. This is because muscle has radiological properties closer to water than adipose tissue with a linear attenuation coefficient  $\mu$  only 4% higher than water at 28 keV, whereas the same quantity for adipose tissue is 30% lower than water.

Figure 3.4: ISGE percent error distributions for the prostate (a) adipose and (b) muscle tissues. Both the IMC and ICMC errors relative to UMC are shown for voxels with greater than 50% of  $D_{90}$ .

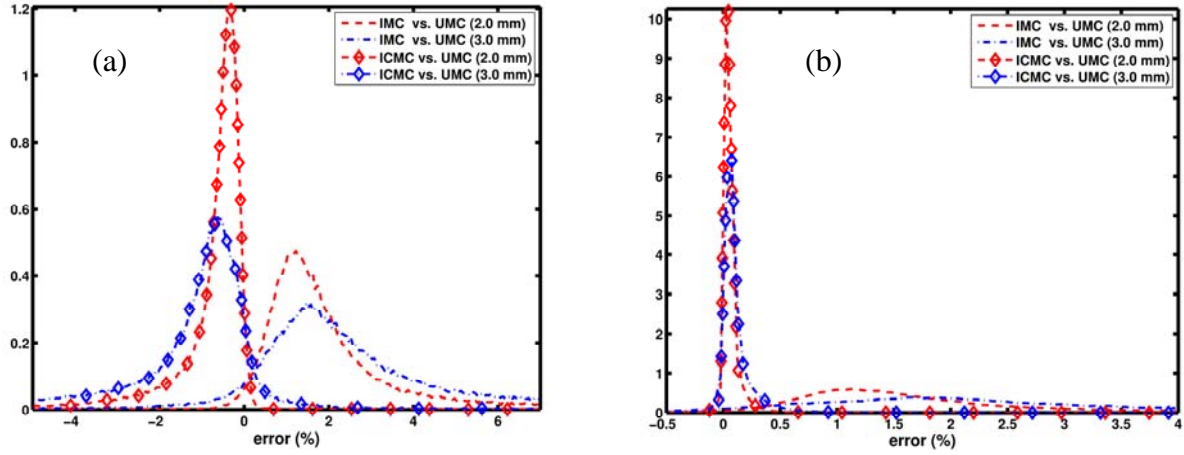


Table 3-V: Prostate case ISGE percent error distribution metrics relative to UMC 1 mm for the uniform adipose and muscle tissue assignments. Only voxels with doses greater than 50% of  $D_{90}$  were included.

Adipose	Mean	Std. Deviation	20 <sup>th</sup> Percentile	80 <sup>th</sup> Percentile	MPV
IMC (2.0 mm)	1.95	4.24	0.85	2.63	1.25
IMC (3.0 mm)	2.67	6.57	0.85	3.51	1.45
ICMC (2.0 mm)	-0.76	2.30	-1.05	-0.23	-0.39
ICMC 3.0 mm)	-1.42	3.51	-1.79	-0.23	-0.59
Muscle					
IMC (2.0 mm)	1.92	4.39	0.85	2.18	1.15
IMC (3.0 mm)	2.90	6.62	0.90	2.80	1.88
ICMC (2.0 mm)	0.05	0.12	0.03	0.09	0.05
ICMC (3.0 mm)	0.09	0.18	0.03	0.16	0.06

Table 3-VI: DVH Metrics for the ISGE prostate geometries with adipose and muscle tissues.

Adipose	$D_{90}$ (Gy)	$D_{90}$ Error (%)	$D_{90}$ Error (Gy)	$V_{200}$ (cc)	$V_{200}$ Error (%)	$V_{200}$ Error (cc)
HR-UMC	91.0	N/A	N/A	4.34	N/A	N/A
IMC (2.0 mm)		1.05	0.97		16.38	0.85
IMC (3.0 mm)		1.70	1.57		1.23	0.05
ICMC (2.0 mm)		-0.53	-0.48		-6.47	-0.26
ICMC 3.0 mm)		-1.07	-0.97		-0.55	-0.02
Muscle						
HR-UMC	109.3	N/A	N/A	11.37	N/A	N/A
IMC (2.0 mm)		1.31	1.45		14.15	1.87
IMC (3.0 mm)		2.27	2.53		19.63	2.78
ICMC (2.0 mm)		0.11	0.12		0.40	0.05
ICMC (3.0 mm)		0.11	0.12		0.59	0.07

4. The ICMC DVH metrics show 3 fold improvements in accuracy to the  $D_{90}$  and  $V_{200}$  relative to IMC, with an error 1% or less except for the adipose ICMC 2 mm  $V_{200}$ .

Although the adipose tissue presented poorer ISGE errors, it is still only a 2% effect. Furthermore, an entire adipose prostate is extremely unlikely as recommended elemental compositions<sup>17</sup> assume that the prostate closely resembles muscle tissue. Therefore, in clinical practice, the data presented suggests that the average prostate will exhibit negligible ISGE errors of less than 0.5%.

For the breast ISGE geometries, Figure 3.5 shows the distribution of percent ISGE errors relative to UMC for the breast adipose and mammary glandular tissue, and Table 3-VII lists the corresponding quantitative metrics with Table 3-VIII showing the DVH metrics. Similar to the prostate ISGE, the following observations can be made:

1. The same trends found in Figure 3.4 are seen here as well: IMC generally over-estimates  $D_{ijk}^{het}$  and the 3 mm ICMC approximation exhibits larger errors than 2 mm ICMC.
2. The breast adipose ISGE error is lower than 0.2%. This is similar to Figure 3.4(b) for the prostate muscle simulation. Recall that in the breast case, the homogeneous medium is not water but average breast tissue assuming an 85% adipose and 15% mammary glandular tissue mixture. The adipose tissue has a linear attenuation coefficient 5% lower than that of average breast tissue at 20 keV, while for glandular tissue, it is 40% greater. The large difference between the attenuation properties breast and mammary glandular tissues leads to the larger ISGE errors for the mammary gland simulation.
3. The  $D_{90}$  for the full adipose breast essentially has zero error with only a 0.05% error in the  $V_{200}$  for both ICMC LR grids. This represents phenomenal dose volume agreement with HR-UMC. The mammary gland ICMC breast exhibits 10 fold improvements in

accuracy, relative to IMC, for the  $D_{90}$ . The  $V_{200}$  shows drastic improvements for the 3 mm ICMC calculation bringing the error to just over 1% down from over 80% for the IMC 3 mm.

Similar to the prostate case, we can conclude that for clinically plausible tissue elemental compositions, the ISGE error is negligible, yielding errors less than 1%, with the majority below 0.5%. Citing the study of Yaffe *et al*<sup>11</sup>, the average breast cancer patient has relatively high (> 50%) adipose tissue fractions. Their final conclusion gives the 85/15 ratio for adipose and glandular tissue respectively. With this conclusion, the ISGE errors associated with using ICMC in the breast will more closely align with Figure 3.5(a) than Figure 3.5(b) yielding negligible dose volume errors.

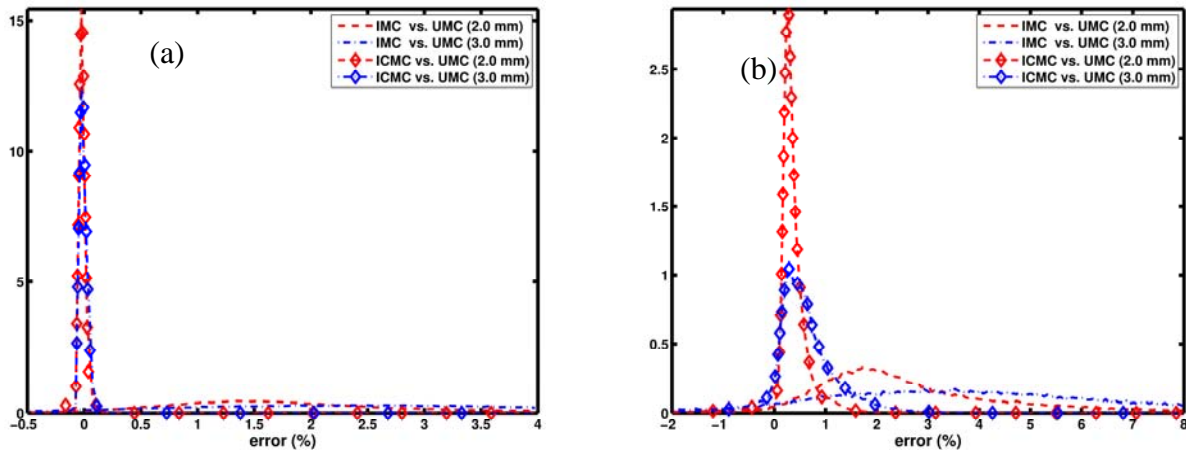


Figure 3.5: ISGE percent error distributions for the breast assuming uniform (a) adipose and (b) mammary glandular tissue assignments for all voxels. Both the IMC and ICMC errors relative to UMC are shown.

Table 3-VII: ISGE percent error distribution metrics relative to UMC for both the breast adipose and mammary glandular tissues for all voxels with greater than 50% of D<sub>90</sub>.

Adipose	Mean	Std. Deviation	20 <sup>th</sup> Percentile	80 <sup>th</sup> Percentile	MPV
IMC (2.0 mm)	2.04	5.39	0.90	2.53	1.31
IMC (3.0 mm)	2.93	8.66	0.94	3.17	2.57
CMCI (2.0 mm)	-0.01	0.03	-0.03	0.01	-0.02
CMCI 3.0 mm)	-0.003	0.03	-0.03	0.02	-0.02
<b>Mammary Gland</b>					
IMC (2.0 mm)	2.61	5.98	1.23	3.90	1.71
IMC (3.0 mm)	3.80	10.03	1.33	5.54	3.52
ICMC (2.0 mm)	0.33	0.46	0.21	0.52	0.27
ICMC (3.0 mm)	0.52	0.82	0.21	0.99	0.30

Table 3-VIII: DVH Metrics for the ISGE breast geometries with adipose and mammary glandular tissues.

Adipose	D <sub>90</sub> (Gy)	D <sub>90</sub> Error (%)	D <sub>90</sub> Error (Gy)	V <sub>200</sub> (cc)	V <sub>200</sub> Error (%)	V <sub>200</sub> Error (cc)
HR-UMC	89.7	N/A	N/A	2.46	N/A	N/A
IMC (2.0 mm)		2.05	1.88		4.36	0.11
IMC (3.0 mm)		3.32	3.08		-59.76	-0.92
ICMC(2.0 mm)		0.00	0.00		0.05	0.001
ICMC 3.0 mm)		0.00	0.00		0.05	0.001
<b>Mammary Gland</b>						
HR-UMC	77.1	N/A	N/A	2.28	N/A	N/A
IMC (2.0 mm)		2.10	1.65		2.85	0.07
IMC (3.0 mm)		3.75	3.00		-86.83	-1.06
ICMC (2.0 mm)		0.29	0.23		0.58	0.01
ICMC (3.0 mm)		0.48	0.38		-1.19	-0.03

In summary, for both the breast and prostate cases, all metrics show that ICMC effectively reduces ISGE error from the IMC 2-6% to under 0.5% for anatomically realistic geometries.

### 3.5.3 Cross-Section Gradient Effect

The next source of error arises from averaging the HR individual interaction cross-sections over the LR voxel volume. We call this the cross-section gradient effect (CSGE), which affects the particle fluence distribution in the simulation geometry. To isolate CSGE errors, simulations were performed with the mass-energy absorption coefficient for all materials set to that of liquid water and average breast tissue for the prostate and breast cases, respectively. Meanwhile interaction cross-sections were kept at values corresponding to the heterogeneous environment. These assignments removed any errors caused by differences in the local absorption properties.

Since the ISGE error was found in the previous section to be negligible, no attempt was made to correct for ISGE effects on the CSGE error distributions.

Table 3-X contains the DVH metrics for the CSGE geometry, and Figure 3.6 shows the error distributions relative to UMC. There are many observations that can be made from this data and I list only a few more prominent ones here:

1. In all three geometries and for both LR grids, the CSGE errors from ICMC are less than 3%.
2. The normalized curves for the 2 mm and 3 mm ICMC distribution in Figure 3.6 show only small differences relative to each other, confirmed by the quantitative metrics in Table 3-IX. This suggests that there is only a small advantage, in terms of accuracy, by using the 2 mm grid over the 3 mm grid.

Table 3-IX: Quantitative metrics describing the CSGE percent error distributions for the ICMC and IMC simulations relative to corresponding UMC calculations. MPV stands for most probable value.

Custom Ramp Prostate	Mean	Std. Deviation	20 <sup>th</sup> Percentile	80 <sup>th</sup> Percentile	MPV
IMC (2.0 mm)	1.98	2.13	0.83	2.83	1.30
IMC (3.0 mm)	2.42	3.13	0.70	3.97	1.77
ICMC (2.0 mm)	0.84	0.94	0.37	1.37	0.57
ICMC (3.0 mm)	0.61	1.35	0.10	1.30	0.43
<b>Breast</b>					
IMC (2.0 mm)	2.67	2.74	0.83	4.17	1.30
IMC (3.0 mm)	4.05	3.998	0.90	7.23	2.10
ICMC (2.0 mm)	-0.07	0.64	-0.50	0.30	-0.30
ICMC (3.0 mm)	-0.11	0.88	-0.77	0.43	-0.30
<b>Default Ramp Prostate</b>					
IMC (2.0 mm)	2.11	1.97	0.90	2.83	1.50
IMC (3.0 mm)	2.80	2.78	0.97	4.10	2.03
ICMC (2.0 mm)	0.91	0.85	0.37	1.37	0.50
ICMC (3.0 mm)	0.85	0.99	0.23	1.37	0.37

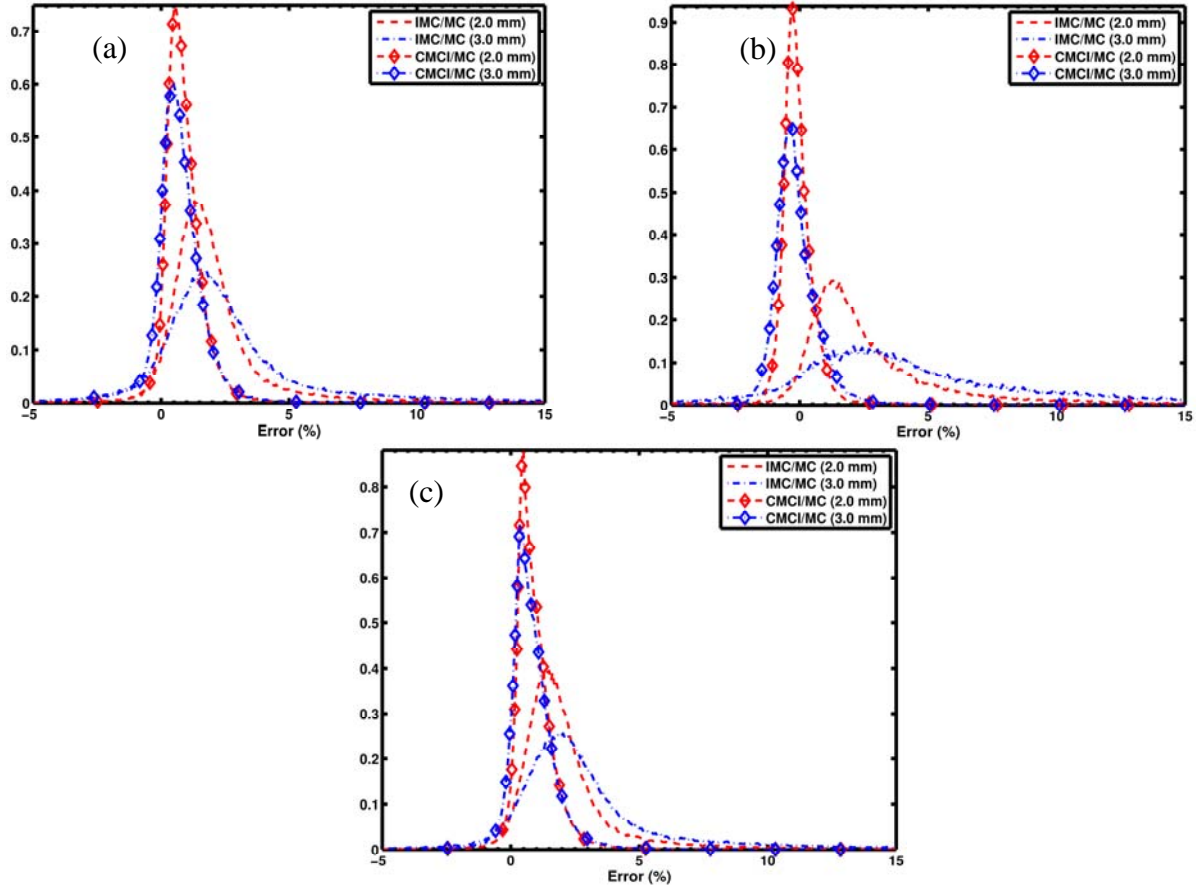


Figure 3.6: CSGE error distributions based on simulation geometries with LAGE error suppressed. The custom ramp prostate, breast, and default ramp prostate cases are shown in (a), (b), and (c), respectively.

Table 3-X: DVH metrics for ICMC, IMC, and UMC for the three cases showing CSGE error for the dose to liquid water in heterogeneous media.

Custom Ramp Prostate	$D_{90}$ (Gy)	$D_{90}$ Error (%)	$D_{90}$ Error (Gy)	$V_{200}$ (cc)	$V_{200}$ Error (%)	$V_{200}$ Error (cc)
HR UMC	111.1	N/A	N/A	11.03	N/A	N/A
IMC 2.0 mm		1.71	1.93		15.44	2.01
IMC 3.0 mm		2.23	2.54		20.22	2.79
ICMC 2.0 mm		0.76	0.85		-1.06	-0.12
ICMC 3.0 mm		0.65	0.73		-1.97	-0.21
Breast						
HR MC	83.5	N/A	N/A	2.14	N/A	N/A
IMC 2.0 mm		1.85	1.58		1.17	0.025
IMC 3.0 mm		3.3	2.85		-106.98	-1.11
ICMC 2.0 mm		0.0	0.0		-8.98	-0.18
ICMC 3.0 mm		-0.09	-0.075		-7.09	-0.14
Default Ramp Prostate						
HR MC	116.8	N/A	N/A	12.25	N/A	N/A
IMC 2.0 mm		1.43	1.69		14.61	2.10
IMC 3.0 mm		2.03	2.42		19.82	3.03
ICMC 2.0 mm		0.72	0.85		-0.65	-0.079
ICMC 3.0 mm		0.72	0.85		-1.73	-0.21

3. Relative to IMC, ICMC yields a 2-4 fold increase in the  $D_{90}$  accuracy for the prostate cases, with a greater than 30 fold improvement for the breast. Additionally, the  $V_{200}$  exhibits an 11-15 fold improvement in accuracy for all three cases.

Observation #2 is expected since the CSGE only affects the energy fluence distribution. Since the interaction cross-sections for each LR-ICMC voxel are an average over the corresponding HR volume, the fluence differences between the 2 mm and 3 mm geometries will be small. In the brachytherapy applications discussed in this study, since there is no charged particle transport, the absorbed dose can be computed as the collision kerma integrated over all energy and solid angle,

$$D(\mathbf{r}) = K_c^{\text{CPE}}(\mathbf{r}) = \int_0^\infty \int_0^{4\pi} E \cdot \Phi'(\mathbf{r}, \boldsymbol{\Omega}, E) \left( \frac{\mu_{\text{en}}}{\rho} \right) (\mathbf{r}, E) d\boldsymbol{\Omega} dE \quad (3.5.1)$$

In this expression,  $\Phi'(\mathbf{r}, \boldsymbol{\Omega}, E)$  represents differential particle fluence, and  $\mu_{\text{en}} / \rho$  is the mass-energy absorption coefficient. In the CSGE geometry, the  $\mu_{\text{en}} / \rho$  is the same between the HR-UMC and both ICMC calculations, effectively making any comparison between the two methods a comparison of energy fluence. The differences between the 2 mm and 3 mm ICMC calculations seen in Figure 3.6 and Table 3-IX and Table 3-X confirm that the fluence differences between them are small. This suggests that neglecting local absorption heterogeneities, ICMC based on 3 mm CMC has comparable accuracy to ICMC based on 2 mm CMC, which is within 3% of HR-UMC.

To summarize, in the region that receives half of  $D_{90}$ , CSGE error is generally a 3% effect with the voxel majority posting errors below 1.5% for all cases and both LR grids.



### 3.5.4 Local Absorption Gradient Effect

The final effect leading to errors in  $D_{ijk,HR}^{ICMC}$ , called the local absorption gradient effect (LAGE), stems from differences in local energy absorption properties between UMC and ICMC simulations. These differences arise from averaging HR voxel mass-energy absorption coefficients in regions of high  $\mu_{en} / \rho$  spatial gradients. As shown in eq. (3.5.1), absorbed dose is directly related to  $\mu_{en} / \rho$  allowing potential for significant ICMC LAGE errors. This effect was isolated by fixing the individual cross-sections to be that of liquid water and average breast medium, in the prostate and breast cases respectively, effectively eliminating any CSGE errors that arise from differences in the particle fluence. Recalling from Section 3.5.2 that ISGE errors were negligible, no attempt was made to correct for them in the LAGE error distributions.

Figure 3.7 shows the error distributions of IMC and ICMC calculations relative to UMC in the LAGE geometry. Table 3-XI presents the DVH metrics for comparison, and Table 3-XII contains the corresponding quantitative metrics for the distributions in Figure 3.7. Following are some observations:

1. In Figure 3.7, the custom ramp prostate shows a broad distribution of error, with a large number of voxels (about 35% of total) with errors in excess of 10%. Additionally, for this same case, it does not appear that the ICMC method shows any advantage, in terms of accuracy, relative to IMC. Figure 3.8 shows the relationship between error and the spatial gradient magnitude of the HR  $\mu_{en} / \rho$  for 28 keV. This was computed for soft tissues by discretizing the gradient magnitude for soft tissues and finding the distribution of corresponding dose errors for each gradient bin. The mean is plotted with an “x,” and the error bars represent 2 standard deviations about the mean for the error distribution within

each gradient bin. This shows the dose error is correlated to the voxel-to-voxel variability of  $\mu_{en} / \rho$ .

2. Even with the broad errors distribution for the custom ramp prostate, the  $D_{90}$  improved relative to IMC 5-10 fold with errors below half a percent. Similarly,  $V_{200}$  improved by more than half relative to IMC calculations.

Table 3-XI: DVH metrics for ICMC, IMC, and UMC for the three cases showing LAGE error for the dose to heterogeneous media in liquid water.

Custom Ramp Prostate	$D_{90}$ (Gy)	$D_{90}$ Error (%)	$D_{90}$ Error (Gy)	$V_{200}$ (cc)	$V_{200}$ Error (%)	$V_{200}$ Error (cc)
HR UMC	100.2	N/A	N/A	8.63	N/A	N/A
IMC 2.0 mm		1.81	1.81		13.66	1.18
IMC 3.0 mm		2.65	2.66		16.66	1.43
ICMC 2.0 mm		0.36	0.36		-8.27	-0.71
ICMC 3.0 mm		0.24	0.24		-9.39	-0.81
Breast						
HR MC	88.9	N/A	N/A	2.62	N/A	N/A
IMC 2.0 mm		2.78	2.48		5.27	0.14
IMC 3.0 mm		4.13	3.68		-31.87	-0.83
ICMC 2.0 mm		0.84	0.75		-0.15	-0.004
ICMC 3.0 mm		1.10	0.98		-0.56	-0.01
Default Ramp Prostate						
HR MC	96.4	N/A	N/A	8.56	N/A	N/A
IMC 2.0 mm		2.92	2.81		16.91	1.45
IMC 3.0 mm		3.95	3.81		19.83	1.70
ICMC 2.0 mm		1.41	1.36		-3.30	-0.28
ICMC 3.0 mm		1.51	1.45		-2.94	-0.25

In stark contrast with the custom ramp prostate, the breast and default ramp prostate geometries exhibit much narrower error distributions. Additionally, the breast DVH metric errors are reduced relative to IMC to under 1% while the default ramp prostate experienced 1.5% errors in  $D_{90}$  and a roughly 3% underestimation of the  $V_{200}$ .

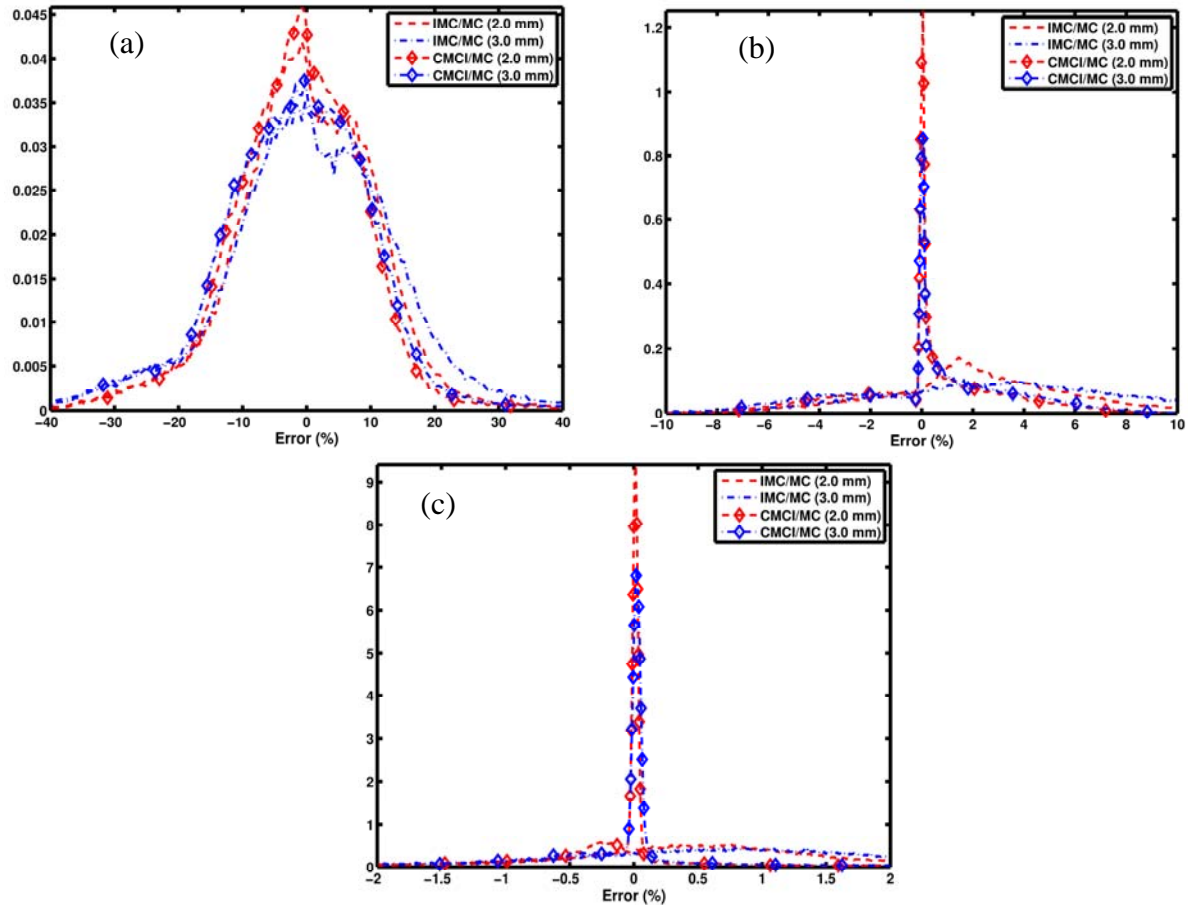


Figure 3.7: Error from the LAGE simulation geometries with CSGE errors removed. The custom ramp prostate, breast, and default ramp prostate cases are shown in (a), (b), and (c), respectively.

Table 3-XII: Numerical descriptors for the percent error distribution relative to UMC in the LAGE geometry for the breast case and both prostate cases.

Custom Ramp Prostate	Mean	Std. Deviation	20 <sup>th</sup> Percentile	80 <sup>th</sup> Percentile	MPV
IMC (2.0 mm)	-0.16	10.97	-8.40	8.83	-0.98
IMC (3.0 mm)	0.51	12.95	-9.25	11.05	-0.35
ICMC (2.0 mm)	-1.36	10.18	-9.35	6.85	-0.05
ICMC (3.0 mm)	-1.67	11.50	-10.75	7.65	-0.05
<b>Breast</b>					
IMC (2.0 mm)	2.04	3.49	-0.59	4.95	1.51
IMC (3.0 mm)	2.39	4.22	-1.29	6.21	3.55
ICMC (2.0 mm)	0.11	2.92	-2.06	2.15	-0.03
ICMC (3.0 mm)	0.16	3.36	-2.76	2.85	-0.03
<b>Default Ramp Prostate</b>					
IMC (2.0 mm)	0.74	1.15	-0.16	1.56	0.51
IMC (3.0 mm)	0.95	1.27	-0.13	2.04	0.87
ICMC (2.0 mm)	-0.01	0.84	-0.40	0.03	0.03
ICMC (3.0 mm)	0.00	0.88	-0.49	0.09	0.03

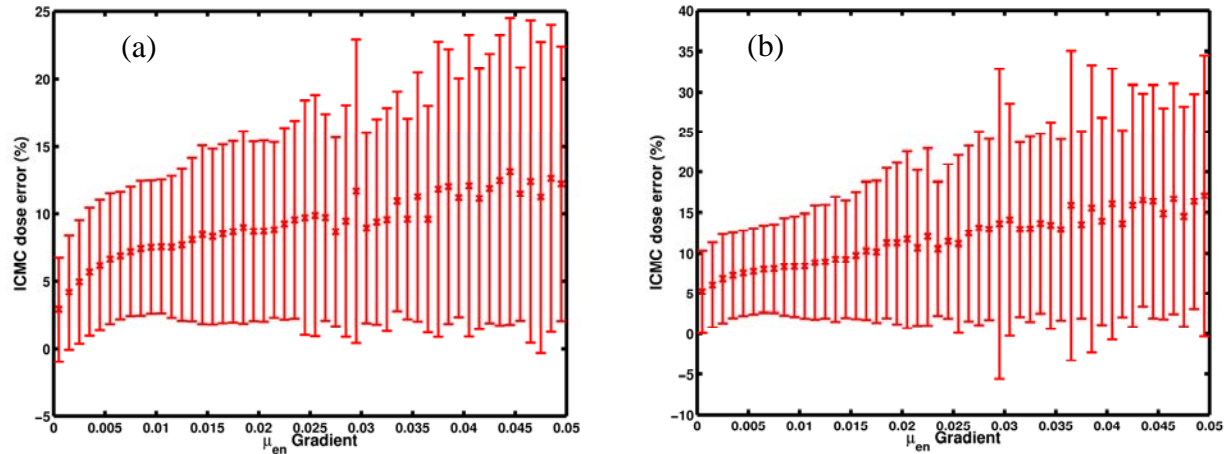


Figure 3.8: Mean ICMC LAGE error for each  $\mu_{en}$  gradient bin with corresponding bars showing  $2\sigma$  for the (a) 2 mm and (b) 3 mm ICMC custom ramp prostate simulations.

The source of the broad error distribution for the custom ramp prostate lies in the method used to specify voxel-to-voxel tissue elemental compositions. Recall that breast tissues were assigned following tissue segmentation from a breast-dedicated CBCT with tissue elemental compositions taken from Woodard and White<sup>17</sup>. The tissues were chest wall muscle, adipose, two different mammary glandular tissues and skin for a total of five tissues in the entire geometry. The default ramp prostate originally included only 4 tissue type: lung, skeletal bone, air, and muscle with the 3 additional soft tissues presented in Table 3-I. In contrast, each voxel in the custom ramp prostate was assigned from a list of 55 materials based on HU. Though this method has been used extensively and accurately for a number of years in external, high-energy beam radiotherapy, it has been shown to be very unreliable for low-energy applications<sup>88</sup>. Furthermore, the HU is more influenced by Compton scattering, instead of the photoelectric effect which is the dominant interaction in low-energy brachytherapy.

To illustrate the unreliability of using single-energy CT to assign tissue for low-energy Monte Carlo transport, the prostate HU's in the post-implant CT used in this study range from -18 to 56,

representing an attenuation coefficient 1.8% lower to 5.6% higher than that of water. After the custom ramp CTCREATE tissue assignment, the range of attenuation coefficients within the prostate at 28 keV becomes 16% lower and 6% higher than that of liquid water. Within the prostate, these tissue assignments also represent frequent, unrealistic deviations of 15% from the  $\mu_{\text{en}} / \rho$  for liquid water. Therefore, the LAGE errors presented in Figure 3.7(a) do not suggest that ICMC is inappropriate for anatomically realistic prostate geometries. Rather the large errors stem from artifacts introduced from incorrect voxel-to-voxel tissue composition assignments. These artifacts could also have been aided from the incomplete mitigation of streaking artifacts in the post-implant CT.

### 3.6 Discussion

The ISGE error distributions plotted in Figure 3.4 and Figure 3.5 confirm our hypothesis that the inverse square law effects are mitigated effectively in  $\overline{\Delta D}_{ijk,LR}^{\text{ICMC}}$  showing errors of less than 0.5% for anatomically reasonable geometries. For the three geometries studied here, CSGE exhibited 3% errors, representing the small changes in particle fluence that occur from using averaged individual cross-sections.

The largest potential contributor to ICMC error is LAGE. Though the LAGE error is minimal for the breast and default ramp prostate geometries, it induces dose computation errors as large as 30% for the custom ramp prostate due to the high variability of  $\mu_{\text{en}} / \rho$  within the CTV. However, with emergence of model based dose calculations methods in brachytherapy, there is an ongoing debate on the merits of reporting absorbed dose to water in medium,  $D_{w,m}$ , vs. absorbed dose to medium in medium,  $D_{m,m}$ <sup>98-100</sup>. The AAPM TG-186 only requires reporting  $D_{m,m}$ , but notes this is only due to insufficient data to support use of  $D_{w,m}$ . Within the past year,

data has been published to show that  $D_{w,m}$  more accurately estimates the dose to cell nuclei, and therefore more correlated to biological events that lead to cell death<sup>101,102</sup>. If  $D_{w,m}$  was reported, then LAGE errors would be eliminated, since the voxel-to-voxel variation of local absorption properties would be removed. Furthermore, the setup for a  $D_{w,m}$  calculations using ICMC is equivalent to CSGE geometry, leading to errors of less than 3% relative to HR-UMC calculations. One method to reduce ICMC LAGE errors in  $D_{m,m}$  would be to separate the dose scoring grid from the material voxel grid. This would allow a HR representation of the patient, but maintain the efficiency of computing dose on a LR grid. This adds a slight increase to overhead from additional ray-tracing, but maintains the efficiency advantage from scoring  $\Delta D_{ijk}$  on an LR grid. Under these circumstances, ICMC errors would be reduced down to the ISGE level of 0.5%.

As stated previously, the large LAGE errors observed in our custom ramp prostate case are likely due to anatomically unrealistic voxel-to-voxel elemental tissue composition assignments, leading to anomalously high  $\mu_{en} / \rho$  spatial gradients. In our test case, these effects are exaggerated by residual streaking artifacts due to the metal seeds implanted within the patient's prostate and an unrealistically dense cross-section table vs. Hounsfield number lookup table. Analysis is complicated by the un-answered question of how to assign tissue cross-section tables to organs or individual voxels for the low energy brachytherapy regime. Furthermore, the single-energy CT imaging approach of cross-section mapping in patient geometries, of which our custom and default ramp assignments are examples, is inadequate<sup>88,90</sup>. Elemental analyses of tissue samples fail to address this issue, since sufficiently accurate and comprehensive studies are lacking and are also inadequate. Landry *et al*<sup>88</sup> has shown that low-energy brachytherapy dose variations as

high as 10% can be found in the breast due to the wide range of published tissue compositions for adipose and mammary glandular tissues. This uncertainty could potentially be addressed through dual-energy CT methods such as those proposed by Williamson *et al*<sup>92</sup>, Landry *et al*<sup>90</sup>, or Malusek *et al*<sup>91</sup>.

The efficiency gains arising from interpolated-correlated Monte Carlo (ICMC) relative to already optimized un-correlated Monte Carlo (UMC) are immense. Gains upward of 1500 were reported for the 3.0 mm LR grid. This translates to 0.4 sec and 1.1 sec run-times for the breast and prostate CTV's, respectively, to reach an average uncertainty of 2% our HR  $1 \times 1 \times 1 \text{ mm}^3$  voxels. To perform optimization of seed location using a genetic optimization approach<sup>96,97</sup>, only 7 min and 18 min of ICMC runtime on a 3 mm voxel grid would be needed for our HR breast and prostate examples, on a single CPU. Furthermore, given cost-effective availability of multi-CPU and multi-core computer architectures, parallel processing is readily available to anyone, adding further reductions to MC run time. Following optimization, CMC could compute a highly accurate final dose map. Similar to external beam radiotherapy's use of the pencil-beam algorithm for IMRT optimization, use of ICMC for brachytherapy optimization would produce only convergence errors, while the final CMC calculation would yield very low dose evaluation errors.

As mentioned previously, the times reported here are for radiation transport only and do not include the extra time needed for averaging cross-sections and  $\mu_{\text{en}} / \rho$ , nor the time to read in the input file and create the simulation geometry. The time reported here were for a single radiation transport simulation. In the clinical setting of treatment planning optimization, the radiation transport could be computed multiple times, while the geometry setup and the averaging of

cross-sections and  $\mu_{\text{en}} / \rho$  is computed only once. Therefore, the time and efficiency gains reported for the radiation transport is more representative of the clinical setting. As a side note, the time required for set-up is below 1-2 seconds for a wide range of problems.

### 3.7 Conclusion

ICMC has been shown to be accurate relative to UMC with errors smaller than 3% for 80% of the voxels given anatomically realistic cross-section and local absorption mapping. Errors from the inverse square law were isolated to the high dose regions, but were very small while errors associated with cross-section differences between the HR and LR grid were greatest in the low-dose regions. Errors associated with local absorption properties were sensitive to the spatial gradient of the mass-energy absorption coefficient corresponding to the HR spatial grid. Further study on accuracy is warranted as more accurate methods become available for voxel cross-section mapping. However, ICMC is the most efficient MBDCAs introduced to date, producing HR dose maps in under a minute, and is a perfect candidate to drive seed placement optimization algorithms.



# 4. Adjoint Biased Forward Monte Carlo

## 4.1 Introduction

As discussed previously, adjoint-biased forward Monte Carlo (ABFMC) is a promising method to increase the efficiency of CBCT Monte Carlo (MC) scatter simulations. A brief derivation of my ABFMC implementation is presented in this chapter followed by a presentation of its performance and corresponding conclusions.

## 4.2 Theory

### 4.2.1 Weight Windows

I start with an abbreviated description of the weight window method: More details can be found in Appendix D. As stated in Chapter 1, systematic splitting/rouletting is an alternate implementation of biased importance sampling that avoids explicitly drawing random samples from the biased PDF<sup>63,64,69</sup>. Remember that  $\beta_{m,n} = (\mathbf{r}_{m,n}, \mathbf{\Omega}_{m,n}, E_{m,n}, W_{m,n})$  is a randomly sampled collision within the phase space,  $\mathbf{P} = (\mathbf{r}, \mathbf{\Omega}, E)$ , for the  $m^{\text{th}}$  history leaving the  $n^{\text{th}}$  collision, where  $\mathbf{r}_{m,n}$  is the site of interaction,  $\mathbf{\Omega}_{m,n}$  is the trajectory of the particle leaving the collision,  $E_{m,n}$  and  $W_{m,n}$  are the particle energy and statistical weight (or weight for short), respectively, following collision.

Weight windowing (WW) constrains the weight,  $W_{m,n}$ , to be within a certain interval or “window” centered about a desired target value,  $W_T$  as illustrated by Figure 4.1. If  $W_{m,n}$  is

within the window, then the particle is allowed to be transported freely without interference. For particles that have  $W_{m,n}$  greater than  $W_U$ , particles are split into multiple particles, each with a new  $W_{m,n} = W_T$ . If a particle has  $W_{m,n}$  below  $W_L$ , then Russian roulette is played with a surviving probability of  $W_{m,n} / W_T$ . If the particle survives, then  $W_{m,n}$  is set to  $W_T$ . Weight windowing is applied at the beginning of the  $n+1$  interaction loop before transport to next collision.

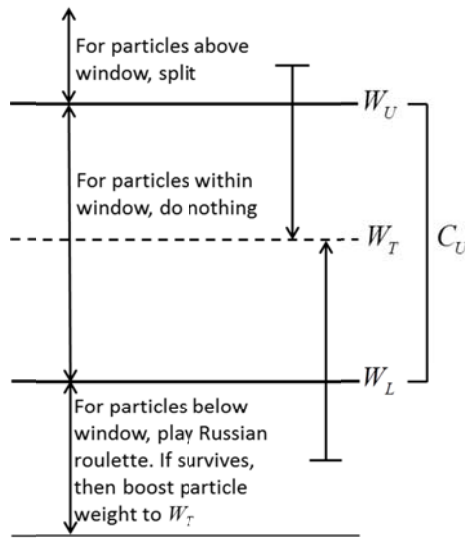


Figure 4.1: Picture of the weight window. Adapted from Figure 2-24 in the MCNP manual<sup>65</sup>

Weight windowing can be used for importance sampling by exploiting the property that a particle's weight is inversely proportional to its importance. Setting an appropriate value for  $W_T$  to be inversely proportional to the importance of a point in  $\mathbf{P}$  will preferentially transport important particles and roulette the non-important ones.

#### 4.2.2 The Forward and Adjoint Boltzmann Transport Equation

To define the importance of a phase-space point,  $\mathbf{P}$ , an introduction to the forward and adjoint Boltzmann transport equation is necessary.

A forward Monte Carlo (FMC) simulation is a numerical solution of the forward Boltzmann transport equation (FBTE), given below in integral form:

$$\Phi(\mathbf{P}) = \int K(\mathbf{P}' \rightarrow \mathbf{P})\Phi(\mathbf{P}')d\mathbf{P}' + \Phi_0(\mathbf{P}) \quad (4.2.1)$$

where  $\Phi(\mathbf{P})$  represents the angular particle fluence, the transition operator  $K(\mathbf{P}' \rightarrow \mathbf{P})$  describes the likelihood of the state transition  $\mathbf{P}' \rightarrow \mathbf{P}$ , taking into account particle attenuation and scattering, and  $\Phi_0(\mathbf{P})$  is the primary particle fluence distribution arising from the emission of primary particles from the source distribution  $q(\mathbf{P})$ . The FBTE describes the transport of particles in the forward direction, i.e. from  $\mathbf{P}' \rightarrow \mathbf{P}$ , tracking from source to detector and, generally, from higher energy states to lower energy states. In CBCT scatter simulation, the Monte Carloist is interested in computing a particular score,  $R$ , e.g., energy imparted to a particular pixel of the CBCT flat panel detector:

$$R = \int f(\mathbf{P}) \cdot \Phi(\mathbf{P}) \cdot d\mathbf{P} \quad (4.2.2)$$

where the detector-response function,  $f(\mathbf{P})$ , is the contribution to the detector reading of a particle at phase location  $\mathbf{P}$ .

Our generic detector-response problem can be also be solved via the corresponding adjoint Boltzmann transport equation (ABTE), which tracks particles in the reverse direction, i.e. from  $\mathbf{P} \rightarrow \mathbf{P}'$ , starting from the detector and moving towards the source, and from lower energy states to higher energy states:

$$\Phi^*(\mathbf{P}) = \int K(\mathbf{P} \rightarrow \mathbf{P}')\Phi^*(\mathbf{P}')d\mathbf{P}' + \Phi_0^*(\mathbf{P}) \quad (4.2.3)$$

where  $\Phi^*(\mathbf{P})$  is the adjoint particle flux. In this expression,  $\Phi_0^*(\mathbf{P})$  is the distribution of “primary” adjoint particles emerging from the adjoint source  $q^*(\mathbf{P})$ , which is represented by the

detector response function,  $f(\mathbf{P})$ , in the ABTE formulation. Similar to the forward direction, the detector response,  $R$  can also be computed, but instead using the adjoint flux,  $\Phi^*(\mathbf{P})$ . Notably, it can be shown that<sup>103</sup>

$$R = \int q(\mathbf{P}) \cdot \Phi^*(\mathbf{P}) \cdot d\mathbf{P} = \int f(\mathbf{P}) \cdot \Phi(\mathbf{P}) \cdot d\mathbf{P} \quad (4.2.4)$$

### 4.2.3 Optimal Weight Window Target Value

It can be shown that the adjoint flux,  $\Phi^*(\mathbf{P})$ , has a fundamental physical interpretation:  $\Phi^*(\mathbf{P})$  is the expected (mean) contribution to the detector response  $R$  from a point,  $\mathbf{P}$ , in phase space and all its progeny. The term “expected value” refers to averaging the detector response contributions over all possible photon random walks originating at  $\mathbf{P}$ . Thus,  $\Phi^*(\mathbf{P})$  is a direct measurement of the importance of  $\mathbf{P}$  to  $R$ . In fact, it can further be shown that the optimal weight window target value,  $W_T$ , for importance sampling via weight windowing is<sup>64,70</sup>

$$W_T^\dagger(\mathbf{P}) = \frac{R}{\Phi^*(\mathbf{P})} \quad (4.2.5)$$

where  $R$  acts as a normalization factor for the importance of  $\mathbf{P}$ . Unfortunately, using an exact adjoint is impractical as it requires the same amount of CPU resources as a forward MC simulation to compute. However, during the last decade, fast ABTE solvers that yield approximate 3D adjoint solutions,  $\Phi_{app}^*(\mathbf{P})$ , have been developed using the deterministic discrete ordinates method (DOM).

#### 4.2.4 Importance Sampling Revisited

Suppose we have an approximate deterministic adjoint solution, and  $R_{app} = \int \Phi_{app}^*(\mathbf{P})q(\mathbf{P})d\mathbf{P}$ .

The resulting importance map yields a biased FMC scheme described by the following modified BTE<sup>70</sup>:

$$\hat{\Phi}(\mathbf{P}) = \int \left[ K(\mathbf{P}' \rightarrow \mathbf{P}) \frac{\Phi_{app}^*(\mathbf{P})}{\Phi_{app}^*(\mathbf{P}')} \right] \hat{\Phi}(\mathbf{P}')d\mathbf{P}' + \hat{\Phi}_0(\mathbf{P}) \text{ where } \hat{\Phi}(\mathbf{P}) = \Phi(\mathbf{P})\Phi_{app}^*(\mathbf{P}) / R_{app} \quad (4.2.6)$$

Here,  $\beta_{m,0}$  is sampled from a biased source (discussed below) that gives rise to  $\hat{\Phi}_0(\mathbf{P})$  and biased kernel PDF's. In FMC,  $\beta_{m,0}$  is first sampled from a biased source for primary photons while successive samplings of  $\beta_{m,n}$  for secondary photons are taken from the biased transition kernel,  $K(\mathbf{P}' \rightarrow \mathbf{P})\Phi_{app}^*(\mathbf{P}) / \Phi_{app}^*(\mathbf{P}')$ . Evaluating the FMC score is then acquired by taking the average over histories of the detector scores times their appropriate weight correction factors,

$$\bar{R} = \frac{1}{N} \sum_{m=1}^M \sum_{n=0}^{N_m} W_{m,n} f(\beta_{m,n}) = \frac{1}{N} \sum_{m=1}^M \sum_{n=1}^{N_m} \frac{R_{app} \cdot f(\beta_{m,n})}{\Phi_{app}^*(\beta_{m,n})}, \quad (4.2.7)$$

$$\text{where } W_{m,n} = \prod_{\xi=1}^n w_{m,\xi} = w_{m,0} \cdot w_{m,1} \cdot \dots \cdot w_{m,n}$$

In this expression  $\beta_{m,n}$  represents the phase-space samples derived from a MC solution of eq. (4.2.6), and  $w_{m,n}$  represents a photon weight from history  $m$  at following interaction  $n$  where weight corrections are applied to yield an unbiased estimate. Under certain circumstances, by using a next event-type scoring function, exact adjoint-based importance sampling yields a zero-variance forward MC simulation<sup>68</sup>. More practically, using approximate DOM solutions,  $\Phi_{app}^*(\mathbf{P})$ , to implement this scheme in nuclear engineering applications increases efficiency up to three orders of magnitude above purely analog techniques<sup>64,70,104</sup>. The coupling of DOM

techniques with MC simulation is sometimes referred to as hybrid MC (h-MC) and is an implementation of ABFMC.

#### 4.2.5 Consistent adjoint-driven importance sampling (CADIS)

The biased transport process described in eq. (4.2.6) is the basis of the consistent adjoint driven importance sampling (CADIS) proposed by Wagner *et al*<sup>70</sup>. CADIS consists of the following three components.

- 1) Compute  $\Phi_{app}^*$  from some benchmarked DOM code
- 2) Use  $\Phi_{app}^*(\mathbf{P})$  to derive an importance-biased source distribution,  $\hat{q}(\mathbf{P})$ , for sampling primary particles in the forward MC simulation:

$$\hat{q}(\mathbf{P}) = \frac{\Phi_{app}^*(\mathbf{P})q(\mathbf{P})}{\int \Phi_{app}^*(\mathbf{P})q(\mathbf{P})d\mathbf{P}} = \frac{\Phi_{app}^*(\mathbf{P})q(\mathbf{P})}{R_{app}} \quad (4.2.8)$$

The simplifying step comes from eq. (4.2.4). This source biasing will bias the primary particle sampling process towards histories that strongly contribute to the detector score.

- 3) Rather than sample directly from the biased kernel  $K(\mathbf{P}' \rightarrow \mathbf{P})\Phi_{app}^*(\mathbf{P})/\Phi_{app}^*(\mathbf{P}')$  in eq. (4.2.6), sample from the analogue kernel  $K(\mathbf{P}' \rightarrow \mathbf{P})$  and then use WW to split important particles and kill, via Russian roulette, unimportant particles based on a target weight value of

$$W_T(\mathbf{r}, E) = \frac{R_{app}}{\Phi_{app}^*(\mathbf{r}, E)} \quad (4.2.9)$$

Equation (4.2.9) employs an angle-independent adjoint solution, that has been integrated over all solid angle,  $\Phi_{app}^*(\mathbf{r}, E) = \int_{4\pi} \Phi_{app}^*(\mathbf{r}, \boldsymbol{\Omega}, E)d\boldsymbol{\Omega}$ . Though the angle-dependent solution (angular

biasing in addition to energy- and spatial-biasing) theoretically would yield greater efficiency gains over traditional MC techniques, it requires > 20GB of RAM for typical problems, making its application impractical. Using a coarse angular grid has the danger of introducing “ray effects” in the ABFMC solution. Ignoring angular biasing (by using an angle-independent adjoint solution) has no effect on the final accuracy of the Monte Carlo solution, but does result in some loss in efficiency.

#### 4.2.6 Forward Adjoint Importance Generator

Another approach to ABFMC is to compute an “on-the-fly” estimate of the importance function during a forward Monte Carlo calculation. The forward-adjoint importance generator (FAIG)<sup>69</sup> computes a statistically noisy approximation to the importance function on a coarse phase-space grid by averaging over the ratio of each colliding particle’s weight in a given phase-space cell and the contribution of the particle and all subsequent collisions to the detector score. The weight normalization is to account for any biased transport mechanisms that alter particle statistical weight. The first 10% of the simulation histories are used to estimate the initial importance function following this “ramp-up” period during which, no transport biasing is applied. For the remainder of the simulation, the importance map is continually computed and updated “on-the-fly”. Therefore, when weight windowing is initiated, it uses a statistically noisy importance map that converges to the true value as the simulation progresses. The normalization factor,  $R$ , is simply computed as the average detector score implicitly during the FAIG process. Unlike the CADIS methodology, this implementation does not bias the primary source sampling, and only influences the particle transport through weight windowing. This is the ABFMC implementation presented in Appendix C. It can be used to compute the importance function “on-the-fly,” OTF-FAIG, or to pre-compute a low-uncertainty importance map, PC-FAIG.

## 4.3 CADIS Implementation

### 4.3.1 Multigroup Approximation

Since the discrete ordinate method (DOM) solves the BTE in a discretized, non-continuous phase space, eq. (4.2.9) must be converted to discretized form. To start, the BTE is discretized in energy using the multigroup approximation. The following derivation is adapted from Lewis and Miller<sup>105</sup>. First, let's start with the FBTE in differential form,

$$\begin{aligned} \Omega \cdot \nabla [\Phi(\mathbf{r}, \Omega, E)] + \mu(\mathbf{r}, E)\Phi(\mathbf{r}, \Omega, E) = \dots \\ q(\mathbf{r}, \Omega, E) + \int_0^{\infty} \int \Phi(\mathbf{r}, \Omega', E') \hat{\mu}(\Omega', E' \rightarrow \Omega, E | \mathbf{r}) d\Omega' dE' \end{aligned} \quad (4.3.1)$$

In the multigroup approximation, the energy range is divided up into  $G$  intervals. By convention the group number increases as the energy decreases. Thus,  $E_G$  and  $E_0$  are the minimum and maximum energy investigated, respectively. The min and max bounds of group,  $g$ , are then described as  $[E_g, E_{g-1}]$ . By integrating over the group bounds, the group fluence is defined as:

$$\Phi_g(\mathbf{r}, \Omega) = \int_{E_g}^{E_{g-1}} \Phi(\mathbf{r}, \Omega, E) dE = \int_g \Phi(\mathbf{r}, \Omega, E) dE \quad (4.3.2)$$

Likewise, the energy integral in eq. (4.3.1) can be divided up into the sum of contributions from each group,

$$\int_0^{\infty} dE' = \sum_{g'=1}^G \int_{g'} dE' \quad (4.3.3)$$

Next, integrating eq. (4.3.1) between  $E_g$  and  $E_{g-1}$  leads to,



$$\begin{aligned} \Omega \cdot \nabla \int_g \Phi(\mathbf{r}, \Omega, E) dE + \int_g \mu(\mathbf{r}, E) \Phi(\mathbf{r}, \Omega, E) dE &= \int_g q(\mathbf{r}, \Omega, E) dE \\ + \sum_{g'=1}^G \int_g \int_{g'} \Phi(\mathbf{r}, \Omega', E') \hat{\mu}(\Omega', E' \rightarrow \Omega, E | \mathbf{r}) d\Omega' dE' dE & \end{aligned} \quad (4.3.4)$$

This expression can be simplified by assuming energy separability. Suppose that within each energy group, the angular fluence can be reasonably approximated as a product between an energy-dependent function,  $\xi(E)$ , and the group fluence,  $\Phi_g(\mathbf{r}, \Omega)$ , as follows:

$$\Phi(\mathbf{r}, \Omega, E) \approx \xi_g(E) \Phi_g(\mathbf{r}, \Omega) \quad \text{for } g \text{ in } [E_{g-1}, E_g] \quad (4.3.5)$$

$\xi_g(E)$  is called the spectral weighting function and is normalized over the group fluence,

$$\int_g \xi_g(E) dE = 1 \quad (4.3.6)$$

PTRAN has been modified to compute  $\xi_g(E)$  for a user defined energy group structure.

Substituting eqs. (4.3.5) and (4.3.6) into eq. (4.3.4) yields the following expression for the BTE in multigroup form,

$$\begin{aligned} \Omega \cdot \nabla \Phi_g(\mathbf{r}, \Omega) + \Phi_g(\mathbf{r}, \Omega) \int_g \mu(\mathbf{r}, E) \xi_g(E) dE &= \int_g q(\mathbf{r}, \Omega, E) dE \\ + \sum_{g'=1}^G \int_g \int_{g'} \Phi_g(\mathbf{r}, \Omega') \hat{\mu}(\Omega', E' \rightarrow \Omega, E | \mathbf{r}) \xi_g(E') d\Omega' dE' dE & \end{aligned} \quad (4.3.7)$$

From this expression, the multigroup cross-sections can now be defined as

$$\mu_g(\mathbf{r}) = \int_g \mu(\mathbf{r}, E) \xi_g(E) dE \quad (4.3.8)$$

$$\hat{\mu}_{gg'}(\Omega' \rightarrow \Omega | \mathbf{r}) = \int_g \int_{g'} \hat{\mu}(E', \Omega' \rightarrow E, \Omega | \mathbf{r}) \xi_g(E') dE' dE \quad (4.3.9)$$

Since the spectral weighting function,  $\xi_g(E)$ , is normalized within each energy group, eqs.

(4.3.8) and (4.3.9) are simply expectation value integrals over the energy group range. The multigroup cross-sections are simply weighted averages of the continuous cross-section over the energy group range.

Finally, we can define our multigroup source as

$$q_g(\mathbf{r}, \boldsymbol{\Omega}) = \int_g q(\mathbf{r}, \boldsymbol{\Omega}, E) dE \quad (4.3.10)$$

The multigroup source differs from the multigroup cross-sections in that it is not an expectation value integral: It is the continuous integral of the source over the group energy range. Substituting eqs. (4.3.8), (4.3.9), and (4.3.10) into eq. (4.3.7) yields the FBTE in the conventional multigroup form,

$$\left[ \boldsymbol{\Omega} \cdot \nabla + \mu_g(\mathbf{r}) \right] \Phi_g(\mathbf{r}, \boldsymbol{\Omega}) = q_g(\mathbf{r}, \boldsymbol{\Omega}) + \sum_{g'=1}^G \int \hat{\mu}_{gg'}(\boldsymbol{\Omega}' \rightarrow \boldsymbol{\Omega} | \mathbf{r}) \Phi_{g'}(\mathbf{r}, \boldsymbol{\Omega}') d\boldsymbol{\Omega}' \quad (4.3.11)$$

The corresponding adjoint expression is:

$$\left[ \boldsymbol{\Omega}' \cdot \nabla + \mu_g(\mathbf{r}) \right] \Phi_g^*(\mathbf{r}, \boldsymbol{\Omega}') = f_g(\mathbf{r}, \boldsymbol{\Omega}') + \sum_{g'=1}^G \int \hat{\mu}_{gg'}(\boldsymbol{\Omega} \rightarrow \boldsymbol{\Omega}' | \mathbf{r}) \Phi_{g'}^*(\mathbf{r}, \boldsymbol{\Omega}') d\boldsymbol{\Omega} \quad (4.3.12)$$

where the group detector response function is defined as

$$f_g(\mathbf{r}, \boldsymbol{\Omega}) = \int_g f(\mathbf{r}, \boldsymbol{\Omega}, E) dE \quad (4.3.13)$$

The remaining BTE can be fully discretized in space and angle: the ambitious reader is referred to Lewis and Miller<sup>106</sup> for a readable derivation.

### 4.3.2 Choice of Forward Source Function

The biased transport process described in eq. (4.2.6) includes a biased source represented by eq. (4.2.8). The non-biased forward source function,  $q(\mathbf{P})$ , employed in CBCT simulations in this dissertation, is defined at the anode focal point,  $\mathbf{r}_0$ , approximated as an isotropic point source,

$$q(\mathbf{r}_0, E) = \frac{1}{4\pi} \delta(\mathbf{r}_0 - \mathbf{r}) \cdot \mathbf{P}_E^{\text{pri}}(E) \quad (4.3.14)$$

This expression uses the central axis primary spectrum  $P_E^{\text{pri}}(E)$  of the CBCT scanner in question.

The corresponding biased source is as follows with some simplifications,

$$\hat{q}(\mathbf{r}_0, E) = \frac{\delta(\mathbf{r}_0 - \mathbf{r}) \cdot P_E^{\text{pri}}(E) \cdot \Phi_{\text{app}}^*(\mathbf{r}, E)}{\int \Phi_{\text{app}}^*(\mathbf{r}_0, E) \cdot P_E^{\text{pri}}(E) dE} \quad (4.3.15)$$

In eq. (4.3.15), the denominator is simply the detector response  $4\pi \times R$ ,

$$R = \frac{1}{4\pi} \int \Phi_{\text{app}}^*(\mathbf{r}_0, E) \cdot P_E^{\text{pri}}(E) dE \quad (4.3.16)$$

and a corresponding weight window target of

$$W_T(\mathbf{r}, E) = \frac{\int \Phi_{\text{app}}^*(\mathbf{r}_0, E) \cdot P_E^{\text{pri}}(E) dE}{4\pi \cdot \Phi_{\text{app}}^*(\mathbf{r}, E)} \quad (4.3.17)$$

#### 4.3.2.1 Detector Response Multigroup Form

Eq. (4.3.16) can also be expressed in the multigroup form. Following the same steps used in Section 4.3.1 and applying the angular independent approximation, eqs. (4.3.3) and (4.3.5) can be substituted in eq. (4.3.16) to yield,

$$R = \frac{1}{4\pi} \sum_{g'=1}^G \Phi_{g'}^*(\mathbf{r}_0) \int_{g'} P_E^{\text{pri}}(E) \xi_{g'}(E) dE \quad (4.3.18)$$

The corresponding weight window target in multigroup form would then be

$$W_{T,g}(\mathbf{r}, E) = \frac{\sum_{g'=1}^G \Phi_{g'}^*(\mathbf{r}_0) \int_{g'} P_E^{\text{pri}}(E) \xi_{g'}(E) dE}{4\pi \cdot \Phi_g^*(\mathbf{r}) \xi_g(E)} \quad (4.3.19)$$

The continuous energy dependence of the weight window target value is not yet removed because of the energy dependent weight function  $\xi(E)$  in the denominator and further

manipulation is warranted. The energy dependence on the target weight could be removed by setting  $\xi$  to a constant value such as,

$$\xi_g(E) = \frac{1}{\Delta E_g} \quad (4.3.20)$$

where  $\Delta E_g = E_{g-1} - E_g$ . Eq. (4.3.19) now simplifies to:

$$W_{T,g}(\mathbf{r}) = \frac{\sum_{g'=1}^G \left[ \Phi_{g'}^*(\mathbf{r}_0) \int_{g'} P_E^{\text{pri}}(E) dE \right]}{4\pi \cdot \Phi_g^*(\mathbf{r})} \quad (4.3.21)$$

Note that this definition for  $\xi$  is different from the energy weighting function utilized to compute the multigroup cross-section libraries. Though this is inconsistent, in the hands of ORNL investigator, this approach to target weight evaluation has proven to be quite effective in nuclear engineering applications<sup>64,70</sup>.

Following this same process, the biased source can similarly be expressed as,

$$\hat{q}(\mathbf{r}_0, E) = \frac{P_E^{\text{pri}}(E) \cdot \Phi_g^*(\mathbf{r}_0)}{\sum_{g'=1}^G \left[ \Phi_{g'}^*(\mathbf{r}_0) \int_{g'} P_E^{\text{pri}}(E) dE \right]} \quad (4.3.22)$$

with a corresponding primary particle weight correction factor of,

$$W_{\text{corr}}^{\text{pri}} = \frac{\sum_{g'=1}^G \left[ \Phi_{g'}^*(\mathbf{r}_0) \int_{g'} P_E^{\text{pri}}(E) dE \right]}{4\pi \cdot \Phi_g^*(\mathbf{r}_0)} \quad (4.3.23)$$

For practical use in PTRAN equations (4.3.22) and (4.3.23), a numerical integration over a sub grid is performed to compute  $\int_{g'} P_E^{\text{pri}}(E) dE$ .

### 4.3.3 Detector Response Function

As mentioned previously, the detector response function,  $f(E)$ , is used as the adjoint source in DOM calculations. For my purposes, using eq. (4.2.4), the detected response is the energy, in keV, deposited to the detector. The units of  $f(E)$ , then, are in  $\text{keV}\cdot\text{cm}^2$ . Treating the flat panel detector as having 100% detection efficiency for scattered photons released in scintillating crystal (not 100% detection efficiency of incident photons), the following detector response function was used in all the PARTISN calculations,

$$f(E, \boldsymbol{\Omega}) = E(1 - e^{-\mu_{\text{CsI}}(E) \cdot l_{\text{CsI}}}) \cdot A_d, \quad \text{where} \quad l_{\text{CsI}} = \frac{t}{\boldsymbol{\Omega} \cdot \boldsymbol{\Omega}_{\text{det}}} \quad (4.3.24)$$

In the above expression,  $\mu_{\text{CsI}}(E)$  is the linear attenuation coefficient for the CsI scintillating crystal,  $l_{\text{CsI}}$  is the path length through the crystal,  $t$  is the thickness of the crystal,  $\boldsymbol{\Omega}_{\text{det}}$  is the unit vector normal to the detector plate, and  $A_d$  is the detector area. The same detector response function used in the PTRAN Monte Carlo calculations.

#### 4.3.3.1 Multigroup Form

For the DOM multigroup calculations, eq. (4.3.24) can be expressed in multigroup form by integrating over each energy group as follows,

$$f_g = A_d \int_g E(1 - e^{-\mu_{\text{CsI}}(E) \cdot l_{\text{CsI}}}) dE \quad (4.3.25)$$

### 4.3.4 PARTISN Implementation

For testing CADIS, DOM calculations were completed with PARTISN<sup>107</sup> from the Los Alamos National Laboratory (LANL). PARTISN calculations used  $S_n=32$  angular quadrature with a  $P_n$  order of 5 to remove ray-effects. The IGEOM variable was set to X-Y-Z to accommodate a 3-D voxelized geometry. Figure 4.2 contains two different PARTISN calculation grids that were

investigated. The fine grid (FG) contained  $41 \times 100 \times 31$  spatial cells, while the coarse grid (CG) had  $15 \times 30 \times 15$  spatial cells. The PTRAN y-axis corresponds to the z-axis in PARTISN, and the z-axis in PTRAN corresponds to the y-axis in PARTISN. To remove confusion, all future references to coordinate axes, including discussions of PARTISN, will assume the PTRAN coordinate system.

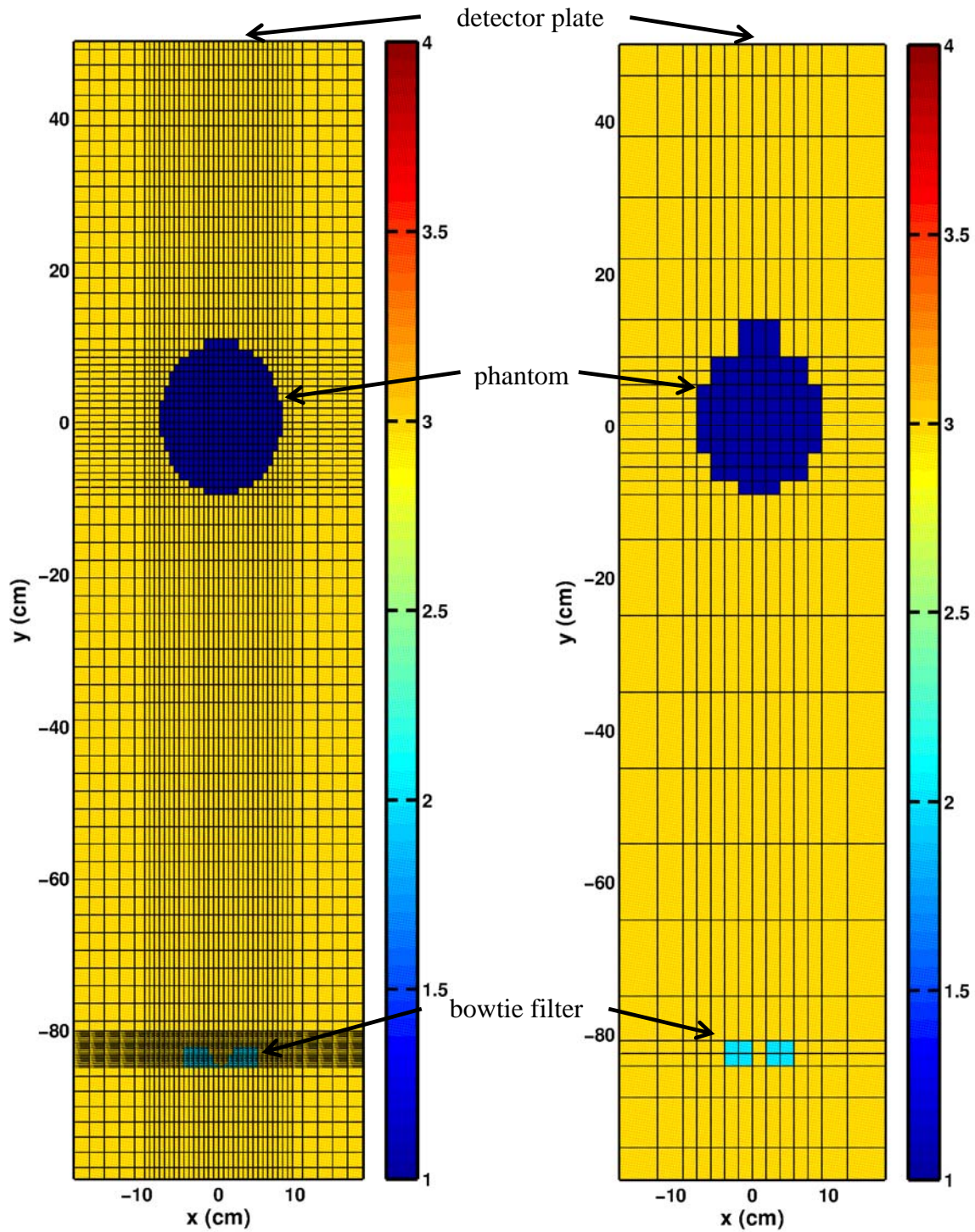


Figure 4.2: Cross-section of PARTISN DOM calculation grid assuming CBCT MC primary source at anode for the fine grid (left) and the coarse grid (right) showing the bow-tie filter (cyan), the cylindrical phantom (blue), and the surrounding air (orange). The detector plate is located at the positive y-bound.

The different colors in Figure 4.2 correspond to the three different media simulated: aluminum bow-tie filter (cyan), an elliptical cylinder consisting of water with major- and minor-axes of 10 cm and 8 cm respectively with a 12.5 cm length (blue), and the air background (orange). This figure was generated using a MATLAB m-file, contained in Appendix D and called “PARTISN\_gridStructure.m,” created to assist the user in writing PARTISN input files.

The variable NGROUP was set to 8, specifying eight energy groups, with energy bounds in keV of [1, 21, 29, 39, 53, 61, 69, 90, 124], to increase the efficiency of computing  $\Phi_g^*$ . The group cross-section libraries were computed using the NJOY code system, again from LANL. The NJOY input file, containing the energy group structure, used to compute the multigroup cross section library is included within this dissertation as Appendix E. For a thorough description on computing the weighting function, the reader is invited to read Daskalov *et al*<sup>31</sup>. PTRAN was modified with an option to produce the weighting function as output for a central voxel of the simulated phantom.

#### 4.3.5 PTRAN Modifications

For the alterations in PTRAN to perform weight windowing, please read Appendix D which contains a detailed description. PTRAN was modified to accept the DOM adjoint flux as input for the importance function. Furthermore, an additional modification to PTRAN was made to allow a non-uniform importance grid that matches the PARTISN calculation grid.

### 4.4 ABFMC Performance Assessment

#### 4.4.1 Assessing Accuracy

The accuracy of our CADIS implementation was assessed with the same technique used in Appendix 2, eq. (8) taken from Kawrakov *et al*<sup>82</sup> :



$$p(z_{ik}) = \frac{1}{\sqrt{2\pi}} \left[ \alpha_1 e^{(\beta_1 - z_{ik})^2/2} + \alpha_2 e^{(\beta_2 - z_{ik})^2/2} + (1 - \alpha_1 - \alpha_2) e^{z_{ik}^2/2} \right] \quad (4.4.1)$$

In this expression,  $z_{ik}$  is defined as the difference between the Monte Carlo computed signals at  $ik$  as computed using the ABFMC scheme,  $\bar{R}_{ik}^{WW}$ , and the regular, non-ABFMC MC,  $\bar{R}_{ik}^{MC}$ , expressed as the number of standard deviations:

$$z_{ik} = \frac{\bar{R}_{ik}^{WW} - \bar{R}_{ik}^{MC}}{\sqrt{\sigma_{\bar{R}_{ik}^{WW}}^2 + \sigma_{\bar{R}_{ik}^{MC}}^2}} \quad (4.4.2)$$

Figure 4.3 shows the distribution of  $z_{ik}$  plotted along with a fit of  $p(z_{ik})$  to the data using Matlab. The fit parameters were:  $\alpha_1 = 0.0001$ ,  $\beta_1 = 0.9618$ ,  $\alpha_2 = 0.00593$ , and  $\beta_2 = -1.81$ . Due to the average value of  $\sigma_{\bar{R}_{ik}^{WW}}^2$  to be 2.5%, these parameters suggest that 0.01% of the pixels have a 2.4% error, and 0.5% of the pixels are underestimated by 4.5%. These errors affect only 0.51% of the pixels, supporting our hypothesis that ABFMC results in unbiased results relative to conventional FMC..

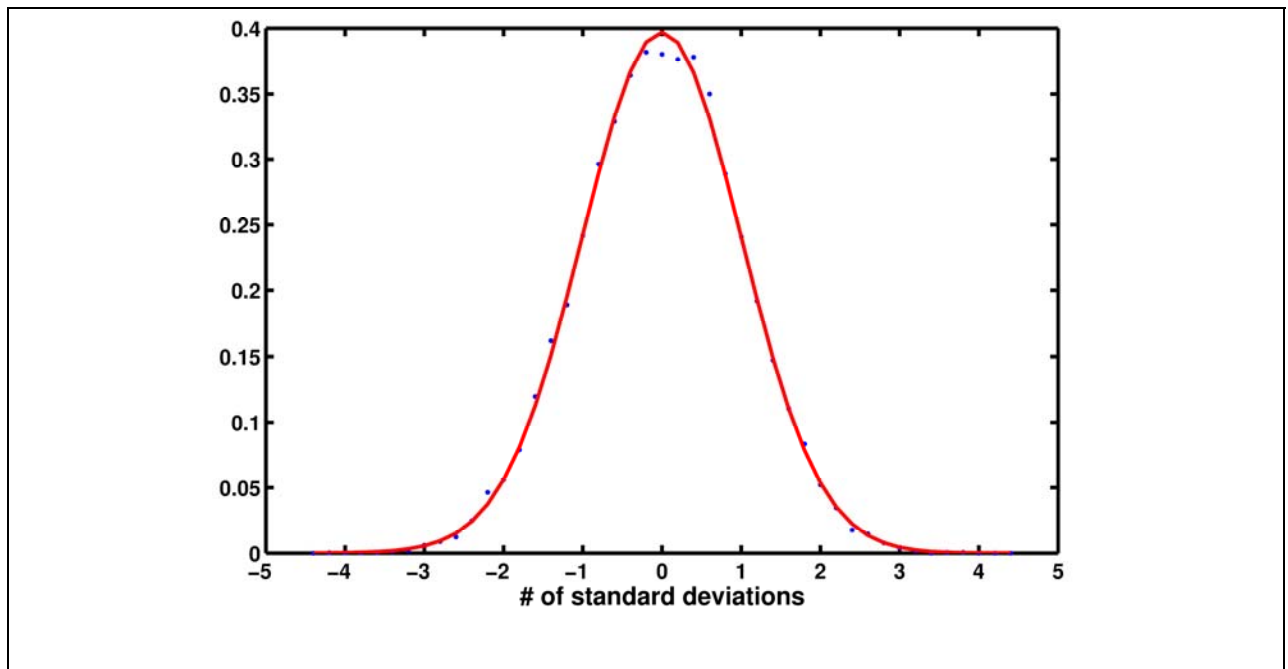


Figure 4.3: The distribution of  $p(z_{ik})$  using the ABFMC implementation with corresponding fit.

## 4.4.2 Efficiency Assessment

### 4.4.2.1 Efficiency Metric

As a reminder from Chapter 2, the figure of merit,  $FOM$  for each flat panel detector pixel  $ik$  is defined as,

$$FOM_{ik} = \frac{1}{\bar{\sigma}_{ik}^2 \cdot T_{CPU}} \quad (4.4.3)$$

where  $T_{CPU}$  is the CPU time for the respective simulation. The efficiency gained from using ABFMC over normal MC,  $G_{ik}$ , is then defined as the  $FOM_{ik}$  ratio,

$$G_{ik}^{ww} = \frac{FOM_{ik}^{ww}}{FOM_{ik}^{MC}} \quad (4.4.4)$$

### 4.4.3 ABFMC Candidate Comparison

The efficiency assessment was completed for four different approaches to ABFMC presented implicitly and explicitly in this chapter. I list them here with corresponding summaries for convenience.

1. CADIS: The biased transport process using weight windowing outlined in eqs. (4.3.21) through (4.3.23), using adjoint PARTISN with eq. (4.3.25) as the adjoint source.
2. Adjoint: The same as CADIS minus the source biasing. Primary particles are randomly generated using the non-biased central axis primary spectrum,  $P_E^{pri}(E_{g,n})$ .
3. OTF-FAIG: This is the forward adjoint generator discussed in Section 4.2.6 and presented in Appendix D.
4. PC-FAIG: At the end of simulation using the OTF-FAIG, PTRAN has the option of re-using the last updated importance function at the beginning of a new simulation. In this

way, the OTF-FAIG can be used to pre-compute a low-uncertainty solution to the importance function that can be used by a future PTRAN simulation with the same geometry. This is what I call PC-FAIG. In other words, the importance function is computed in a separate calculation and used for the PC-FAIG simulation.

The efficiency gains resulting from the above approaches are compared against each other in two ways. First, 20 million histories were run for both non-weight windowed (NWW) and for each ABFMC simulation for both the FG and CG importance grids. The efficiency gain distribution with respect to detector module pixels,  $ik$ , was computed using eq. (4.4.4). The second comparison involved running PTRAN with the NWW and above ABFMC approaches for 2 min and comparing the distribution of the percent standard deviation about the mean for every  $ik$  pixel vs. the energy scatter signal produced for a low-uncertainty calculation.

#### 4.4.4 PTRAN Simulation Environment

To explore the affect from ABFMC on Monte Carlo CBCT scatter projection efficiency, two source models were tested: true primary photon isotropic point source at the x-ray tube anode and a phase space source which includes effects of beam hardening and scattering from the bowtie filter. For the primary photon source, incorporating CADIS source biasing using eq. (4.3.15) is trivial. In both cases, the same elliptical cylinder described in Section 4.3.4 was imaged in full-fan geometry with the bowtie filter included. The CBCT detector was modeled as a slab of CsI with dimensions of 20cm×15cm broken into 2.5 mm square 160×120 detector pixels (A sample PTRAN input file is included as Appendix G). In practice, fewer detector modules can be simulated, for example a 40×30 grid, and the full 1024×768 resolution can be reclaimed through interpolation since the amount of high frequency content in the scatter signal is low<sup>48</sup>.

The phase space source consisted of a list of phase space coordinates describing particles that have crossed a spatial boundary of some sort. For the CBCT simulation geometry, the boundary was a plane 200 mm downstream of the bowtie filter: when a particle crosses this plane, the particle is tallied and its phase space parameters (position, trajectory, energy, weight) are added to the phase space file. When utilizing a phase space source, instead of randomly launching particles from the x-ray tube focal spot, a particle is read from the previously generated file in consecutive order and transported as a primary particle. Use of a phase space source in and of itself can be a powerful variance reduction technique (source biasing) when the geometry upstream of the threshold remains constant for various simulation geometries (in our case for all patient anatomies and gantry angles). This is especially true when there is a highly scattering attenuator upstream, such as a bowtie filter. Unfortunately, because of the difficulty in describing this source in closed form and/or numerically, the CADIS source biasing is difficult to implement and therefore was not implemented for our study. Instead, the DOM adjoint fluence was used to initialize the importance function, using eq. (4.3.21), without the coupled source biasing. To dispel confusion, whenever the phase-space source is used in conjunction with ABFMC, the acronym will be preceded by an additional “PS” for phase space. For example, if the adjoint importance function was used in combination with a forward MC a phase space source model, the results would be referred to as “PS-Adjoint.”

#### 4.4.4.1 Full Primary Source at Anode

##### 4.4.4.1.1 Efficiency Gain

Figure 4.4 shows the distribution of  $G_{ik}^{WW}$  over simulated detector pixels. Table 4-I and Table 4-II show parameters that numerically describe the shape of the distributions plotted in Figure 4.4, namely the mean, most probable value (MPV), median, and the 20<sup>th</sup> and 80<sup>th</sup> percentile values specifying the minimum gains for which 20% or 80% of the pixels have smaller gains.

Table 4-I.  $G_{ik}^{WW}$  distribution statistic for comparing ABFMC approaches to the non-weight windowed PTRAN using a fine grid (FG) for the importance function.

	Mean	MPV	Median	20 <sup>th</sup> Percentile	80 <sup>th</sup> Percentile
NWW vs. CADIS	30.84	30.78	30.56	26.58	40.52
NWW vs. Adjoint	30.11	29.29	29.92	25.99	39.84
NWW vs. OTF-FAIG	14.21	0.75	12.15	12.16	32.38
NWW vs. PC-FAIG	37.08	36.20	37.22	32.68	49.55

Table 4-II.  $G_{ik}^{WW}$  distribution descriptors for comparison of the ABFMC approaches to the non-weight windowed PTRAN using a coarse grid (CG) for the importance function.

	Mean	MPV	Median	20 <sup>th</sup> Percentile	80 <sup>th</sup> Percentile
NWW vs. CADIS	16.72	16.16	16.59	14.38	22.04
NWW vs. Adjoint	16.35	14.96	16.11	13.89	21.44
NWW vs. OTF-FAIG	18.13	15.88	17.54	15.02	24.33
NWW vs. PC-FAIG	37.21	37.25	37.38	32.65	49.35

Comparison of these distributions leads to the following observations:

1. When using the multigroup adjoint fluence to define the importance map, the marginal efficiency improvement from CADIS source biasing using eqs. (4.3.22) and (4.3.23) are small. Both the plots in Figure 4.4 and the table data in Table 4-I and Table 4-II show very little advantage in efficiency from using CADIS over Adjoint. This suggests that in this problem, the coupling between primary source particle generation and subsequent weight windowing is not an effective method to further increase the efficiency of these

scatter calculations. Since we are only interested in the scatter component of the projection, it would more appropriate to bias the sampling of a first-collision source. Use of such a source could potentially take advantage of the consistency in coupling the source generation and particle transport biasing. The first collision source would be of interest to future studies.

2. Changing from fine to coarse importance grids reduces the efficacy of adjoint biased, both CADIS and Adjoint, Monte Carlo by half. Because PARTISN uses the same spatial grid for representing fluence and radiological uniform spatial cells, FG and CG do not model the bowtie filter with equivalent accuracy. Referring back to Figure 4.2, the bowtie filter is modeled more accurately in the FG than in the CG grid. In fact, in the CG geometry, there is a gap between the two cuboids modeling the bowtie filter body allowing adjoint particles to pass through un-attenuated. This was a non-physical effect, and an artifact from how the analytical representation of the bowtie filter was mapped to the PARTISN calculation grid. This hole caused an increase in the adjoint flux at the location of the primary source. Figure 4.5 shows the  $\Phi_g^*(\mathbf{r})$  ratio of the CG to FG importance grids following the interpolation of the CG grid to match the FG grid. At the primary source, the CG PARTISN  $\Phi_g^*(\mathbf{r})$  is roughly 2.5 times higher than that of the FG calculation. Referring to eq. (4.3.21), results in weight window target values 2.5-fold larger than the corresponding FG values leading to a decrease in efficiency from using an inaccurate importance map. This could be fixed by using a slab attenuator in place of the bowtie filter approximation. Since the OTF- and PC-FAIG implementations are immune to this difficulty (since importance function grid has nothing to do with MC modeling accuracy), the CG and FG efficiency gain distributions are much more similar.

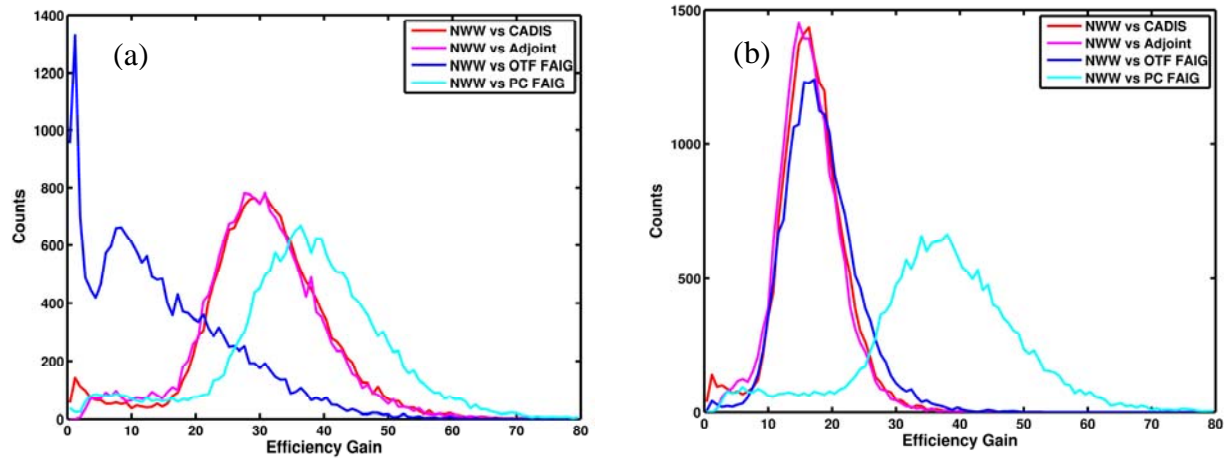


Figure 4.4: The  $G_{ik}^{WW}$  distribution using the primary point source for the (a) FG and (b) CG importance grids. “NWW” refers to conventional MC simulation without importance sampling.

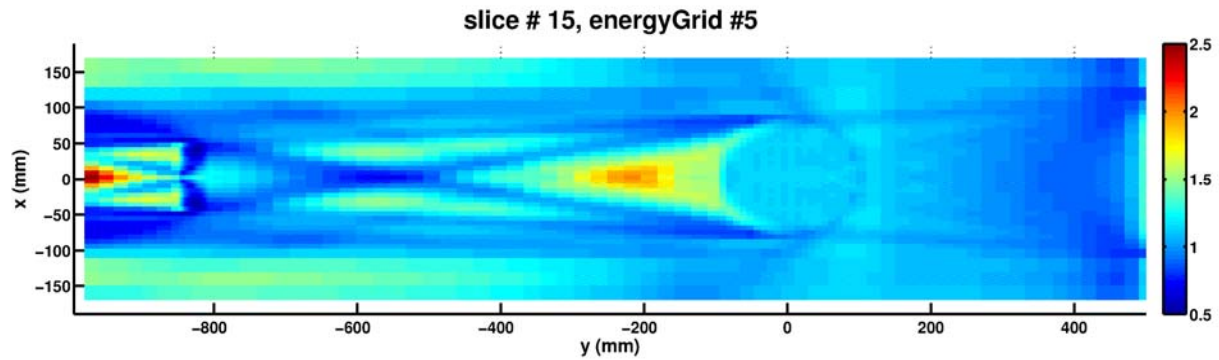


Figure 4.5: The adjoint flux,  $\Phi_g^*(\mathbf{r})$ , ratio between the CG and FG importance grids with the CG adjoint flux interpolated onto the FG grid.

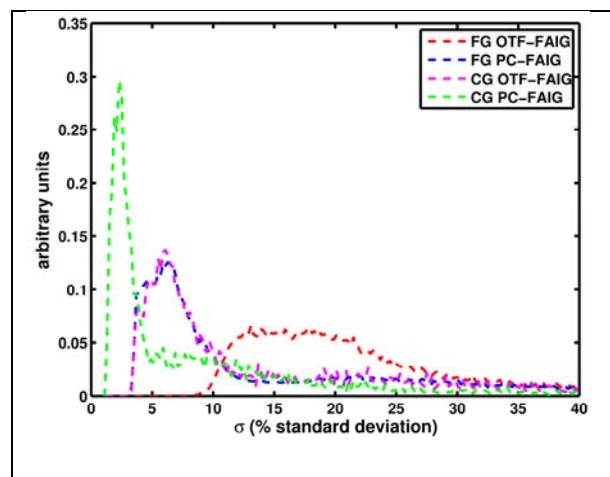


Figure 4.6: Distributions of the percent standard deviation about the mean for the four importance grids generated by the forward adjoint importance generator (FAIG).

3. A high level of statistical uncertainty in the PC or OTF importance map negatively impacts the efficiency gain realizable through ABFMC. This is shown through the stark contrast in efficiency performance for the OTF-FAIG between the FG and CG importance grids. In fact, the most probable value (MPV) for the OTF-FAIG using the FG importance grid is 0.75, an efficiency decrease not increase, while the CG efficiency performance is similar to the Adjoint and CADIS implementations. The explanation is found in Figure 4.6 which shows the distributions of the percent standard deviations about the mean for the four importance grids generated by the forward adjoint importance generator used in these simulations. The red dotted curve corresponds to the OTF-FAIG for the FG importance grid, and demonstrates a generally high statistical uncertainty with a broad peak between 12% and 22%. Note that this is the uncertainty at the end of the 20 million photon histories used to compute the scatter projections. The uncertainty was much higher immediately following the ramp-up stage of the simulation, likely leading to the peak at 0.75 in Figure 4.4(a). While the FG importance grid has  $1.0168 \times 10^6$  importance cells, the CG has only  $5.4 \times 10^4$  cells, and both have  $20 \times 10^6$  histories to resolve the importance grid with a ramp-up phase of only  $4 \times 10^6$  histories before the importance grid is used no matter what its associated uncertainty. The high uncertainty associated to the importance grid, as generated using the OTF-FAIG method, leads to decreased efficiency performance and could lead to efficiency losses as compared with non-weight windowed Monte Carlo.
4. Another observation from Figure 4.4 is that there is no additional gain from using a more accurate importance grid with the FAIG in terms of spatial resolution. In fact, the CG performs slightly better due to lower importance function statistical uncertainty (see



Figure 4.6). This suggests that there is no reason to use a high spatial resolution importance grid when using FAIG. The lower spatial resolution grid will also decrease the amount of time required for the PARTISN DOM calculations, though more accurate methods need to be adapted to model the BT filter. This is a promising result as it leads to decreased calculation times for DOM and the time required for the forward adjoint generator to resolve a usable importance map

5. A final observation from Figure 4.4Figure 4.6 is that while a high uncertainty in the FAIG importance grid leads to efficiency losses, the uncertainty does not necessarily have to be extremely low either. The uncertainty in the importance map used by the PC-FAIG simulation in Figure 4.4 is shown in the blue curve in Figure 4.6. As stated before, there is only a small difference between the PC-FAIG in the FG and the PC-FAIG in the CG where the importance map uncertainty was much lower (green curve in Figure 4.6). This suggests that the importance map is allowed some noise with little loss to efficiency allowing roughly a 7% uncertainty for an efficient calculation.

Table 4-III: Percent standard deviation about the mean vs. scatter signal distribution quantitative metrics for each ABFMC approaches to the non-weight windowed PTRAN using a fine grid (FG) for the importance function following only a 2 min CPU time.

	Mean	MPV	Median	20 <sup>th</sup> Percentile	80 <sup>th</sup> Percentile
NWW	65.78	99.75	63.50	52.84	77.34
CADIS	14.41	12.70	13.80	12.50	15.59
OTF-FAIG	36.89	18.07	29.63	18.68	55.93
PC-FAIG	13.05	11.70	12.40	11.41	13.90

Table 4-IV: Percent standard deviation about the mean vs. scatter signal distribution quantitative metrics for each ABFMC approaches to the non-weight windowed PTRAN using a fine grid (CG) for the importance function following only a 2 min CPU time.

	Mean	MPV	Median	20 <sup>th</sup> Percentile	80 <sup>th</sup> Percentile
NWW	65.78	99.75	63.50	52.84	77.34
CADIS	19.32	17.68	18.58	16.68	21.27
OTF-FAIG	20.46	13.40	15.89	13.50	24.85
PC-FAIG	13.05	11.70	12.50	11.41	14.00

#### 4.4.4.1.2 Two minute Uncertainty Distributions

Figure 4.7 shows the scatter statistical uncertainty distributions vs. expected scatter signal. Table 4-III and Table 4-IV contain a few specific parameters that describe the shape of the uncertainty distributions for the 2min simulations. The same observation seen in the previous section, Section 4.4.4.1.1, can also be seen here, but expressed differently. For example, observation number 3, that a high level of uncertainty in the FAIG-produced importance map can lead to decreased effectiveness, is manifested in Figure 4.7(a) as the large spread in the statistical uncertainty.

#### 4.4.4.2 Phase Space Source

As stated before, modeling the source as a phase space file can be an extremely effective variance reduction technique by itself when the collecting threshold is downstream of a highly scattering attenuator and every geometry element upstream of the threshold remains constant for wide variety of simulation geometries. Since CBCT meets these requirements, it is a perfect candidate for phase space source modeling. Figure 4.8 shows the distribution of  $G_{ik}^{WW}$ , comparing the ABFMC approaches using a phase space source, against the non-WW Monte Carlo simulation using the full primary source. The distribution of using the phase space source alone, with no weight windowing is also plotted to show its individual effect.

Table 4-V:  $G_{ik}^{WW}$  distribution descriptors comparing the full-primary source, non-weight windowed PTRAN (NWW) to the phase-space source, non-weight windowed PTRAN (PS-NWW) and the ABFMC approaches using a fine grid (FG) for the importance function and the phase-space source.

	Mean	MPV	Median	20 <sup>th</sup> Percentile	80 <sup>th</sup> Percentile
NWW vs. PS-NWW	14.65	12.60	14.15	12.11	18.89
NWW vs. PS-Adjoint	199.47	206.50	201.69	177.49	271.76
NWW vs. PS-OTF-FAIG	106.12	11.41	104.54	93.48	182.24
NWW vs. PS-PC-FAIF	220.47	211.77	218.64	190.13	291.00

Table 4-VI:  $G_{ik}^{WW}$  distribution descriptors comparing the primary point source, non-weight windowed PTRAN (NWW) to the phase-space source, non-weight windowed PTRAN (PS-NWW) and the ABFMC approaches using a coarse grid (CG) for the importance function and the phase-space source.

	Mean	MPV	Median	20 <sup>th</sup> Percentile	80 <sup>th</sup> Percentile
NWW vs. PS-NWW	14.65	12.60	14.15	12.11	18.89
NWW vs. PS-Adjoint	148.90	144.04	148.60	129.46	200.20
NWW vs. PS-OTF-FAIG	134.06	108.62	129.39	109.41	200.87
NWW vs. PS-PC-FAIF	224.50	228.31	222.03	192.99	295.40

The distributions shown in Figure 4.8 and Table 4-V and Table 4-VI show the same behavior as those for the primary point source in addition to the large benefit achievable from utilizing the phase space source. This source is realized do to the loss of need to transport particles through the bowtie attenuator where many particles are lost due to scattering in trajectories away from the detector plate.

Figure 4.9 shows percent standard deviations for 2 minute run times for the phase-space source NWW and ABFMC in comparison to the full-primary source NWW. These plots are again very similar in shape and distribution to the full primary source, leading to the same conclusions, but show the great advantage of using the phase-space source for CBCT scatter projection simulations. Table 4-VII and Table 4-VIII list the distribution quantitative metrics allowing further comparison.

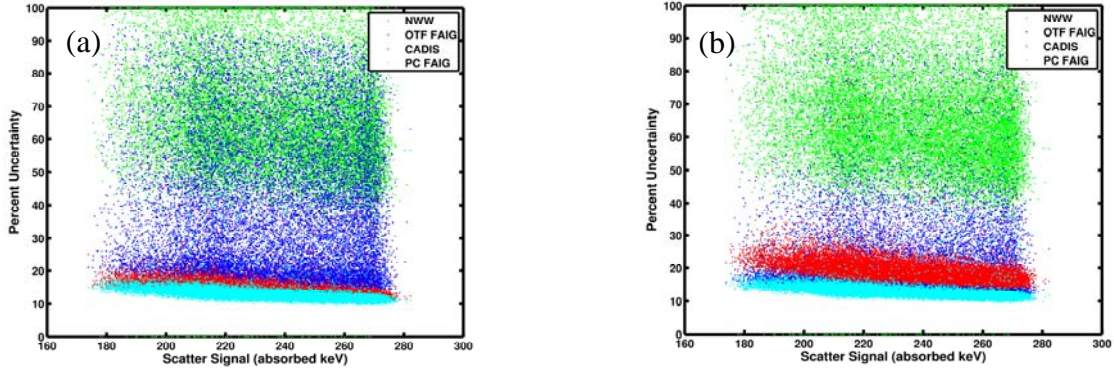


Figure 4.7: Scatter plots of the percent standard deviation for each  $ik$  simulated detector pixel plotted against the scatter signal expected at the detector for the (green) non-weight windowed PTRAN, (blue) OTF-FAIG, (red) CADIS, and (cyan) PC-FAIG in the (a) FG and (b) CG importance grids following 2 min CPU Time

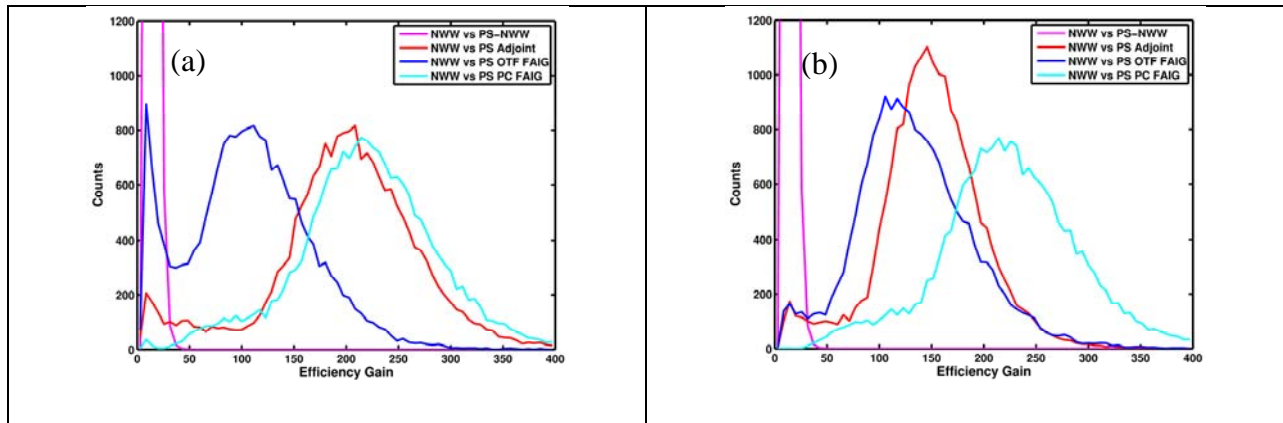


Figure 4.8: The  $G_{ik}^{WW}$  distribution using the phase space source for the (a) FG and (b) CG importance grids. Also plotted here is the efficiency gain just from using the phase space source alone (magenta), and the peak is not shown to allow the shape of the other distributions to be seen.

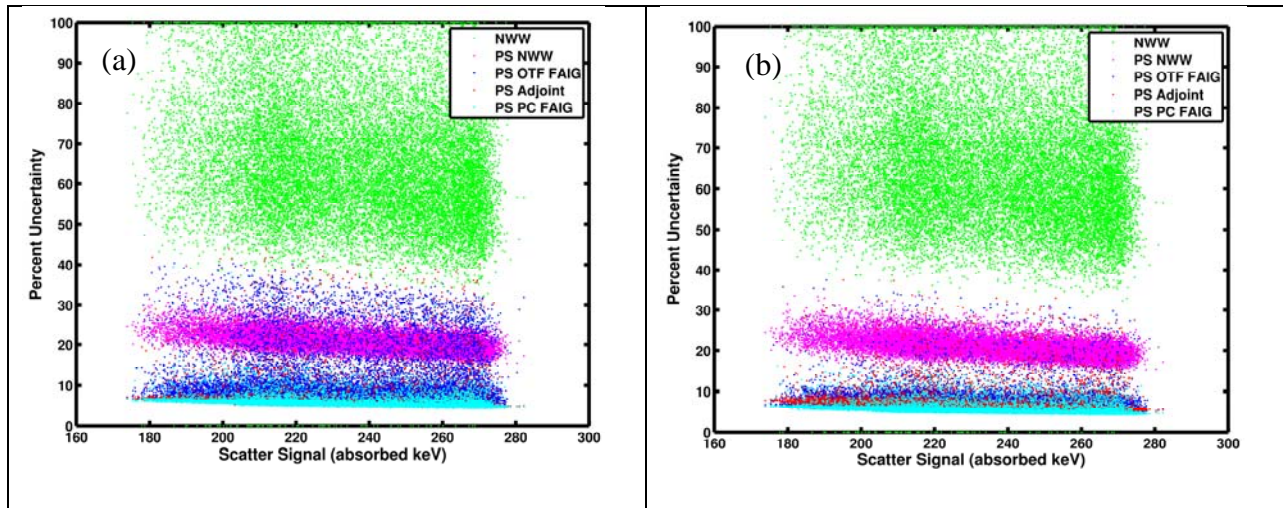


Figure 4.9: Scatter plots of the percent standard deviation for each  $ik$  simulated detector pixel plotted against the scatter signal expected at the detector for the (green) non-weight windowed PTRAN, (magenta) phase-space source NWW PTRAN, (blue) OTF-FAIG, (red) CADIS, and (cyan) PC-FAIG in the (a) FG and (b) CG importance grids. The ABFMC simulations utilized the phase space source for a 2 min CPU time

Table 4-VII: Quantitative Metrics for the percent standard deviation about the mean distribution following only 2 min of single CPU run time for the non-weight windowed PTRAN using the phase space source, (PS-NWW), adjoint function biasing using the phase-space source (PS-Adjoint), the on-the-fly forward adjoint importance generator using the phase space source (PS-OTF-FAIG), and the pre-computed importance map from the forward adjoint generator using a phase-space source (PS-PC-FAIG). This was on the fine importance grid.

	Mean	MPV	Median	20 <sup>th</sup> Percentile	80 <sup>th</sup> Percentile
PS-NWW	20.95	20.27	20.67	18.88	22.86
PS-Adjoint	6.04	4.93	5.33	4.83	6.23
PS-OTF-FAIG	10.39	6.62	7.92	6.43	12.20
PS-PC-FAIG	5.59	4.83	5.23	4.83	5.93

Table 4-VIII: Numerical descriptors for the percent standard deviation about the mean distribution following only 2 min of simulation for the non-weight window PTRAN using the full primary source (NWW), the non-weight windowed PTRAN using the phase space source, (PS-NWW), adjoint function biasing using the phase-space source (PS-Adjoint), the on-the-fly forward adjoint importance generator using the phase space source (PS-OTF-FAIG), and the pre-computed importance map from the forward adjoint generator using a phase-space source (PS-PC-FAIG). This was on the coarse importance grid.

	Mean	MPV	Median	20 <sup>th</sup> Percentile	80 <sup>th</sup> Percentile
PS-NWW	20.95	20.27	20.77	18.88	22.86
PS-Adjoint	6.88	5.83	6.33	2.53	7.22
PS-OTF-FAIG	7.33	6.23	6.72	5.73	8.12
PS-PC-FAIG	5.45	4.83	5.13	4.73	5.83

#### 4.4.4.3 Scatter Projections

A visual comparison of the 2 min scatter projections for the (b) NWW, (c) CADIS, (d) PC-FAIG, (e) PS-NWW, (f) PS-Adjoint, and (g) PS-PC-FAIG can be seen in Figure 4.10 compared with a low-uncertainty scatter projection (a).

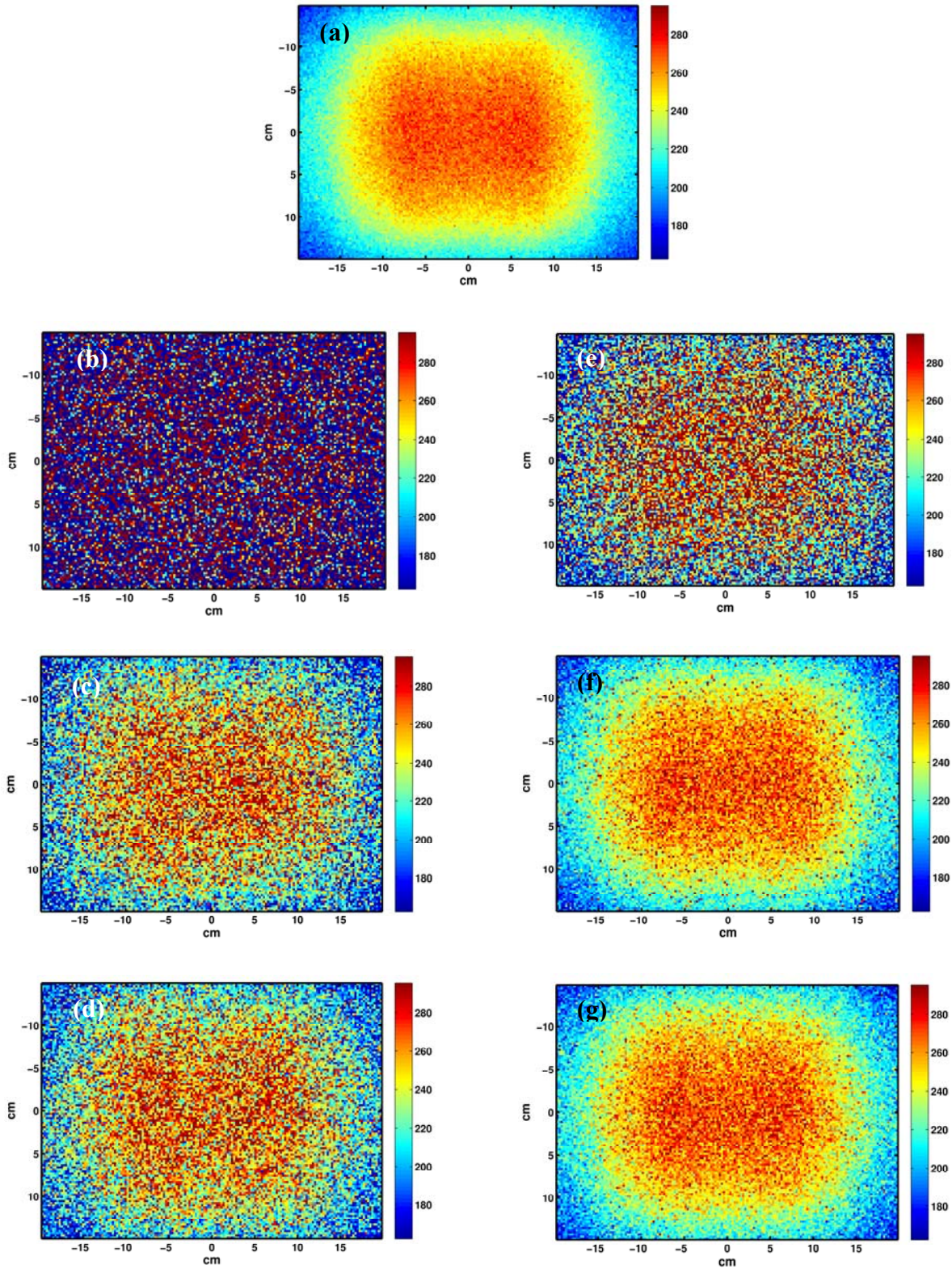


Figure 4.10: Scatter projections for the elliptical water cylinder studied for a (a) low-uncertainty, average 2%, (b) 2 min NWW, (c) 2 min CADIS, (d) 2 min PC-FAIG, (e) 2 min PS-NWW, (f) 2 min PS-Adjoint, and (g) 2 min PS-PC-FAIG. The signal is energy absorbed in keV. All images are with the same window and level

## 4.5 Discussion

In summary, I have shown that ABFMC is highly effective variance reduction strategy for the CBCT projection geometry, yielding 40-fold efficiency gains for PC-FAIG and Adjoint and 18-fold gains for “on-the-fly” continually updated FAIG. Some important observations include the relatively marginal gains from the CADIS source biasing. Since there is not a strong coupling between the source and transport biasing in the CBCT projection geometry, the greatest gains are achieved through the pairing of the ABFMC transport biasing via weight windowing and the phase space source. The combination of PC-FAIG/Adjoint biasing and phase-space source boosts efficiency gains to 250 to 400-fold range relative to non-biased forward Monte Carlo using the primary point source. In Addition, the resolution of the spatial importance grid seems to have little impact on the overall gains achieved. This observation allows for more efficient DOM calculations and faster determination of  $\Phi_g^*(\mathbf{r})$  by the forward adjoint importance generator.

The uncertainty data presented here has been for a  $1024 \times 768$  pixel detector approximated as a  $160 \times 120$  grid. As stated previously, this approximation, followed by interpolation back to the original resolution, is permissible due to the low occurrence of high frequency content in the spatial scatter signal. In fact the grid resolution can be further reduced to a  $40 \times 30$  detector array with little accuracy loss<sup>48</sup>. Under these circumstances, and if an average 5% uncertainty is acceptable in the computed scatter signal, use of a DOM computed adjoint function or an importance map pre-computed using the FAIG will produce a scatter projection in as little as 8 sec. In comparison, the work completed by Mainegra-Hing *et al*<sup>59</sup> would require around 38 sec for a similar calculation. To put this into perspective, a full 360 projections to be computed by the PS-NWW PTRAN would require roughly 13 hours of CPU time. If instead the PS-Adjoint or

PS-PC-FAIG were utilized, only 48 min would be needed to reach 5% uncertainty. By using cost effective parallel computing environments, this time would reduce linearly with the number of CPU cores used for parallel computation. For example, if an 8 CPU core workstation is available, only 6 minutes would be required to compute the 360 scatter projections for the geometry studied here.

The full benefit from ABFMC is realized by using a pre-determined adjoint function, whether by DOM calculations or FAIG. Both these methods would require an additional computational burden that has the potential to offset gains achieved in computational efficiency. For example, the PARTISN coarse grid calculations took roughly 4 min per projection simulated. For clinical acceptance of DOM-based ABFMC implementations, then more efficient DOM solutions must be applied as well. Some ideas to increase the efficiency would be to implement adaptive mesh refinement, reduce the Sn order in connection with a first collision source, or by reducing the mesh sizes. On the other hand, Appendix D shows that the use of an importance map from a previously computed scatter projection can be reused for a different projection at a nearby angle. This suggests that DOM calculations will not need to be completed for every angle while a projection's adjoint function is reused, thus reducing the computational burden of DOM solutions. Furthermore, Figure 4.11 shows the average efficiency gains achieved over a 360 degree rotation using an average importance function computed using the FAIG for two preceding projections. In short, each projection uses an importance map generated as an average from the two projections preceding it, or over 8 degrees in this case. Using this strategy removes the computational burden of pre-computing an importance function while still reaping the additional benefits. The sinusoidal behavior of the efficiency gain over angle is due to the



increased and decreased effective radiological path-length as the source rotates around the phantom. FAIG is more efficient in regions of deeper penetration.

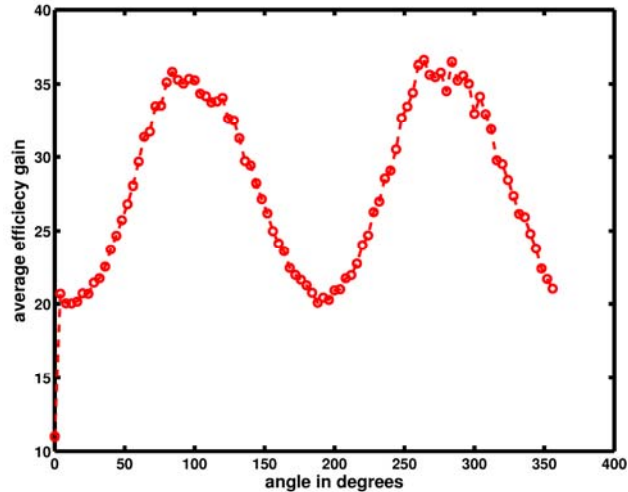


Figure 4.11: The average efficiency gain using the forward adjoint importance generator for a pelvic phantom around a 360 degree rotation. Each projection uses an average importance function from the two projections preceding it.

The study presented in this chapter was for a single cylindrical type water phantom mimicking the size of an adult head. The extensive study included as Appendix D extends the application of the forward adjoint importance generator to two additional geometries: a simulated head and body phantom. Future work should focus on expanding the application to more realistic patient geometries such as single and dual energy CT patient representations. Furthermore, the effect on scatter projection statistical uncertainty on reconstructed image quality needs to be assessed so the optimal relationship between efficiency and quality can be ascertained. Another area of future work aimed at decreasing the amount of time required for CBCT scatter correction is to look at the effect on reconstructed image quality from under-sampling the scatter projection sonogram. The missing angular data in the sonogram could be recovered through interpolation. The relationship between image quality and level of under-sampling could be determined to find the optimal interval between MC computed scatter projections.

Lastly, CBCT scatter calculation efficiency is not the only barrier to improve image quality. It has been shown that after subtracting the scatter signal the measured projections, the scatter noise left behind decreases the contrast to noise ratio<sup>48</sup>, affecting low-contrast detectability. Effective and time efficient strategies to mitigate the scatter noise have resulted in notable improvements to reconstructed image quality<sup>45,108</sup>. Any comprehensive CBCT scatter correction method must include some approach to correct for the residual scatter noise. Upon complete correction with a comprehensive CBCT reconstruction algorithm, one method to test corrected CBCT image quality would be to repeat Weiss *et al's*<sup>47</sup> study on physician contouring.

Similar to the Chapters 2 and 3, the CPU time and efficiency gains reported here only incorporate radiation transport of one angle and not the time for variable initialization or geometry setup. In practice, multiple angles will be computed simultaneously (via parallel processing) and consecutively, initializing the geometry only once for an entire simulation. For the phantom geometries presented in this study, the initialization time was less than 1 second.

## 4.6 Conclusion

We have shown that adjoint-biased forward Monte Carlo (ABFMC) is a powerful tool for increasing the efficiency of Monte Carlo computed scatter projections for CBCT imaging. Additional work should focus more on additional phantom and patient geometries and incorporating the ABFMC approach in a comprehensive CBCT reconstruction package.

# 5. Discussion

## 5.1 Correlated Monte Carlo

Correlated Monte Carlo is able to reduce the maximum and mean uncertainty in anatomical regions of clinical interest in all circumstances investigated in our study. This shows that CMC is globally advantageous regardless of the small number of voxels that exhibit increased statistical uncertainty relative to UMC. Diminished gains were associated with inter-seed attenuation effects and anatomical regions that have radiological properties that vary substantially from the corresponding homogeneous environment.

Comparing with other optimized codes, CMC, as implemented in PTRAN is the most efficient non-biased solution for brachytherapy model based dose calculations reported to date. CMC is able to compute accurate, HR patient-specific dose maps in fewer than 40 sec. Others have only been able to achieve such efficiency for lower-resolution spatial grids<sup>6,84-86</sup>. Although the techniques used to produce the previously reported times were accurate and more efficient than their predecessors, CMC is still stands out with a more than 8-fold efficiency advantage above the others.

Further improvements in efficiency, with minimal loss to accuracy for anatomically realistic simulation environments, can be achieved through the ICMC approximation. Because of the immense efficiency gains from using ICMC relative to UMC allow the use of iterative treatment planning optimization to be clinically applied. Gains upward of 1500 for the 3.0 mm LR grids allow treatment planning optimization through the genetic algorithm<sup>96,97</sup> to be computed in less than 7 min and 18 min for the breast and prostate cases, respectively, used in our study.

Additionally, the current cost-effectiveness of multi-CPU and multi-core computer architectures would further reduced these times through the application of parallel processing.

Unfortunately, CPU-time is not the only barrier to clinical acceptance of model based dose calculation algorithms. There still remains the un-answered question of how to assign tissue elemental compositions to voxels within an organ for each individual patient. Difficulties arise from patient-to-patient anatomical variability and the lack of definitive experimental assessments of tissue elemental compositions. For example, volumetric studies of the breast show that the percentage of fibro-glandular tissue ranges from 5% to 65%<sup>11</sup>. Additionally, Hammerstein's<sup>109</sup> study of mastectomy specimens showed that glandular and adipose tissues exhibit 8%-10% variations in compositions by weight of carbon and oxygen, which translate into 8%-15% deviations in the linear attenuation coefficient at 20 keV. Recommended compositions of the prostate come from the ICRP Reference Man are based on a small number of studies completed prior to 1960 using only a few specimens which may not be representative of a larger patient population<sup>15</sup>. Variations in the elemental composition for prostate tumor specimens translate into 8% uncertainties in the linear attenuation coefficient for the 20-30 keV range<sup>110</sup>.

Future work towards clinical adoption of model-based dose calculation algorithms must focus on the unsolved problem of tissue composition uncertainties. The dual-energy CT methods proposed by Williamson *et al*<sup>92</sup>, Landry *et al*<sup>90</sup>, or Malusek *et al*<sup>91</sup> are promising quantitative imaging methods to reconstruct the radiological properties of tissue with their corresponding energy dependence.

The combination of fast and accurate model based dose calculations algorithms, as presented in this dissertation, and accurate elemental representation of patient tissues can lead to the correct

characterization of the dose-response relationship for low-energy brachytherapy leading to more positive patient outcomes.

## 5.2 Adjoint Biased Forward Monte Carlo

We have demonstrated that ABFMC is an effective variance-reduction strategy for the CBCT projection geometry. The combination of using a phase-space source with ABFMC transport biasing via weight windowing, either with DOM or PC-FAIG computed importance functions, can yield average gains of 250 and upward to 400 relative to the non-weight windowed forward Monte Carlo using the primary point source. To put this into perspective, a full set of 360 projections for a  $40 \times 30$  detector grid, requires roughly 325 hrs of CPU time for 5% statistical uncertainty, if computed by the non-weight windowed Monte Carlo using a primary point source. In contrast, DOM or PC-FAIG importance sampling in combination with the phase-space source, requires only 48 min for the same calculation.

Furthermore, with the adoption of cost-effective parallel computing environments, for example with 8 CPU cores, only 6 minutes would be needed. Additional reductions could be also be gained from sampling scatter projections on a coarser angular grid and recovering the full angular signal spectrum through interpolating in sinogram space<sup>111</sup>. The relationship between the reconstructed image quality and computational efficiency could be assessed to find the optimal angular sampling interval.

Likewise, the effect of scatter projection statistical uncertainty on reconstructed image quality needs to be assessed so that the optimal relationship between efficiency and quality can be ascertained. Colijn *et al*<sup>56</sup> were able to recover smooth and accurate CBCT projections from

noisy data after applying an adaptive de-noising filter suggesting that 10% uncertainty would be acceptable.

Lastly, any future work to adopt these methods in clinical reconstructed CBCT images must address the issue of increased projection relative noise that results from scatter signal subtraction<sup>48</sup>. While scatter subtraction has been shown to diminish cupping, streaking, and non-uniformity artifacts, in general it does not improve the contrast-to-noise ratio<sup>48</sup>, a widely used surrogate for low contrast structure detectability. Several groups have introduced adaptive filtering<sup>45,108</sup> or penalized statistical iterative reconstruction<sup>112</sup> techniques that are able to reduce image noise without significant loss of spatial resolution. Any comprehensive CBCT scatter-correction method must include an approach to edge-preserving noise reduction.

### **5.3 Conclusion**

To conclude this dissertation, principled variance reduction strategies are powerful and effective tools for increasing the efficiency of low-energy Monte Carlo simulation, with only modest losses to accuracy in worst-case scenarios, for both therapeutic and diagnostic clinical applications.

# 6. My Contributions

## 6.1 Correlated Monte Carlo

- Consolidated two separate correlated Monte Carlo codes, one for analytical geometries and the other for patient CT defined geometries, into one single code.
- Optimized the consolidated code to yield efficiency gains an order of magnitude above previous performance.
- Expanded the phase-space source model to be generalized for all brachytherapy seed configuration.
- Identified, isolated, and characterized a phenomenon within correlated sampling for heterogeneous histories to receive an inflated weight. It was this discovery that led me to propose and implement the homogeneous radiation transport to be completed in a homogeneous breast environment.
- Performed all calculations and analysis presented in this work.

## 6.2 Interpolated Correlated Monte Carlo

- Incorporated the ICMC framework within PTRAN
- Wrote the ability for ICMC to use spatially averaged cross-sections and local absorption properties instead of an assigned tissue mixture from ctcreate.
- Identified and isolated the three sources of error in the ICMC methodology: inverse square law gradient effect, cross-section gradient effect, and the local absorption gradient effect.

- Proposed its application within treatment planning optimization algorithms.
- Performed all calculations and analysis presented in this work.

### 6.3 Adjoint Biased Forward Monte Carlo

- Expanded PTRAN to include both CBCT and fan-beam CT simulation.
  - Programmed an expected track-length estimator for both the primary and scatter components of the projection signals.
  - Generalized the phase-space source model from brachytherapy to external beam geometry.
  - Restructured the ray-tracing routines for more general composite geometries of analytical objects and CT-defined patients.
- Expanded the idea further from one of Dr. Jeffrey Williamson's research grants.
  - I proposed that we use ABFMC for CBCT
- Solved all problems related to hardware incompatibilities, which involved the re-writing the declarations and initializations of most variables, for the NJOY and TRANSX code systems (used to generate multi-group cross-section libraries for DOM calculations).
- Successfully adapted and implemented the ABFMC infrastructure in PTRAN.
  - Set up the weight windowing in PTRAN.
    - Though this specifically targets the CBCT geometry, I programmed it to easily be utilized for the brachytherapy geometry as well.
  - Implemented the CADIS, adjoint, and forward adjoint importance generator approaches to ABFMC.
    - I adapted the forward adjoint importance generator concept from the weight window generator used in MCNP to help me understand the DOM



computed adjoint function, but it turned into an effective variance reduction strategy by itself.

- Conceived and implemented the multiple-angle forward adjoint importance generator concept.
- Obtained, installed, troubleshot, and learned to use PARTISN, NJOY, and TRANSX (from scratch) for discrete ordinate solutions to the forward and adjoint Boltzmann transport equation.
- Performed all calculations and analysis presented in this work.

## 7. References

- <sup>1</sup>N. Metropolis, "The beginning of the Monte Carlo Method," *Los Alamos Science* **15**, 125-120 (1987).
- <sup>2</sup>M. J. Berger, "Methods in Computational Physics," edited by B. A. S. Fernbach, M. Rothenberg (Academic, New York, 1963), Vol. 1.
- <sup>3</sup>M. J. Rivard, B. M. Coursey, L. A. DeWerd, W. F. Hanson, M. S. Huq, G. S. Ibbott *et al.*, "Update of AAPM Task Group No. 43 Report: A revised AAPM protocol for brachytherapy dose calculations," *Med Phys* **31** (3), 633-74 (2004).
- <sup>4</sup>J. F. Carrier, L. Beaulieu, F. Therriault-Proulx, and R. Roy, "Impact of interseed attenuation and tissue composition for permanent prostate implants," *Med Phys* **33** (3), 595-604 (2006).
- <sup>5</sup>J. F. Carrier, M. D'Amours, F. Verhaegen, B. Reniers, A. G. Martin, E. Vigneault *et al.*, "Postimplant dosimetry using a Monte Carlo dose calculation engine: a new clinical standard," *Int J Radiat Oncol Biol Phys* **68** (4), 1190-8 (2007).
- <sup>6</sup>O. Chibani and J. F. Williamson, "MCPI: a sub-minute Monte Carlo dose calculation engine for prostate implants," *Med Phys* **32** (12), 3688-98 (2005).
- <sup>7</sup>O. Chibani, J. F. Williamson, and D. Todor, "Dosimetric effects of seed anisotropy and interseed attenuation for 103Pd and 125I prostate implants," *Med Phys* **32** (8), 2557-66 (2005).
- <sup>8</sup>J. J. DeMarco, J. B. Smathers, C. M. Burnison, Q. K. Ncube, and T. D. Solberg, "CT-based dosimetry calculations for 125I prostate implants," *Int J Radiat Oncol Biol Phys* **45** (5), 1347-53 (1999).
- <sup>9</sup>A. S. Meigooni, J. A. Meli, and R. Nath, "Interseed effects on dose for 125I brachytherapy implants," *Med Phys* **19** (2), 385-90 (1992).
- <sup>10</sup>C. Furstoss, B. Reniers, M. J. Bertrand, E. Poon, J. F. Carrier, B. M. Keller *et al.*, "Monte Carlo study of LDR seed dosimetry with an application in a clinical brachytherapy breast implant," *Med Phys* **36** (5), 1848-58 (2009).
- <sup>11</sup>M. J. Yaffe, J. M. Boone, N. Packard, O. Alonzo-Proulx, S. Y. Huang, C. L. Peressotti *et al.*, "The myth of the 50-50 breast," *Med Phys* **36** (12), 5437-43 (2009).
- <sup>12</sup>K. A. Gifford, F. Mourtada, S. H. Cho, A. Lawyer, and J. L. Horton, Jr., "Monte Carlo calculations of the dose distribution around a commercial gynecologic tandem applicator," *Radiother Oncol* **77** (2), 210-5 (2005).
- <sup>13</sup>R. L. Maughan, P. Chuba, A. T. Porter, and E. Ben-Josef, "Mass energy-absorption coefficients and mass collision stopping powers for electrons in tumors of various histologies," *Med Phys* **26** (3), 472-477 (1999).
- <sup>14</sup>ICRU, "Tissue substitutes in radiation dosimetry and measurement," Report No. 44, International Commission on Radiation Units and Measurements, Bethesda, MD, 1989.
- <sup>15</sup>ICRP, "ICRP Publication 23: Reference Man: Anatomical, Physiological and Metabolic Characteristics," Report No., Oxford, 1975.
- <sup>16</sup>G. R. Hammerstein, D. W. Miller, D. R. White, M. E. Masterson, H. Q. Woodard, and J. S. Laughlin, "Absorbed radiation dose in mammography," *Radiology* **130** (2), 485-91 (1979).

- <sup>17</sup>H. Q. Woodard and D. R. White, "The composition of body tissues," *Br J Radiol* **59** (708), 1209-18 (1986).
- <sup>18</sup>D. R. White and H. Q. Woodard, "The effects of adult human tissue composition on the dosimetry of photons and electrons," *Health Phys* **55** (4), 653-63 (1988).
- <sup>19</sup>A. H. Neufeld, "Contributions to the biochemistry of bromine: II. the bromine content of human tissues," *Canadian Journal of Research* **15B**, 132-138 (1937).
- <sup>20</sup>D. R. Dance, C. L. Skinner, and G. A. Carlsson, "Breast dosimetry," *Appl Radiat Isot* **50** (1), 185-203 (1999).
- <sup>21</sup>N. N. Stone, L. Potters, B. J. Davis, J. P. Ciezki, M. J. Zelefsky, M. Roach *et al.*, "Customized dose prescription for permanent prostate brachytherapy: insights from a multicenter analysis of dosimetry outcomes," *Int J Radiat Oncol Biol Phys* **69** (5), 1472-7 (2007).
- <sup>22</sup>N. N. Stone, R. G. Stock, I. White, and P. Unger, "Patterns of local failure following prostate brachytherapy," *J Urol* **177** (5), 1759-63; discussion 1763-4 (2007).
- <sup>23</sup>A. B. Chen, A. V. D'Amico, B. A. Neville, and C. C. Earle, "Patient and treatment factors associated with complications after prostate brachytherapy," *J Clin Oncol* **24** (33), 5298-304 (2006).
- <sup>24</sup>B. M. Keller, A. Ravi, R. Sankrecha, and J. P. Pignol, "Permanent breast seed implant dosimetry quality assurance," *Int J Radiat Oncol Biol Phys* **83** (1), 84-92 (2012).
- <sup>25</sup>A. Brahme, "Dosimetric precision requirements in radiation therapy," *Acta Radiol Oncol* **23** (5), 379-91 (1984).
- <sup>26</sup>A. Ahnesjo, "Collapsed cone convolution of radiant energy for photon dose calculation in heterogeneous media," *Med Phys* **16** (4), 577-92 (1989).
- <sup>27</sup>A. K. Carlsson and A. Ahnesjo, "The collapsed cone superposition algorithm applied to scatter dose calculations in brachytherapy," *Med Phys* **27** (10), 2320-32 (2000).
- <sup>28</sup>K. A. Gifford, J. L. Horton, T. A. Wareing, G. Failla, and F. Mourtada, "Comparison of a finite-element multigroup discrete-ordinates code with Monte Carlo for radiotherapy calculations," *Phys Med Biol* **51** (9), 2253-65 (2006).
- <sup>29</sup>A. Carlsson Tedgren and A. Ahnesjo, "Optimization of the computational efficiency of a 3D, collapsed cone dose calculation algorithm for brachytherapy," *Med Phys* **35** (4), 1611-8 (2008).
- <sup>30</sup>K. Zourari, E. Pantelis, A. Moutsatsos, L. Petrokokkinos, P. Karaiskos, L. Sakelliou *et al.*, "Dosimetric accuracy of a deterministic radiation transport based <sup>192</sup>Ir brachytherapy treatment planning system. Part I: single sources and bounded homogeneous geometries," *Med Phys* **37** (2), 649-61 (2010).
- <sup>31</sup>G. M. Daskalov, R. S. Baker, D. W. Rogers, and J. F. Williamson, "Multigroup discrete ordinates modeling of <sup>125</sup>I 6702 seed dose distributions using a broad energy-group cross section representation," *Med Phys* **29** (2), 113-24 (2002).
- <sup>32</sup>R. M. Thomson and D. W. Rogers, "Monte Carlo dosimetry for <sup>125</sup>I and <sup>103</sup>Pd eye plaque brachytherapy with various seed models," *Med Phys* **37** (1), 368-76 (2010).
- <sup>33</sup>A. Sampson, Y. Le, and J. F. Williamson, "Fast patient-specific Monte Carlo brachytherapy dose calculations via the correlated sampling variance reduction technique," *Med Phys* **39** (2), 1058-68 (2012).
- <sup>34</sup>Y. Le, O. Chibani, D. Todor, J. Siebers, and J. F. Williamson, "MO-E-T-618-01: An Integrated CT-Based Monte Carlo dose-evaluation system for brachytherapy and its application to permanent prostate implant postprocedural dosimetric analysis," *Med Phys* **32**, 2068 (2005).

- <sup>35</sup>Y. Le, J. F. Williamson, and D. Todor, "Correlated Sampling for Accelerating CT-Based Monte Carlo Dose Calculations for Brachytherapy Treatment Planning," in *Proceedings of 48th Annual American Association of Physicists in Medicine (AAPM) Meeting*, Orlando, Florida, edited by Medical Physics, 33, 2006.
- <sup>36</sup>A. L. Kwan, J. M. Boone, and N. Shah, "Evaluation of x-ray scatter properties in a dedicated cone-beam breast CT scanner," *Med Phys* **32** (9), 2967-75 (2005).
- <sup>37</sup>J. M. Boone, A. L. Kwan, J. A. Seibert, N. Shah, K. K. Lindfors, and T. R. Nelson, "Technique factors and their relationship to radiation dose in pendant geometry breast CT," *Med Phys* **32** (12), 3767-76 (2005).
- <sup>38</sup>A. Suomalainen, T. Kiljunen, Y. Kaser, J. Peltola, and M. Kortensniemi, "Dosimetry and image quality of four dental cone beam computed tomography scanners compared with multislice computed tomography scanners," *Dentomaxillofac Radiol* **38** (6), 367-78 (2009).
- <sup>39</sup>P. Mozzo, C. Procacci, A. Tacconi, P. T. Martini, and I. A. Andreis, "A new volumetric CT machine for dental imaging based on the cone-beam technique: preliminary results," *Eur Radiol* **8** (9), 1558-64 (1998).
- <sup>40</sup>Y. Chen, B. Liu, J. M. O'Connor, C. S. Didier, and S. J. Glick, "Characterization of scatter in cone-beam CT breast imaging: comparison of experimental measurements and Monte Carlo simulation," *Med Phys* **36** (3), 857-69 (2009).
- <sup>41</sup>P. C. Johns and M. Yaffe, "Scattered radiation in fan beam imaging systems," *Med Phys* **9** (2), 231-9 (1982).
- <sup>42</sup>P. M. Joseph and R. D. Spital, "The effects of scatter in x-ray computed tomography," *Med Phys* **9** (4), 464-72 (1982).
- <sup>43</sup>J. H. Siewerdsen and D. A. Jaffray, "Cone-beam computed tomography with a flat-panel imager: magnitude and effects of x-ray scatter," *Med Phys* **28** (2), 220-31 (2001).
- <sup>44</sup>T. R. Nelson, L. I. Cervino, J. M. Boone, and K. K. Lindfors, "Classification of breast computed tomography data," *Med Phys* **35** (3), 1078-86 (2008).
- <sup>45</sup>L. Zhu, Y. Xie, J. Wang, and L. Xing, "Scatter correction for cone-beam CT in radiation therapy," *Med Phys* **36** (6), 2258-68 (2009).
- <sup>46</sup>M. C. Altunbas, C. C. Shaw, L. Chen, C. Lai, X. Liu, T. Han *et al.*, "A post-reconstruction method to correct cupping artifacts in cone beam breast computed tomography," *Med Phys* **34** (7), 3109-18 (2007).
- <sup>47</sup>E. Weiss, J. Wu, W. Sleeman, J. Bryant, P. Mitra, M. Myers *et al.*, "Clinical evaluation of soft tissue organ boundary visualization on cone-beam computed tomographic imaging," *Int J Radiat Oncol Biol Phys* **78** (3), 929-36 (2010).
- <sup>48</sup>D. Lazos and J. F. Williamson, "Monte Carlo evaluation of scatter mitigation strategies in cone-beam CT," *Med Phys* **37** (10), 5456-70 (2010).
- <sup>49</sup>J. H. Siewerdsen, D. J. Moseley, B. Bakhtiar, S. Richard, and D. A. Jaffray, "The influence of antiscatter grids on soft-tissue detectability in cone-beam computed tomography with flat-panel detectors," *Med Phys* **31** (12), 3506-20 (2004).
- <sup>50</sup>Y. Kyriakou and W. Kalender, "Efficiency of antiscatter grids for flat-detector CT," *Phys Med Biol* **52** (20), 6275-93 (2007).
- <sup>51</sup>H. Gao, R. Fahrig, N. R. Bennett, M. Sun, J. Star-Lack, and L. Zhu, "Scatter correction method for x-ray CT using primary modulation: phantom studies," *Med Phys* **37** (2), 934-46 (2010).

- <sup>52</sup>M. Meyer, W. A. Kalender, and Y. Kyriakou, "A fast and pragmatic approach for scatter correction in flat-detector CT using elliptic modeling and iterative optimization," *Phys Med Biol* **55** (1), 99-120 (2010).
- <sup>53</sup>G. Poludniowski, P. M. Evans, V. N. Hansen, and S. Webb, "An efficient Monte Carlo-based algorithm for scatter correction in keV cone-beam CT," *Phys Med Biol* **54** (12), 3847-64 (2009).
- <sup>54</sup>I. Reitz, B. M. Hesse, S. Nill, T. Tucking, and U. Oelfke, "Enhancement of image quality with a fast iterative scatter and beam hardening correction method for kV CBCT," *Z Med Phys* **19** (3), 158-72 (2009).
- <sup>55</sup>J. H. Siewerdsen, M. J. Daly, B. Bakhtiar, D. J. Moseley, S. Richard, H. Keller *et al.*, "A simple, direct method for x-ray scatter estimation and correction in digital radiography and cone-beam CT," *Med Phys* **33** (1), 187-97 (2006).
- <sup>56</sup>A. P. Colijn and F. J. Beekman, "Accelerated simulation of cone beam X-ray scatter projections," *IEEE Trans Med Imaging* **23** (5), 584-90 (2004).
- <sup>57</sup>Y. Kyriakou, T. Riedel, and W. A. Kalender, "Combining deterministic and Monte Carlo calculations for fast estimation of scatter intensities in CT," *Phys Med Biol* **51** (18), 4567-86 (2006).
- <sup>58</sup>R. Ning, X. Tang, and D. Conover, "X-ray scatter correction algorithm for cone beam CT imaging," *Med Phys* **31** (5), 1195-202 (2004).
- <sup>59</sup>E. Mainegra-Hing and I. Kawrakow, "Variance reduction techniques for fast Monte Carlo CBCT scatter correction calculations," *Phys Med Biol* **55** (16), 4495-507 (2010).
- <sup>60</sup>A. Badal and A. Badano, "Accelerating Monte Carlo simulations of photon transport in a voxelized geometry using a massively parallel graphics processing unit," *Med Phys* **36** (11), 4878-80 (2009).
- <sup>61</sup>X. Jia, H. Yan, L. Cervino, M. Folkerts, and S. B. Jiang, "A GPU tool for efficient, accurate, and realistic simulation of cone beam CT projections," *Med Phys* **39** (12), 7368-78 (2012).
- <sup>62</sup>X. Jia, H. Yan, X. Gu, and S. B. Jiang, "Fast Monte Carlo simulation for patient-specific CT/CBCT imaging dose calculation," *Phys Med Biol* **57** (3), 577-90 (2012).
- <sup>63</sup>I. Lux and L. Koblinger, *Monte Carlo Particle Transport Methods: Neutron and Photon Calculations* (CRC Press, Boca Raton, FL, 1991).
- <sup>64</sup>A. Haghighat and J. C. Wagner, "Monte Carlo Variance Reduction with Deterministic Importance Functions," *Progress in Nuclear Energy* **42**, 25-53 (2003).
- <sup>65</sup>J. E. Sweezy, "MCNP-A General Monte Carlo N-particle Transport Code, Version 5," Report No. LA-UR-03-1987, Los Alamos National Laboratory, Los Alamos, NM, 2005.
- <sup>66</sup>A. J. Sampson, J. F. Williamson, Y. Le, and D. Todor, "Using correlated-sampling to accelerate CT-based Monte Carlo dose calculations for brachytherapy treatment planning," in *Proceedings of World Congress on Medical Physics and Biomedical Engineering*, Munich, Germany, edited by Springer Berlin Heidelberg, 25/1, 2009.
- <sup>67</sup>H. Hedtjarn, G. A. Carlsson, and J. F. Williamson, "Accelerated Monte Carlo based dose calculations for brachytherapy planning using correlated sampling," *Phys Med Biol* **47** (3), 351-76 (2002).
- <sup>68</sup>S. R. Dwivedi, "Zero Variance Biasing Schemes for Monte-Carlo Calculations of Neutron and Radiation Transport Problems," *Nuclear Science and Engineering* **80** (1), 172-178 (1982).

- <sup>69</sup>T. Booth, "A Weight Window/Importance Generator for Monte Carlo Streaming Problems," in *Sixth International Conference on Radiation Shielding* (Tokyo, Japan, 1983).
- <sup>70</sup>J. C. Wagner and A. Haghghat, "Automated Variance Reduction of Monte Carlo Shielding Calculations Using Discrete Ordinates Adjoint Function," *Nuclear Science and Engineering* **128**, 186-208 (1998).
- <sup>71</sup>J. Dolan, Z. Lia, and J. F. Williamson, "Monte Carlo and experimental dosimetry of an 125I brachytherapy seed," *Med Phys* **33** (12), 4675-84 (2006).
- <sup>72</sup>Z. Li and J. F. Williamson, "Volume-based geometric modeling for radiation transport calculations," *Med Phys* **19** (3), 667-77 (1992).
- <sup>73</sup>J. I. Monroe and J. F. Williamson, "Monte Carlo-aided dosimetry of the theragenics TheraSeed model 200 103Pd interstitial brachytherapy seed," *Med Phys* **29** (4), 609-21 (2002).
- <sup>74</sup>J. F. Williamson, "Monte Carlo evaluation of kerma at a point for photon transport problems," *Med Phys* **14** (4), 567-76 (1987).
- <sup>75</sup>J. F. Williamson, "Monte Carlo modeling of the transverse-axis dose distribution of the model 200 103Pd interstitial brachytherapy source," *Med Phys* **27** (4), 643-54 (2000).
- <sup>76</sup>J. F. Williamson and M. J. Rivard, "Thermoluminescent Detector and Monte Carlo Techniques for Reference-Quality Brachytherapy Dosimetry," in *Clinical Dosimetry Measurements in Radiotherapy*, edited by D. Rogers and J. Cygler (Medical Physics Publishing Corporation, Madison, Wisconsin, 2009).
- <sup>77</sup>N. D. Mukhopadhyay, A. J. Sampson, D. Deniz, G. Alm Carlsson, J. Williamson, and A. Malusek, "Estimating statistical uncertainty of Monte Carlo efficiency-gain in the context of a correlated sampling Monte Carlo code for brachytherapy treatment planning with non-normal dose distribution," *Appl Radiat Isot* **70** (1), 315-23 (2012).
- <sup>78</sup>H. Hedtjarn, G. A. Carlsson, and J. F. Williamson, "Monte Carlo-aided dosimetry of the Symmetra model I25.S06 125I, interstitial brachytherapy seed," *Med Phys* **27** (5), 1076-85 (2000).
- <sup>79</sup>B. Walters, I. Kawrakow, and D. W. Rogers, "DOSXYZnrc User Manual," Report No. PIRS-794 revB, Ionizing Radiation Standards, National Research Council of Canada, 2009.
- <sup>80</sup>N. Packard and J. M. Boone, "Glandular segmentation of cone beam breast CT images," *Proc. SPIE* **6510**, 1-8 (2007).
- <sup>81</sup>J. P. Pignol, B. Keller, E. Rakovitch, R. Sankrecha, H. Easton, and W. Que, "First report of a permanent breast 103Pd seed implant as adjuvant radiation treatment for early-stage breast cancer," *Int J Radiat Oncol Biol Phys* **64** (1), 176-81 (2006).
- <sup>82</sup>I. Kawrakow and M. Fippel, "Investigation of variance reduction techniques for Monte Carlo photon dose calculation using XVMC," *Phys Med Biol* **45** (8), 2163-83 (2000).
- <sup>83</sup>J. Sempau, A. Sanchez-Reyes, F. Salvat, H. O. ben Tahar, S. B. Jiang, and J. M. Fernandez-Varea, "Monte Carlo simulation of electron beams from an accelerator head using PENELOPE," *Physics in medicine and biology* **46** (4), 1163-86 (2001).
- <sup>84</sup>G. Yegin, R. E. Taylor, and D. W. Rogers, "BrachyDose: A new fast Monte Carlo code for brachytherapy calculations," *Med Phys* **33**, 2075(abs) (2006).
- <sup>85</sup>R. E. Taylor, G. Yegin, and D. W. Rogers, "Benchmarking brachydose: Voxel based EGSnrc Monte Carlo calculations of TG-43 dosimetry parameters," *Med Phys* **34** (2), 445-57 (2007).
- <sup>86</sup>R. Thomson, G. Yegin, R. Taylor, J. Sutherland, and D. Rogers, "Fast Monte Carlo dose calculations for brachytherapy with BrachyDose," *Med Phys* **37** (7), 3910 (2010).

- <sup>87</sup>H. Afsharpour, J. P. Pignol, B. Keller, J. F. Carrier, B. Reniers, F. Verhaegen *et al.*, “Influence of breast composition and interseed attenuation in dose calculations for post-implant assessment of permanent breast 103Pd seed implant,” *Phys Med Biol* **55** (16), 4547-61 (2010).
- <sup>88</sup>G. Landry, B. Reniers, L. Murrer, L. Lutgens, E. B. Gurp, J. P. Pignol *et al.*, “Sensitivity of low energy brachytherapy Monte Carlo dose calculations to uncertainties in human tissue composition,” *Med Phys* **37** (10), 5188-98 (2010).
- <sup>89</sup>F. Verhaegen and S. Devic, “Sensitivity study for CT image use in Monte Carlo treatment planning,” *Phys Med Biol* **50** (5), 937-46 (2005).
- <sup>90</sup>G. Landry, P. V. Granton, B. Reniers, M. C. Ollers, L. Beaulieu, J. E. Wildberger *et al.*, “Simulation study on potential accuracy gains from dual energy CT tissue segmentation for low-energy brachytherapy Monte Carlo dose calculations,” *Phys Med Biol* **56** (19), 6257-78 (2011).
- <sup>91</sup>A. Malusek, M. Karlsson, M. Magnusson, and G. A. Carlsson, “The potential of dual-energy computed tomography for quantitative decomposition of soft tissues to water, protein and lipid in brachytherapy,” *Phys Med Biol* **58** (4), 771-85 (2013).
- <sup>92</sup>J. F. Williamson, S. Li, S. Devic, B. R. Whiting, and F. A. Lerma, “On two-parameter models of photon cross sections: application to dual-energy CT imaging,” *Med Phys* **33** (11), 4115-29 (2006).
- <sup>93</sup>E. K. Lee, R. J. Gallagher, D. Silvern, C. S. Wu, and M. Zaider, “Treatment planning for brachytherapy: an integer programming model, two computational approaches and experiments with permanent prostate implant planning,” *Phys Med Biol* **44** (1), 145-65 (1999).
- <sup>94</sup>W. D. D’Souza, R. R. Meyer, B. R. Thomadsen, and M. C. Ferris, “An iterative sequential mixed-integer approach to automated prostate brachytherapy treatment plan optimization,” *Phys Med Biol* **46** (2), 297-322 (2001).
- <sup>95</sup>J. Pouliot, D. Tremblay, J. Roy, and S. Filice, “Optimization of permanent 125I prostate implants using fast simulated annealing,” *Int J Radiat Oncol Biol Phys* **36** (3), 711-20 (1996).
- <sup>96</sup>Y. Yu and M. C. Schell, “A genetic algorithm for the optimization of prostate implants,” *Med Phys* **23** (12), 2085-91 (1996).
- <sup>97</sup>G. Yang, L. E. Reinstein, S. Pai, Z. Xu, and D. L. Carroll, “A new genetic algorithm technique in optimization of permanent 125I prostate implants,” *Med Phys* **25** (12), 2308-15 (1998).
- <sup>98</sup>B. R. Walters, R. Kramer, and I. Kawrakow, “Dose to medium versus dose to water as an estimator of dose to sensitive skeletal tissue,” *Phys Med Biol* **55** (16), 4535-46 (2010).
- <sup>99</sup>C. M. Ma and J. Li, “Dose specification for radiation therapy: dose to water or dose to medium?,” *Phys Med Biol* **56** (10), 3073-89 (2011).
- <sup>100</sup>A. Carlsson Tedgren and G. A. Carlsson, “Specification of absorbed dose to water using model-based dose calculation algorithms for treatment planning in brachytherapy,” *Phys Med Biol* **58** (8), 2561-79 (2013).
- <sup>101</sup>S. A. Enger, A. Ahnesjo, F. Verhaegen, and L. Beaulieu, “Dose to tissue medium or water cavities as surrogate for the dose to cell nuclei at brachytherapy photon energies,” *Phys Med Biol* **57** (14), 4489-500 (2012).
- <sup>102</sup>R. M. Thomson, A. C. Tedgren, and J. F. Williamson, “On the biological basis for competing macroscopic dose descriptors for kilovoltage dosimetry: cellular dosimetry for brachytherapy and diagnostic radiology,” *Phys Med Biol* **58** (4), 1123-50 (2013).

- <sup>103</sup>G. I. Bell and S. Glasstone, *Nuclear Reactor Theory* (Robert E. Krieger Publishing Company, Malabar, FL, 1970).
- <sup>104</sup>J. E. Sweezy, F. Brown, T. Booth, J. Chiamonte, and B. Pegg, "Automated Variance Reduction for MCNP using Deterministic Methods," *Radiation Protection Dosimetry* **116**, 508-512 (2005).
- <sup>105</sup>E. E. Lewis and J. W.F. Miller, *Computational Methods of Neutron Transport* (Wiley-Interscience, New York, 1984).
- <sup>106</sup>W. F. J. Miller and E. E. Lewis, *Computational Methods of Neutron Transport* (American Nuclear Society, Inc, La Grange Park, Illinois, 1993).
- <sup>107</sup>R. E. Alcouffe and R. S. Baker, "PARTISN manual," Report No. LA-UR-08-07258, Los Alamos National Laboratory, Los Alamos, NM, 2008.
- <sup>108</sup>L. Zhu, J. Wang, and L. Xing, "Noise suppression in scatter correction for cone-beam CT," *Med Phys* **36** (3), 741-52 (2009).
- <sup>109</sup>G. R. Hammerstein, D. W. Miller, D. R. White, M. E. Masterson, H. Q. Woodard, and J. S. Laughlin, "Absorbed Radiation-Dose in Mammography," *Radiology* **130** (2), 485-491 (1979).
- <sup>110</sup>R. L. Maughan, P. J. Chuba, A. T. Porter, E. Ben-Josef, and D. R. Lucas, "The elemental composition of tumors: kerma data for neutrons," *Med Phys* **24** (8), 1241-4 (1997).
- <sup>111</sup>M. Bertram, J. Wiegert, D. Schafer, T. Aach, and G. Rose, "Directional view interpolation for compensation of sparse angular sampling in cone-beam CT," *IEEE Trans Med Imaging* **28** (7), 1011-22 (2009).
- <sup>112</sup>J. D. Evans, D. G. Polite, B. R. Whiting, J. A. O'Sullivan, and J. F. Williamson, "Noise-resolution tradeoffs in x-ray CT imaging: a comparison of penalized alternating minimization and filtered backprojection algorithms," *Med Phys* **38** (3), 1444-58 (2011).



# Appendices

# Appendix A

# Using Correlated Sampling to Accelerate CT-Based Monte Carlo Dose Calculations for Brachytherapy Treatment Planning

A. Sampson<sup>1</sup>, Y. Le<sup>2</sup>, D. Todor<sup>1</sup>, J. Williamson<sup>1</sup>

<sup>1</sup> Department of Radiation Oncology, Virginia Commonwealth University, Richmond, USA

<sup>2</sup> Department of Radiation Oncology & Molecular Radiation Sciences, Johns Hopkins University, Baltimore, USA

**Abstract**— The aim of this study was to assess the impact on efficiency and accuracy of a correlated sampling Monte Carlo simulation code for evaluating clinical brachytherapy dose distributions, accounting for tissue-composition and applicator heterogeneities. This code was built upon an extensively benchmarked Monte Carlo code, PTRAN\_CCG and a CT-like cross-section map derived from patient single-energy CT images. Differences between PTRAN\_CCG and the correlated code, expressed relative to the statistical uncertainty were found to be normally distributed with a standard deviation of 1.00 and a mean of -0.109 indicating that the correlated and conventional Monte Carlo agree within statistical error. Correlated sampling increases efficiency by factors of 7.1, 9.1, and 10.4, for greater than 20%, 50% and 90% of  $D_{90}$ , respectively, for a 2x2x2 mm voxel grid.

**Keywords**— Monte Carlo, brachytherapy, correlated sampling.

## I. INTRODUCTION

Currently, LDR brachytherapy dose calculations are performed using the TG-43 protocol [1], which assumes that patients are composed of liquid water and ignores seed-to-seed attenuation and other applicator-shielding effects. Several studies have documented that tissue heterogeneities, inter-seed attenuation, and seed anisotropy significantly influence low-energy (125I or 103Pd) prostate seed implants [2-4]. For example, Chibani *et al* [3] showed that these effects can influence clinical dose descriptors, e.g.,  $D_{90}$ , by as much as 10% in the prostate. They also showed that as little as 1% of calcified prostate tissue by weight can reduce  $D_{90}$  by as much as 8-10%.

CT-based Monte Carlo (MC) codes can rigorously account for applicator-attenuation and tissue-heterogeneity effects which are ignored by conventional treatment planning systems (TPS). However, the CPU time-intensiveness of MC transport solutions has limited Monte Carlo applications in the clinical setting. For example, Carrier *et al* (2007) reported post-implant Monte Carlo dose calculations run times of 4 hrs on a cluster of 8 Intel Xenon 2.4 GHz CPU's to give a statistical uncertainty of 0.1% in the  $V_{200}$ . This is neither realistic for pretreatment planning nor for intraoperative plan adjustment.

In this abstract, we describe implementation of a general variance reduction technique, correlated sampling, in a CT-based MC brachytherapy dose-calculation engine. We investigate its accuracy and efficiency.

## II. METHOD AND MATERIALS

### A. Correlated Sampling Concepts

We have previously described the correlated sampling theory in detail [5]. Conceptually, deviations from unit density and water composition (including applicators) are treated as a perturbation of the corresponding homogenous (unperturbed) system. Photon histories are generated for the unperturbed geometry and the same set of histories are 're-scored' by computing weight-correction factors to reflect the presence of the heterogeneities. In conventional MC,  $D_{het}$  and  $D_{hom}$  are estimated from independent MC runs which must be statistically very precise to give a reliable estimate of  $\Delta D = D_{het} - D_{hom}$ , requiring many photon histories and long CPU times. In contrast correlated sampling scores  $\Delta D$  contribution for each simulated collision by subtracting the contributions made by each history to each voxel. Additionally the same set of histories is used for both homogenous and heterogeneous geometries. Thus, the  $D_{het}$  and  $D_{hom}$  estimates are strongly correlated. For small perturbations the random deviations from their expected values will be in the same direction resulting in a positive covariance [6]. The variance,  $V(\Delta D^{corr})$ , of the estimate of  $\Delta D^{corr}$  may be significantly less than the conventional (uncorrelated) methods:  $V(\Delta D^{corr}) \ll V(D_{het}^{uncorr}) + V(D_{hom}^{uncorr})$ . However, a positive covariance cannot be guaranteed implying that correlated sampling could increase the variance depending on the size of perturbation.

If the homogenous dose,  $D_{hom}$ , can be obtained by deterministic methods (e.g. 2D TG-43 formalism), the patient doses are calculated as corrections to those of the homogenous geometry,  $D_{het}^* = HCF \cdot D_{hom}^{nonMC}$ , where  $HCF = 1 + \Delta D^{corr} / D_{hom}^{nonMC}$ , is the heterogeneity correction factor. The variance of the patient dose obtained in this

way,  $V(D_{het}^*) = V(\Delta D^{corr})$ , may be significantly less than that of uncorrelated MC simulation.

### B. Implementation

The correlated sampling technique described above was implemented in a CT-based MC dose calculation code, PTRAN\_CT [7]. PTRAN\_CT is a MC photon transport (MCPT) code designed specifically for fast brachytherapy dose calculation. It supports history-by-history uncertainty estimation and an optional phase-space source model. It also utilizes a fast ray-tracing algorithm by combining voxel-based modeling of patient anatomy with general complex combinatorial geometry (CCG) ray-tracing capability. The CCG models sources and applicators as set-theoretical combinations of analytically described surfaces such as ellipsoids, cuboids, cylinders and planes. CTCREATE [8] was used to convert Single-energy CT data to voxel tissue assignment and density. Tissue compositions were taken from ICRU report 44[9] and cross sections were derived by a method previously described by Monroe *et al* [10].

To simplify calculation of the weight correction factors, a simplified physical model of photon interactions with tissue was used that considers only free-electron Klein-Nishina scattering and photoelectric absorption with no characteristic x-ray emission. The expected track length (ETL) scoring method [11] was used to calculate  $D_{het}^{corr}$ ,  $D_{hom}^{corr}$  and  $\Delta D^{corr}$ .

To generate photon histories, a phase space model, which incorporates atomic relaxation, characteristic x-ray emission, and electron binding, of the source was used. Since the phase space model includes self-attenuation of the source in the homogeneous dose distribution, the difference between the homogeneous and heterogeneous does is lessened. This allows more heterogeneity to be treated as small perturbations. Figure 1 illustrates that if a phase space model of the source is not used, then very limited efficiency gain and much more loss is observed since the heterogeneous perturbations are too large for a positive covariance between homogeneous and heterogeneous dose distributions. Also, characteristic x-rays arising within the seed (e.g. by interactions of primaries with the Model 6711 silver rod) are accounted for to a first order approximation.

### C. Evaluating Accuracy and Efficiency

A clinical permanent prostate-seed implant, consisting of 78 Model-6711 I-125 seeds, was used to evaluate the accuracy and efficiency of PTRAN\_CT\_corr relative to the uncorrelated Monte Carlo code PTRAN\_CT. The same

patient geometry and scoring method (ETL) were used for both codes.

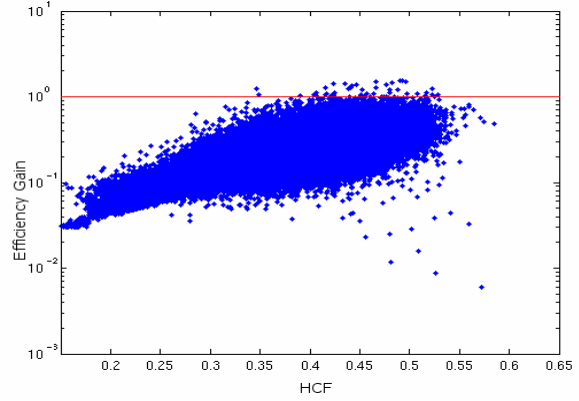


Fig. 1 Efficiency gain/loss for each voxel is plotted against its corresponding HCF. This was for a patient CT geometry with 78 seeds placed in an ideal configuration with no phase space model.

To quantitatively compare correlated MC dose distributions,  $D_{ijk}^{corr}$ , against conventional MC simulations,  $D_{ijk}^{uncorr}$ , the distribution of dose differences at each voxel  $ijk$ ,  $\Delta d_{ijk}$ , expressed as multiples of the combined statistical uncertainty:

$$\Delta d_{ijk} = (D_{ijk}^{corr} - D_{ijk}^{uncorr}) / \sqrt{\sigma_{D_{ijk}^{corr}}^2 + \sigma_{D_{ijk}^{uncorr}}^2} \quad (1)$$

was examined. For purely statistical differences, the distribution of  $\Delta d_{ijk}$  should be a Gaussian with mean of zero and standard deviation equal to 1.

The efficiency of a MC simulation is given by  $\varepsilon = 1/(V \cdot T)$ , where  $V = \sigma^2$  is the variance and  $T$  is CPU time. For each individual voxel  $ijk$ , the efficiency gain,  $G_{ijk}$ , between PTRAN\_CT\_corr and PTRAN\_CT is defined as:

$$G_{ijk} = (V(D_{ijk}^{uncorr}) \cdot T^{uncorr}) / (V(D_{ijk}^{corr}) \cdot T^{corr}) \quad (2)$$

Because  $G_{ijk}$  varies significantly with dose level and value of  $HCF_{ijk}$ , we computed the mean efficiency gains for those voxels with doses greater than 20%, 50% and 90% of  $D_{90}$  in uncorrelated simulation, denoted as  $G_{20}$ ,  $G_{50}$ ,  $G_{90}$ . The efficiency gains within clinical interest regions like prostate and rectum were also calculated.

2.5 million photon histories were used for both correlated and uncorrelated PTRAN\_CT for a 78 seed patient prostate implant on a single P4 1.9 GHz processor. The simulation volume was kept the same as  $9 \times 6.5 \times 8 \text{ cm}^3$  with voxel sizes of  $2 \times 2 \times 2 \text{ mm}^3$ ,  $1 \times 1 \times 3 \text{ mm}^3$  and  $1 \times 1 \times 1 \text{ mm}^3$ , respectively. This yielded average percent standard devia-

tions,  $\sigma_{\Delta D} / D_{het}$ , of 0.56% for  $2 \times 2 \times 2 \text{ mm}^3$  voxels for  $D_{ijk}^{het} \geq 0.5 \times D_{90}$  for correlated MC simulations.

### III. RESULTS

The distribution of  $\Delta d_{ijk}$  comparing correlated MC with uncorrelated PTRAN\_CT is plotted in Fig. 2 along with a Gaussian fit with a mean of -0.109 and standard deviation of 1.012. The R-square value equal to 0.9999 demonstrates the goodness of the fit. The negative 0.109 standard deviation shift with corresponding 3.5% combined statistical uncertainty only indicates 0.38% of average dose difference which is negligible.

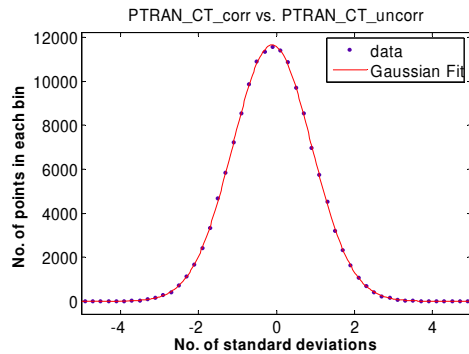


Fig 2 The distribution of  $\Delta d_{ijk}$  as defined in (1) with Gaussian fit

The simulation time and the efficiency gains,  $G_{20}$ ,  $G_{50}$ ,  $G_{90}$  are listed in Table I. Efficiency gains of 4-15 are observed.

Table 1

		Time (min)	$G_{20}$	$G_{50}$	$G_{90}$
$2 \times 2 \times 2 \text{ mm}^3$	correlated	4.8	7.11	9.08	10.41
	uncorrelated	3.0			
$1 \times 1 \times 3 \text{ mm}^3$	correlated	6.6	9.43	12.94	15.76
	uncorrelated	4.2			
$1 \times 1 \times 1 \text{ mm}^3$	correlated	8.4	4.68	5.62	6.46
	uncorrelated	5.4			

Although a phase space source model was used, an efficiency loss was still observed in the regions of the pubic bone. Fig. 3 shows this effect along with reduced efficiency in regions of periprostatic adipose tissue. In relation to dose, it was found that most voxels that experienced an efficiency loss also received less than 50% of  $D_{90}$ . Fig. 4 additionally shows that correlated sampling can reduce the percent standard deviation for regions receiving doses greater than 10 Gy (6.25% of  $D_{90}$ ).

Finally, the distribution of efficiency gains in different anatomical regions as shown in Fig. 5 was studied. Within the prostate volume, the mean gain is 15 fold whereas in the

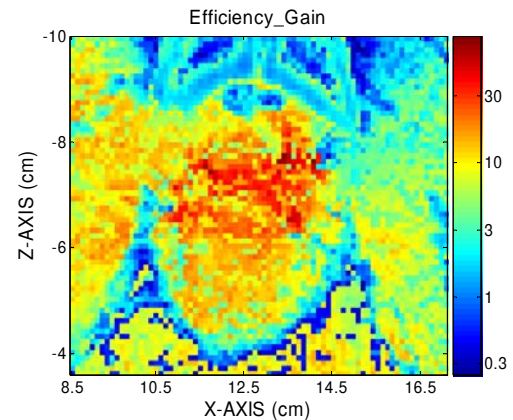


Fig. 3 2D Efficiency gain distribution from a mid slice in the coronal plane

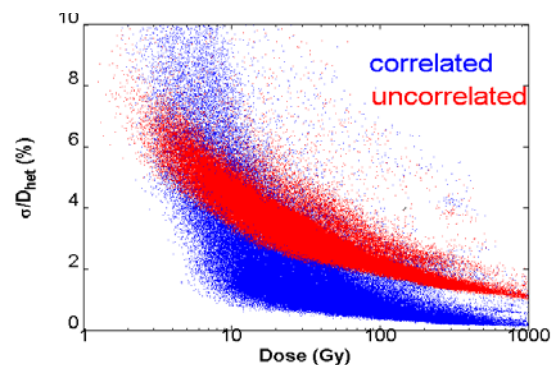


Fig. 4 Percent standard deviation vs. dose ( $1 \times 1 \times 3 \text{ mm}^3$  voxel)

rectal volume with doses greater than 50% of  $D_{90}$ , correlated sampling increases efficiency 7 fold on average. Table 2 additionally shows the time required for various voxel sizes to achieve a standard deviation of 2% or less in the prostate and the rectum volume that receives dose greater than 50% of  $D_{90}$ .

Table 2 CPU time (in seconds) to achieve 2% SD for different voxel sizes using correlated sampling in PTRAN\_CT\_corr

	Prostate	Rectum (>50% $D_{90}$ )
$2 \times 2 \times 2 \text{ mm}^3$	17	24
$1 \times 1 \times 3 \text{ mm}^3$	33	50
$1 \times 1 \times 1 \text{ mm}^3$	180	240

### IV. CONCLUSION

Correlated sampling effectively reduces variance under many circumstances. However, regions of low dose or large dose perturbations can experience efficiency losses although in most cases the maximum dose uncertainty in the 3D calculation grid is reduced.

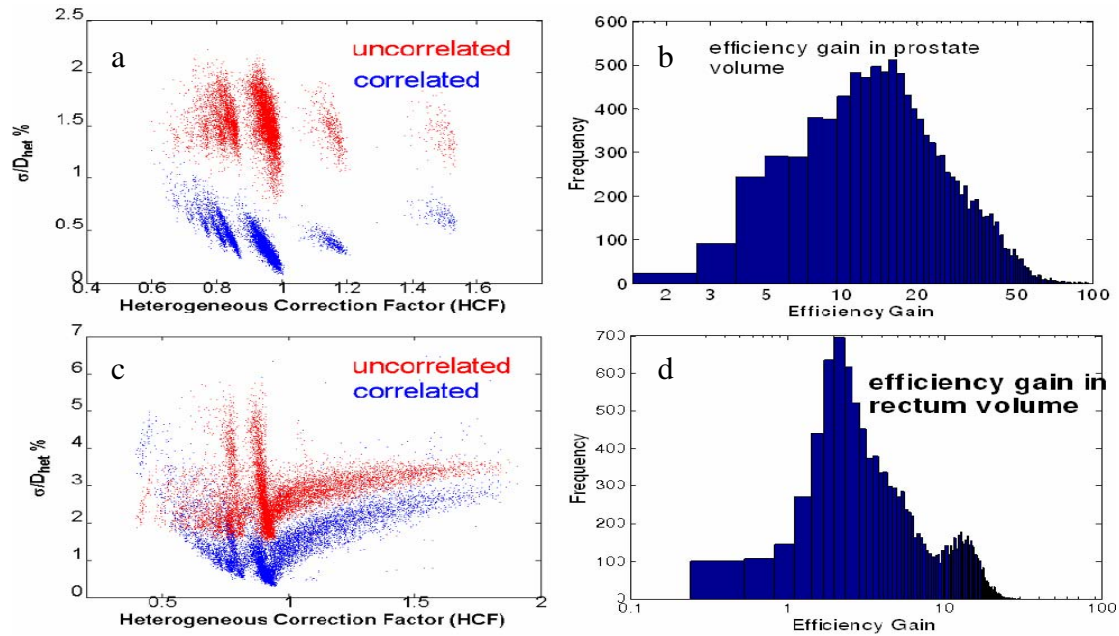


Fig 5 a. scatter plot of percent standard deviation vs. HCF for voxels within the prostate; b. histogram of efficiency gain for voxels within prostate; c. scatter plot of percent standard deviation vs. HCF for voxels within rectum; d. histogram of efficiency gain for voxels within rectum volume that receives  $>50\%$  of  $D_{90}$ .

Investigations are underway to identify the source of this evident particle decorrelation and to determine if additional variance reduction techniques, e.g., systematic Russian roulette and splitting, can further enhance efficiency and robustness of algorithm performance.

For organs relevant to brachytherapy treatment planning, we have shown that mean efficiency increases of 7-15 are realized compared to our conventional Monte Carlo dose calculations. It should be noted that these results are for one patient only, and are not representative of a large patient population. Additional study should be completed on a larger patient population to determine general efficiency gains for the prostate and rectum as well as other planning relevant sites such as the urethra, bladder, and seminal vesicles.

Overall, PTRAN\_CT\_corr has been shown to be a fast and efficient brachytherapy planning tool to assess the heterogeneous dose distribution delivered to the patient.

#### ACKNOWLEDGMENT

Funded in part by grant R01 CA 46640 awarded by the National Institutes of Health.

#### REFERENCES

1. Rivard M, Coursey B, *et al.* (2004) Update of AAPM Task Group No. 43 Report: A revised AAPM protocol for brachytherapy treatment planning. *Med. Phys.* 31:633-674

2. Carrier J, D'Amours M, *et al* (2007) Postimplant dosimetry using a Monte Carlo dose calculation engine: A new clinical standard. *Int. J. Radiation Oncology Biol. Phys.* 68:1190-1198
3. Chibani O, Williamson J (2005) MCPI<sup>®</sup>: A sub-minute Monte Carlo dose calculation engine for prostate implants. *Med. Phys.* 32:3688-3698
4. Chibani O, Williamson J, *et al* (2005) Dosimetric effects of seed anisotropy and interseed attenuation for <sup>103</sup>Pd and <sup>125</sup>I prostate implants. *Med. Phys.* 32:2557-2566
5. Hedtjörn H, Carlsson G, *et al* (2002) Accelerated Monte Carlo based dose calculations for brachytherapy planning using correlated sampling. *Phys. Med. Biol.* 47:351-376
6. Lux I, Koblinger L (1991) Monte Carlo particle transport methods: Neutron and Photon calculations. CRC Press, Boca Raton
7. Le Y, Chibani O, *et al* (2005) An integrated CT-based Monte Carlo dose-evaluation system for brachytherapy and its application to permanent prostate implant. *Med. Phys.* 32:2068
8. Walters B, Rogers D (2002) DOSXYZnrc users manual. NRCC Report PIRS-794
9. White D, Booz J, *et al* (1989) Tissue Substitutes in Radiation Dosimetry and Measurement. ICRU Report 44
10. Monroe J, Williamson J (2002) Monte Carlo-aided dosimetry of the Theragenics TheraSeed<sup>®</sup> Model 200 <sup>103</sup>Pd interstitial brachytherapy seed. *Med. Phys.* 29:609-621
11. Williamson J (1987) Monte Carlo evaluation of kerma at a point for photon transport problems. *Med. Phys.* 14:567-576

Author: Jeffrey Williamson  
 Institute: Virginia Commonwealth University  
 Street: 401 College Street, B-129  
 City: Richmond  
 Country: United State of America  
 Email: JWilliamson@mcvh-vcu.edu

# Appendix B

# Fast patient-specific Monte Carlo brachytherapy dose calculations via the correlated sampling variance reduction technique

Andrew Sampson, Yi Le<sup>b)</sup>, and Jeffrey F. Williamson<sup>a)</sup>

Department of Radiation Oncology, Virginia Commonwealth University, Richmond, Virginia 23298

(Received 21 September 2011; revised 16 December 2011; accepted for publication 5 January 2012; published 3 February 2012)

**Purpose:** To demonstrate potential of correlated sampling Monte Carlo (CMC) simulation to improve the calculation efficiency for permanent seed brachytherapy (PSB) implants without loss of accuracy.

**Methods:** CMC was implemented within an in-house MC code family (PTRAN) and used to compute 3D dose distributions for two patient cases: a clinical PSB postimplant prostate CT imaging study and a simulated post lumpectomy breast PSB implant planned on a screening dedicated breast cone-beam CT patient exam. CMC tallies the dose difference,  $\Delta D$ , between highly correlated histories in homogeneous and heterogeneous geometries. The heterogeneous geometry histories were derived from photon collisions sampled in a geometrically identical but purely homogeneous medium geometry, by altering their particle weights to correct for bias. The prostate case consisted of 78 Model-6711  $^{125}\text{I}$  seeds. The breast case consisted of 87 Model-200  $^{103}\text{Pd}$  seeds embedded around a simulated lumpectomy cavity. Systematic and random errors in CMC were unfolded using low-uncertainty uncorrelated MC (UMC) as the benchmark. CMC efficiency gains, relative to UMC, were computed for all voxels, and the mean was classified in regions that received minimum doses greater than 20%, 50%, and 90% of  $D_{90}$ , as well as for various anatomical regions.

**Results:** Systematic errors in CMC relative to UMC were less than 0.6% for 99% of the voxels and 0.04% for 100% of the voxels for the prostate and breast cases, respectively. For a  $1 \times 1 \times 1 \text{ mm}^3$  dose grid, efficiency gains were realized in all structures with 38.1- and 59.8-fold average gains within the prostate and breast clinical target volumes (CTVs), respectively. Greater than 99% of the voxels within the prostate and breast CTVs experienced an efficiency gain. Additionally, it was shown that efficiency losses were confined to low dose regions while the largest gains were located where little difference exists between the homogeneous and heterogeneous doses. On an AMD 1090T processor, computing times of 38 and 21 sec were required to achieve an average statistical uncertainty of 2% within the prostate ( $1 \times 1 \times 1 \text{ mm}^3$ ) and breast ( $0.67 \times 0.67 \times 0.8 \text{ mm}^3$ ) CTVs, respectively.

**Conclusions:** CMC supports an additional average 38–60 fold improvement in average efficiency relative to conventional uncorrelated MC techniques, although some voxels experience no gain or even efficiency losses. However, for the two investigated case studies, the maximum variance within clinically significant structures was always reduced (on average by a factor of 6) in the therapeutic dose range generally. CMC takes only seconds to produce an accurate, high-resolution, low-uncertainty dose distribution for the low-energy PSB implants investigated in this study. © 2012 American Association of Physicists in Medicine. [DOI: 10.1118/1.3679018]

Key words: brachytherapy, correlated sampling, Monte Carlo, TG-43

## I. INTRODUCTION

The current standard of practice for brachytherapy dose computation is the lookup table-based AAPM Task Group 43 protocol (TG-43),<sup>1</sup> which assumes that patients are homogeneous water spheres and neglects seed-to-seed attenuation and other applicator-shielding effects. In response to numerous studies<sup>2–10</sup> documenting significant dosimetric effects caused by tissue heterogeneities and interseed attenuation, the AAPM formed a task group (TG-186) to address this issue.<sup>11</sup>

For example, in  $^{125}\text{I}$  and  $^{103}\text{Pd}$  prostate permanent seed brachytherapy (PSB) implants, tissue heterogeneities and

interseed attenuation reduce  $D_{90}$  (minimum dose delivered to 90% of the treatment volume, CTV) and  $V_{200}$  (volume receiving at least 200% of the prescribed dose) in postimplant dose evaluation by as much as 13% (Refs. 2–6 and 9) and 7% (Ref. 4), respectively. Furthermore Chibani *et al.* showed that the presence of calcifications constituting 1%–5% of the prostate mass decreased  $D_{100}$  by as much as 58% (Ref. 2). For a  $^{125}\text{I}$  PSB simulated breast implant (50% mammary gland—50% adipose by mass), a decrease in  $D_{90}$  of 10.3% was observed.<sup>10</sup> In addition, the authors demonstrated that higher volumes of adipose tissue, relative to mammary glandular tissue, increased this effect. Overall,



these studies show that dose to bony/calcified tissues and adipose tissues differ by as much as a factor of two from absorbed dose to water in the 15–40 keV energy range.

Three classes of model-based dose calculation algorithms have been proposed to address the deficiencies of TG-43: collapsed-cone superposition-convolution (CCSC),<sup>12,13</sup> discrete-ordinate finite-element methods (DOFE),<sup>14</sup> and Monte Carlo simulation (MC). Carlsson-Tedgren *et al.*<sup>15</sup> has shown the efficacy of using CCSC for accurate subminute brachytherapy dose calculations, but to date their studies have been limited to simple applicator scatter corrections and not applied to patient-specific treatment planning. Recently, Varian Medical Systems released Acuros<sup>®</sup>,<sup>16</sup> a radiation-therapy specific rewrite of the DOFE code ATTILA<sup>®</sup> (Ref. 14) within its BrachyVision<sup>™</sup> planning software. Acuros can compute most high dose-rate (HDR) brachytherapy dose distributions in fewer than 10 min. Deterministic solutions offer substantial speed enhancements, but are subject to systematic bias, e.g., ray-effects, due to overly coarse discretization of the radiation transport phase-space. For a single <sup>192</sup>Ir source in homogeneous medium, Zourari *et al.*<sup>16</sup> found differences between Acuros and MC less than 1% in most voxels, illustrating that DOFE parameters can be tuned to produce accurate results with reasonable computing times within a certain problem domain.<sup>17</sup>

CT-based MC methods can also be applied to both applicator-attenuation and tissue-heterogeneity effects for both low and high energy brachytherapy but unlike DOFE and CCSC, give rise to statistically noisy solutions that are generally unbiased, i.e., converge to the exact unbiased solution of the transport equation. However, the central processing unit (CPU) time-intensiveness of MC transport solutions has limited their use in the clinical setting<sup>5</sup> until recent advent of accelerated MC codes.<sup>18</sup> Although these codes can compute dose distributions in fewer than 5 min, such performance is clinically marginal since treatment planning optimization routines require the dose distribution to be computed multiple times.<sup>19–21</sup> To overcome this limitation, additional sophisticated variance reduction techniques must be employed to further reduce the CPU time to achieve clinically acceptable uncertainties on cost effective hardware. Due to the limitations imposed by current DOFE and MC solutions, there is still need for an efficient, robust, and accurate general purpose brachytherapy dose calculation engine that overcomes the deficiencies of TG-43.

In this study we describe the implementation of a sophisticated and general variance reduction technique called correlated sampling.<sup>22,23</sup> We believe this to be first application of correlated sampling Monte Carlo (CMC) to CT-based brachytherapy dose calculation in clinically realistic geometries. Specifically, we investigate its accuracy and efficiency for two patient case studies.

## II. METHODS

### II.A. Correlated Sampling

To aid the reader, the symbols and acronyms used in this paper are defined in Table I. Correlated sampling was first

proposed for accelerating MC brachytherapy dose calculations by Hedtj rn *et al.*<sup>22</sup> who demonstrated the potential of order-of-magnitude efficiency gains in simple two-dimensional geometries. Since their paper described the correlated sampling theory in detail,<sup>22</sup> only a brief summary will be given here. Rather than computing absorbed dose directly, CMC estimates the dose difference between heterogeneous and homogeneous geometries on a voxel-by-voxel basis. Conceptually, deviations from unit density water composition (including applicators and tissue composition heterogeneities) are treated as perturbations of the corresponding homogeneous (unperturbed) system. This is done by randomly sampling each photon history, consisting of collision sequence,  $\mathbf{p}_n^{\text{hom}} = (\mathbf{r}_n, E_n, \Omega_n, W_n^{\text{hom}})$ , from the photon-source and transition-kernel probability density functions (PDFs) characteristic of purely homogeneous geometry. In this nomenclature,  $n$  denotes order of scattering within the history ( $n = 0$  for primary);  $\mathbf{r}_n$  denotes the  $n$ th interaction location; and  $E_n$ ,  $\Omega_n$ , and  $W_n^{\text{hom}}$  denote the energy, direction, and statistical weight of the photon leaving  $\mathbf{r}_n$ , respectively. To score the dose difference between heterogeneous and homogeneous geometries, a corresponding heterogeneous geometry history  $^*\mathbf{p}_n^{\text{het}} = (\mathbf{r}_n, E_n, \Omega_n, W_n^{\text{het}})$ , is constructed that utilizes the same sequence of collision sites and emergent directions and energies, but a different weight correction factor,  $W_n^{\text{het}}$ .

The weight correction factor is designed to eliminate the bias due to representing photon transport in the heterogeneous geometry by a sequence of histories derived from the homogeneous transport and scattering kernels and is given by

$$W_n^{\text{het}} = W_n^{\text{hom}} \times \frac{P_{\text{het}}(\mathbf{p}_0^{\text{hom}}, \dots, \mathbf{p}_n^{\text{hom}})}{P_{\text{hom}}(\mathbf{p}_0^{\text{hom}}, \dots, \mathbf{p}_n^{\text{hom}})}, \quad (1)$$

where  $P_{\chi}(\mathbf{p}_0^{\text{hom}}, \dots, \mathbf{p}_n^{\text{hom}})$  is the probability of sampling the history  $\mathbf{p}_0^{\text{hom}}, \dots, \mathbf{p}_n^{\text{hom}}$  in geometry  $\chi$ . To simplify calculation of  $W_n^{\text{het}}$ , a free-electron Compton scattering model that neglects characteristic x-ray emission and coherent scattering is assumed. For the distance between 0 and 10 cm from a model 6711 <sup>125</sup>I seed, the Klein-Nishina scatter approximation has been shown to support dose estimates that agree within 1% of that delivered in low-Z media by an incoherent and coherent scatter physics model.<sup>24</sup> Because  $^*\mathbf{p}_n^{\text{het}}$  and  $\mathbf{p}_n^{\text{hom}}$  use the same sequence of collisions to score dose, their respective dose tallies are tightly correlated. In practice, this correlation is exploited by scoring the dose difference

$$\Delta d_{ijk,m,n}^c = f_{ijk}^{\text{het}}(^*\mathbf{p}_{m,n}^{\text{het}}) - f_{ijk}^{\text{hom}}(\mathbf{p}_{m,n}^{\text{hom}}), \quad (2)$$

where  $m$  and  $n$  denote history number and order of scatter, respectively;  $ijk$  denote the voxel indices along the x, y, and z axes, respectively;  $f_{ijk}^{\chi}$  is the scoring estimator for geometry  $\chi$ ; and  $\Delta d_{ijk,m,n}^c$  represents the dose difference between the heterogeneous and homogeneous dose tallies. The final sample mean, obtained by summing over interactions within each history and averaging over histories, is given by

$$\overline{\Delta d}_{ijk}^c = \frac{1}{N} \sum_{m=1}^N \sum_{n=1}^{M_m} \Delta d_{ijk,m,n}^c. \quad (3)$$

The heterogeneous dose,  $\overline{D}_{ijk}^{\text{het,c}}$  is an estimate of the true mean

TABLE I. Symbols listed in order of appearance.

$\Delta D$	$D^{\text{het}} - D^{\text{hom}}$ , the difference between the dose to the heterogeneous and homogeneous media
$\beta_n^{\text{hom}}$	Photon history phase-space vector at collision $n$ sampled assuming a purely homogeneous surrounding media
$N$	Order of scatter
$\mathbf{r}_n$	Position of the $n$ th interaction
$E_n$	Energy leaving $\mathbf{r}_n$
$\Omega_n$	Trajectory leaving $\mathbf{r}_n$
$W_n^{\text{hom}}$	Weight of the photon leaving $\mathbf{r}_n$ in the homogeneous media
$*\beta_n^{\text{het}}$	Photon history phase-space vector at collision $n$ sampling assuming a purely homogenous surrounding media, but having an altered weight correction factor to account for heterogeneities
$W_n^{\text{het}}$	Weight of the photon leaving $\mathbf{r}_n$ in the heterogeneous media
$P_\chi(\beta_0^{\text{hom}}, \dots, \beta_n^{\text{hom}})$	The probability of sampling the history $\beta_0^{\text{hom}}, \dots, \beta_n^{\text{hom}}$ in geometry $\chi$
$\Delta d_{ijk,m,n}^c$	The dose difference between scores to voxel $ijk$ from $*\beta_n^{\text{het}}$ and $\beta_n^{\text{hom}}$ for interaction $n$ in history $m$
$N$	The total number of histories
$M_m$	The number of interactions within history $m$
$f_{ijk}^c$	Scoring estimator for geometry $\chi$
$\overline{\Delta D}_{ijk}^c$	The sample mean of $\Delta D$ obtained by averaging $\sum_{n=1}^{M_m} \Delta d_{ijk,m,n}^c$ , sum over all interactions within a history, over all $N$ histories.
$\overline{D}_{ijk}^{\text{het,c}}$	An estimate of the true mean, $\overline{D}_{ijk}^{\text{het,u}}$
$\overline{D}_{ijk}^{\text{het,u}}$	A sample mean of the true mean, $D_{ijk}^{\text{het}}$
$D_{ijk}^{\text{het}}$	The true, “unbiased” value for the dose to $ijk$ to the heterogeneous media
$HCF$	The heterogeneous correction factor defined as the ratio between $D^{\text{het}}$ and $D^{\text{hom}}$
$HCF_{ijk}$	$D_{ijk}^{\text{het}}/D_{ijk}^{\text{hom}}$ , for voxel $ijk$
$\overline{HCF}_{ijk}^c$	$\overline{D}_{ijk}^{\text{het,c}}/D_{ijk}^{\text{hom}}$
$\overline{D}_{ijk}^{\text{het,u}}$	Sample mean of heterogeneous dose to voxel $ijk$ through means of UMC, and is an unbiased estimator of $D_{ijk}^{\text{het}}$
$D_{ijk}^{\text{TG43}}$	AAPM TG-43 solution to homogeneous dose to voxel $ijk$
$V(v)$	The variance of enclosed value, $v$

$$\begin{aligned} \overline{D}_{ijk}^{\text{het,c}} &= D_{ijk}^{\text{hom}} \cdot \overline{HCF}_{ijk}^c, \text{ where } \overline{HCF}_{ijk}^c = 1 + \overline{\Delta D}_{ijk}^c / D_{ijk}^{\text{hom}} \\ &= 1 + \overline{\Delta D}_{ijk}^c / D_{ijk}^{\text{TG43}}, \end{aligned} \quad (4)$$

where the symbols with macron (over line), e.g.,  $\overline{D}_{ijk}^{\text{het,c}}$  denote sample means derived from a finite set of histories as in Eq. (3), and the corresponding macron-less symbol,  $D_{ijk}^{\text{het}}$ , denotes the corresponding unbiased “true” value. The heterogeneous correction factor (HCF) is defined as  $HCF_{ijk} = D_{ijk}^{\text{het}}/D_{ijk}^{\text{hom}}$ , and the corresponding CMC estimate is given by  $\overline{HCF}_{ijk}^c = \overline{D}_{ijk}^{\text{het,c}}/D_{ijk}^{\text{hom}}$ .  $\overline{D}_{ijk}^{\text{het,u}}$  is the sample mean of heterogeneous dose obtained from traditional, uncorrelated MC (UMC) methodology and, unlike  $\overline{D}_{ijk}^{\text{het,c}}$ , is assumed to be an unbiased estimator of  $D_{ijk}^{\text{het}}$ . We assume that  $D_{ijk}^{\text{hom}}$  can be closely approximated by a noiseless and accurate fast deterministic calculation: in our study, the TG-43 formalism was used:  $D_{ijk}^{\text{hom}} = D_{ijk}^{\text{TG43}}$  as illustrated in Eq. (4). Since  $D_{ijk}^{\text{TG43}}$  can be known with negligible statistical uncertainty, it follows that<sup>22</sup>

$$V(\overline{D}_{ijk}^{\text{het,c}}) = V(\overline{\Delta D}_{ijk}^c) \ll V(\overline{D}_{ijk}^{\text{het}}), \quad (5)$$

where  $V$  is the variance, provided that the correlation between  $*\beta_n^{\text{het}}$  and  $\beta_n^{\text{hom}}$  remains high. However, a positive covariance cannot be guaranteed,<sup>25</sup> implying that efficiency decreases are possible given circumstances where the correlation between the homogeneous and heterogeneous histories breaks down. If such circumstances exist throughout the treatment volume, the homogeneous water geometry may be replaced by an average tissue-volume composition that would decrease the spread of HCF values, thus increasing the correlation between  $*\beta_n^{\text{het}}$  and  $\beta_n^{\text{hom}}$ . Such areas may include those that contain large volumes of adipose tissue,

such as the breast. With this alteration, the needed TG-43 parameters could be recomputed for such nonaqueous homogeneous media with available Monte Carlo tools, enabling use of TG-43.

## II.B. Implementation

The correlated sampling technique, described above, was implemented as an option within the more general CT-based MC dose calculation code, PTRAN\_CT, which is a member of the PTRAN code family developed by Williamson and colleagues.<sup>7,8,23,26–28</sup> PTRAN\_CT is a MC photon-transport code designed specifically for fast brachytherapy dose calculation, utilizing several novel variance reduction strategies (noted below) previously developed by Chibani and Williamson<sup>2</sup> within a different code family. Since secondary electrons are not transported, energy deposition is assumed to occur locally when an ionizing event occurs. In contrast to PTRAN\_CT CMC option, the uncorrelated MC (UMC) PTRAN\_CT option uses a more complete collisional physics model, including characteristic x-ray emission following photoelectric absorption, electron binding corrections to Compton scattering, and coherent scattering. Both the PTRAN\_CT UMC and CMC options support history-by-history uncertainty estimation<sup>29</sup> and an optional phase-space source model.<sup>2</sup> A fast ray-tracing algorithm is used to track photons through a voxel-based patient anatomy model and through seeds and applicators based upon a general complex combinatorial geometry (CCG) modeling system.<sup>30</sup> Voxel indexing,<sup>2</sup> which restricts CCG ray-tracing to those modeled structures that intersect voxels along the direct path of the

photon, greatly improves the efficiency of photon tracking in this hybrid geometry. The expected track-length (ETL) scoring method was used by both the CMC and UMC PTRAN\_CT runs to further reduce variance.<sup>22</sup>

An in-house TG-43 computation engine was used to compute  $D_{ijk}^{TG43}$ . To ensure that voxel averaging effects will not confound comparison of  $\bar{D}_{ijk}^{het,u}$  to  $\bar{D}_{ijk}^{het,c}$ , our code integrates the TG-43 dose-at-a-point distribution over each voxel, excluding any voxel subvolumes partially occupied by brachytherapy seeds, the same convention used by the PTRAN\_CT ETL implementation. To compare Monte Carlo output with TG-43 calculations, the  $\Delta S_k$  (the mean air-kerma strength per simulated disintegration<sup>24</sup>) values used for <sup>103</sup>Pd Theragenics model-200 and <sup>125</sup>I model 6711 were  $0.731 \text{cGy} \cdot \text{cm}^2/\text{mCi} \cdot \text{h}$  (Ref. 8) and  $0.7559 \text{cGy} \cdot \text{cm}^2/\text{mCi} \cdot \text{h}$  (Ref. 7), respectively.

## II.C. Patient Cases

Two patient CT image sets are used to evaluate the accuracy and efficiency of CMC relative to UMC. The first case is a simulated <sup>103</sup>Pd PSB breast implant designed as recommended by Pignol *et al.*<sup>31</sup> High-resolution images ( $0.335 \times 0.335 \times 0.4 \text{ mm}^3$  voxels) of a patient's right breast in pendant geometry were obtained on a dedicated cone-beam CT imaging system.<sup>32</sup> Using a method previously described<sup>33,34</sup> six tissue types were automatically segmented: skin, chest wall muscle, air, adipose, and two different mammary gland tissues with differences in density. Tissue compositions are taken from Woodard *et al.*<sup>35</sup> where the low density glandular tissue was assigned the composition of "mammary gland 1," while elemental compositions of "mammary gland 2" and "mammary gland 3" were averaged and assigned to higher density glandular tissue. The CTV is contoured as a 1 cm isotropic expansion of a simulated spherical lumpectomy cavity (2.4 cm diameter) having the average CTV dimensions reported by Pignol *et al.*'s study with a CTV volume of 44.6 cc. An implant consisting of 87 Model 200 seeds with air-kerma strengths of 1.590 U ( $U = 1 \mu\text{Gy} \cdot \text{m}^2/\text{h}$ ) was designed to deliver a prescribed  $D_{100}$  dose of 90 Gy to the CTV using a commercial treatment planning system (Varian VeriSeed 8.0). Because of the high adipose tissue-volume in the breast, rather than using liquid water for computation of  $D_{ijk}^{hom}$  via the TG-43 method, we utilized a homogeneous average breast composition<sup>36</sup> medium consisting of 85% adipose and 15% fibroglandular tissue to reduce the range of HCF values, and hence, the decorrelation of heterogeneous and homogeneous photon histories.

The second case consisted of a postimplant CT of a PSB patient with an  $82 \text{ cm}^3$  prostate implanted with 78 Model-6711 <sup>125</sup>I seeds with air-kerma strengths 0.636 U/seed and a prescribed  $D_{100}$  of 145 Gy. VariSeed was used to identify seed coordinates in the postimplant CT. A modified version of CTCREATE, taken from the DOSXYZNRC (Ref. 37) code family, was used to convert single-energy CT intensity data to voxel-specific tissue composition and density assignments. Post CTCREATE, streaking artifacts in the postimplant prostate CT were partially mitigated by assigning ICRU adult muscle to voxels within the prostate with attenu-

ation coefficients at 28 keV outside the allowed window of  $[0.3716 \text{ cm}^{-1}, 0.4544 \text{ cm}^{-1}]$  corresponding to the range of soft tissue assigned within the prostate. While this method eliminates the seeds and their associated artifacts from the CT images, the seeds themselves were modeled analytically using PTRAN's CCG capability and the VariSeed coordinates. Tissue compositions were taken from ICRU report 44 (Ref. 38), and cross sections derived as previously described by Monroe *et al.*<sup>8</sup>

For both patient studies, the phase-space source model was used. As described previously,<sup>2,23</sup> in the phase-space source model a single-seed Monte Carlo simulation (based on the full collisional physics model and detailed CCG model of the seed structure), is performed to transport primary and scattered photons to the surface of the seed's titanium capsule. For each of the simulated histories, the resultant state vectors,  $\beta_0$ , are saved in the phase-space file. During PTRAN\_CT execution, primary photons are "sampled" by sequentially reading  $\beta_0$  vectors from the phase-space file and using them to launch histories from the surfaces of randomly selected seeds. This improves the correlation between  $\beta_n^{het}$  and  $\beta_n^{hom}$  by eliminating attenuation and scattering of primary photons within the seed structure.

Using the postimplant CT coordinates, the prostate case dose was computed in a rectangular region of interest (ROI) of  $10.2 \times 15.0 \times 7.2 \text{ cm}^3$  with  $1 \times 1 \times 1 \text{ mm}^3$ ,  $2 \times 2 \times 2 \text{ mm}^3$ , and  $3 \times 3 \times 3 \text{ mm}^3$  voxel dimensions for both CMC and UMC. The simulated breast implant ROI had dimensions of  $10.47 \times 10.47 \times 7.44 \text{ cm}^3$  with dose grid voxel sizes of  $0.67 \times 0.67 \times 0.8 \text{ mm}^3$  and  $1.34 \times 1.34 \times 1.6 \text{ mm}^3$ . Hundred million photon histories were simulated by both CMC and UMC simulations. We denote these results as low-uncertainty (LU) CMC (LU-CMC) and LU-UMC, respectively. To minimize confusion, the phrase "finest grid" refers to  $1 \times 1 \times 1 \text{ mm}^3$  and  $0.67 \times 0.67 \times 0.8 \text{ mm}^3$  voxel sizes for the prostate and breast cases, respectively.

## II.D. Evaluating Efficiency and Accuracy

MC simulation efficiency is defined by  $\epsilon_{ijk} = 1/(\bar{\sigma}_D^2 \cdot T)$  where T is CPU time required to achieve the sample standard deviation about the mean (SDM),  $\bar{\sigma}_D$  (generally expressed as percentage of the corresponding local mean,  $\bar{D}$ ). For each individual voxel  $ijk$ , the efficiency gain,  $G_{ijk}$ , of CMC relative to UMC is given by

$$G_{ijk} = \frac{\bar{\sigma}_{D_{ijk}}^{het,u} \cdot T^{het,u}}{\bar{\sigma}_{D_{ijk}}^{het,c} \cdot T^{het,c}} \quad (6)$$

Because  $G_{ijk}$  varies significantly with  $\bar{D}_{ijk}^{het}$  and  $\overline{HCF}_{ijk}$ , the mean efficiency gain was computed separately for ROIs containing voxels receiving doses greater than 20%, 50% and 90% of  $D_{90}$ , denoted as  $G_{20}$ ,  $G_{50}$ ,  $G_{90}$ , respectively. Additionally, the percentage of voxels in each ROI enjoying a positive gain in efficiency ( $G_{ijk} > 1$ ) was tallied. Finally, mean efficiency gains within the prostate (CTV), the urethra, and rectum ROI subvolumes, for voxels receiving doses greater than 50% of the  $D_{90}$ , were calculated. To test the feasibility of

TABLE II. Best fit parameters values of the  $f(z)$  distribution, Eq. (8), for the breast and prostate plans.

			Corresponding Error	
	Prostate	Breast	Prostate	Breast
$\alpha_1$	0.9993	0.05124	$3.2 \times 10^{-3}$ % underestimation in	0.039% underestimation in 5.1% of the voxels
$\beta_1$	-0.01822	-0.4502	99.9% of the voxels	
$\alpha_2$	0.0006508	0.002814	0.54% overestimation in 0.065% of the voxels	0.099% underestimation in 0.28% of the voxels
$\beta_2$	3.047	-1.1318		

CMC-based dose planning, the time required for CMC to achieve an average percent SDM of 2% within the CTV,  $T_{2\%SDM}^{\text{het.c}}$ , was estimated, assuming that variance is inversely proportional to the MC CPU time. The UMC and CMC percent SDMs vs dose and HCF on a voxel-by-voxel basis were compared for the ROI's after using  $T_{2\%SDM}^{\text{het.c}}$  for CPU runtime.

To quantitatively evaluate accuracy of  $\bar{D}_{ijk}^{\text{het.c}}$  relative to  $\bar{D}_{ijk}^{\text{het.u}}$  benchmarks the distribution of dose differences at each voxel  $ijk$  receiving more than 50% of the prescribed dose is evaluated, expressed as multiples of the combined absolute statistical uncertainty

$$z_{ijk} = \left( \left( \bar{D}_{ijk}^{\text{het.c}} - \bar{D}_{ijk}^{\text{het.u}} \right) / \sqrt{\bar{\sigma}_{\bar{D}_{ijk}^{\text{het.c}}}^2 + \bar{\sigma}_{\bar{D}_{ijk}^{\text{het.u}}}^2} \right) - 1. \quad (7)$$

In this expression,  $\bar{\sigma}$  represents the absolute SDM. In the absence of any systematic error or bias, the distribution of  $z_{ijk}$  should be a Gaussian with a mean of zero and standard deviation of 1. To separate the systematic and random components of CMC error, the  $z_{ijk}$  frequency histogram was fit to the model proposed by Kawrakow *et al.*<sup>39</sup>

$$f(z) = \frac{1}{\sqrt{2\pi}} \left[ \alpha_1 e^{-\frac{(z-\beta_1)^2}{2}} + \alpha_2 e^{-\frac{(z-\beta_2)^2}{2}} + (1 - \alpha_1 - \alpha_2) e^{-\frac{z^2}{2}} \right], \quad (8)$$

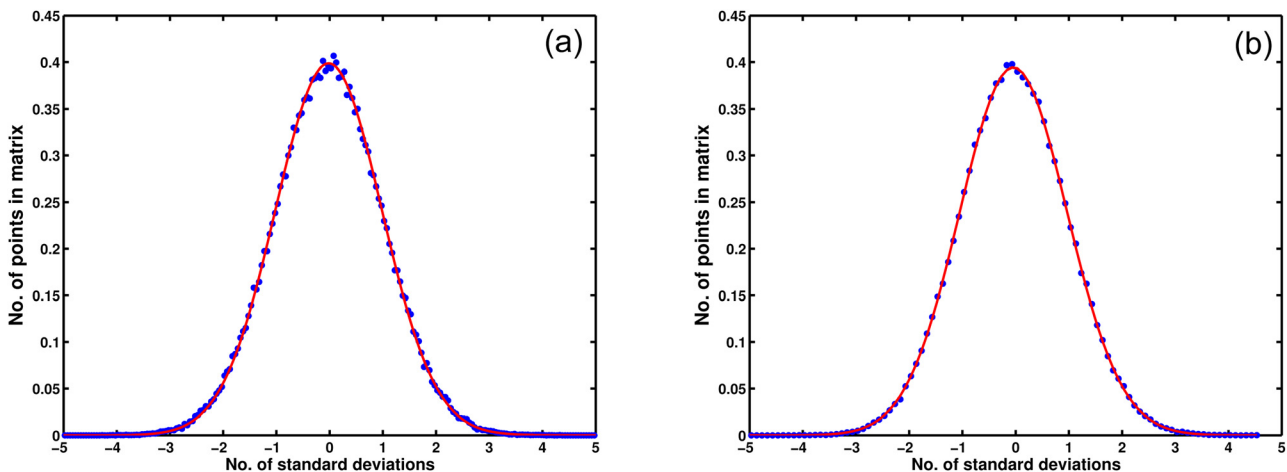
where  $f(z)dz$  is the probability that a voxel has a normalized error in the interval  $(z, z + dz)$ . This model includes two normally distributed systematic errors with means of  $\beta_i$ , standard deviations of 1.0, and probability of occurrence  $\alpha_i$ , where  $i = 1, 2$  with the remaining voxels exhibiting only random

errors described by a Gaussian with zero mean and unit standard deviation. The quantity  $\alpha_i$  represents the fraction of voxels that exhibit a mean systematic error  $\beta_i$ . The percentage difference between LU-CMC and LU-UMC corresponding to  $\beta_i$  is estimated by taking the product of  $\beta_i$  and the average percent SDM within investigated region. Fitting was performed using MATLAB's curve-fitting toolbox (MATLAB 7.10.0 (R2010a), Trust-Region algorithm utilizing the least absolute residuals technique for robust fitting).

### III. RESULTS

The finest grid with 100 million histories resulted in a mean percent SDM of 0.18% and 0.62% for prostate and 0.087% and 0.77% within the breast for LU-CMC and LU-UMC, respectively, within regions that receive greater than 50%  $D_{90}$ . Corresponding run times on an AMD Phenom II X6 1090T processor utilizing only one core were 4.4 and 3.95 h for prostate LU-CMC and LU-UMC, respectively, and 3.84 and 2.33 h for the breast case. This very large number of photon histories was simulated in order to minimize statistical fluctuations.

For the prostate case, Table II shows that nearly all voxels are affected by a very small 0.003% mean systematic error while 0.1% voxels have a larger error of 0.5%. For the breast case, approximately 5% of the voxels have mean systematic errors of 0.04%–0.1%. These data demonstrate that systematic discrepancies between the two codes are very small, i.e., that CMC accurately reproduces UMC results. The distribution of  $z_{ijk}$  comparing LU-CMC with LU-UMC for all voxels that receive greater than 50%  $D_{90}$  is plotted in Fig. 1 for both

FIG. 1. Plots of  $z_{ijk}$  distributions, dots, for prostate (a) and breast (b) with their corresponding fits, line. Fit parameters are in Table II.

the prostate and breast implants along with fits to Eq. (8). Corresponding fit parameters and percentage errors are tabulated in Table II. The R-squared values for prostate and breast implants were 0.99995 and 0.999985, respectively, and clearly demonstrate a good fit. Since the UMC calculations utilized the full collisional physics model, these results demonstrate that the simplified free-electron scattering model used by CMC does not introduce significant systematic errors.

Figure 2 shows that the  $G_{ijk}$  distributions with respect to  $\bar{D}_{ijk}^{\text{het}}$  and  $\overline{HCF}_{ijk}$  have different shapes for the breast and prostate geometries, highlighting the sensitivity of CMC results to underlying implant and tissue geometry differences. For the prostate implant [Fig. 2(a)], the  $G_{ijk}$  distribution is sharply peaked around unity HCF; rapidly falls off with larger and smaller values; and displays a large range (a factor of five smaller and larger than unity). Prostate HCF values range from about 0.1 in areas shielded by the pelvic bone to about 10 inside the pelvic bone. Large deviations of HCF from unity are associated with reduced efficiency gain or even efficiency losses. In contrast, breast HCF values have a much smaller range [Fig. 2(b)], ranging from about 0.7 to 1.8, with the majority of voxels falling within 0.10 of

unity. This is due to using a weighted average of glandular and adipose media for the homogeneous medium. Figure 2(b) also reveals a broader maximum near unity HCF with very few voxels experiencing even modest efficiency losses in the limited HCF range of this body site. In contrast, the distributions of  $G_{ijk}$  as a function of dose have a much more similar appearance, except that almost no breast PSB voxels experience efficiency losses. In both sites, the largest efficiency gains are generally doses near or exceeding  $D_{90}$  while the average efficiency gain systematically decreases with decreasing dose.

Tables III and IV present efficiency summary statistics for the two clinical sites. For the prostate plan, all the voxels within the CTV experience an increase in runtime efficiency with an average  $G_{ijk}$  of 38.1 for the finest voxel grid. In contrast, the breast plan shows larger average  $G_{ijk}$  of 59.8 with 99.9% of the voxels within the CTV experiencing an efficiency gain for the finest grid. The average  $G_{ijk}$  is larger for the breast case due both to the smaller range of HCF corrections and the fact that an average breast medium was used for the homogeneous geometry, which more closely models the heterogeneous breast than water does the prostate geometry (See discussion below).

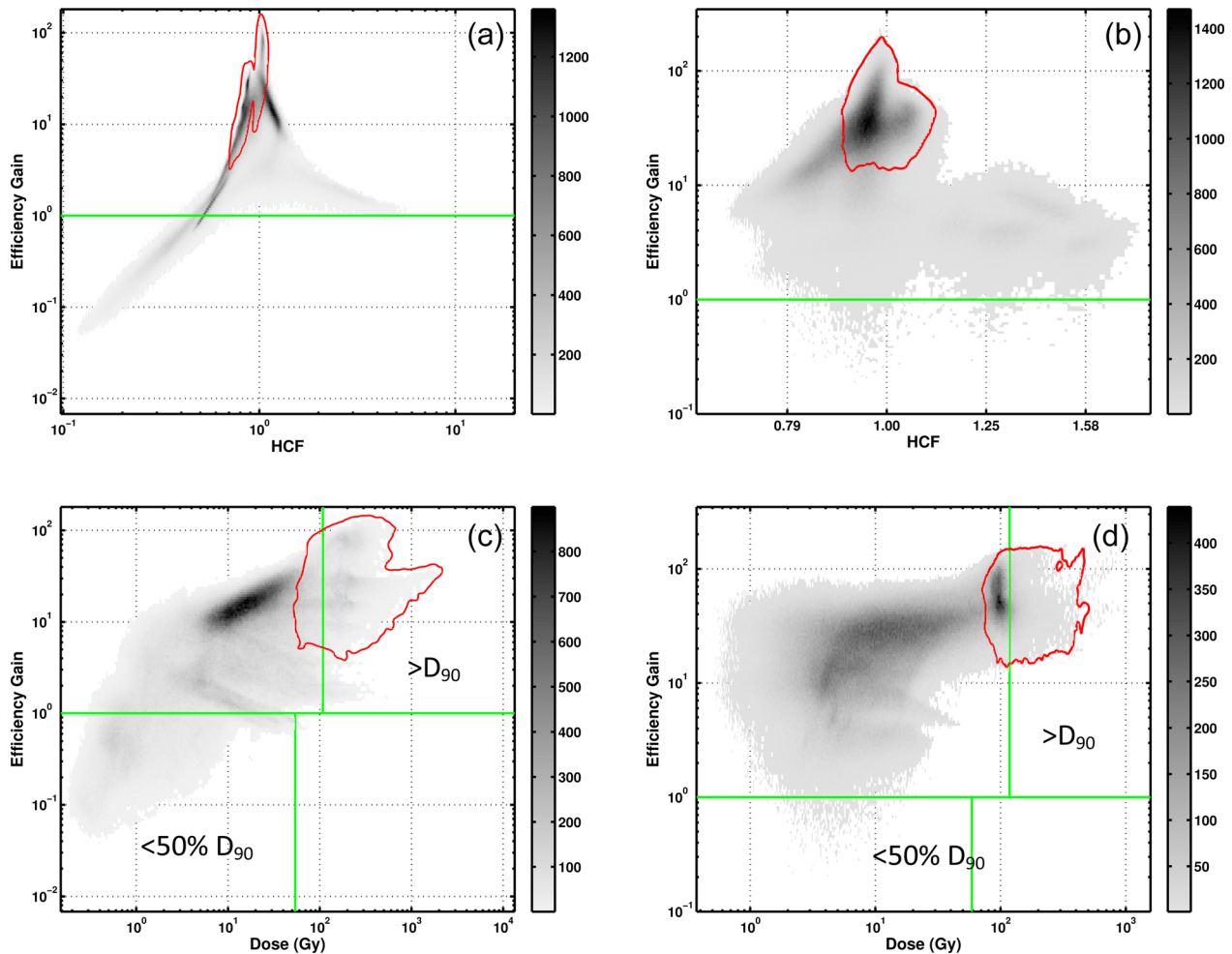


FIG. 2. Scatter plot of the efficiency gain vs the HCF for all voxels in the prostate (a) and breast (b) geometries; scatter plot of the efficiency gain vs the delivered dose (Gy) for all voxels in the prostate (c) and breast (d) geometries. The area outlined in circumscribes the voxels originating from the CTV.

TABLE III. Average efficiency gain for the breast and prostate plans for various ROI's along with the estimated time required to compute Monte Carlo dose to achieve 2% mean standard deviations about the mean. For the prostate plan, data are given for three different voxel dimensions:  $(1.0 \text{ mm})^3$ ,  $(2.0 \text{ mm})^3$ , and  $(3.0 \text{ mm})^3$  relative to uncorrelated Monte Carlo. Percentages within parentheses are the percentage of voxels within the corresponding structure that experience and efficiency gain greater than unity. The times listed are estimated to achieve average 2% standard deviation about the mean within corresponding structure at all dose levels.

Breast	MC Type	Time to achieve mean %SDM of 2%			Average Efficiency Gain ( $0.67 \text{ mm}^3$ )		
Lumpectomy Cavity.	UMC	16.9 min			55.7 (100%)		
	CMC	20.2 s					
CTV	UMC	18.7 min			59.8 (>99.9%)		
	CMC	21.1 s					
Prostate	MC Type	Time			Average Efficiency Gain		
		$(1.0 \text{ mm})^3$	$(2.0 \text{ mm})^3$	$(3.0 \text{ mm})^3$	$(1.0 \text{ mm})^3$	$(2.0 \text{ mm})^3$	$(3.0 \text{ mm})^3$
Prostate (CTV)	UMC	15.3min	1.59 min	30.9 s	37.1 (100%)	44.7 (100%)	41.6 (100%)
	CMC	38.6 s	3.3 s	1.1 s			
Bladder	UMC	113 min	12.0 min	4.0 min	12.3 (99.3%)	13.5 (99.0%)	12.7 (97.5%)
	CMC	16.5 min	1.63 min	38.9 s			
Rectum	UMC	45.2 min	4.55 min	1.44 min	14.0 (99.7%)	14.9 (99.1%)	14.3 (98.7%)
	CMC	4.7 min	27.4 s	8.9 s			
Seminal Vesicles.	UMC	29.1 min	3.02 min	56.9 s	12.6 (99.4%)	14.0 (99.8%)	13.3 (99.3%)
	CMC	3.5 min	17.9 s	6.23 s			
Urethra	UMC	18.0 min	1.90 min	36.4 s	43.2 (100%)	54.0 (100%)	54.1 (100%)
	CMC	38.9 s	3.49 s	1.13 s			

The assumption that Monte Carlo variance estimates are inversely proportional to the square-root of runtime, suggests CPU times,  $T_{2\%SDM}^{\text{het,c}}$ , of only 39 and 21 s are necessary for prostate and breast CTVs, respectively, to achieve 2% statistics. The CMC and UMC dose distributions were recomputed using the smaller number of histories corresponding to these rescaled  $T_{2\%SDM}^{\text{het,c}}$  runtimes. Figures 3 and 4 show the resultant distributions of %SDM with respect to  $\bar{D}_{ijk}^{\text{het,u}}$  for the clinical ROI regions receiving greater than 50% of  $D_{90}$ . The UMC simulations yielded mean %SDM's of 11.3%, 5.1%, and 4.6% for the bladder, rectum and seminal vesicles, respectively. These plots exhibit a dramatic separation between CMC and UMC statistical uncertainties with tightly grouped distributions with moderate dependence on dose. Despite the fact that some voxels experience little efficiency gain or even efficiency losses, for a fixed CPU time, CMC always reduces uncertainty within a given organ, generally by a factor of 6. The UMC SDM distributions are

consistently broader than for CMC for all structures shown, except for the rectum where the SDM spread appears to be equal. Figure 5 shows a central slice through the prostate plan with isodose curves from LU-UMC with and CMC using  $T_{2\%SDM}^{\text{het,c}}$  for run time. The differences between them are difficult to distinguish visually.

#### IV. DISCUSSION

CMC effectively reduces variance under many circumstances. However, regions with low dose or large dose perturbations due to tissue composition heterogeneities can experience diminished gains or even efficiency losses in both breast and prostate plans. Theoretical analyses of CMC indicate that, while the correlated sampling algorithm leads to unbiased results, there is no guarantee of improved efficiency.<sup>25</sup> This result is consistent with Hedtj rn's study<sup>22</sup> who realized efficiency gains of four orders of magnitude across a wide keV energy spectrum for a simple uniform water geometry with different single cylindrical heterogeneities. Despite efficiency losses in a small number of voxels, both cases investigated by our study demonstrated reduction of the maximum and mean dose-uncertainty in clinically relevant regions of interest. Voxels experiencing CMC efficiency loss generally already have UMC standard deviations well below the mean and maximum UMC standard deviations. Thus, CMC is globally advantageous despite the small number of voxels that exhibit increased statistical uncertainty. The prostate plan demonstrates the greatest loss of CMC efficiency advantage in regions where HCF deviates from unity by more than 20%. Both cases also show that regions with little dose deposition have a higher tendency to experience an efficiency loss. These regions include those

TABLE IV.  $G_{20}$ ,  $G_{50}$ , and  $G_{90}$  (average efficiency gain for voxels receiving greater than or equal to 20%, 50%, and 90% of the prescribed dose, respectively) for the breast and prostate plans. The prostate also shows values for larger voxel dimensions (2mm and 3mm). The percentage of the voxel contained in these regions that experience and efficiency gain are contained within the parentheses.

Breast	$G_{20}$	$G_{50}$	$G_{90}$
$0.67 \times 0.67 \times 0.8 \text{ mm}^3$	44.8 (>99.9%)	55.0 (100%)	54.9 (100%)
Prostate			
$1.0 \times 1.0 \times 1.0 \text{ mm}^3$	20.3 (98.2%)	26.8 (99.7%)	33.6 (>99.9%)
$2.0 \times 2.0 \times 2.0 \text{ mm}^3$	23.4 (97.8%)	31.8 (99.7%)	40.5 (100%)
$3.0 \times 3.0 \times 3.0 \text{ mm}^3$	22.2 (97.7%)	30.0 (99.8%)	38.1 (100%)

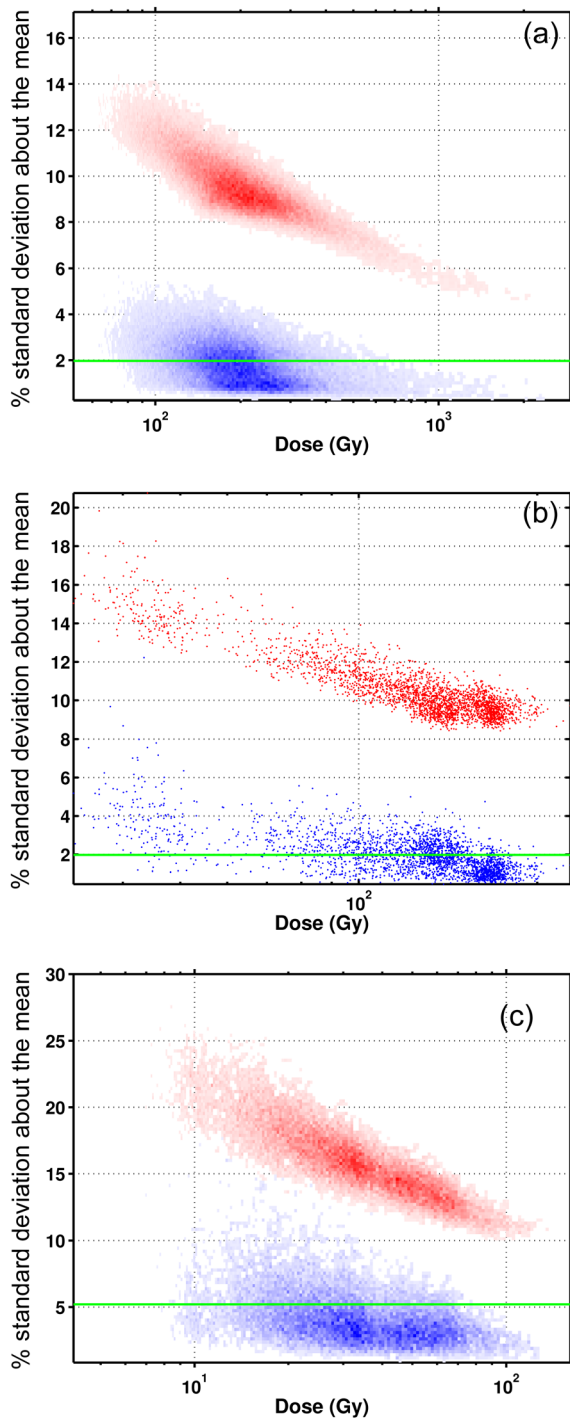


FIG. 3. Scatter plot of percent standard deviation about the mean vs dose for each individual voxel within the prostate (a), urethra (b), and the rectum (c), for correlated Monte Carlo (lower) and uncorrelated Monte Carlo (upper). The average percent standard deviation about the mean value for correlated Monte Carlo is plotted as green line. The CPU time was 39 s.

shielded by the pelvic bone and those regions outside the CTV in the breast where decorrelation between the homogeneous and heterogeneous histories is greatest, thus leading to the efficiency losses reported.

The larger CMC efficiency advantage realized in the breast cancer plan compared to the prostate implant can be explained by increased correlation between  $\beta_n^{\text{hom}}$  and  $\beta_n^{\text{het}}$ . This arises from using a uniform mixture of 85% adipose

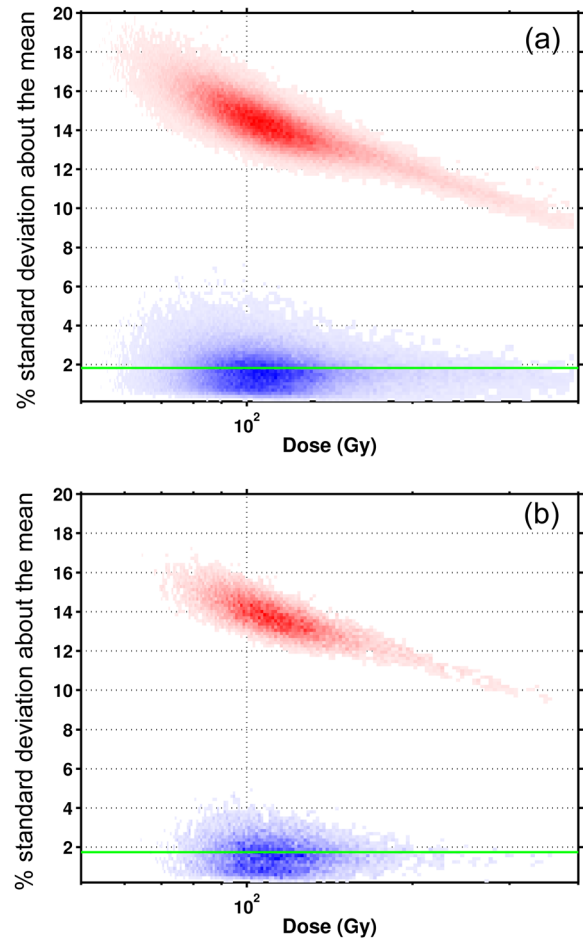


FIG. 4. Scatter plot of percent standard deviation about the mean vs dose for each individual voxel within the breast CTV (a), and the breast simulated lumpectomy cavity (b) for correlated Monte Carlo (lower) and uncorrelated Monte Carlo (upper). The average percent standard deviation about the mean value for correlated Monte Carlo is plotted as green line. The CPU time is 21 s.

and 15% fibroglandular tissue, which closely matches the mean composition of the breast,<sup>36</sup> for the homogeneous medium in the CMC calculations, resulting in heterogeneity corrections no larger than a factor of two. As shown in Fig. 6, if water is used instead, the average HCF of the CTV is approximately 0.5, compared to the prostate CTV, where the distribution of HCFs is centered on unity. This is because the breast CTV and normal parenchyma contains a large fraction of adipose tissue which has a 2–3 fold smaller attenuation coefficient than water at low energies. Every interaction within adipose tissue progressively increases the variability of heterogeneous photon weights, relative to water medium, through repeated application of the weight correction factor, Eq. (1). In future work, we intend to quantify this effect and determine if additional variance reduction techniques, e.g., systematic Russian roulette and splitting, i.e., weight windowing (WW), will further enhance efficiency and robustness of algorithm performance.<sup>40,41</sup> WW can be used to either constrain photon weights within a desired range, or can be used to implement importance sampling variance reduction that roughly sets photon weights proportional to their detector score “importance.”<sup>42</sup>

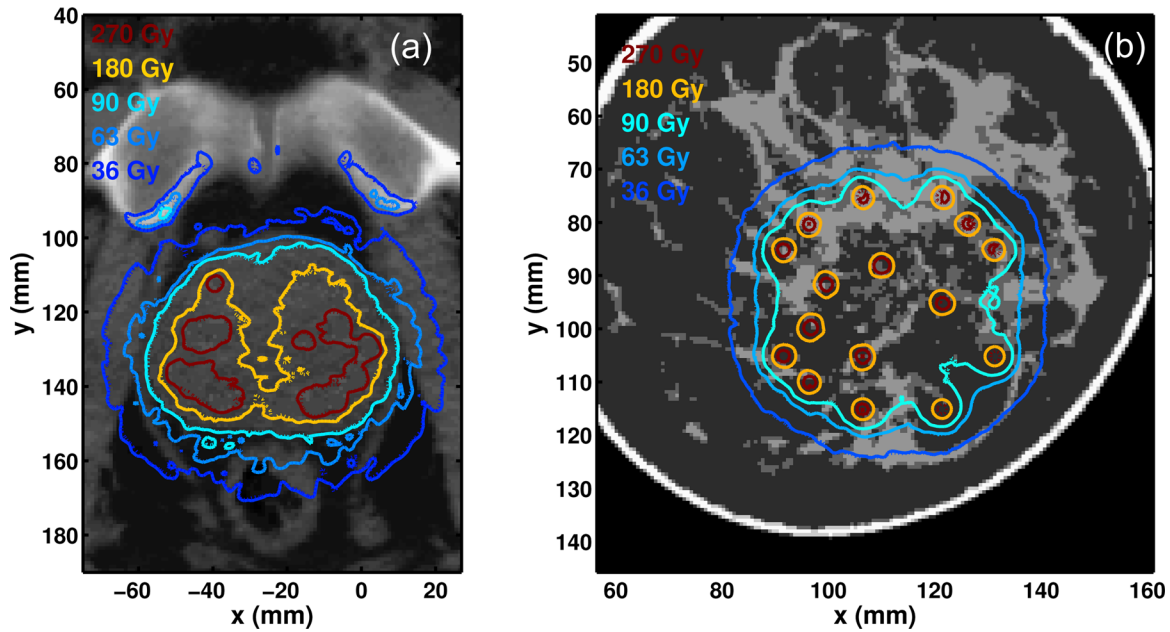


FIG. 5. Isodose curves for low-uncertainty uncorrelated Monte Carlo (dashed lines) and correlated Monte Carlo (solid) for prostate (a) and breast (b) using  $T_{2\%SDM}^{het,c}$  CPU times. All calculations use the finest dose grid.

For organs relevant to brachytherapy treatment planning, we have shown that 10- to 41-fold mean efficiency increases can be realized relative to conventional Monte Carlo dose calculations when performed on the finest voxel meshes explored in this study. It should be noted that these proof-of-principle results are based on a sample of only two patients, and, while encouraging, may not be representative of a large patient population. An additional limitation of this study was that the single prostate patient data set used had metal streaking artifacts that were mitigated only incompletely by post reconstruction image processing. Residual artifacts could have diminished potential efficiency gains. Further studies on larger artifact free patient data sets are needed to support claims that our results are representative in general of breast

and prostate patients. Furthermore, testing CMC for higher energy sources, e.g., HDR brachytherapy, and other treatment sites and techniques are also needed to provide the general characteristics of CMC.

A potential application for a fast MC code is in optimized PSB treatment planning optimization (OTP) where dose maps for many candidate seed configurations are computed and tested for quality.<sup>21,43-46</sup> If the widespread implementation of patient-specific MC-based OTP can be realized, the dose-outcome relationship could be greatly improved, potentially decreasing the incidence of toxicities.<sup>47</sup> Unfortunately, utilizing CMC, as presented in this study on the finest grid, PSB OTP still requires many hours of computation time. To further increase efficiency, additional studies are underway to assess the clinical practicality of recovering a high spatial resolution dose map from the summation between a low spatial resolution CMC  $\overline{\Delta D}_{ijk}^c$  and a high spatial resolution  $D_{ijk}^{TG43}$ .

Correlated PTRAN\_CT run times compare favorably with other specialized PSB Monte Carlo codes reported in the literature. Taylor *et al.*<sup>48</sup> and Yegin *et al.*<sup>49</sup> reported that BrachyDose, an EGSNRC based code, computes full PSB prostate dose distributions within 5 min. More recently, BrachyDose has been shown to compute the prostate dose distribution with an average 2% SDM using  $(2\text{ mm})^3$  voxels in 30 s.<sup>50</sup> Chibani *et al.*<sup>2</sup> reported calculations in under 1 min for a  $2 \times 2 \times 2\text{ mm}^3$  voxel mesh. In contrast, PTRAN\_CT CMC computes dose under these conditions in 3.3 s. VMC++ has also recently been commissioned for low-energy brachytherapy, though time benchmarks have not yet been reported.<sup>51</sup> Common variance reduction techniques utilized in these codes include Russian roulette, particle splitting, track-length estimation, and the reuse of photon histories. CMC differs from these techniques as it was directly derived from a transport equation solution to yield unbiased solutions. Though these

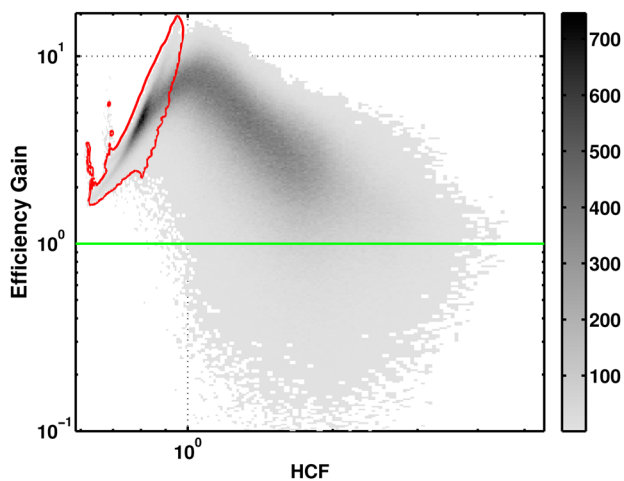


FIG. 6. Scatter plot of  $G_{ijk}$  vs HCF for all voxels in the simulated breast plan for correlated Monte Carlo based upon generation of photon histories in homogeneous water rather than average breast medium. The area outlined in red circumscribes the voxels originating from the CTV.



techniques were accurate and more efficient than their predecessors, CMC appears to be substantially more efficient, although more rigorous testing (controlling for implant geometry; seed structure complexity; dose specification; and processor speed) are needed to quantitatively measure such performance differences.

Fast dose-computation execution is not the only barrier to clinical implementation of tissue composition heterogeneity corrections in brachytherapy treatment planning. For low-energy brachytherapy, the task of correctly assigning tissue cross sections to organs or individual voxels is an important unsolved problem.<sup>52–54</sup> Potentially, this issue could be addressed through quantitative imaging techniques such as dual-energy CT.<sup>55,56</sup>

## V. CONCLUSIONS

We have demonstrated that correlated Monte Carlo simulations results in 38–60 fold improvements in average efficiency relative to conventional uncorrelated sampling Monte Carlo in typical low-energy seed implant geometries. Despite the possibility of lowering efficiency in limited subvolumes, CMC appears to reduce maximum variance in the dose grid for all low-energy interstitial implant cases investigated to date. On typical single-processor workstations, CMC has been shown to be a fast and efficient brachytherapy planning tool for more realistically assessing high-resolution dose distributions with run times of the order of 1 min in our hands. Further investigation is needed to mitigate the negative impact of particle weight decorrelation on efficiency.

## ACKNOWLEDGMENTS

The authors would like to thank John Boone from UC-Davis for providing the tissue-segmented, high-resolution breast-dedicated cone-beam CT image. This work was supported in part by grants R01-CA-46640 and R01-CA-149305 awarded by the National Institutes of Health.

<sup>a)</sup> Author to whom correspondence should be addressed. Electronic mail: jwilliamson@mcvh-vcu.edu. Telephone: 804-828-8451.

<sup>b)</sup> Present address: Johns Hopkins University, Baltimore, Maryland 21231.

<sup>1</sup> M. J. Rivard, B. M. Coursey, L. A. DeWerd, W. F. Hanson, M. S. Huq, G. S. Ibbott, M. G. Mitch, R. Nath, and J. F. Williamson, "Update of AAPM Task Group No. 43 Report: A revised AAPM protocol for brachytherapy dose calculations," *Med. Phys.* **31**, 633–674 (2004).

<sup>2</sup> O. Chibani and J. F. Williamson, "MCPI: A sub-minute Monte Carlo dose calculation engine for prostate implants," *Med. Phys.* **32**, 3688–3698 (2005).

<sup>3</sup> O. Chibani, J. F. Williamson, and D. Todor, "Dosimetric effects of seed anisotropy and interseed attenuation for <sup>103</sup>Pd and <sup>125</sup>I prostate implants," *Med. Phys.* **32**, 2557–2566 (2005).

<sup>4</sup> J. F. Carrier, L. Beaulieu, F. Therriault-Proulx, and R. Roy, "Impact of interseed attenuation and tissue composition for permanent prostate implants," *Med. Phys.* **33**, 595–604 (2006).

<sup>5</sup> J. F. Carrier, M. D'Amours, F. Verhaegen, B. Reniers, A. G. Martin, E. Vigneault, and L. Beaulieu, "Postimplant dosimetry using a Monte Carlo dose calculation engine: A new clinical standard," *Int. J. Radiat. Oncol., Biol., Phys.* **68**, 1190–1198 (2007).

<sup>6</sup> J. F. DeMarco, J. B. Smathers, C. M. Burnison, Q. K. Ncube, and T. D. Solberg, "CT-based dosimetry calculations for <sup>125</sup>I prostate implants," *Int. J. Radiat. Oncol., Biol., Phys.* **45**, 1347–1353 (1999).

<sup>7</sup> J. Dolan, Z. Lia, and J. F. Williamson, "Monte Carlo and experimental dosimetry of an <sup>125</sup>I brachytherapy seed," *Med. Phys.* **33**, 4675–4684 (2006).

<sup>8</sup> J. I. Monroe and J. F. Williamson, "Monte Carlo-aided dosimetry of the theragenics TheraSeed model 200 <sup>103</sup>Pd interstitial brachytherapy seed," *Med. Phys.* **29**, 609–621 (2002).

<sup>9</sup> A. S. Meigooni, J. A. Meli, and R. Nath, "Interseed effects on dose for <sup>125</sup>I brachytherapy implants," *Med. Phys.* **19**, 385–390 (1992).

<sup>10</sup> C. Furstoss, B. Reniers, M. J. Bertrand, E. Poon, J. F. Carrier, B. M. Keller, J. P. Pignol, L. Beaulieu, and F. Verhaegen, "Monte Carlo study of LDR seed dosimetry with an application in a clinical brachytherapy breast implant," *Med. Phys.* **36**, 1848–1858 (2009).

<sup>11</sup> L. Beaulieu, A. Carlsson Tedgren, J. Carrier, S. Davis, F. Mourrada, R. Thomson, F. Verhaegen, T. Wareing, and J. F. Williamson, "SU-E-T-701: Guidance for early adoption of model based dose calculation algorithms in brachytherapy: Progress report from AAPM Task Group 186," *Med. Phys.* **38**, 3651 (2011).

<sup>12</sup> A. Ahnesjo, "Collapsed cone convolution of radiant energy for photon dose calculation in heterogeneous media," *Med. Phys.* **16**, 577–592 (1989).

<sup>13</sup> A. K. Carlsson and A. Ahnesjo, "The collapsed cone superposition algorithm applied to scatter dose calculations in brachytherapy," *Med. Phys.* **27**, 2320–2332 (2000).

<sup>14</sup> K. A. Gifford, J. L. Horton, T. A. Wareing, G. Failla, and F. Mourrada, "Comparison of a finite-element multigroup discrete-ordinates code with Monte Carlo for radiotherapy calculations," *Phys. Med. Biol.* **51**, 2253–2265 (2006).

<sup>15</sup> A. C. Tedgren and A. Ahnesjo, "Optimization of the computational efficiency of a 3D, collapsed cone dose calculation algorithm for brachytherapy," *Med. Phys.* **35**, 1611–1618 (2008).

<sup>16</sup> K. Zourari, E. Pantelis, A. Moutsatsos, L. Petrokokkinos, P. Karaiskos, L. Sakelliou, E. Georgiou, and P. Papagiannis, "Dosimetric accuracy of a deterministic radiation transport based <sup>192</sup>Ir brachytherapy treatment planning system. Part I: Single sources and bounded homogeneous geometries," *Med. Phys.* **37**, 649–661 (2010).

<sup>17</sup> G. M. Daskalov, R. S. Baker, D. W. Rogers, and J. F. Williamson, "Multigroup discrete ordinates modeling of <sup>125</sup>I 6702 seed dose distributions using a broad energy-group cross section representation," *Med. Phys.* **29**, 113–124 (2002).

<sup>18</sup> R. M. Thomson and D. W. Rogers, "Monte Carlo dosimetry for <sup>125</sup>I and <sup>103</sup>Pd eye plaque brachytherapy with various seed models," *Med. Phys.* **37**, 368–376 (2010).

<sup>19</sup> S. Yoo, M. E. Kowalok, B. R. Thomadsen, and D. L. Henderson, "Treatment planning for prostate brachytherapy using region of interest adjoint functions and a greedy heuristic," *Phys. Med. Biol.* **48**, 4077–4090 (2003).

<sup>20</sup> S. Yoo, M. E. Kowalok, B. R. Thomadsen, and D. L. Henderson, "A greedy heuristic using adjoint functions for the optimization of seed and needle configurations in prostate seed implant," *Phys. Med. Biol.* **52**, 815–828 (2007).

<sup>21</sup> G. Yang, L. E. Reinstein, S. Pai, Z. Xu, and D. L. Carroll, "A new genetic algorithm technique in optimization of permanent <sup>125</sup>I prostate implants," *Med. Phys.* **25**, 2308–2315 (1998).

<sup>22</sup> H. Hedtjarn, G. A. Carlsson, and J. F. Williamson, "Accelerated Monte Carlo based dose calculations for brachytherapy planning using correlated sampling," *Phys. Med. Biol.* **47**, 351–376 (2002).

<sup>23</sup> A. J. Sampson, J. F. Williamson, Y. Le, and D. Todor, *Presented at the World Congress on Medical Physics and Biomedical Engineering*, Munich, Germany, 2009 (unpublished).

<sup>24</sup> J. F. Williamson and M. J. Rivard, "Thermoluminescent Detector and Monte Carlo Techniques for Reference-Quality Brachytherapy Dosimetry," in *Clinical Dosimetry Measurements in Radiotherapy*, edited by D. Rogers and J. Cygler (Medical Physics Publishing Corporation, Madison, Wisconsin, 2009).

<sup>25</sup> I. Lux and L. Koblinger, *Monte Carlo Particle Transport Methods: Neutron and Photon Calculations* (CRC, Boca Raton, FL, 1991).

<sup>26</sup> H. Hedtjarn, G. A. Carlsson, and J. F. Williamson, "Monte Carlo-aided dosimetry of the Symmetra model 125.S06 <sup>125</sup>I, interstitial brachytherapy seed," *Med. Phys.* **27**, 1076–1085 (2000).

<sup>27</sup> J. F. Williamson, "Monte Carlo evaluation of kerma at a point for photon transport problems," *Med. Phys.* **14**, 567–576 (1987).

<sup>28</sup> J. F. Williamson, "Monte Carlo modeling of the transverse-axis dose distribution of the model 200 <sup>103</sup>Pd interstitial brachytherapy source," *Med. Phys.* **27**, 643–654 (2000).

- <sup>29</sup>J. Sempau, A. Sanchez-Reyes, F. Salvat, H. O. ben Tahar, S. B. Jiang, and J. M. Fernandez-Varea, "Monte Carlo simulation of electron beams from an accelerator head using PENELOPE," *Phys. Med. Biol.* **46**, 1163–1186 (2001).
- <sup>30</sup>Z. Li and J. F. Williamson, "Volume-based geometric modeling for radiation transport calculations," *Med. Phys.* **19**, 667–677 (1992).
- <sup>31</sup>J. P. Pignol, B. Keller, E. Rakovitch, R. Sankrecha, H. Easton, and W. Que, "First report of a permanent breast 103Pd seed implant as adjuvant radiation treatment for early-stage breast cancer," *Int. J. Radiat. Oncol., Biol., Phys.* **64**, 176–181 (2006).
- <sup>32</sup>A. L. Kwan, J. M. Boone, and N. Shah, "Evaluation of x-ray scatter properties in a dedicated cone-beam breast CT scanner," *Med. Phys.* **32**, 2967–2975 (2005).
- <sup>33</sup>N. Packard and J. M. Boone, "Glandular segmentation of cone beam breast CT images," *Proc. SPIE* **6510**, 1–8 (2007).
- <sup>34</sup>T. R. Nelson, L. I. Cervino, J. M. Boone, and K. K. Lindfors, "Classification of breast computed tomography data," *Med. Phys.* **35**, 1078–1086 (2008).
- <sup>35</sup>H. Q. Woodard and D. R. White, "The composition of body tissues," *Br. J. Radiol.* **59**, 1209–1218 (1986).
- <sup>36</sup>M. J. Yaffe, J. M. Boone, N. Packard, O. Alonzo-Proulx, S. Y. Huang, C. L. Peressotti, A. Al-Mayah, and K. Brock, "The myth of the 50-50 breast," *Med. Phys.* **36**, 5437–5443 (2009).
- <sup>37</sup>B. Walters, I. Kawrakow, and D. W. Rogers, Report No. PIRS-794 revB, 2009.
- <sup>38</sup>ICRU, Report No. 44, 1989.
- <sup>39</sup>I. Kawrakow and M. Fippel, "Investigation of variance reduction techniques for Monte Carlo photon dose calculation using XVMC," *Phys. Med. Biol.* **45**, 2163–2183 (2000).
- <sup>40</sup>A. Haghigat and J. C. Wagner, "Monte Carlo variance reduction with deterministic importance functions," *Prog. Nucl. Energy* **42**, 25–53 (2003).
- <sup>41</sup>J. C. Wagner and A. Haghigat, "Automated variance reduction of Monte Carlo shielding calculations using discrete ordinates adjoint function," *Nucl. Sci. Eng.* **128**, 186–208 (1998).
- <sup>42</sup>J. E. Sweezy, Report No. LA-UR-03-1987, 2005.
- <sup>43</sup>E. K. Lee, R. J. Gallagher, D. Silvern, C. S. Wu, and M. Zaider, "Treatment planning for brachytherapy: An integer programming model, two computational approaches and experiments with permanent prostate implant planning," *Phys. Med. Biol.* **44**, 145–165 (1999).
- <sup>44</sup>W. D. D'Souza, R. R. Meyer, B. R. Thomadsen, and M. C. Ferris, "An iterative sequential mixed-integer approach to automated prostate brachytherapy treatment plan optimization," *Phys. Med. Biol.* **46**, 297–322 (2001).
- <sup>45</sup>J. Pouliot, D. Tremblay, J. Roy, and S. Filice, "Optimization of permanent 125I prostate implants using fast simulated annealing," *Int. J. Radiat. Oncol., Biol., Phys.* **36**, 711–720 (1996).
- <sup>46</sup>Y. Yu and M. C. Schell, "A genetic algorithm for the optimization of prostate implants," *Med. Phys.* **23**, 2085–2091 (1996).
- <sup>47</sup>A. Brahme, "Dosimetric precision requirements in radiation therapy," *Acta Radiol. Oncol.* **23**, 379–391 (1984).
- <sup>48</sup>R. E. Taylor, G. Yegin, and D. W. Rogers, "Benchmarking brachydose: Voxel based EGSnrc Monte Carlo calculations of TG-43 dosimetry parameters," *Med. Phys.* **34**, 445–457 (2007).
- <sup>49</sup>G. Yegin, R. E. Taylor, and D. W. Rogers, "BrachyDose: A new fast Monte Carlo code for brachytherapy calculations," *Med. Phys.* **33**, 2074–2075 (2006).
- <sup>50</sup>R. Thomson, G. Yegin, R. Taylor, J. Sutherland, and D. Rogers, "Fast Monte Carlo dose calculations for brachytherapy with BrachyDose," *Med. Phys.* **37**, 3910 (2010).
- <sup>51</sup>D. Terribilini, M. K. Fix, D. Frei, W. Volken, and P. Manser, "VMC++ validation for photon beams in the energy range of 20-1000 keV," *Med. Phys.* **37**, 5218–5227 (2010).
- <sup>52</sup>H. Afsharpour, J. P. Pignol, B. Keller, J. F. Carrier, B. Reniers, F. Verhaegen, and L. Beaulieu, "Influence of breast composition and interseed attenuation in dose calculations for post-implant assessment of permanent breast <sup>103</sup>Pd seed implant," *Phys. Med. Biol.* **55**, 4547–4561 (2010).
- <sup>53</sup>G. Landry, B. Reniers, L. Murrer, L. Lutgens, E. B. Gulp, J. P. Pignol, B. Keller, L. Beaulieu, and F. Verhaegen, "Sensitivity of low energy brachytherapy Monte Carlo dose calculations to uncertainties in human tissue composition," *Med. Phys.* **37**, 5188–5198 (2010).
- <sup>54</sup>F. Verhaegen and S. Devic, "Sensitivity study for CT image use in Monte Carlo treatment planning," *Phys. Med. Biol.* **50**, 937–946 (2005).
- <sup>55</sup>J. F. Williamson, S. Li, S. Devic, B. R. Whiting, and F. A. Lerma, "On two-parameter models of photon cross sections: Application to dual-energy CT imaging," *Med. Phys.* **33**, 4115–4129 (2006).
- <sup>56</sup>G. Landry, P. V. Granton, B. Reniers, M. C. Ollers, L. Beaulieu, J. E. Wildberger, and F. Verhaegen, "Simulation study on potential accuracy gains from dual-energy CT tissue segmentation for low-energy brachytherapy Monte Carlo dose calculations," *Phys. Med. Biol.* **56**, 6257–6278 (2011).

# Appendix C

## 1 Introduction

Cone-beam computed tomography (CBCT) has received widespread reception in radiotherapy and diagnostic imaging over the past decade. For radiotherapy, CBCT is an important tool for patient ridged boney alignment, and in more recent years, CBCT has also gained more reception in operating rooms, breast-dedicated CBCT<sup>1,2</sup>, and dental imaging<sup>3,4</sup>.

CBCT also has potential for image-guided radiotherapy that utilizes deformable image registration and online treatment re-planning. Unfortunately, this application is limited due to constraints on CBCT performance such a high propensity for motion induced artifacts<sup>5</sup>. The most prominent limitation to CBCT is that reconstructed images are plagued with scatter induced artifacts<sup>1,6-8</sup>. These include streaking, loss of contrast, and cupping: all of which are summarized as inaccuracies in the reconstructed Hounsfield unit (HU). These artifacts diminish CBCT image quality and limit the potential of CBCT for quantitative imaging applications and image guided radiotherapy. For example, Weiss *et al*<sup>9</sup> found that inter-operator contouring variability in pelvis scans is significantly greater for CBCT images than for fan-beam computed tomography (FBCT).

The proposed methods to mitigate CBCT scatter effects fall under one of the following three approaches: additional hardware<sup>10-13</sup>, image post-processing<sup>7,14-19</sup>, or a combination between them<sup>20</sup>. Those that require additional hardware, such as beam stop arrays, can be very effective, but have limited application as they require multiple scans, thereby increasing patient dose and/or scanning time. While increased dose may be acceptable in radiotherapy, other applications require dose to be at minimum, such as breast-dedicated CBCT where dose is constrained to that of two-view mammography<sup>2</sup>. More recently, Gao *et al*<sup>20</sup> presented an effective scatter mitigation strategy using primary beam modulation. Though this method is promising, its robustness is hindered by a potential to introduce artifacts caused by strong modulation effects.

Many of the post-processing algorithms are highly approximate and produce inaccurate scatter estimates leading to diminished, instead of increased, image quality. Of the post-processing

algorithms presented to date, the most accurate and robust are those that subtract scatter estimates derived from patient-specific Monte Carlo (MC) simulations<sup>7</sup>. Unfortunately, all the MC solutions advanced to date require too much time for clinical practicality. For the 500-660 projections used in CBCT, the method proposed by Kyriakou *et al* would require 4 to 5.5 hours of CPU time<sup>21</sup>. Mainegra-Hing *et al*<sup>22</sup> proposed a series of variance reduction techniques to overcome the time limitation of MC scatter simulation but were still unsuccessful in realizing acceptable CPU time intervals on clinically available systems. Instead of using VR techniques, a more recent approach to increase computational efficiency involves adaptation of the Monte Carlo approach for graphics processing units (GPU)<sup>23</sup>. Unfortunately, MC particle transport does not map easily to the GPU programming model, yielding only modest gains, and calculational efficiency is highly sensitive to the developer's level of experience<sup>24</sup>.

As with all other scatter subtraction methods, the scatter noise is left causing an increase to the contrast-to-noise ratio. Zhu *et al*<sup>25</sup> has proposed using a penalized weighted least squares algorithm suppress the noise, showing contrast errors following scatter correction and application of their method of less than 2% on average. The scatter noise suppression is not within the scope of our study.

To significantly improve the run-time efficiency of MC computed scatter projections, this study introduces a principled variance reduction (VR) strategy called importance sampling via weight-windowing (ISWW) using a forward-adjoint importance generator (FAIG). We explore its effect on efficiency in computing CBCT scatter projections. Though this method has been routinely used in nuclear engineering for radiation shielding and criticality simulations<sup>26</sup>, to our knowledge this is the first application of this technique in the medical physics community.

## 2 Methods

### 2.1 Importance Sampling

Simulated MC particles can be described by a multi-dimensional phase space vector,

$$\beta_{m,n} = (\mathbf{r}_{m,n}, \Omega_{m,n}, E_{m,n}, W_{m,n}) \quad (1)$$

where  $\mathbf{r}_{m,n}$  represents the spatial location of the  $m^{\text{th}}$  particle's  $n^{\text{th}}$  collision; and  $\Omega_{m,n}$ ,  $E_{m,n}$ , and  $W_{m,n}$  represent the trajectory, energy, and weight respectively of the particle leaving the collision at  $\mathbf{r}_{m,n}$ . Specifically,  $\beta_{m,n}$  represents a collision randomly sampled from probability density functions (PDF's) that describe the radiation transport mechanisms. Importance sampling (IS) consists of sampling  $\beta_{m,n}$  from biased PDF's to drive simulated particles into phase-space regions of greater importance to the estimated detector signal. For example, in CBCT simulations employing purely analog sampling techniques, many low-energy photons are absorbed in the proximal layers of the patient anatomy and never strike the detector. Defining the importance, denoted as  $\Phi^*(\mathbf{P})$ , of a point in phase space,  $\mathbf{P} = (\mathbf{r}, \Omega, E)$ , as the expected contribution from a collision with coordinates  $\mathbf{P}$ , and its progeny, to the detector score, these absorbed photons have limited importance since the likelihood of making a nonzero contribution to the detector is small. Instead, IS biases the sampling of  $\beta_{m,n}$  to regions in  $\mathbf{P}$  that do contribute to the detector score and have a high  $\Phi^*(\mathbf{P})$  value. To remove any bias to the detector score, a particle weight correction factor is applied to  $W_{m,n}$ .

## 2.2 Weight Windows

Systematic splitting/rouletting is an alternate implementation of importance sampling from biased distributions that avoids explicitly drawing random samples from the biased PDF<sup>27-29</sup>. In weight windows (WW), the particle's weight in  $\beta_{m,n}$  is constrained within a certain interval or "window" centered about a desired target value. Figure 1 is an adaptation of Figure 2-24 in the MCNP manual<sup>30</sup> illustrating how weight windowing works. For each point in  $\mathbf{P}$ , the window is defined by an upper and lower bound,  $W_U$  and  $W_L$ , around a targeted weight value,  $W_T$  such that,

$$\begin{aligned}
 C_U &= W_U / W_L \\
 W_L &= 2 \frac{W_T}{1 + C_U} \\
 W_U &= W_L \cdot C_U
 \end{aligned} \tag{2}$$

If the particle's  $W_{m,n}$  is within the window, then it is allowed to pass through freely. For particles that have  $W_{m,n} > W_U$  particles are split into multiple particles, each with a new  $W_{m,n} = W_T$ .

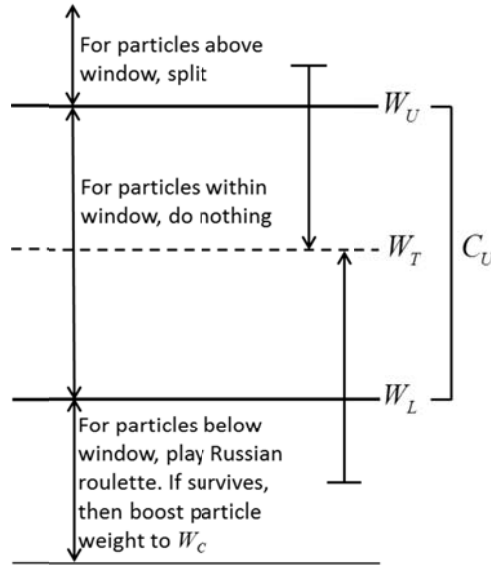


Figure 1: A diagram showing the process of the weight window.

If a particle has  $W_{m,n} < W_L$ , then Russian roulette is played with a surviving probability of  $W_{m,n} / W_T$ . If the particle survives, then  $W_{m,n}$  is set to  $W_T$ . Since this method ultimately conserves particle weight in  $\mathbf{P}$ , it is an unbiased process, thereby allowing the choice of  $W_T$  to be independent of accuracy.

Weight windows can be used for importance sampling by exploiting the property that a particle's weight is inversely proportional to its importance. By setting an appropriate value for  $W_T$  to be inversely proportional to the importance of a point in  $\mathbf{P}$ , efficiency increases of 2 orders of magnitude have been reported, for nuclear engineering applications, relative to the analog case<sup>29</sup>.

### 2.3 Forward-Adjoint Importance Generator

The adjoint function, or flux  $\Phi^*(\mathbf{P})$  (also called the importance), is the solution to the adjoint Boltzmann transport equation (BTE). Unlike the forward-BTE, where the solution is the particle flux  $\Phi(\mathbf{P})$  and tracks particles originating in the photon source  $q(\mathbf{P})$  to the detector scoring function  $f(\mathbf{P})$ , adjoint particles originate from the detector response function  $f(\mathbf{P})$  and undergo transition from lower to higher energy states as they are transported from the detector to

the source. It can be shown that  $\Phi^*(\mathbf{P})$  denotes the importance of a point phase-space to some scoring function,  $f(\mathbf{P})$ <sup>26,29</sup>.

In the forward calculation the detector response,  $R$ , is given as

$$R = \int_{\mathbf{P}} \Phi(\mathbf{P})f(\mathbf{P})d\mathbf{P} \quad (3)$$

We approximate the CBCT detector signal to be proportional to the energy imparted to the CsI scintillator. For this purpose,  $R$  is defined as the energy imparted to each detector pixel integrated over detector area. Similar to eq. (3), it can be shown that,

$$R = \int_{\mathbf{P}} \Phi^*(\mathbf{P})q(\mathbf{P})d\mathbf{P} \quad (4)$$

where  $q(\mathbf{P})$  describes the source in the forward problem. The detector response,  $R$ , can be thought of as a normalization factor for the importance defining the target weight  $W_T$ . It can be shown<sup>26,27</sup> that the optimal value of  $W_T$  of a point in  $\mathbf{P}$ , is defined as:

$$W_T^\dagger(\mathbf{P}) = \frac{R}{\Phi^*(\mathbf{P})} \quad (5)$$

For this relationship to be applied it requires a determination of  $\Phi^*(\mathbf{P})$ ,  $R$ , and knowledge of  $q(\mathbf{P})$ . Under certain circumstances, full and accurate characterization of  $\Phi^*(\mathbf{P})$  leads to a zero variance forward Monte Carlo solution. Computing  $\Phi^*(\mathbf{P})$  often requires the same or greater computational resources as computing the forward flux, thus negating any increase in efficiency. Additionally, sometimes analytical characterization of  $q(\mathbf{P})$  is unknown, such as when utilizing a phase-space source.

Instead of pre-computing  $W_T^\dagger(\mathbf{P})$ , it can be approximated through an online, adaptive method that is very similar to the forward-adjoint importance generator in MCNP<sup>29,30</sup>. First, the phase space,  $\mathbf{P}$ , for the relative importance is discretized into energy and spatial bins where importance is presumed to be constant. Our initial approach neglects any angular dependence of  $W_T^\dagger(\mathbf{P})$ . The normalization factor,  $R$ , is computed as the average scatter score to the flat panel detector per



history. The importance,  $\Phi^*(\mathbf{r}_{ijk}, E_l)$ , of each bin is approximated by the ratio of the average flat-panel detector scatter score from photon collisions in  $(\mathbf{r}_{ijk}, E_l)$ , including all of their progeny, and the total particle weight carried by particles colliding in  $(\mathbf{r}_{ijk}, E_l)$ , independent of angle. In this notation,  $\mathbf{r}_{ijk}$  and  $E_l$  refer to the spatial and energy midpoints of the importance region:  $ijk$  and  $l$  are the importance voxel and energy bin indices respectively. Both  $R$  and  $\Phi^*(\mathbf{r}_{ijk}, E_l)$  are updated each history, while updating  $W_T(\mathbf{r}_{ijk}, E_l)$  occurs every 10 thousand histories to ease computational overhead. We call this process “forward-adjoint importance generator (FAIG),” and computes a Monte Carlo estimate of the expectation value of the importance,  $\Phi^*(\mathbf{r}_{ijk}, E_l)$ . Because of this, there is a level of uncertainty corresponding to each importance cell. In the results, for the final estimated importance function, the average uncertainty of the importance function will be presented.

Since there can be regions of little importance, such as behind a highly attenuating material,  $W_T(\mathbf{r}_{ijk}, E_l)$  can be quite large. In such regions, Russian roulette will occur frequently, with a very slight chance of survival. When survival does occur, the photon will be given an extremely high weight that can cause large deviations in the detector score, potentially increasing statistical uncertainty. To mitigate the deleterious impact of such events on statistical convergence, a maximum allowed  $W_T(\mathbf{r}_{ijk}, E_l)$  value,  $W_{\max}$ , can be set in the PTRAN input file.

The importance function is not initially known; therefore, all target weights are set to a default value,  $0.5 \times W_i$ , where  $W_i$  represents the initial photon weight. These initial weight window target values are used during the first 10% of simulated photon histories, during which the importance map is estimated. Following the first 10% of histories, this early estimate is utilized and updated throughout the simulation as explained above. Additionally, to incorporate some angular biasing, if a photon trajectory does not intersect the flat-panel detector, a weight window with  $W_T = W_{\max}$  is applied.

## 2.4 Implementation and Test Cases

The FAIG process was implemented as an option within the more general low-energy Monte Carlo code family, PTRAN<sup>31-36</sup>, which was recently expanded to simulate CBCT primary and scatter projections<sup>7,37,38</sup>. It is capable of simulating analytical geometries, as well as voxelized patient models derived from single energy CT scans using a modified version of the DOSXYZnrc<sup>39</sup> tool, CTCREATE.

For the CBCT expansion, an expected track length estimator<sup>33</sup> was implemented for the flat-panel detector, allowing any photon to contribute a nonzero score if its extrapolated trajectory intersects the panel. A phase space source model downstream of the bow-tie filter is utilized to mimic an apparent primary source, treating the bow-tie filter scatter as primary. This allows detection of true patient scatter and imitates scatter measurements with a beam-stop array. Because of the absence of high spatial frequency content in the scatter signals<sup>7,25,40</sup>, the  $1024 \times 768$  detector array was approximated to be  $160 \times 120$ ,  $2.5 \times 2.5 \text{ mm}^2$  voxels. Our previous publication, Lazos *et al*<sup>7</sup>, contains the remaining specification of the CBCT geometry implemented in PTRAN.

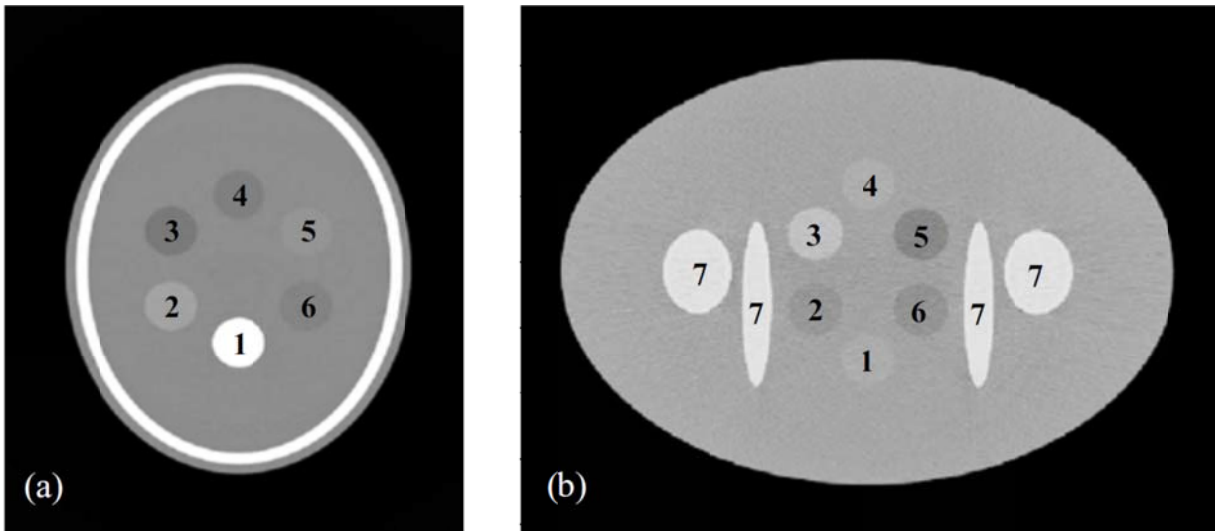


Figure 2: Head (a) and pelvic (b) phantoms used in the study. Contrast inserts for head Phantom: 1, cortical bone; 2, PMMA; 3, lipid; 4, adipose tissue; 5, muscle; and 6, 50/50 breast tissue. Contrast inserts for pelvic phantom: 1, prostate; 2, 50/50 breast tissue; 3, PMMA; 4, muscle; 5, adipose tissue; 6, adipose tissue 2; and 7, bone.

For all our simulations, we used 40 million histories, with a  $W_{\max}$  set to  $3.0 \times W_i$  at a projection angle of  $0^\circ$ , unless otherwise specified. Two phantom cases were considered in our study and presented in Figure 2. First, the simulated, digital head phantom in Figure 2(a), modeled as an

elliptical water cylinder with major and minor axes of 20 cm and 16 cm respectively with a height of 30 cm, was imaged in full-fan geometry. It contains 6 cylindrical contrast inserts with 2 cm diameters. The pelvic phantom in Figure 2(b), also modeled as an elliptical cylinder with major and minor axes of 36 cm and 26 cm respectively, was imaged in half-fan geometry and contains four bony structures and 6 contrast inserts. More details about these phantoms can be found in Lazos *et al*<sup>7</sup>.

## 2.5 Evaluation of Efficiency

The efficiency of the Monte Carlo simulation for pixel  $ik$  on the detector plate is defined as follows and is often referred to as the figure of merit (FOM),

$$FOM_{ik} = \frac{1}{\sigma_{ik}^2 \cdot T} \quad (6)$$

where  $\sigma_{ik}^2$  is the statistical variance of detector pixel with indices  $ik$  (x and z dimensions in the DICOM imaging coordinate system) and  $T$  is the CPU time for the simulation. The efficiency gain,  $G_{ik}$ , is defined as the ratio of  $FOM_{ik}$  for the WW and traditional, non-weight windowed, Monte Carlo (TMC) simulations:

$$G_{ik} = \frac{FOM_{ik}^{WW}}{FOM_{ik}^{TMC}} \quad (7)$$

$G_{ik}$  was computed for each pixel on the detector plate described in the preceding section. The size of the importance spatial and energy grids and the value  $C_U$  were all varied to quantify impact on efficiency. For all calculations, the default values for  $C_U$  and the number of energy bins were 2.0 and 10, respectively, yielding an energy bin width of 12.25 keV, respectively. The default spatial grid resolutions were  $7 \times 9 \times 11$  (voxel size =  $2.3 \times 2.2 \times 2.3 \text{ cm}^3$ ) and  $10 \times 8 \times 7$  (voxel size =  $3.6 \times 3.3 \times 3.6 \text{ cm}^3$ ) for the head and pelvic geometries, respectively. All simulations used these default values, unless they were being varied as indicated. For the head and pelvic phantoms, a rectangular volume just bounding the phantoms was discretized to yield the importance spatial grid.

In addition to computing importance function on the fly, PTRAN is able to use a pre-computed importance function throughout the entire simulation instead of using the forward-adjoint generator described here. This capability was tested for efficiency by using 40 million histories to pre-computing an importance function using FAIG. This pre-computed importance and feeding it back into PTRAN at the start of the simulation. Simulations using these Monte Carlo pre-computed importance maps from FAIG are called “pre-computed”, or PC. Conversely for simulations that compute the importance maps “on-the-fly” using FAIG are called “on-the-fly,” or OTF.

Furthermore, the time necessary to compute the detector signal for a  $40 \times 30$  ( $10 \times 10 \text{ mm}^2$  pixels) with an average 3% uncertainty using PC-FAIG was estimated assuming that statistical uncertainty is inversely proportional to the square root of CPU time. This time value,  $T_{2\%}^{\text{PC-FAIG}}$ , was then used as run time for PC-FAIG, OTF-FAIG, and non-weight windowed Monte Carlo, followed by a comparison of their respective uncertainty distributions.

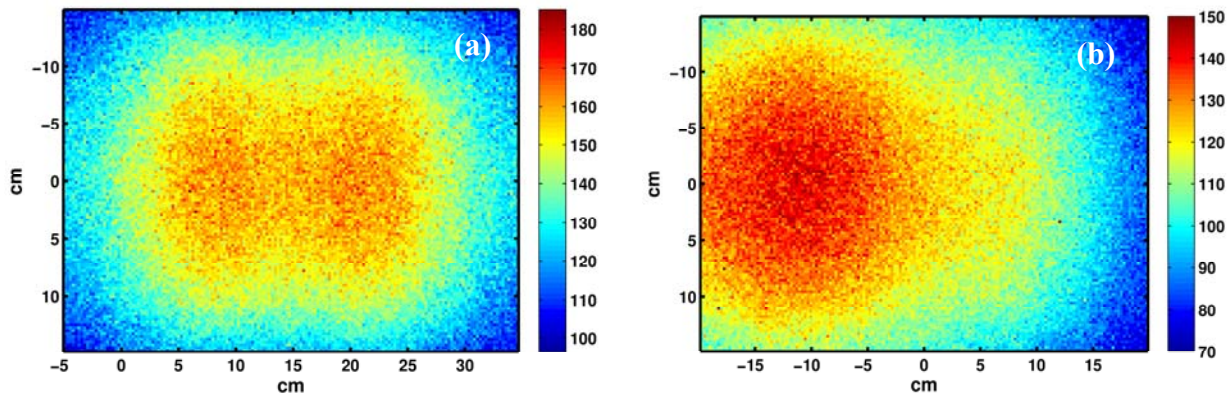


Figure 3: Scatter projection signals (energy absorbed in keV) for the head (a) and body (b) phantoms used in this study. The average uncertainty for both across the detector plate was 3.5%.

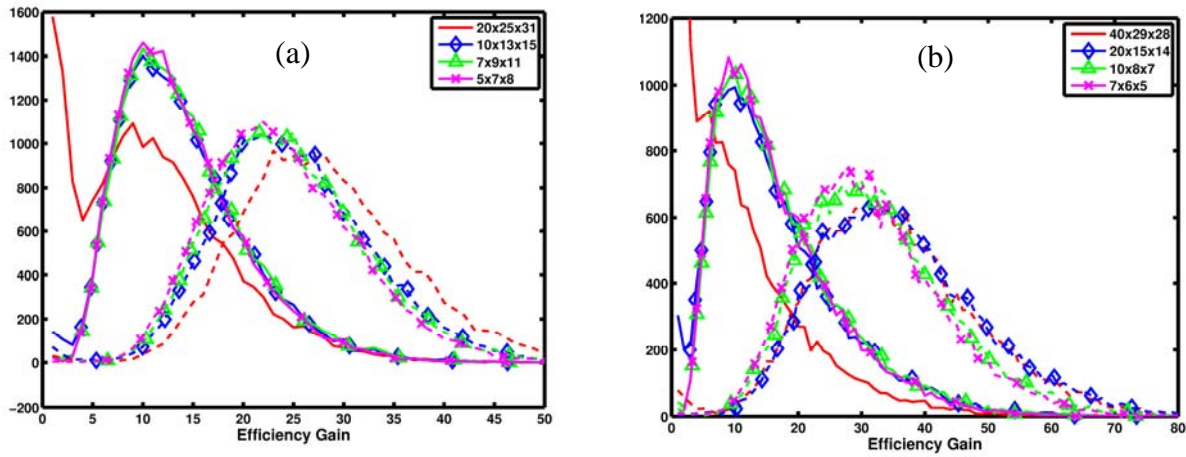


Figure 4: Plots of the efficiency gain for both (a) head and (b) pelvic phantoms using OTF (solid) and PC (dashed) importance functions on various spatial grid sizes.

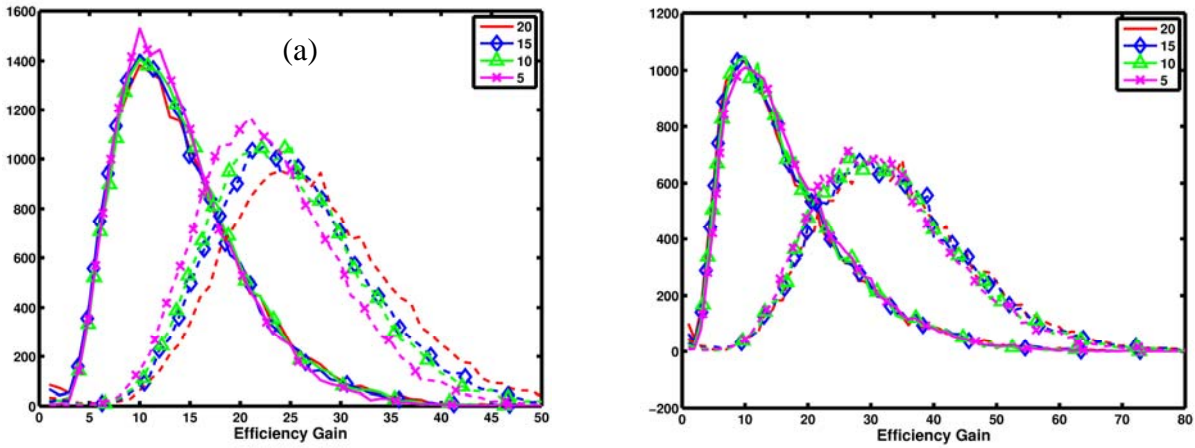


Figure 5: Plots of the efficiency gain for both (a) head and (b) pelvic phantoms using OTF (solid) and PC (dashed) importance functions with different levels of energy discretization.

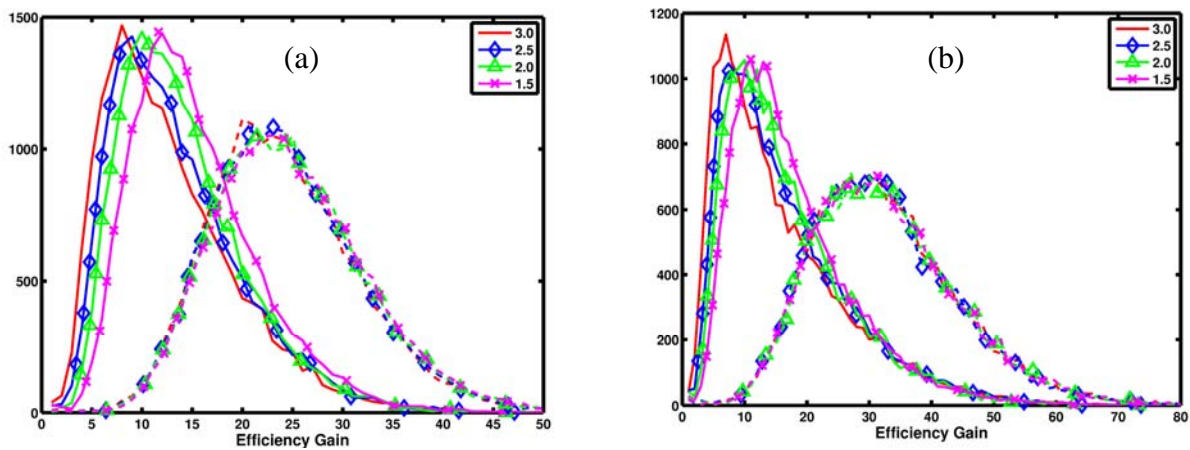


Figure 6: Plots of the efficiency gain for both (a) head and (b) pelvic phantoms using OTF (solid) and PC (dashed) importance function with different values for  $C_U$ .

### 3 Results

The scatter projections, with 3.5% uncertainty, for the head and body phantoms used in this study are shown in Figure 3, and look like previously published data.

Figure 4 shows the distribution of  $G_{ik}$  for both the head and pelvic phantoms when varying the size of the importance spatial cell. Corresponding quantitative metrics for the distributions are found in Table I for the head phantom and Table II for the body phantom. Using OTF, there appears to be no advantage to using higher resolution importance cells. In fact, the highest resolution spatial grid is associated with a large decrease in efficiency compared to TMC. However, when using PC, higher resolution importance cells are associated with larger increases in efficiency, as verified by increase mean and most peak values reported in Table I and Table II.

Effects from varying the number of energy bins from 5 to 20 are shown in Figure 5 and Table I and Table II. The same behavior between the OTF and PC with respect to spatial cell size (Figure 4), is also seen for energy bin width. For both phantoms there appears to be no additional benefit from using more energy bins. Visually inspecting the graphs show that the OTF calculations perform most efficiently with the smallest number of energy bins studied.

Figure 6 contains the plots for varying the WW width,  $C_U$ , from 1.5 to 3.0 and the corresponding distribution metrics are found in Table I and Table II. Varying  $C_U$  does not affect efficiency gain for PC. For the head phantom, the mean and most probable values increased 20% and 56%, respectively, relative to a  $C_U$  value of 3.0. Likewise, for the body phantom, the mean and most probable values increased 12% and 56%, respectively, relative to a  $C_U$  of 3.0. This suggests that when using OTF, a tighter window will be more efficient.

Table I: Quantitative metrics for the efficiency gain distributions shown in Figure 4-Figure 6 for the digital head phantom. Values are listed for the mean, standard deviation about the mean, 20<sup>th</sup> and 80<sup>th</sup> percentiles, and the most probable value (MPV).

Grid Sizes	Mean		Std. Deviation		20 <sup>th</sup> Percentile		80 <sup>th</sup> Percentile		MPV	
	OTF	PC	OTF	PC	OTF	PC	OTF	PC	OTF	PC
20×25×31	10.5	27.5	7.5	8.4	3.7	20.4	16.6	33.9	1.1	22.3
10×13×15	13.4	24.6	6.5	7.8	8.1	18.2	18.3	30.8	9.8	21.5
7×9×11	13.7	24.1	6.4	8.6	8.3	17.7	18.4	30.1	9.9	21.6
5×7×8	13.4	23.5	6.2	7.4	8.2	17.1	18.0	29.5	10.0	20.9
Energy Bins										
20	13.7	26.4	6.7	8.5	8.1	19.3	18.7	33.0	9.9	25.1
15	13.5	24.6	6.4	7.8	8.1	18.0	18.2	30.7	9.8	22.6
10	13.7	24.0	6.4	7.5	8.4	17.6	18.6	30.0	9.9	24.3
5	13.3	22.5	6.0	7.0	8.3	16.5	17.9	28.1	11.2	20.1
$C_U$ Values										
3.0	12.3	23.7	6.7	7.4	6.6	17.4	17.3	29.5	7.6	19.5
2.5	13.0	23.9	6.6	7.5	7.4	17.4	18.0	29.7	8.3	20.8
2.0	13.5	24.1	6.3	7.6	8.2	17.7	18.3	30.1	9.8	21.7
1.5	14.8	24.3	6.3	7.6	9.5	17.8	19.6	30.4	11.1	22.1

Table II: Quantitative metrics for the efficiency gain distributions shown in Figure 4-Figure 6 for the digital pelvic phantom. Values are listed for the mean, standard deviation about the mean, 20<sup>th</sup> and 80<sup>th</sup> percentiles, and the most probable value (MPV).

Grid Sizes	Mean		Std. Deviation		20 <sup>th</sup> Percentile		80 <sup>th</sup> Percentile		MPV	
	OTF	PC	OTF	PC	OTF	PC	OTF	PC	OTF	PC
40×29×28	9.4	34.7	9.7	13.3	1.7	23.7	16.7	45.0	0.4	33.8
20×15×14	16.0	35.6	10.4	13.0	7.5	24.4	23.5	25.7	8.3	33.8
10×8×7	16.6	31.9	10.1	11.7	8.3	21.9	24.0	41.1	9.8	26.0
7×6×5	16.1	30.9	9.6	11.2	8.0	21.4	23.1	39.8	8.4	26.9
Energy Bins										
20	16.3	33.6	10.4	12.5	7.8	23.1	23.7	43.4	8.4	34.2
15	16.4	33.1	10.2	12.2	8.0	22.7	23.7	42.7	8.4	31.1
10	16.4	32.5	10.0	11.8	8.1	22.3	23.6	41.8	9.8	26.6
5	16.7	31.8	9.9	11.6	8.5	21.9	24.0	41.0	9.0	26.0
$C_U$ Values										
3.0	15.3	32.0	10.8	11.7	6.3	22.1	23.2	41.2	6.5	28.9
2.5	16.2	31.9	10.5	11.7	7.4	21.9	23.9	441.1	7.4	31.5
2.0	16.4	32.2	10.0	11.8	8.1	22.1	23.5	41.4	9.3	26.5
1.5	17.2	32.1	9.7	11.8	9.3	22.2	24.1	41.3	10.2	31.2

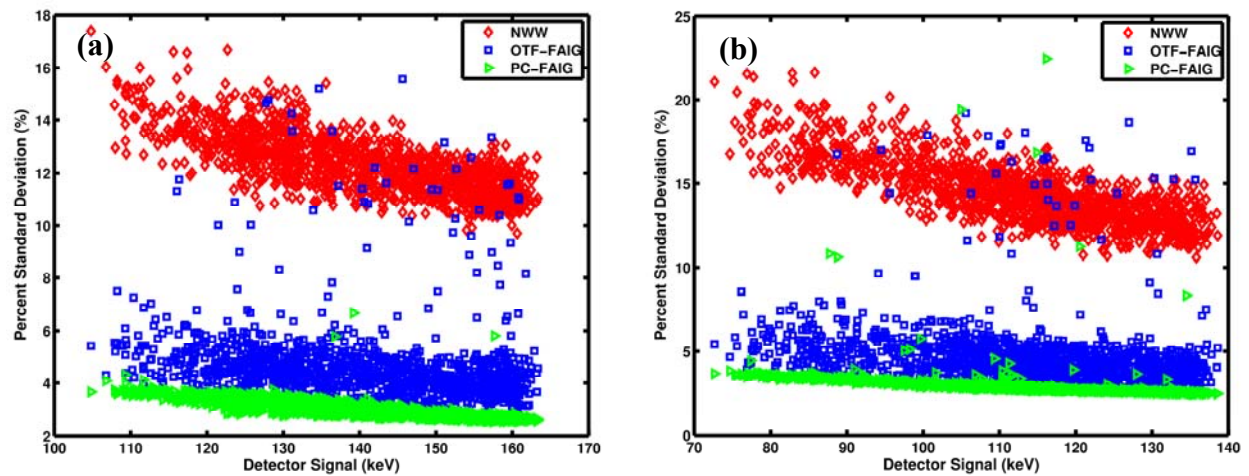


Figure 7: Scatter plots of the percent standard deviation vs. detected signal (keV) for the (a) head and (b) body phantom following a run-time of 37 sec to yield an average 3% uncertainty for PC-FAIG.

Figure 7 shows the distributions of percent standard deviation about the mean using PC-FAIG, OTF-FAIG, and the non-weight windowed, standard Monte Carlo for both the head and body phantoms. The time required for PC-FAIG to achieve a 3% uncertainty, 37 sec, was used as run-time for all three methods. This figure clearly shows the advantage of both OTF and PC-FAIG over the non-weight windowed Monte Carlo. Additionally, there is an additional advantage of PC-FAIG over OTF-FAIG. Table III contains some quantitative descriptors corresponding to the distributions plotted in Figure 7.

Table III: Quantitative metrics corresponding to the distributions plotted in Figure 7 for the head and body phantom.

Case	Mean			Std. Deviation			20 <sup>th</sup> Percentile			80 <sup>th</sup> Percentile			MPV		
	OTF	PC	NWW	OTF	PC	NWW	OTF	PC	NWW	OTF	PC	NWW	OTF	PC	NWW
Head	4.66	3.00	12.3	1.53	0.36	1.14	3.79	2.69	11.31	4.98	3.33	13.30	4.35	2.71	11.89
Body	4.82	2.95	14.42	2.10	1.00	1.87	3.65	2.63	12.81	5.27	3.13	15.87	4.16	2.68	13.05

Table IV: Time benchmarks for OTF-FAIG, PC-FAIG and non-weight windowed (NWW) Monte Carlo for two different pixel sizes for the head and body phantoms. Default importance grids were used.

Case	Time Required for Average 3% Uncertainty			Time Required for Average 10% Uncertainty		
	OTF	PC	NWW	OTF	PC	NWW
Head (pixel area)						
10×10 mm <sup>2</sup>	89.5 sec	37.1 sec	10.6 min	8.1 sec	3.3 sec	60.0 sec
2.5×2.5 mm <sup>2</sup>	14.1 min	7.4 min	2.9 hrs	76.0 sec	40.2 sec	15.5 min
Body (pixel area)						
10×10 mm <sup>2</sup>	100.3 sec	36.9 sec	14.4 min	9.0 sec	3.2 sec	77.9 sec
2.5×2.5 mm <sup>2</sup>	17.0 min	7.4 min	3.82 min	92.0 sec	40.1 sec	20.7 min



Table IV contains the amount of time required by each method (OTF-FAIG, PC-FAIG, and NWW-MC) to reach an average 3% and 10% statistical uncertainty for both phantoms projected onto  $10 \times 10 \text{mm}^2$  and  $2.5 \times 2.5 \text{mm}^2$  pixels. The default importance grids were used for these calculations. It was found that only both OTF and PC-FAIG can compute scatter projections in fewer than 10 sec, only 3.3 sec for PC-FAIG, if 10% uncertainty was enough with a  $10 \times 10 \text{mm}^2$  pixel area.

While Figure 4 and Figure 7 and Table III-Table IV demonstrate an obvious gain from using PC importance function over OTF-OTF-FAIG in general, such pre-computed importance maps will not be available. OTF-FAIG is more appropriate in this scenario. However, some of the benefits of PC can be salvaged when computing scatter projections for consecutive angles. For example, On the first angle,  $\alpha_0$ , use OTF-FAIG to compute the importance function corresponding to  $\alpha_0$ ,  $\Phi^*(\mathbf{P})_{\alpha_0}$ , and also to bias the photon transport for the projection corresponding to  $\alpha_0$ . On the next angle,  $\alpha_1$ , use the pre-computed importance function,  $\Phi^*(\mathbf{P})_{\alpha_0}$ , to bias the transport for the projection corresponding to  $\alpha_1$ , but use OTF-FAIG to compute  $\Phi^*(\mathbf{P})_{\alpha_1}$ . Though  $\Phi^*(\mathbf{P})_{\alpha_1}$  corresponds to the projection taken at angle  $\alpha_1$ , it is then used to bias the transport of  $\alpha_2$  while OTF-FAIG produces  $\Phi^*(\mathbf{P})_{\alpha_2}$  to be used for  $\alpha_3$  and so on. This process is repeated for all the angles simulated we call it prior-angle FAIG, PA-FAIG. To improve the statistics in the computed importance functions, it may be desirable to average the last two or three previous projections' importance maps, to bias the transport of particles corresponding to the current projection, to reduce statistical noise in the importance function. We have taken this approach and averaged the last two previous importance functions to bias the transport of the projection being currently simulated.

Figure 8 contains the average efficiency gain for each of 90 projections uniformly spaced around a 360 degree arc using both OTF-FAIG and PA-FAIG. The default spatial grids were used along with 5 energy bins to decrease the statistical uncertainty of the importance function. Four million histories were used for each projection and a  $C_U = 1.5$ . Figure 8 shows that using PA-FAIG increases the efficiency beyond the gains achieved solely by OTF. The lower efficiency of the first gantry-angle computation is due to using the OTF-FAIG method for that angle. Compared

to the mean efficiency gains in Figure 4Figure 6 for PC-FAIG, our approximate FAIG technique exhibits efficiency gains only 70% as large, due to the extra overhead incurred by computing its own importance map for the next projection's use. Taking this overhead into account, re-use of the previous projection's importance function for the current angle is still more than twice as fast as solely using the OTF-FAIG.

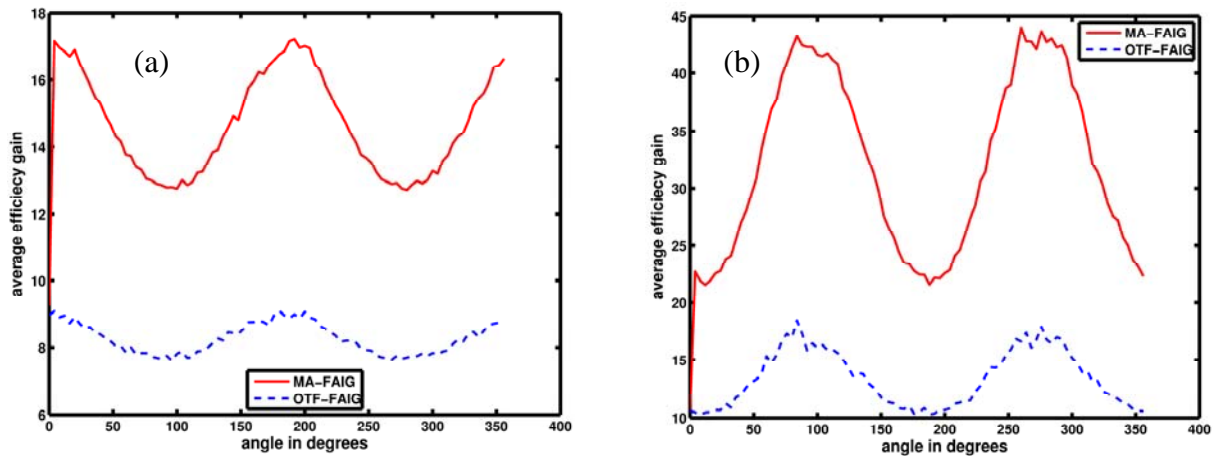


Figure 8: plots of the average efficiency gain for the (a) head and (b) pelvic phantom around a 360 degree rotation. Each projection uses an average importance function from the two projections preceding it.

Figure 9 shows the relationship between phantom thicknesses as the gantry is rotated and average efficiency gain using MA-FAIG and OTF-FAIG for both the head and body phantoms. This relationship is plotted separately for each quadrant of the unit circle. For MA-FAIG, Figure 9 shows a slight efficiency advantage in quadrants 2 and 4 for the head phantom and quadrants 1 and 3 for the body phantom.

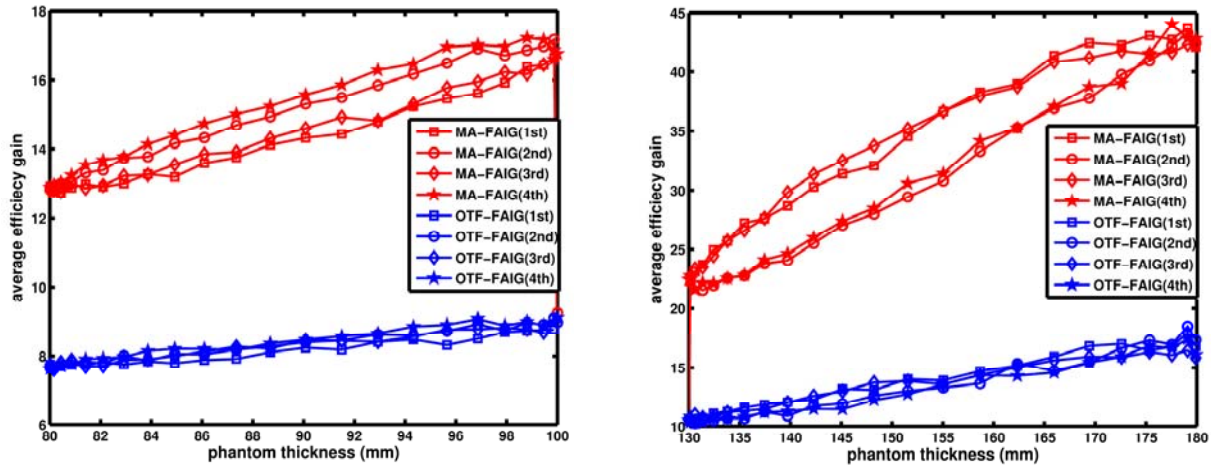


Figure 9: Plotting the average efficiency gain using MA-FAIG (red) and OTF-FAIG (blue) vs. head (a) and body (b) phantom thickness for each quadrant of the unit circle.

## 4 Discussion

Significant gains in computing accurate scatter projections via the Monte Carlo method using the forward-adjoint importance generator were achieved. Additionally, we found that using a “pre-computed” importance function more than doubled the gains, on average, achieved by the “on-the-fly” generator. Though it is uncommon in practice to have such prior knowledge of the importance function, a method was presented, called MA-FAIG, that approximates the projection’s importance function to be the same as the importance function for the previous projection. It was found that MA-FAIG was able to achieve gains close to PC-FAIG. Furthermore, Figure 8 and Figure 9 suggests that our implementation of FAIG is also more efficient as the effective radiological path-length through the patient increases, thus adding additional efficiency for larger patients.

To compare with other published methods, Mainegra-Hing *et al*<sup>22</sup> reported 512 sec to reach an average 10% standard deviation for a  $256 \times 256$  grid for their chest phantom. Using the best combination of our methods, under the same circumstances, only 180 sec for either phantom is required to reach the same level of uncertainty. In practice, since scatter is a slowly varying function, only  $40 \times 30$  detector pixels would need to be simulated<sup>7</sup>. If aiming for an average of 3% standard deviation, only 37 sec for either phantom is required per projection. If only 180 angles were required to characterize the patient scatter in 360 degrees, interpolating the missing angles, and taking advantage of today’s parallel processing power with 8 CPU cores, this

calculation would only require 14 min of MC. On the other hand, Colijn *et al*<sup>15</sup> were able to recover smooth and accurate CBCT projections from noisy data after applying a smoothing filter suggesting that 10% uncertainty would be acceptable. Under these circumstances, OTF- and PC-FAIG would only require 3.0 min and 1.25 min, respectively, using the  $40 \times 30$  detector grid and 180 angles simulated.

Further improvements in the WW efficiency could be achieved through the application of fast, efficient solution to the adjoint-BTE through use of the discrete-ordinate-method (DOM) to pre-compute a non-statistical estimate for  $\Phi^*(\mathbf{r}_{ijk}, E_l)$  and could even include angular biasing. This would unleash the full power of our WW scheme by using more optimal values for  $W_T(\mathbf{r}_{ijk}, E_l)$  throughout the entire simulation and not having to rely on OTF-FAIG to estimate  $\Phi^*(\mathbf{r}_{ijk}, E_l)$ .

## 5 Conclusion

We have demonstrated that importance based weight windowing is a powerful tool that results in 10-35 fold improvements in average efficiency relative to conventional Monte Carlo methods for CBCT simulations. Furthermore, we have shown that our forward-adjoint importance generator is effective in computing the importance function both for “on-the-fly” calculations and for reuse as a pre-computed importance function. Even using importance functions corresponding to a nearby angle was effective in improving the efficiency a projection at a different angle. To fully quantify the efficiency gain for a patient population, further study needs to be done on patient geometries.

## 6 References

- <sup>1</sup>A. L. Kwan, J. M. Boone, and N. Shah, "Evaluation of x-ray scatter properties in a dedicated cone-beam breast CT scanner," *Med Phys* **32** (9), 2967-75 (2005).
- <sup>2</sup>J. M. Boone, A. L. Kwan, J. A. Seibert, N. Shah, K. K. Lindfors, and T. R. Nelson, "Technique factors and their relationship to radiation dose in pendant geometry breast CT," *Med Phys* **32** (12), 3767-76 (2005).
- <sup>3</sup>A. Suomalainen, T. Kiljunen, Y. Kaser, J. Peltola, and M. Kortensniemi, "Dosimetry and image quality of four dental cone beam computed tomography scanners compared with multislice computed tomography scanners," *Dentomaxillofac Radiol* **38** (6), 367-78 (2009).
- <sup>4</sup>P. Mozzo, C. Procacci, A. Tacconi, P. T. Martini, and I. A. Andreis, "A new volumetric CT machine for dental imaging based on the cone-beam technique: preliminary results," *Eur Radiol* **8** (9), 1558-64 (1998).
- <sup>5</sup>D. A. Jaffray and J. H. Siewerdsen, "Cone-beam computed tomography with a flat-panel imager: initial performance characterization," *Med Phys* **27** (6), 1311-23 (2000).
- <sup>6</sup>J. H. Siewerdsen and D. A. Jaffray, "Cone-beam computed tomography with a flat-panel imager: magnitude and effects of x-ray scatter," *Med Phys* **28** (2), 220-31 (2001).
- <sup>7</sup>D. Lazos and J. F. Williamson, "Monte Carlo evaluation of scatter mitigation strategies in cone-beam CT," *Med Phys* **37** (10), 5456-70 (2010).
- <sup>8</sup>Y. Chen, B. Liu, J. M. O'Connor, C. S. Didier, and S. J. Glick, "Characterization of scatter in cone-beam CT breast imaging: comparison of experimental measurements and Monte Carlo simulation," *Med Phys* **36** (3), 857-69 (2009).
- <sup>9</sup>E. Weiss, J. Wu, W. Sleeman, J. Bryant, P. Mitra, M. Myers *et al.*, "Clinical evaluation of soft tissue organ boundary visualization on cone-beam computed tomographic imaging," *Int J Radiat Oncol Biol Phys* **78** (3), 929-36 (2010).
- <sup>10</sup>Y. Kyriakou and W. Kalender, "Efficiency of antiscatter grids for flat-detector CT," *Phys Med Biol* **52** (20), 6275-93 (2007).

- <sup>11</sup>J. H. Siewerdsen, D. J. Moseley, B. Bakhtiar, S. Richard, and D. A. Jaffray, "The influence of antiscatter grids on soft-tissue detectability in cone-beam computed tomography with flat-panel detectors," *Med Phys* **31** (12), 3506-20 (2004).
- <sup>12</sup>R. Ning, X. Tang, and D. Conover, "X-ray scatter correction algorithm for cone beam CT imaging," *Med Phys* **31** (5), 1195-202 (2004).
- <sup>13</sup>L. Zhu, Y. Xie, J. Wang, and L. Xing, "Scatter correction for cone-beam CT in radiation therapy," *Med Phys* **36** (6), 2258-68 (2009).
- <sup>14</sup>M. C. Altunbas, C. C. Shaw, L. Chen, C. Lai, X. Liu, T. Han *et al.*, "A post-reconstruction method to correct cupping artifacts in cone beam breast computed tomography," *Med Phys* **34** (7), 3109-18 (2007).
- <sup>15</sup>A. P. Colijn and F. J. Beekman, "Accelerated simulation of cone beam X-ray scatter projections," *IEEE Trans Med Imaging* **23** (5), 584-90 (2004).
- <sup>16</sup>I. Reitz, B. M. Hesse, S. Nill, T. Tucking, and U. Oelfke, "Enhancement of image quality with a fast iterative scatter and beam hardening correction method for kV CBCT," *Z Med Phys* **19** (3), 158-72 (2009).
- <sup>17</sup>G. Poludniowski, P. M. Evans, V. N. Hansen, and S. Webb, "An efficient Monte Carlo-based algorithm for scatter correction in keV cone-beam CT," *Phys Med Biol* **54** (12), 3847-64 (2009).
- <sup>18</sup>M. Meyer, W. A. Kalender, and Y. Kyriakou, "A fast and pragmatic approach for scatter correction in flat-detector CT using elliptic modeling and iterative optimization," *Phys Med Biol* **55** (1), 99-120 (2010).
- <sup>19</sup>J. H. Siewerdsen, M. J. Daly, B. Bakhtiar, D. J. Moseley, S. Richard, H. Keller *et al.*, "A simple, direct method for x-ray scatter estimation and correction in digital radiography and cone-beam CT," *Med Phys* **33** (1), 187-97 (2006).
- <sup>20</sup>H. Gao, R. Fahrig, N. R. Bennett, M. Sun, J. Star-Lack, and L. Zhu, "Scatter correction method for x-ray CT using primary modulation: phantom studies," *Med Phys* **37** (2), 934-46 (2010).

- <sup>21</sup>Y. Kyriakou, T. Riedel, and W. A. Kalender, "Combining deterministic and Monte Carlo calculations for fast estimation of scatter intensities in CT," *Phys Med Biol* **51** (18), 4567-86 (2006).
- <sup>22</sup>E. Mainegra-Hing and I. Kawrakow, "Variance reduction techniques for fast Monte Carlo CBCT scatter correction calculations," *Phys Med Biol* **55** (16), 4495-507 (2010).
- <sup>23</sup>A. Badal and A. Badano, "Accelerating Monte Carlo simulations of photon transport in a voxelized geometry using a massively parallel graphics processing unit," *Med Phys* **36** (11), 4878-80 (2009).
- <sup>24</sup>G. Prax and L. Xing, "GPU computing in medical physics: a review," *Med Phys* **38** (5), 2685-97 (2011).
- <sup>25</sup>L. Zhu, J. Wang, and L. Xing, "Noise suppression in scatter correction for cone-beam CT," *Med Phys* **36** (3), 741-52 (2009).
- <sup>26</sup>J. C. Wagner and A. Haghghat, "Automated Variance Reduction of Monte Carlo Shielding Calculations Using Discrete Ordinates Adjoint Function," *Nuclear Science and Engineering* **128**, 186-208 (1998).
- <sup>27</sup>A. Haghghat and J. C. Wagner, "Monte Carlo Variance Reduction with Deterministic Importance Functions," *Progress in Nuclear Energy* **42**, 25-53 (2003).
- <sup>28</sup>I. Lux and L. Koblinger, *Monte Carlo Particle Transport Methods: Neutron and Photon Calculations* (CRC Press, Boca Raton, FL, 1991).
- <sup>29</sup>T. Booth, "A Weight Window/Importance Generator for Monte Carlo Streaming Problems," in *Sixth International Conference on Radiation Shielding* (Tokyo, Japan, 1983).
- <sup>30</sup>J. E. Sweezy, "MCNP-A General Monte Carlo N-particle Transport Code, Version 5," Report No. LA-UR-03-1987, Los Alamos National Laboratory, Los Alamos, NM, 2005.
- <sup>31</sup>A. Sampson, Y. Le, and J. F. Williamson, "Fast patient-specific Monte Carlo brachytherapy dose calculations via the correlated sampling variance reduction technique," *Med Phys* **39** (2), 1058-68 (2012).

- <sup>32</sup>Z. Li and J. F. Williamson, "Volume-based geometric modeling for radiation transport calculations," *Med Phys* **19** (3), 667-77 (1992).
- <sup>33</sup>J. F. Williamson, "Monte Carlo evaluation of kerma at a point for photon transport problems," *Med Phys* **14** (4), 567-76 (1987).
- <sup>34</sup>J. I. Monroe and J. F. Williamson, "Monte Carlo-aided dosimetry of the theragenics TheraSeed model 200 103Pd interstitial brachytherapy seed," *Med Phys* **29** (4), 609-21 (2002).
- <sup>35</sup>J. Dolan, Z. Lia, and J. F. Williamson, "Monte Carlo and experimental dosimetry of an 1251 brachytherapy seed," *Med Phys* **33** (12), 4675-84 (2006).
- <sup>36</sup>O. Chibani and J. F. Williamson, "MCPI: a sub-minute Monte Carlo dose calculation engine for prostate implants," *Med Phys* **32** (12), 3688-98 (2005).
- <sup>37</sup>D. Lazos and J. F. Williamson, "Impact of flat panel-imager veiling glare on scatter-estimation accuracy and image quality of a commercial on-board cone-beam CT imaging system," *Med Phys* **39** (9), 5639-51 (2012).
- <sup>38</sup>D. Zheng, J. C. Ford, J. Lu, D. Lazos, G. D. Hugo, D. Pokhrel *et al.*, "Bow-tie wobble artifact: effect of source assembly motion on cone-beam CT," *Med Phys* **38** (5), 2508-14 (2011).
- <sup>39</sup>B. Walters, I. Kawrakow, and D. W. Rogers, "DOSXYZnrc User Manual," Report No. PIRS-794 revB, Ionizing Radiation Standards, National Research Council of Canada, 2009.
- <sup>40</sup>J. H. Siewerdsen and D. A. Jaffray, "Optimization of x-ray imaging geometry (with specific application to flat-panel cone-beam computed tomography)," *Med Phys* **27** (8), 1903-14 (2000).



# Appendix D

```
close all;
more off;
clc;

%This matlab code will help me to form the grid structure of my
% PARTISN calculations. ALL DISTANCES ARE IN CM!!!
% This has now been expanded to write the input file in general,
% and NOT JUST the geometry. This now writes the entire input file.

COMPUTE_GEOMETRY = 1;
if COMPUTE_GEOMETRY
    clear all;
    octave = 0;
    fprintf('hello, I have begun\n')
%Set the projection angle
projAngle = 0.0*pi/180.0;

%Set the outside boundaries of the PARTISN calculation. These
% bounds bound the PARTISN geometry and are the the literally bounds
% for the coarse grid.
xBoundStart = -19.8656;
xBoundEnd = 19.8656;
zBoundStart = -100.0000;
zBoundEnd = 50.0600;
yBoundStart = -14.8992;
yBoundEnd = 14.8992;

%Set the bounds for the object to be imaged within the coarse
% bounds. These will define the structure of the coarse grid within
% that which is important.

xObjectStart = -10.0000;
xObjectEnd = 10.0000;
zObjectStart = -10.0000;
zObjectEnd = 10.0000;
yObjectStart = -12.5000;
yObjectEnd = 12.5000;

%Decide how many voxels you would like in each dimension for the
```

```
% object being imaged
%Fine Grid
NxObject = 31; %(Must be an odd number to localize the forward source)
NzObject = 21; %(Can be either odd or even)
NyObject = 21; %(Must be an odd number to localize the forward source)
% $$$ %Coarse Grid
% $$$ NxObject = 11; %(Must be an odd number to localize the forward source)
% $$$ NzObject = 11; %(Can be either odd or even)
% $$$ NyObject = 11; %(Must be an odd number to localize the forward source)

%Define the voxel thicknesses
dxObject = (xObjectEnd-xObjectStart)/NxObject;
dzObject = (zObjectEnd-zObjectStart)/NzObject;
dyObject = (yObjectEnd-yObjectStart)/NyObject;

%Now at the top of the simulation universe, I need to create
% another extra line in y, so that I can isolate the voxel that
% source is located in.
sourceLineThickness = dzObject;

%Information needed for the detector plate
detectPlateThickness = 0.06;

%AJS 05 Dec 2012
% Describe the y extents of the Bowtie (BT) filter.
zBTStart = -85.0;
zBTEnd = -80.0;
NzBowtie = 20; %FG
% $$$ NzBowtie = 3; %CG
dzBT = (zBTEnd-zBTStart)/NzBowtie;

%Now, would you like to have any other "extra" grid lines in the
% dimensions before and after the object grid. The object grid is
% defined by the '*ObjectStart', '*ObjectEnd', and the 'N*'
% variables. These variables tell me how many voxels you would like
% in each dimension before and after the object grid. It would set
% up the grid lines evenly spaced. It is defined seperately for
% before, the object (relative to the consecutive number line) or
% after the object. This seperation helps facilitate the half fan
% geometry.
```

```
%AJS 05 Dec 2012
% it is importance to remember that the y and z axes are switched
% in PARTISN from the their corresponding axes in the PTRAN geometry.

%AJS 06 Dec 2012
% To include the BT filter, I need to add another section where I
% can solely define the grid spacing. The following will reflect the
% changes.

%Fine Grid
NxBeforeBound = 5;
NzBeforeBTBound = 7;
NyBeforeBound = 5;

NzBetween = 30;

NxAfterBound = 5;
NzAfterBound = 20;
NyAfterBound = 5;

%Coarse Grid
% $$$ NxBeforeBound = 2; %CG
% $$$ NzBeforeBTBound = 2; %CG
% $$$ NyBeforeBound = 2; %CG
% $$$
% $$$ NzBetween = 7; %CG
% $$$
% $$$ NxAfterBound = 2; %CG
% $$$ NzAfterBound = 5; %CG
% $$$ NyAfterBound = 2; %CG

%Now decide whether or not you're going to use the BT filter
bowtie = 1;

%Now it is time to define the thickness of these voxels
dxBeforeBound = (xObjectStart-xBoundStart)/NxBeforeBound;
dzBeforeBTBound = (zBTStart-(zBoundStart+sourceLineThickness))/NzBeforeBTBound;
dyBeforeBound = (yObjectStart-yBoundStart)/NyBeforeBound;

if(bowtie)
    dzBetween = (zObjectStart-zBTEnd)/NzBetween;
```

```

else
    dzBetween      = (zObjectStart-zBoundStart)/NzBetween;
end

dxAfterBound  = (xBoundEnd-xObjectEnd)/NxAfterBound;
dzAfterBound  = (zBoundEnd-zObjectEnd-detectPlateThickness)/NzAfterBound;
dyAfterBound  = (yBoundEnd-yObjectEnd)/NyAfterBound;

%Now it is time to define the x grid
xGrid = zeros(NxBeforeBound+NxAfterBound+NxObject+1,1);
xGrid(1:NxBeforeBound+1) = xBoundStart:dxBeforeBound:xObjectStart;
xGrid(NxBeforeBound+1:NxBeforeBound+NxObject+1) = xObjectStart: ...
    dxObject:xObjectEnd;
xGrid(NxBeforeBound+NxObject+1:NxBeforeBound+NxAfterBound+NxObject+1) = ...
    xObjectEnd:dxAfterBound:xBoundEnd;

%Now it is time to define the z grid
yGrid = zeros(NyBeforeBound+NyAfterBound+NyObject+1,1);
yGrid(1:NyBeforeBound+1) = yBoundStart:dyBeforeBound:yObjectStart;
yGrid(NyBeforeBound+1:NyBeforeBound+NyObject+1) = yObjectStart: ...
    dyObject:yObjectEnd;
yGrid(NyBeforeBound+NyObject+1:NyBeforeBound+NyAfterBound+NyObject+1) = ...
    yObjectEnd:dyAfterBound:yBoundEnd;

%Now the yGrid works a little differently because of the "extra"
% lines associated with the source and detector
if(bowtie)
    zGrid = zeros(2+NzBeforeBTBound+NzAfterBound+NzObject+1+NzBetween+NzBowtie,1);
    zGrid(1) = zBoundStart;
    zGrid(2:NzBeforeBTBound+2) ...
        = zBoundStart+sourceLineThickness:dzBeforeBTBound:zBTStart;
    zGrid(NzBeforeBTBound+2:...
        NzBeforeBTBound+2+NzBowtie) ...
        = zBTStart:dzBT:zBTEnd;
    zGrid(NzBeforeBTBound+2+NzBowtie:...
        NzBeforeBTBound+2+NzBowtie+NzBetween) ...
        = zBTEnd:dzBetween:zObjectStart;
    zGrid(NzBeforeBTBound+2+NzBowtie:...
        NzBeforeBTBound+2+NzBowtie+NzBetween) ...
        = zBTEnd:dzBetween:zObjectStart;
    zGrid(NzBeforeBTBound+2+NzBowtie+NzBetween:...

```

```

    NzBeforeBTBound+2+NzBowtie+NzBetween+NzObject) ...
    = zObjectStart:dzObject:zObjectEnd;
zGrid(NzBeforeBTBound+2+NzBowtie+NzBetween+NzObject:...
    NzBeforeBTBound+2+NzBowtie+NzBetween+NzObject+NzAfterBound) = ...
    zObjectEnd:dzAfterBound:zBoundEnd-detectPlateThickness;
zGrid(end) = zBoundEnd;
else
zGrid = zeros(NzBeforeBTBound+NzAfterBound+NzObject+1+NzBetween+NzBowtie,1);
zGrid(1:...
    NzBeforeBTBound+1+NzBowtie+NzBetween) ...
    = zBoundStart:dzBetween:zObjectStart;
zGrid(NzBeforeBTBound+1+NzBowtie+NzBetween:...
    NzBeforeBTBound+1+NzBowtie+NzBetween+NzObject) ...
    = zObjectStart:dzObject:zObjectEnd;
zGrid(NzBeforeBTBound+1+NzBowtie+NzBetween+NzObject:...
    NzBeforeBTBound+1+NzBowtie+NzBetween+NzObject+NzAfterBound) = ...
    zObjectEnd:dzAfterBound:zBoundEnd;
end

%*****
%*****
%AJ5 05 Dec 2012
%I wonder if I could set up a little diddy here and plot out
% what the grid actually looks like.
% We could do this bt planes
figure
%x-y plane (in PTRAN)
hold on
for j=1:length(zGrid)
    plot([xGrid(1) xGrid(end)], [zGrid(j) zGrid(j)], 'b-', 'LineWidth', 2);
end
for i=1:length(xGrid)
    plot([xGrid(i) xGrid(i)], [zGrid(1) zGrid(end)], 'b-', 'LineWidth', 2);
end
set(gca, 'LineWidth', 2, 'FontSize', 12, 'FontWeight', 'demi');
axis image
title('x-y plane')
% $$$ set(h_title, 'FontSize', 16, 'FontWeight', 'demi');
xlabel('x-axis (cm)')
% $$$ set(h_xlab, 'FontSize', 16, 'FontWeight', 'demi');
ylabel('y-axis (cm)')
% $$$ set(h_ylab, 'FontSize', 16, 'FontWeight', 'demi');

```

```
hold off

figure
%x-z plane (in PTRAN)
hold on
for j=1:length(yGrid)
    plot([xGrid(1) xGrid(end)], [yGrid(j) yGrid(j)], 'b-', 'LineWidth', 2);
end
for i=1:length(xGrid)
    plot([xGrid(i) xGrid(i)], [yGrid(1) yGrid(end)], 'b-', 'LineWidth', 2);
end
set(gca, 'LineWidth', 2, 'FontSize', 12, 'FontWeight', 'demi');
axis image
title('x-z plane')
% $$$ set(h_title, 'FontSize', 16, 'FontWeight', 'demi');
xlabel('x-axis (cm)')
% $$$ set(h_xlab, 'FontSize', 16, 'FontWeight', 'demi');
ylabel('z-axis (cm)')
% $$$ set(h_ylab, 'FontSize', 16, 'FontWeight', 'demi');
hold off

figure
%z-y plane (in PTRAN)
hold on
for j=1:length(zGrid)
    plot([yGrid(1) yGrid(end)], [zGrid(j) zGrid(j)], 'b-', 'LineWidth', 2);
end
for k=1:length(yGrid)
    plot([yGrid(k) yGrid(k)], [zGrid(1) zGrid(end)], 'b-', 'LineWidth', 2);
end
set(gca, 'LineWidth', 2, 'FontSize', 12, 'FontWeight', 'demi');
axis image
title('z-y plane')
% $$$ set(h_title, 'FontSize', 16, 'FontWeight', 'demi');
xlabel('z-axis (cm)')
% $$$ set(h_xlab, 'FontSize', 16, 'FontWeight', 'demi');
ylabel('y-axis (cm)')
% $$$ set(h_ylab, 'FontSize', 16, 'FontWeight', 'demi');
hold off
% $$$
% $$$ asdf;
%*****
```

```
%*****
```

```
%Now that I have the grid set up, I need to set up the "zones"
% variable. The "zones" variable is basically a 3 dimensional
% structure that contains all the cross-section material
% assignment. The materials are automatically numbered in PARTISN
% based on order of appearance in the input file. For our purposes,
% I (AJS) have decided that "air" is the first material in the
% input file and this is what "zones" is initialized with.
```

```
%First, initialize the size of "zones" with "ones" to set the
%default value to "air". Now notice that zones is sized by the
%number of voxels, and not the number of grid lines, like the
%"*Grid" variables are.
```

```
if(bowtie)
    zones = ones(NxBeforeBound+NxAfterBound+NxObject,...
                NyBeforeBound+NyAfterBound+NyObject,...
                2+NzBeforeBTBound+NzAfterBound+NzObject+NzBetween+ ...
                NzBowtie);
else
    zones = ones(NxBeforeBound+NxAfterBound+NxObject,...
                NyBeforeBound+NyAfterBound+NyObject,...
                NzBeforeBTBound+NzAfterBound+NzObject+NzBetween+ ...
                NzBowtie);
end
%Air is material #3;
zones(:,:,:) = zones(:,:,:)*3; %Set it to air
```

```
[NxMax,NyMax,NzMax] = size(zones);
```

```
%Now to compute some help here, I need to have an array that holds
%the centroid for all the voxels. I will need a separate one for
%the x, y, and the z.
```

```
xCentroid = 0.0*zones;
yCentroid = 0.0*zones;
zCentroid = 0.0*zones;
```

```
xCentroid = (xGrid(2:NxMax+1)-xGrid(1:NxMax+1-1))*0.5+xGrid(1:NxMax+1-1);
yCentroid = (yGrid(2:NyMax+1)-yGrid(1:NyMax+1-1))*0.5+yGrid(1:NyMax+1-1);
zCentroid = (zGrid(2:NzMax+1)-zGrid(1:NzMax+1-1))*0.5+zGrid(1:NzMax+1-1);
```

```
%Now decide what structure you would like to include in your
```



```
% simulation

cylinder = 1;

%AJS 05 Dec 2012
if bowtie
    %This is going to be very simple. If the BT point falls within
    % the y-x importance voxel, then we're going to make that space
    % a bow-tie space. I'll need to read in the points and find
    % which x and y (PTRAN y, in partisn it will be a z) place
    % they fall in.

    %First, I need to read in all the BT filter data.
    fidBT = fopen(['/media/RESEARCH/home/ptran/PTRAN9/' ...
                  'ptran_9_50_Try2/input/BTr.txt']);
    dummy = fscanf(fidBT, '%s', [1 2]);
    numPoints = fscanf(fidBT, '%i', [1 1]);
    x = zeros(numPoints,1);
    y = zeros(numPoints,1);
    for n = 1:numPoints
        dummyVal = fscanf(fidBT, '%g', [1 2]);
        x(n) = dummyVal(1);
        y(n) = dummyVal(2);
    end
    %Okay, these points need to be flipped and translated in y, but
    %y only.
    y = (-1)*(y*(-1.0)+850.0);
    %Now both values in x and y need to be converted to cm from
    %their native mm that PTRAN uses.
    x = x/10.0;
    y = y/10.0;

    %Now that I have read in the values, I need to pick out the
    %importance voxels that correspond to the BT filter. To do
    %this, I'm going to loop over the x-y points (in PTRAN)
    %geometry, and if the center points fall within the BT filter,
    %than I'll make that entire voxel assigned to the aluminum for
    %the BT filter. In the following, I am using PARTISN's
    %description for the y and z axes.
    yBTBound = 10;
    xmax = max(x);
```

```
xmin = min(x);
zmax = max(y);
zmin = min(y);
for j=1:NyMax
    fprintf('NyMax = %g, j = %g\n', NyMax, j);
    if(abs(yCentroid(j)) <= yBTBound)
        for k = 1:NzMax
            if(zCentroid(k) >= zmin && zCentroid(k) <= zmax)
                for i=1:NxMax
                    if(xCentroid(i) >= xmin && xCentroid(i) <= xmax)
                        inPoly = inpolygon(xCentroid(i), zCentroid(k), x, ...
                                            y);
                        if(inPoly)
                            zones(i,j,k) = 2;
                        end
                    end
                end
            end
        end
    end
end
end
end
end
end
```

end

```
% $$$ asdf;
```

```
if cylinder
```

```
%This is an elliptical cylinder, where you can define different
% radi and the axes. Also, it must be centered about the
% origin.
```

```
%I need to do a loop over all the centroids and find which ones
% fall within the cylinder bounds.
```

```
%Set the cylinder bounds
```

```
xRadius = 8.00;
zRadius = 10.00;
yLength = 25.00;
```

```
for j=1:NyMax
```

```

if mod(j,10) == 0
    fprintf(' j = %g\n', j);
end
if(abs(yCentroid(j)) <= yLength/2)
    %Now that I'm in the z space that is spanned by the
    % cylinder, I need to to step over the x and y space and
    % check the centroids and find those that are within the
    % cylinder and mark them.
    for i=1:NxMax
        for k=1:NzMax
            %Now check to see if the elliptical cyliner radius at
            % this point covers what it should be.

            %First, I need to compute the x-y radius of
            % this point.
            rVoxel = sqrt(xCentroid(i)^2+zCentroid(k)^2);
            %Second, I need to find the angle of this point with
            % respect to the origin

            if(xCentroid(i) == 0.d0)
                rCylinder = zRadius;
            elseif(zCentroid(k) == 0.d0)
                rCylinder = xRadius;
            else
                rCylinder = abs(rVoxel/(1.0/xRadius^2+(zCentroid(k)...
                    /xCentroid(i)/zRadius)^2)^(1.0/2.0)/xCentroid(i));
            end

            % $$$
            if xCentroid(i) == 0.d0
                theta = pi/2.0;
            else
                theta = atan(yCentroid(j)/xCentroid(i));
            end
            %Now use this theta to find the radius of the
            % cylinder at this angle.
            rCylinder = xRadius*zRadius/sqrt((zRadius* ...
                cos(theta)) ...
                ^2+ ...
                (xRadius*sin(theta))^2);

            % $$$
            if(k == 2 && j == 27 && i == 47)
                fprintf(' rVoxel = %g\n', rVoxel);
                fprintf(' rCylinder = %g\n', rCylinder);
                fprintf(' xCentroid(i) = %g\n', xCentroid(i));
            end
        end
    end
end

```

```

% $$$          fprintf(' yCentroid(j) = %g\n',yCentroid(j));
% $$$          pause
% $$$
% $$$          end
if rVoxel <= rCylinder
    zones(i,j,k) = 1; %Assigned in order from
                    % assign variable.
% $$$          if(k == 2 && j == 27 && i == 47)
% $$$              display('I made it in here')
% $$$              pause
% $$$          end
end
end
end
end
end

end

% $$$ zones(:,:,:) = 3;
%Now set the detector plate

%If we're doing the BT filter, we're also doing the detector plate.
% The new way of doing this uses neither.
if(bowtie)
    zones(:,:,end) = 4;
else
    zones(:,:,end) = 3;
end
% $$$ [lx,lz,ly]=size(zones);
% $$$ for i=1:25
% $$$     imagesc(reshape(zones(:,i,:),lx,ly)')
% $$$     axis image
% $$$     pause
% $$$ end
end %COMPUTE_GEOMETRY

```

```

%*****
%*****
%AJS 05 December 2012
%Write a little something to allow visualization of the geometry
[XCentroid ZCentroid] = meshgrid(xCentroid,zCentroid);
H = reshape(zones(:, floor(NyMax/2), :), NxMax, NzMax);
% $$$ surf(XCentroid,ZCentroid,H', 'EdgeColor', 'none');
% $$$ axis equal
% $$$ view(2)
% $$$ imagesc(xGrid,zGrid, reshape(zones(:, floor(NyMax/2), :), NxMax, NzMax)')
% $$$ axis image

figure
hp = pcolor(XCentroid,ZCentroid,H');
set(gca, 'LineWidth', 2.0, 'FontSize', 12.0, 'FontWeight', 'demi')
xlabel('x (cm)', 'FontSize', 14.0, 'FontWeight', 'demi')
ylabel('y (cm)', 'FontSize', 14.0, 'FontWeight', 'demi')
% $$$ set(hp, 'EdgeColor', 'none');
axis image
lcb = colorbar
set(lcb, 'LineWidth', 2.0, 'FontSize', 12.0, 'FontWeight', 'demi')

% $$$ asdf;

%*****
%*****
%Okay, Now it's time to write this thing out to file so I can
% paste this into the input file.

%Open the file for writing
fid = fopen('./22Mar2013/CBCT_GeomSn32G8P5ADFGTmp.inp', 'w');
% $$$ fid = fopen('fileTmp.inp', 'w');

%write the preface of the file
nhead = 2; %The number of title lines that follow
notty = 0; %Suppress output to online user terminal (Or in other
           % words, would you also like to NOT create an output file?)
           % 0/1 = no/yes
nolist = 1; %Suppress the listing in the output file all the user

```

```

        % input from the input file? 0/1 = no/yes
npass   = 0; % Not used
restart = 0; %Perform a time-dependent restart? 0/1/2 = no/yes/yes
        % (with FILEIO = 1)
fprintf(fid, '%6i%6i%6i%6i\n', nhead, notty, nolist, npass, ...
        restart);
fprintf(fid, 'CBCT water cylinder input file - AJS December 06, 2012\n');
fprintf(fid, 'Cross sections from NJOY DTFR output\n');

%*****
%*****
% START BLOCK I
%write the dillimeter lines to separate this block from the others.
% Block I contains the dimensions and the overall controls.
fprintf(fid, '\n');
fprintf(fid, ['/***** B L O C K I *****/ ...
        '*****\n']);
fprintf(fid, '\n');
fprintf(fid, '/PRINTED BY MATLAB FILE "PARTISN_gridStructure.m".\n');
fprintf(fid, '/ PLEASE CONSULT THAT FILE AND THE PARTISN MANUAL FOR MORE DETAILED\n');
fprintf(fid, '/ EXPLANATION OF WHAT THESE VARIABLES ARE.\n');
igeom = 'x-y-z'; % We have an x-y-z grid geometry
fprintf(fid, 'igeom= %s\n', igeom);
ngroup = 8; % The number of groups in our energy discretization
fprintf(fid, 'ngroup= %i\n', ngroup);
isn = 32; % The level of angular quadrature. The higher this
        % number, the fewer "ray effects" are realized. To
        % find the number of angles per quadrant: isn*(isn+2)/8
fprintf(fid, 'isn= %i\n', isn);
niso = 8; % The number of isotopes in our cross-section file
fprintf(fid, 'niso= %i\n', niso);
mt = 5; % The number of simulated materials or "mixtures"
        % from the "niso" isotopes
fprintf(fid, 'mt= %i\n', mt);
nzone = mt; % The number of Zones. In most cases, each zone
        % will correspond directly to an isotope mixture
        % for our PTRAN calculations
fprintf(fid, 'nzone= %i\n', nzone);
nosolv = 0; % Suppress solver module execution: 0/1 = no/yes
fprintf(fid, 'nosolv= %i\n', nosolv);
noedit = 1; % Suppress edit module execution: 0/1 = no/yes
fprintf(fid, 'noedit= %i\n', noedit);

```

```

im = NxObject+2;          % The total number of coarse grids
                          % intervals in "x"

im = NxMax
fprintf(fid,'im= %i\n',im);
it = NxMax                % The total number of fine mesh intervals in "x"
fprintf(fid,'it= %i\n',it);

jm = NyObject+2; % The total number of coarse grids intervals in
                % "y". 2 extra for the source and detector voxel
                % planes.
jm = NyMax %No longer modeling the two extra pieces.
fprintf(fid,'jm= %i\n',jm);
jt = NyMax                % The total number of fine mesh intervals in "y"
fprintf(fid,'jt= %i\n',jt);

km = NzObject+2+2;        % The total number of coarse grids
                          % intervals in "z"

km = NzMax
fprintf(fid,'km= %i\n',km);
kt = NzMax                % The total number of fine mesh intervals in "z"
fprintf(fid,'kt= %i\n',kt);

iquad = 5;                % The source of the quadrature constants. Consult
                          % PARTISN manual

maxlcm = 50000000;
fprintf(fid,'maxlcm= %i\n',maxlcm);
fprintf(fid,'iquad= %i\n',iquad);

%Alright, you're done, You just need to tell PARTISN.

% Start BLOCK II
% block II contains the geometry information
fprintf(fid,' T\n');
%write the dillimeter lines to separate this block from the others.
fprintf(fid,'/\n');
fprintf(fid,['/****** B L O C K II *****' ...
            '*****\n']]);
fprintf(fid,'/\n');
fprintf(fid,'/PRINTED BY MATLAB FILE "PARTISN_gridStructure.m".\n');
fprintf(fid,'/ PLEASE CONSULT THAT FILE AND THE PARTISN MANUAL FOR MORE DETAILED\n');
fprintf(fid,'/ EXPLANATION OF WHAT THESE VARIABLES ARE.\n');

```

```

%Okay, now write out the xmesh variable. This is the same as xGrid
% in my Matlab implementation. Okay, this is how this will work. I
% will write the data in lines that contain 5 values. The first
% line will be written to contain the variable name, then I will
% loop through and write all the full length lines that contain
% five values. After the loop, I will write the line that contains
% the remainder of the values that don't fit on a full 5 value
% line. Remember that the NxMax, and corresponding y and z, values
% are for the number of voxels that in that dimension. They need to
% incremented once to then correspond to the number of grid lines.

%*****
%*****
%This is for xmesh
xStart = 1;
xPrintNum = 5.0;
xTimes = floor((NxMax+1)/xPrintNum); %How many full length lines that contain
                                     % five values.
xRemain = (NxMax+1)-xTimes*xPrintNum;%The remainder to be written
                                     % on the last line

%Write the first line
fprintf(fid,' xmesh=' );fprintf(fid,'%12.4e',xGrid(xStart:xStart+xPrintNum-1));fprintf(fid,'\n');
xTimes = xTimes-1;
xStart = xStart+xPrintNum;
%Write the main body, minus the remainder line
for i=1:xTimes
    fprintf(fid,' ');fprintf(fid,'%12.4e',xGrid(xStart:xStart+xPrintNum-1));fprintf(fid,'\n');
    xStart = xStart+xPrintNum;
end
%Write the remainder line
fprintf(fid,' ');fprintf(fid,'%12.4e',xGrid(xStart:xStart+xRemain-1));fprintf(fid,'\n');

%*****
%*****
%This is for ymesh
yStart = 1;
yPrintNum = 5.0;
yTimes = floor((NyMax+1)/yPrintNum); %How many full length lines that contain
                                     % five values.
yRemain = (NyMax+1)-yTimes*yPrintNum;%The remainder to be written
                                     % on the last line

```



```

%Write the first line
fprintf(fid, '      ymesh=' ); fprintf(fid, '%12.4e', yGrid(yStart:yStart+yPrintNum-1)); fprintf(fid, '\n' );
yTimes = yTimes-1;
yStart = yStart+yPrintNum;
%Write the main body, minus the remainder line
for i=1:yTimes
    fprintf(fid, '      '); fprintf(fid, '%12.4e', yGrid(yStart:yStart+yPrintNum-1)); fprintf(fid, '\n' );
    yStart = yStart+yPrintNum;
end
%Write the remainder line
fprintf(fid, '      '); fprintf(fid, '%12.4e', yGrid(yStart:yStart+yRemain-1)); fprintf(fid, '\n' );

%*****
%*****
%This is for zmesh
zStart = 1;
zPrintNum = 5.0;
zTimes = floor((NzMax+1)/zPrintNum); %How manz full length lines that contain
                                     % five values.
zRemain = (NzMax+1)-zTimes*zPrintNum;%The remainder to be written
                                     % on the last line

%Write the first line
fprintf(fid, '      zmesh=' ); fprintf(fid, '%12.4e', zGrid(zStart:zStart+zPrintNum-1)); fprintf(fid, '\n' );
zTimes = zTimes-1;
zStart = zStart+zPrintNum;
%Write the main bodz, minus the remainder line
for i=1:zTimes
    fprintf(fid, '      '); fprintf(fid, '%12.4e', zGrid(zStart:zStart+zPrintNum-1)); fprintf(fid, '\n' );
    zStart = zStart+zPrintNum;
end
%Write the remainder line
fprintf(fid, '      '); fprintf(fid, '%12.4e', zGrid(zStart:zStart+zRemain-1)); fprintf(fid, '\n' );

%*****
%*****
%Now I need to write the number of fine mesh voxels that will be
%within the coarse mesh voxels. This will be easy, using the
%PARTISN quick and convenient notation. I will not give an
%explanation here of what this means. The user should consult the
%PARTISN manual.
fprintf(fid, '      xints= f1,  yints= f1,  zints= f1\n' );

```

```
%*****
%*****
%Okay, now I need to write out the zones variable...
%This is going to get VERY MESSY!!!!. According to PARTISN
% nomenclature, each x line for y and z is a "string" of array
% input. "zones" is read in one "string" at a time, so I will need
% to write out one "string" at a time. Also, PARTISN only reads out
% to the 80th character, so I need to keep it within 80 characters
% per line.

%set the prefix for the line to be written
% find your current length
% This is the very first "string", so I need to change what
% my prefix is.
prefix = '      zones=';
lineStr = prefix;
prefix = '      ';
lenCur = length(prefix);
fprintf('Writing the Zones Variable\n');
for k=1:NzMax;
    if mod(k,10) == 0
        fprintf(' k = %g\n',k);
    end
    for j=1:NyMax
        %Give the initial value of the value holder
        ind = 1;
        valHold = zones(ind,j,k);
        KEEP_GOING = 1;
        while(KEEP_GOING) %This will loop until the current string
            % has been written
            %Okay, I need to find how many values have the same
            % value as "valHold" in a row
            SAME = 1;
            count = 1;
            while(SAME && ind < NxMax)
                ind = ind+1;
                if(zones(ind,j,k) == valHold)
                    %If yes, then increment ind and count and keep looking
                    count = count+1;
                else
                    %If no, then kill this round and set it out.
                    ind = ind-1;
                end
            end
        end
    end
end
```

```

        SAME = 0;
    end
end
%Okay, so here, I know how many times the "valHold"
% value has been repeated, and I know the place of the
% next value. Let's work the former first.
if(count > 1)
    %If the count is greater than 1, then the repeated
    % syntax needs to be used to reduce the space needed
    % to represent the geometry in the file.
    tmpStr = sprintf('%3ir%-2i',count,valHold);
    tmpStr = deblank(tmpStr);
else
    %Then print a simple, single value is there is only
    % one of them.
    tmpStr = sprintf('%3i',valHold);
% $$$          fprintf('valHold = %g\n',valHold)
% $$$          fprintf('ind = %3i\n',ind);
% $$$          fprintf('j = %3i\n',j);
% $$$          fprintf('k = %3i\n',k);
% $$$          fprintf('zones(ind,j,k) = %g\n',zones(ind,j,k));
% $$$          pause
end
if ind == NxMax
    %This means that it found the end of the
    % "string", or line of the x values.
    tmpStr = [tmpStr ';' ];
    %Since we found the end of the "string" we need to
    % get out of the loop, and move onto the next y
    % place and therefore, the next "string".
    KEEP_GOING = 0;
else
    %Since, I am not at the end of the "string," I need
    % pick up the next value to find if it is repeated.
    ind = ind+1;
    valHold = zones(ind,j,k);
end
%Contatenate the new string (character string) onto the
% line for writting it.
lineStr = [lineStr ' ' tmpStr];
if(length(lineStr) > 72)
    %If the line is greater than 72 characters, than

```

```

        % write it to the file and set up the next line.
        fprintf(fid,[lineStr '\n']);
        lineStr = prefix;
    end
end
% $$$      fflush(fid);

end
end
% At the end of the line, there will be a partial row that is under
% the 72 character limit, but is a complete row, as it contains the
% rest of the data. This also needs to be written.
if length(lineStr) > length(prefix)
    fprintf(fid,[lineStr '\n']);
end

% $$$ fprintf(fid,'      zones='); fprintf(fid,'%3i', zones(:,1,1)); fprintf(fid,';\n');
% $$$ yStart = 2;
% $$$ for k=1:NzMax
% $$$     for j=yStart:NyMax
% $$$         fprintf(fid,'          '); fprintf(fid,'%3i', zones(:,j,k)); fprintf(fid,';\n');
% $$$     end
% $$$     yStart = 1;
% $$$ end

%END PRINTING ZONES DATA
%*****
%*****
%Alright, you're done, You just need to tell PARTISN.

fprintf(fid,' T\n');

%*****
%*****
% START BLOCK III
% block III contains the nuclear data
%write the dillimeter lines to separate this block from the others.
fprintf(fid,'/\n');
fprintf(fid,'/***** B L O C K III *****\n');
fprintf(fid,'/\n');

```

```

fprintf(fid, '/PRINTED BY MATLAB FILE "PARTISN_gridStructure.m".\n');
fprintf(fid, '/ PLEASE CONSULT THAT FILE AND THE PARTISN MANUAL FOR MORE DETAILED\n');
fprintf(fid, '/ EXPLANATION OF WHAT THESE VARIABLES ARE\n');
lib='xslib';
libname='DG8P5'; %Define the cross-section library
                    % type the library name
fprintf(fid, 'lib=%s; libname=%s\n', lib, libname);
maxord=5; %Legendre Scattering Order (This value represents the
          % order of the Legendre polynomial expansion. The higher
          % this number, the more accurate the scattering is.
fprintf(fid, 'maxord=%i\n', maxord);
ihm=ngroup+3; %Table length: # of Energy Group bound + 3
fprintf(fid, 'ihm=%i\n', ihm);
iht=3; %Position number of the total cross-section.
fprintf(fid, 'iht=%i\n', iht);
ifido=0; % 1: Fixed Field FIDO format: TRANSX "iout" = 3
          % 0: DTF format from NJOY directly
fprintf(fid, 'ifido=%i\n', ifido);
ititl=1; %Specifies that there is a header to each table
fprintf(fid, 'ititl=%i\n', ititl);
% $$$ i2lpl=0; %Specifies that the extra 2L+1 is NOT included in this
% $$$ % file format 0/1: no/yes
% $$$ fprintf(fid, 'i2lpl=%i\n', i2lpl);
savbxs=1; %Save the binary BXSLIB file for subsequent runs.
fprintf(fid, 'savbxs=%i\n', savbxs);
%*****
names=['hydro1'; 'carbn6'; 'nitro7'; 'oxygen8'; 'alum13'; 'argn18'; 'iodn53'; ...
       'csum55'];
%Print the "names" variable to the file
[ii, jj]=size(names);
lineStr = 'names=';
prefix = ' ';
for i=1:ii
    lineStr = [lineStr ' ' names(i, :) ''];
    if length(lineStr) > 72
        fprintf(fid, [lineStr '\n']);
        lineStr = prefix;
    end
end
end
fprintf(fid, [lineStr '\n']);
%*****
%124 equally spaced

```

```

% $$$ ebound = [1.0000E+03 2.0000E+03 3.0000E+03 4.0000E+03 5.0000E+03 ...
% $$$           6.0000E+03 7.0000E+03 8.0000E+03 9.0000E+03 1.0000E+04 ...
% $$$           1.1000E+04 1.2000E+04 1.3000E+04 1.4000E+04 1.5000E+04 ...
% $$$           1.6000E+04 1.7000E+04 1.8000E+04 1.9000E+04 2.0000E+04 ...
% $$$           2.1000E+04 2.2000E+04 2.3000E+04 2.4000E+04 2.5000E+04 ...
% $$$           2.6000E+04 2.7000E+04 2.8000E+04 2.9000E+04 3.0000E+04 ...
% $$$           3.1000E+04 3.2000E+04 3.3000E+04 3.4000E+04 3.5000E+04 ...
% $$$           3.6000E+04 3.7000E+04 3.8000E+04 3.9000E+04 4.0000E+04 ...
% $$$           4.1000E+04 4.2000E+04 4.3000E+04 4.4000E+04 4.5000E+04 ...
% $$$           4.6000E+04 4.7000E+04 4.8000E+04 4.9000E+04 5.0000E+04 ...
% $$$           5.1000E+04 5.2000E+04 5.3000E+04 5.4000E+04 5.5000E+04 ...
% $$$           5.6000E+04 5.7000E+04 5.8000E+04 5.9000E+04 6.0000E+04 ...
% $$$           6.1000E+04 6.2000E+04 6.3000E+04 6.4000E+04 6.5000E+04 ...
% $$$           6.6000E+04 6.7000E+04 6.8000E+04 6.9000E+04 7.0000E+04 ...
% $$$           7.1000E+04 7.2000E+04 7.3000E+04 7.4000E+04 7.5000E+04 ...
% $$$           7.6000E+04 7.7000E+04 7.8000E+04 7.9000E+04 8.0000E+04 ...
% $$$           8.1000E+04 8.2000E+04 8.3000E+04 8.4000E+04 8.5000E+04 ...
% $$$           8.6000E+04 8.7000E+04 8.8000E+04 8.9000E+04 9.0000E+04 ...
% $$$           9.1000E+04 9.2000E+04 9.3000E+04 9.4000E+04 9.5000E+04 ...
% $$$           9.6000E+04 9.7000E+04 9.8000E+04 9.9000E+04 1.0000E+05 ...
% $$$           1.0100E+05 1.0200E+05 1.0300E+05 1.0400E+05 1.0500E+05 ...
% $$$           1.0600E+05 1.0700E+05 1.0800E+05 1.0900E+05 1.1000E+05 ...
% $$$           1.1100E+05 1.1200E+05 1.1300E+05 1.1400E+05 1.1500E+05 ...
% $$$           1.1600E+05 1.1700E+05 1.1800E+05 1.1900E+05 1.2000E+05 ...
% $$$           1.2100E+05 1.2200E+05 1.2300E+05 1.2400E+05 1.2500E+05];
%G10 with weighting function
% $$$ ebound = [2.5000E+03 2.0000E+04 3.0000E+04 3.5000E+04 4.0000E+04 5.4000E+04 6.2000E+04 7.0000E+04 8.7000E+04
1.0500E+05 1.2500E+05];
%G8 with weighting function
ebound = [2.0000E+03 2.2000E+04 3.0000E+04 4.0000E+04 5.4000E+04 6.2000E+04 7.0000E+04 9.0000E+04 1.2500E+05];
%173 adjusted G210
% $$$ ebound=[1000.0 1063.0 1125.0 1250.0 1375.0 1500.0 1625.0 1750.0 1875.0 2000.0...
% $$$           2121.0 2242.0 2484.0 2535.0 2586.0 2793.0 3000.0 3066.0 3310.0 3554.0...
% $$$           3851.0 4000.0 4250.0 4500.0 4750.0 4966.4 5465.1 5989.2 6539.0 7112.0...
% $$$           7708.9 8000.0 8332.8 8500.0 8978.9 9200.0 9658.6 10367.1 10760.0 11215.4...
% $$$           11563.7 11918.7 12099.8 12283.9 12824.1 13418.5 13879.9 14352.8 14839.3...
% $$$           15000.0 15200.0 15860.0 16900.0 17930.0 18970.0 20000.0 21250.0 22500.0...
% $$$           23750.0 25140.0 26250.0 27000.0 27250.0 27600.0 28000.0 28200.0 28500.0...
% $$$           28700.0 29000.0 29250.0 29500.0 29750.0 30000.0 30500.0 31000.0 31500.0...
% $$$           32000.0 32500.0 33169.4 33500.0 34000.0 34500.0 34750.0 35000.0 35550.0...
% $$$           35984.6 36250.0 36500.0 36750.0 37000.0 37250.0 37500.0 37750.0 38000.0...
% $$$           38250.0 38500.0 38750.0 39000.0 39250.0 39500.0 39750.0 40000.0 40500.0...

```

```

% $$$      41000.0 41250.0 41500.0 41750.0 42000.0 42250.0 42500.0 42750.0 43000.0...
% $$$      43250.0 43500.0 43750.0 44000.0 44250.0 45000.0 46000.0 47500.0 48500.0...
% $$$      50000.0 51000.0 52000.0 53000.0 54000.0 55000.0 56000.0 56500.0 57000.0 57500.0 58000.0 58500.0...
% $$$      59000.0 59500.0 60000.0 60500.0 61000.0 62000.0 63000.0 64000.0 65000.0 65500.0 66000.0 66500.0 67000.0
67500.0...
% $$$      68000.0 68500.0 69000.0 69250.0 69525.0 69750.0 70000.0 72000.0...
% $$$      76111.0 77500.0 80724.9 83102.3 86000.0 88000.0 90000.0 91000.0 92000.0...
% $$$      93000.0 94000.0 95000.0 96000.0 97000.0 98000.0 99000.0 100000.0...
% $$$      112500.0 125000.0];
printEnergy = 1;
if printEnergy

    if(octave)
        fidE = fopen(['/media/SEAGATE/RESEARCH/home/ptran/PTRAN9/' ...
                    'ptran_9_50_Try2/input/8GroupBounds06Feb2013.dat'],'w');
    else
        fidE = fopen(['/media/RESEARCH/home/ptran/PTRAN9/' ...
                    'ptran_9_50_Try2/input/' ...
                    '8GroupBounds22Mar2013FG.dat'],'w');
    end

    fprintf(fidE,'8 PARTISN energy group structure for G7Fido\n');
    fprintf(fidE,'%d\n',ngroup+1);
    %The energies must be converted from eV to keV
    for i=1:length(ebound)
        fprintf(fidE,'%12.5e\n',ebound(i)*0.001);
    end

    %I also must include the x, y, and z grid as well,
    % not forgetting to convert from cm to mm for PTRAN.
    fprintf(fidE,'xGrid, %d\n',it+1);
    for i=1:it+1
        fprintf(fidE,'%12.5e\n',xGrid(i)*10.0);
    end
    fprintf(fidE,'yGrid, %d\n',jt+1);
    for j=1:jt+1
        fprintf(fidE,'%12.5e\n',yGrid(j)*10.0);
    end
    fprintf(fidE,'zGrid, %d\n',kt+1);
    for k=1:kt+1
        fprintf(fidE,'%12.5e\n',zGrid(k)*10.0);
    end
end

```

```

% $$$      fclose(fidE);

end

%AJS 23 Octoboer 2012
% I need to flip the ebound variable before I write this to file
% since PARTISN works from largest to smallest.
eboundTmp = 0.0*ebound;
for n=1:length(ebound)
    eboundTmp(n) = ebound(length(ebound)-n+1);
end
clear ebound
ebound = eboundTmp;

%Print the "ebound" variable to file
lineStr = 'ebound=';
prefix = '      ';
for i=1:length(ebound)
    tmpStr=sprintf(' %12.5E',ebound(i));
    lineStr = [lineStr tmpStr];
    if length(lineStr) > 68
        fprintf(fid,[lineStr '\n']);
        lineStr = prefix;
    end
end
fprintf(fid,[lineStr '\n']);
%*****

%Alright, you're done, You just need to tell PARTISN.

fprintf(fid,' T\n');
%*****
%*****
% START BLOCK IV
% block IV contains the material mixing specifics
%write the dillimeter lines to separate this block from the others.
fprintf(fid,'\n');
fprintf(fid,'/***** B L O C K IV *****\n');
fprintf(fid,'\n');
fprintf(fid,'/PRINTED BY MATLAB FILE "PARTISN_gridStructure.m".\n');

```



```

fprintf(fid, '// PLEASE CONSULT PARTISN MANUAL FOR MORE DETAILED EXPLANATION\n');
fprintf(fid, '// OF WHAT THESE VARIABLES ARE AND THEIR FORMAT\n');
fprintf(fid, 'matspec=atfrac /Mix the variables based on atomic fractions.\n');
fprintf(fid, '          / This means that the mixing input\n');
fprintf(fid, '          / for matls will be in mole fractions.\n');
fprintf(fid, ['atwt=hydro1 1.0 carbn6 11.74 nitro7 14.0 oxygn8 16.0 alum13 26.98 \n']);
fprintf(fid, '      argn18 39.95 iodn53 126.90 csum55 132.91;\n');
fprintf(fid, '          /define the atomic weights of the materials\n');
fprintf(fid, '          / found in the xslib cross-section file.\n');
fprintf(fid, 'matls= waterm  hydro1  0.6667\n');
fprintf(fid, '          oxygn8  0.3333;\n');
fprintf(fid, '\n');
fprintf(fid, '      alumm  alum13  1.0000;\n');
fprintf(fid, '\n');
fprintf(fid, '      airm   nitro7  8.07081-1\n');
fprintf(fid, '          oxygn8  1.89534-1\n');
fprintf(fid, '          argn18  3.38488-3;\n');
fprintf(fid, '\n');
fprintf(fid, '      csim   iodn53  0.5000\n');
fprintf(fid, '          csum55  0.5000;\n');
fprintf(fid, '\n');
fprintf(fid, '      adi3m  hydro1  6.1307-1\n');
fprintf(fid, '          carbn6  3.0201-1\n');
fprintf(fid, '          nitro7  1.9010-2\n');
fprintf(fid, '          oxygn8  6.5910-2;\n');
fprintf(fid, '\n');
fprintf(fid, 'assign= water  waterm  1.00;\n');
fprintf(fid, '      alum  alumm  2.70;\n');
fprintf(fid, '      air   airm   1.20-3;\n');
fprintf(fid, '      csi   csim   4.51;\n');
fprintf(fid, '      adi3  adi3m  0.930;\n');
%Alright, you're done, You just need to tell PARTISN.

fprintf(fid, ' T\n');

%*****
%*****
% START BLOCK V
% Solver input
%write the dillimeter lines to separate this block from the others.
fprintf(fid, '\n');
fprintf(fid, '/****** B L O C K V *****\n');

```

```
fprintf(fid, '\n');
fprintf(fid, '/PRINTED BY MATLAB FILE "PARTISN_gridStructure.m".\n');
fprintf(fid, '/ PLEASE CONSULT THAT FILE AND THE PARTISN MANUAL FOR A MORE DETAILED\n');
fprintf(fid, '/ EXPLANATION OF WHAT THESE VARIABLES ARE\n');

%Set the desired Parameters
ievt=0;      %What type of calculation? "0" means source. This should never
            % change for PTRAN
fprintf(fid, 'ievt= %i\n',ievt);
isct=maxord; %Legendre Scattering Order.
fprintf(fid, 'isct= %i\n',isct);
ith=1;      %"0" for direct, "1" for ADJOINT
fprintf(fid, 'ith= %i\n',ith);
ibl=0;      %Left Boundary Condition
            % : 0/1/2/3/4 =
            % vacuum/reflective/periodic/white/rotational
fprintf(fid, 'ibl= %i\n',ibl);
ibr=0;      %Right Boundary Condition
            % : 0/1/2/3/4 = vacuum/reflective/periodic/white/rotational
fprintf(fid, 'ibr= %i\n',ibr);
ibt=0;      %Top Boundary Condition
            % : 0/1/2/3/4 = vacuum/reflective/periodic/white/rotational
fprintf(fid, 'ibt= %i\n',ibt);
ibb=0;      %Bottom Boundary Condition
            % : 0/1/2/3/4 = vacuum/reflective/periodic/white/rotational
fprintf(fid, 'ibb= %i\n',ibb);
ibfrnt=0;   %Front Boundary Condition
            % : 0/1/2/3/4 = vacuum/reflective/periodic/white/rotational
fprintf(fid, 'ibfrnt= %i\n',ibfrnt);
ibback=0;   %Back Boundary Condition
            % : 0/1/2/3/4 = vacuum/reflective/periodic/white/rotational
fprintf(fid, 'ibback= %i\n',ibback);
epsi=1.0E-10; %Global Convergence Precision
fprintf(fid, 'epsi= %7.2E\n',epsi);
iitl=20;    %Maximum number of inner group iterations "at first." I don't
            % know what "at first" means
fprintf(fid, 'iitl= %i\n',iitl);
srcacc='dsa'; %Diffusion source acceleration
fprintf(fid, 'srcacc= %s\n',srcacc);
diffsol='mg'; %Diffusion operator solver: "mg" = multi-grid solver with
            % 3 line relaxation
fprintf(fid, 'diffsol= %s\n',diffsol);
```

```

fluxp=1;      %Final Flux Print: 0/1/2/ = none/isotropic
              %(scalar)/moments
fprintf(fid,'fluxp= %i\n',fluxp);
kprint=1;    %The K-Plane the fluxes will be output for
fprintf(fid,'kprint= %i\n',kprint);
xsectp=0;    %Final cross-section output: 0/1/2 =
              %none/principal/all
fprintf(fid,'xsectp= %i\n',xsectp);
sourcp=0;    %Final source output: 0/1/2/3 = none/as
              %input/normalized/both
fprintf(fid,'sourcp= %i\n',sourcp);
norm=1.0;    %Source Normalization
fprintf(fid,'norm= %12.5E\n',norm);
trnsol=1;    %Transport solver type: "1" for "seqdp". I really have no idea
              % why I'm using this.
fprintf(fid,'trnsol= %i\n',trnsol);
nodal=0;     %Spatial differencing scheme: "0" = Standard,
              %low-order
fprintf(fid,'nodal= %i\n',nodal);
wdamp='f3.0'; %????????????????????????????????????????????????????????/
fprintf(fid,'wdamp= %s\n',wdamp);
npey=2; npez=1; nchunk=7;%parallel details: use just one processor
fprintf(fid,'npey= %i npez= %i nchunk= %i\n',npey,npez,nchunk);
timedep=0;   %Run in time dependent mode: 0/1 = no/yes !!!This should
              % always be "0"
fprintf(fid,'timedep= %i\n',timedep);
%/fcsrc=umcflux fcsrstr=0 fcnray=25440 fcntr=20 fcseed=0 fcwco=0.1
              %Data for forced collisions. Currently this
              % is here for reference purposes only

if(ith == 0)
  %This defines the volumetric source for forward calculations.
  % I need to read in the spectrum data.
  spectrumFile = ['/media/RESEARCH/home/ptran/PTRAN9/ptran_9_50_Try2/' ...
                  'data/CAX_spect_125kVp.txt'];
  fidSpect = fopen(spectrumFile,'r');
  %read in the spectrum description
  dummy=fscanf(fidSpect,'%s',[1,3]);
  %read in the number of spectrum values
  nptSpect = fscanf(fidSpect,'%d',[1,1]);
  %read in the spectrum data.
  % The first row contains the energy data, while the second row

```

```
% contains the spectrum data.
ptranSpect = fscanf(fidSpect,'%f',[2 nptSpect]);
%Since I don't like dealing with rows, I will transpose it so
% that the like data is in columns.
ptranSpect = ptranSpect';
%Now I have to normalize the data properly and get it into the
% correct units.
%The energy in PTRAN is in keV. For PARTISN it needs to be eV.
ptranSpect(:,1) = ptranSpect(:,1)*1000;
%I also need to normalize the spectrum data.
sumSpect = trapz(ptranSpect(:,1),ptranSpect(:,2));
ptranSpect(:,2) = ptranSpect(:,2)/sumSpect;

%Okay, now I have the ptran Spectrum. I now need to interpolate
% the ptran Spectrum onto the PARTISN energy Grid
%First I need to find the PARTISN energy grid centers.
numGroups = ngroup;
NMQ = (maxord+1)*(maxord+1);
energyGroupCenters = (ebound(1:end-1)+ebound(2:end))/2;
ptranSpectGroup = interp1(ptranSpect(:,1),ptranSpect(:,2),energyGroupCenters,'linear',0.0);

plot(energyGroupCenters,ptranSpectGroup,'b-');

%AJS 25 June 2012
% Let's do a boundary source for this as well.
%This defines the boundary source for adjoint calculations
sileft = zeros(ngroup,jt*kt);
sirite = zeros(ngroup,jt*kt);
sibott = zeros(ngroup,it*kt);
sitop = zeros(ngroup,it*kt);
sifrnt = zeros(ngroup,it*jt);
siback = zeros(ngroup,it*jt);

%this could be much more difficult, complex, and much more general
%to implement. for now, I'm just doing it the easy way.
% I ned to do some alterations of sibott.
count = 0;
Normalization = 9.01754E+13/25e-3;
Normalization = 1.0;
for i = 1:it
    for j = 1:jt
```

```

    count = count+1;
    if i == ceil(it/2) && j == ceil(jt/2)
        sifrnt(:,count) = ptranSpectGroup(:)*Normalization;
    end
end
end
%Write the left and right source declarations (x-axis)
tmpStr = sprintf('%i', jt*kt-1);
fprintf(fid, ['sileft= f0; ' tmpStr 'Y1;\n']);
fprintf(fid, ['sirite= f0; ' tmpStr 'Y1;\n']);

tmpStr = sprintf('%i', it*kt-1);
fprintf(fid, ['sibott= f0; ' tmpStr 'Y1;\n']);
fprintf(fid, ['sitop= f0; ' tmpStr 'Y1;\n']);

%Write the front and back source declarations (z-axis)
%Write the top and bottom source declarations (y-axis)
lineStr = 'sifrnt=';
prefix = ' ';
for j=1:it*jt;
    if mod(j,30) == 0
        fprintf('j = %g\n', j);
    end
    %Give the initial value of the value holder
    ind = 1;
    valHold = sifrnt(ind, j);
    KEEP_GOING = 1;
    while(KEEP_GOING) %This will loop until the current string
                        % has been written
                        %Okay, I need to find how many values have the same
                        % value as "valHold" in a row
        SAME = 1;
        count = 1;
        while(SAME && ind < ngroup)
            ind = ind+1;
            if(sifrnt(ind, j) == valHold)
                %If yes, then increment ind and count and keep looking
                count = count+1;
            else
                %If no, then kill this round and set it out.
                ind = ind-1;
                SAME = 0;
            end
        end
    end
end

```

```

        end
    end
    %Okay, so here, I know how many times the "valHold"
    % value has been repeated, and I know the place of the
    % next value. Let's work the former first.
    if(count > 1)
        %If the count is greater than 1, then the repeated
        % syntax needs to be used to reduce the space needed
        % to represent the geometry in the file.
        tmpStr = sprintf('%3ir%-12.5E',count,valHold);
        tmpStr = deblank(tmpStr);
    else
        %Then print a simple, single value is there is only
        % one of them.
        tmpStr = sprintf('%12.5E',valHold);
        % $$$
        fprintf('valHold = %g\n',valHold)
        % $$$
        fprintf('ind = %3i\n',ind);
        % $$$
        fprintf('j = %3i\n',j);
        % $$$
        fprintf('k = %3i\n',k);
        % $$$
        fprintf('zones(ind,j,k) = %g\n',zones(ind,j,k));
        % $$$
        pause
    end
    if ind == ngroup
        %This means that it found the end of the
        % "string", or line of the x values.
        tmpStr = [tmpStr ';' ];
        %Since we found the end of the "string" we need to
        % get out of the loop, and move onto the next y
        % place and therefore, the next "string".
        KEEP_GOING = 0;
    else
        %Since, I am not at the end of the "string," I need
        % pick up the next value to find if it is repeated.
        ind = ind+1;
        valHold = sifrrt(ind,j);
    end
    %Contatenate the new string (character string) onto the
    % line for writting it.
    lineStr = [lineStr ' ' tmpStr];
    if(length(lineStr) > 68)
        %If the line is greater than 72 characters, than
        % write it to the file and set up the next line.

```

```

        fprintf(fid, [lineStr '\n']);
        lineStr = prefix;
    end
end
% $$$          fflush(fid);

end
% At the end of the line, there will be a partial row that is under
% the 72 character limit, but is a complete row, as it contains the
% rest of the data. This also needs to be written.
if length(lineStr) > length(prefix)
    fprintf(fid, [lineStr '\n']);
end
tmpStr = sprintf('%i', it*jt-1);
% $$$          fprintf(fid, ['sifront= f0; ' tmpStr 'Y1;\n']);
                fprintf(fid, ['siback= f0; ' tmpStr 'Y1;\n']);

elseif(ith == 1)
    %This defines the boundary source for adjoint calculations
    sileft = zeros(ngroup, jt*kt);
    sirite = zeros(ngroup, jt*kt);
    sibott = zeros(ngroup, it*kt);
    sitop  = ones(ngroup, it*kt);
    sifront = zeros(ngroup, it*jt);
    siback  = zeros(ngroup, it*jt);

    %This is where I compute my detector response function for my
    % simluation. Now, I must be clear. PARTISN accepts this
    % detector response function as a normalized PDF over the
    % energy bounds you're interested in.

    %mu is from The NIST XCOM database for CsI. This is the mass
    % attenuation coefficient so it needs to be scaled by density
    % for the detector response function to have the right units.
    density = 4.51; %grams per cm^3

    %*****
    %*****
    %AJS 24 Octoboer 2012
    % I'm going to read in the CsI cross-sections from PTRAN, and

```

```
% then interpolate on the corresponding energy Group
% structure. This interpolation would benefit from an assumption
% of the flux at the detector to compose a weighting function,
% but for now this just uses the midpoint within the energy
% group to define the attenuation coefficient. Remember that
% PTRAN uses mm for its length unit and PARTISN uses cm, so a
% conversion will be done. PARTISN also uses eV instead of KeV
% so a corresponding change will also be made there.

% Define which file you're going to use for the attenuation
% coefficient.
if(octave)
    muFileName = ['/media/SEAGATE/RESEARCH/home/ptran/PTRAN9/' ...
                 'ptran_9_50_Try2/dlc146/xsect_CsI.dat']
else
    muFileName = ['/media/RESEARCH/home/ptran/PTRAN9/' ...
                 'ptran_9_50_Try2/dlc146/xsect_CsI.dat']
end

% Open the file for reading
fidMu = fopen(muFileName,'r');

% Read in the length of the attenuation energy table
tableLength = fscanf(fidMu,'%g',[1 1]);

% Read in the attenuation data. The columns are set up as the
% following:
% 1. Energy in keV
% 2. The attenuation coefficient in 1/mm
% 3. The fraction of the attenuation coefficient that is from
%    photoelectric absorption.
% 4. The fraction of the attenuation coefficient that is from
%    coherent scattering.
% 5. The fraction of the attenuation coefficient that is from
%    incoherent scattering.
% 6. The fraction of the attenuation coefficient that is from
%    pair production.

attenTable = fscanf(fidMu,'%g',[6 tableLength]);
% Transpose the array to match PTRAN description
attenTable = attenTable';
% Convert the attenuation table to PARTISN units. Note that this
```



```
% only affects the first two columns.
attenTable(:,1) = attenTable(:,1)*1000;
attenTable(:,2) = attenTable(:,2)*10;

% Now I need to find the centerpoints of my energy group
% structure. ebound has been flipped, so energyGroupCenters
% needs to be flipped as well;
energyGroupCenters = (ebound(1:end-1)+ebound(2:end))/2.0;
energyGroupCenters = fliplr(energyGroupCenters)';

% Now I need to find the interpolated values of mu for these
% energyGroupCenters. muGroupCenters represents the
% attenuation coefficient that corresponds to the
% energyGroupCenters.
muGroupCenters = interp1(attenTable(:,1),attenTable(:,2), ...
    energyGroupCenters,'linear');

% $$$
% $$$ plot(energyGroupCenters,muGroupCenters','r*');
% $$$ hold on
% $$$ plot(attenTable(:,1),attenTable(:,2),'b-o');
% $$$ hold off
% $$$ asdf;
% $$$
% $$$ mu = [5.628E+1 1.690E+1 2.056E+1 2.000E+1 1.500E+1 7.900E+0 ...
% $$$ 5.586E+0 3.514E+0 2.400E+0 1.200E+0]*density;

%This is not used for the angular dependent source.
detectorResponseFunction = energyGroupCenters.* ...
    muGroupCenters;

%I now need to normalize the response function
DRF_sum = sum(detectorResponseFunction);
% $$$ detectorResponseFunction = detectorResponseFunction/DRF_sum;

%We need to flip this order for PARTISN
DRF_tmp = 0.0*detectorResponseFunction;
for n = 1:length(detectorResponseFunction)
    DRF_tmp(n) = ...
        detectorResponseFunction(length(detectorResponseFunction)-n+1);
end
clear detectorResponseFunction
detectorResponseFunction = DRF_tmp;
```

```
%*****
%*****

%write the sum to the printEnergy file
if(printEnergy)
    fprintf(fidE,' DRF_sum\n');
    fprintf(fidE,'%g\n',DRF_sum);
    fclose(fidE);
    fprintf(' energy group file printed\n')
end

%*****
%*****
%AJS 08 November 2012
% I need to add the angular dependence of the detector response
% function. This is a cos(theta) detector. This has been split
% up for options using an isotropic source, or an angular
% dependent source.

isotropic = 0;
if(isotropic ~= 1)
    %The angular dependent source has been picked.
    % This will be fun.
    %First, we need to define xi for all the steps of the
    %quadrature triangle. Note that this is only good for IQUAD
    %== 5.
    if(iquad ~= 5)
        fprintf('*****\n');
        fprintf('*****\n');
        fprintf('ERROR\n');
        fprintf(' Value of IQUAD does not equal 5\n');
        fprintf(' Only IQUAD = 5 is currently supported\n');
        asdf;
    end
    %Compute the number of angles per octant;
    mm = isn*(isn+2)/8;
    %These cos(theta)'s are taken from the PARTISN output file
    %under the heading of "key start sn constants". They are
```

```

%the xi value, and represent the cos(theta), where theta is
%the angle from direction vector to the x-y plane. Please
%consult the PARTISN input manual for more detailed
%information under the seciton describing the quadrature
%deails in the methods section.
if(isn == 16)
    xi = [0.98940093E+00 ...
          0.94457502E+00 0.94457502E+00 ...
          0.86563120E+00 0.86563120E+00 0.86563120E+00 ...
          0.75540441E+00 0.75540441E+00 0.75540441E+00 0.75540441E+00 ...
          0.61787624E+00 0.61787624E+00 0.61787624E+00 0.61787624E+00 0.61787624E+00 ...
          0.45801678E+00 0.45801678E+00 0.45801678E+00 0.45801678E+00 0.45801678E+00 0.45801678E+00 ...
          0.28160355E+00 0.28160355E+00 0.28160355E+00 0.28160355E+00 0.28160355E+00 0.28160355E+00 0.28160355E+00
E+00 ...
          0.95012510E-01 0.95012510E-01 0.95012510E-01 0.95012510E-01 0.95012510E-01 0.95012510E-01 0.95012510E-01 0.95012510E-01
E-01 0.95012510E-01 ];
    elseif(isn == 32)
        xi = [0.99726386E+00 ...
              0.98561151E+00 0.98561151E+00 ...
              0.96476226E+00 0.96476226E+00 0.96476226E+00 ...
              0.93490608E+00 0.96476226E+00 0.96476226E+00 0.96476226E+00 ...
              0.89632116E+00 0.89632116E+00 0.89632116E+00 0.89632116E+00 0.89632116E+00 ...
              0.84936761E+00 0.89632116E+00 0.89632116E+00 0.89632116E+00 0.89632116E+00 0.89632116E+00 ...
              0.79448380E+00 0.79448380E+00 0.79448380E+00 0.79448380E+00 0.79448380E+00 0.79448380E+00 0.79448380E+00
E+00 ...
              0.73218212E+00 0.73218212E+00 0.73218212E+00 0.73218212E+00 0.73218212E+00 0.73218212E+00 0.73218212E+00 0.73218212E+00
E+00 0.73218212E+00 ...
              0.66304427E+00 0.66304427E+00 0.66304427E+00 0.66304427E+00 0.66304427E+00 0.66304427E+00 0.66304427E+00 0.66304427E+00
E+00 0.66304427E+00 0.66304427E+00 ...
              0.58771576E+00 0.58771576E+00 0.58771576E+00 0.58771576E+00 0.58771576E+00 0.58771576E+00 0.58771576E+00 0.58771576E+00
E+00 0.58771576E+00 0.58771576E+00 0.58771576E+00 ...
              0.50689991E+00 0.50689991E+00 0.50689991E+00 0.50689991E+00 0.50689991E+00 0.50689991E+00 0.50689991E+00 0.50689991E+00
E+00 0.50689991E+00 0.50689991E+00 0.50689991E+00 ...
              0.42135128E+00 0.42135128E+00 0.42135128E+00 0.42135128E+00 0.42135128E+00 0.42135128E+00 0.42135128E+00 0.42135128E+00
E+00 0.42135128E+00 0.42135128E+00 0.42135128E+00 ...
              0.33186860E+00 0.33186860E+00 0.33186860E+00 0.33186860E+00 0.33186860E+00 0.33186860E+00 0.33186860E+00 0.33186860E+00
E+00 0.33186860E+00 0.33186860E+00 0.33186860E+00 ...
              0.23928736E+00 0.23928736E+00 0.23928736E+00 0.23928736E+00 0.23928736E+00 0.23928736E+00 0.23928736E+00 0.23928736E+00
E+00 0.23928736E+00 0.23928736E+00 0.23928736E+00 ...
              0.14447196E+00 0.14447196E+00 0.14447196E+00 0.14447196E+00 0.14447196E+00 0.14447196E+00 0.14447196E+00 0.14447196E+00
E+00 0.14447196E+00 0.14447196E+00 0.14447196E+00 ...
              0.14447196E+00 ...
0.14447196E+00 ...

```

```

0.48307666E-01 0.48307666E-01 0.48307666E-01 0.48307666E-01 0.48307666E-01 0.48307666E-01 0.48307666E-01 0.48307666E-01
E-01 0.48307666E-01 0.48307666E-01 0.48307666E-01 0.48307666E-01 0.48307666E-01 0.48307666E-01 0.48307666E-01
0.48307666E-01 0.48307666E-01];
    elseif(isn == 64)
        xi = [0.99930504E+00 ...
              0.99634012E+00 0.99634012E+00 ...
              0.99101337E+00 0.99101337E+00 ...
              0.98333625E+00 0.98333625E+00 0.98333625E+00 ...
              0.97332683E+00 0.97332683E+00 0.97332683E+00 ...
              0.96100880E+00 0.96100880E+00 0.96100880E+00 ...
              0.94641137E+00 0.94641137E+00 0.94641137E+00 ...
E+00 ...
              0.92956917E+00 0.92956917E+00 0.92956917E+00 ...
E+00 0.92956917E+00 ...
              0.91052214E+00 0.91052214E+00 0.91052214E+00 ...
E+00 0.91052214E+00 0.91052214E+00 ...
              0.88931545E+00 0.88931545E+00 0.88931545E+00 ...
E+00 0.88931545E+00 0.88931545E+00 ...
              0.86599940E+00 0.86599940E+00 0.86599940E+00 ...
E+00 0.86599940E+00 0.86599940E+00 ...
              0.84062930E+00 0.84062930E+00 0.84062930E+00 ...
E+00 0.84062930E+00 0.84062930E+00 ...
              0.81326532E+00 0.81326532E+00 0.81326532E+00 ...
E+00 0.81326532E+00 0.81326532E+00 ...
              0.78397236E+00 0.78397236E+00 0.78397236E+00 ...
E+00 0.78397236E+00 0.78397236E+00 ...
              0.75281991E+00 0.75281991E+00 0.75281991E+00 ...
E+00 0.75281991E+00 0.75281991E+00 ...
              0.71988185E+00 0.71988185E+00 0.71988185E+00 ...
E+00 0.71988185E+00 0.71988185E+00 ...
              0.68523631E+00 0.68523631E+00 0.68523631E+00 ...
E+00 0.68523631E+00 0.68523631E+00 ...
              0.64896547E+00 0.64896547E+00 0.64896547E+00 ...
E+00 0.64896547E+00 0.64896547E+00 ...
              0.61115536E+00 0.61115536E+00 0.61115536E+00 ...
E+00 0.61115536E+00 0.61115536E+00 ...
              0.57189565E+00 0.57189565E+00 0.57189565E+00 ...
E+00 0.57189565E+00 0.57189565E+00 ...

```



```

        0.72993122E-01 0.72993122E-01 0.72993122E-01 0.72993122E-01 0.72993122E-01 0.72993122E-01 0.72993122E-01 0.72993122E-01 0.72993122E-01 0.72993122E-01
E-01 0.72993122E-01 0.72993122E-01 0.72993122E-01 0.72993122E-01 0.72993122E-01 0.72993122E-01 0.72993122E-01 0.72993122E-01 0.72993122E-01
0.72993122E-01 0.72993122E-01 0.72993122E-01 0.72993122E-01 0.72993122E-01 0.72993122E-01 0.72993122E-01 0.72993122E-01 0.72993122E-01 0.72993122E-01
01 0.72993122E-01 0.72993122E-01 0.72993122E-01 0.72993122E-01 0.72993122E-01 0.72993122E-01 0.72993122E-01 0.72993122E-01 0.72993122E-01 0.72993122E-01 0.72993122E-01
E-01 0.72993122E-01 ...
        0.24350293E-01 0.24350293E-01 0.24350293E-01 0.24350293E-01 0.24350293E-01 0.24350293E-01 0.24350293E-01 0.24350293E-01 0.24350293E-01 0.24350293E-01
E-01 0.24350293E-01 0.24350293E-01 0.24350293E-01 0.24350293E-01 0.24350293E-01 0.24350293E-01 0.24350293E-01 0.24350293E-01 0.24350293E-01 0.24350293E-01
0.24350293E-01 0.24350293E-01 0.24350293E-01 0.24350293E-01 0.24350293E-01 0.24350293E-01 0.24350293E-01 0.24350293E-01 0.24350293E-01 0.24350293E-01 0.24350293E-01
01 0.24350293E-01 0.24350293E-01 0.24350293E-01 0.24350293E-01 0.24350293E-01 0.24350293E-01 0.24350293E-01 0.24350293E-01 0.24350293E-01 0.24350293E-01 0.24350293E-01
E-01 0.24350293E-01 0.24350293E-01];

```

```

else
    allowed_values = [16 32 64];
    fprintf('*****\n');
    fprintf('*****\n');
    fprintf('ERROR\n');
    fprintf(' S\n order is not allowed!\n');
    fprintf(' Supported values are: %i\n',allowed_values);
    asdf;
end

```

```

%In this particular geometry, xi is the cos(theta) that I
%need. Now I just need to write this data to file.

```

```

tmpStr = sprintf('%i',ngroup*jt*kt-1);
fprintf(fid,['saleft= f0; ' tmpStr 'Y1;\n']);
fprintf(fid,['sarite= f0; ' tmpStr 'Y1;\n']);
tmpStr = sprintf('%i',ngroup*it*kt-1);
fprintf(fid,['sabott= f0; ' tmpStr 'Y1;\n']);
fprintf(fid,['satop= f0; ' tmpStr 'Y1;\n']);
tmpStr = sprintf('%i',ngroup*it*jt-1);
fprintf(fid,['safrnt= f0; ' tmpStr 'Y1;\n']);

```

```

%Now that I have those all written all nice an neat, it's
%time to get a little messy. First, I need to create the
%saback array.

```

```

%AJS 16 March 2013
% I need to read in the weighting function created for the
% the multigroup cross-sections.
fileNameWF = ['/media/RESEARCH/home/ptran/PTRAN9/' ...

```

```

        'ptran_9_50_Try2/supp_matlab_files/NJOY_WeightTables/MC_weightFunctWatG8New.txt'];
fidWF = fopen(fileNameWF,'r');
eGBNInd = fscanf(fidWF,'%i',[ngroup+1,1]);
energyNum = fscanf(fidWF,'%i',[1,1]);
% $$$
    arrayWF = zeros(energyNum,2);
arrayWF = fscanf(fidWF,'%e,%e',[2,energyNum]);
energyVal = arrayWF(:,1);
weightFunction = arrayWF(:,2);
energyBounds = fscanf(fidWF,'%e',[energyNum+1,1]);
% $$$
    plot(energyVal,weightFunction,'r-')
% $$$
    pause
% $$$
    for ien=1:energyNum
% $$$
        energyVal(ien) = fscanf(fidWF,'%E',[1 1])
% $$$
        weightFunction(ien) = fscanf(fidWF,'%E',[1 1])
% $$$
    end
saback = zeros(mm*4,ngroup*it*jt);
count = 0;
areaTotal = (xBoundEnd-xBoundStart)*(yBoundEnd-yBoundStart);
fprintf('Computing the Detector Response Fucntion\n');
for im = 1:mm
    fprintf('  im = %i out of %i\n',im,mm);

    count = 0;
    for j = 1:jt
        fprintf('      j = %i out of %i\n',j,jt);
        for i = 1:it
            areaCorr = (xGrid(i+1)-xGrid(i))*(yGrid(j+1)- ...
                yGrid(j))/areaTotal;
            areaDet = (xGrid(i+1)-xGrid(i))*(yGrid(j+1)-yGrid(j));
            for ign = ngroup:-1:1
                count = count+1;
                energyIndStart = eGBNInd(ign);
                if(ign == ngroup)
                    energyIndEnd = eGBNInd(ign+1);
                else
                    energyIndEnd = eGBNInd(ign+1)-1;
                end
            end
            saback(im,count) = energyGroupCenters(ign)* ...
                (1.0-exp(-muGroupCenters(ign)* ...
                    detectPlateThickness/xi(im)))* ...
            areaDet;
        end
    end
end
for ien =energyIndStart:energyIndEnd

```

```

% $$$          deltaE = energyBounds(ien+1)-energyBounds(ien);
% $$$          muInterp = interp1(attenTable(:,1),attenTable(:,2),energyVal(ien));
% $$$          saback(im,count) = saback(im,count)+energyVal(ien)* ...
% $$$          (1.0-exp(-muInterp* ...
% $$$          detectPlateThickness/xi(im)))* ...
% $$$          areaDet*weightFunction(ien)*deltaE;
deltaE = energyBounds(ien+1)-energyBounds(ien);
muInterp = interp1(attenTable(:,1),attenTable(:,2),energyVal(ien));
saback(im,count) = saback(im,count)+energyVal(ien)* ...
(1.0-exp(-muInterp* ...
detectPlateThickness/xi(im)))* ...
areaDet*deltaE;
        end
    end
end
end
end
for im = 1:mm
    count = 0;
    for j = 1:jt
        for i = 1:it
            for ign = 1:ngroup
                count = count+1;
                saback(im,count) = xi(im)*detectorResponseFunction(ign);
            end
        end
    end
end
end
end

%Write this adjoint source to file
lineStr = 'saback=';
prefix = ' ';

valHold = saback(1,1);

for n=1:it*jt
    for ign = 1:ngroup
        ind = 1;
        KEEP_GOING = 1;
        while(KEEP_GOING) %This will loop until the current string
            % has been written
            %Okay, I need to find how many values have the same

```



```

        % value as "valHold" in a row
SAME = 1;
count = 1;
while(SAME && ind < mm)
    ind = ind+1;
    if(saback(ind,ign+ngroup*(n-1)) == valHold)
        %If yes, then increment ind and count and keep looking
        count = count+1;
    else
        %If no, then kill this round and set it out.
        ind = ind-1;
        SAME = 0;
    end
end
%Okay, so here, I know how many times the "valHold"
% value has been repeated, and I know the place of the
% next value. Let's work the former first.
if(count > 1)
    %If the count is greater than 1, then the repeated
    % syntax needs to be used to reduce the space needed
    % to represent the geometry in the file.
    tmpStr = sprintf('%3ir%-12.5E',count,valHold);
    tmpStr = deblank(tmpStr);
else
    %Then print a simple, single value is there is only
    % one of them.
    tmpStr = sprintf('%12.5E',valHold);
    % $$$
    fprintf('valHold = %g\n',valHold)
    % $$$
    fprintf('ind = %3i\n',ind);
    % $$$
    fprintf('j = %3i\n',j);
    % $$$
    fprintf('k = %3i\n',k);
    % $$$
    fprintf('zones(ind,j,k) = %g\n',zones(ind,j,k));
    % $$$
    pause
end
%Contatenate the new string (character string) onto the
% line for writing it.
lineStr = [lineStr ' ' tmpStr];
if ind == mm
    %This means that it found the end of the
    % "string", or line of the x values.
    %AJS 09 November 2012
    % Repeat the mm values for each octant as well.

```

```

%Before adding this one, you need to check to see
%if it's too long on the line.
if(length(lineStr) > 57)
    fprintf(fid,[lineStr '\n']);
    lineStr = [prefix sprintf(' 3Q%i',mm) ';''];
else
    lineStr = [lineStr sprintf(' 3Q%i',mm) ';''];
end
%Since we found the end of the "string" we need to
% get out of the loop, and move onto the next y
% place and therefore, the next "string".
KEEP_GOING = 0;
else
    %Since, I am not at the end of the "string," I need
    % pick up the next value to find if it is repeated.
    ind = ind+1;
    valHold = saback(ind,ign+ngroup*(n-1));
end
if(length(lineStr) > 57)
    %If the line is greater than 72 characters, than
    % write it to the file and set up the next line.
    fprintf(fid,[lineStr '\n']);
    lineStr = prefix;
end
end
end %End of for loop over the energy groups
% $$$      fflush(fid);
end %End of loop over all detectors

% At the end of the line, there will be a partial row that is under
% the 72 character limit, but is a complete row, as it contains the
% rest of the data. This also needs to be written.
if length(lineStr) > length(prefix)
    fprintf(fid,[lineStr '\n']);
end

%This repeats the value for pixel (1,1) for the rest of the
% pixels. Each pixel has the same detector response function
% $$$      tmpStr = sprintf('%i',it*jt-1);
% $$$      fprintf(fid,[prefix tmpStr 'Y%i;\n'],ngroup);

% $$$      %This repeats the detector response function for all the

```

```

% $$$          % octants.
% $$$          tmpStr = sprintf('%i',ngroup*it*jt-1);
% $$$          fprintf(fid,[prefix '4Y' tmpStr ';' '\n']);

else
    %Then pick the isotropic point source.
    %Write this to the PARTISN input file.
    %this could be much more difficult, complex, and much more general
    %to implement. for now, I'm just doing it the easy way.
    tmpStr = sprintf('%i',jt*kt-1);
    fprintf(fid,['sileft= f0; ' tmpStr 'Y1;\n']);
    fprintf(fid,['sirite= f0; ' tmpStr 'Y1;\n']);
    tmpStr = sprintf('%i',it*kt-1);
    fprintf(fid,['sibott= f0; ' tmpStr 'Y1;\n']);
    fprintf(fid,['sitop= f0; ' tmpStr 'Y1;\n']);
    tmpStr = sprintf('%i',it*jt-1);
    fprintf(fid,['sifrnt= f0; ' tmpStr 'Y1;\n']);
    %Under the current string of things, I need to do this a little
    % different. The detector response function currently equals
    % just the energy. phi*E*mu. Phi is the forward flux, E*mu is
    % the detector response function. mu is part of the geometry,
    % so it just leaves E to be the adjoint
    % source. But... Shouldn't this be a PDF?
    %AJS 07 November 2012
    % this last statement is wrong. Eventhough the mu is part of
    % the geometry, it is still part of the detector response
    % function, or the adjoint source. This has been fixed above.
    count = 0;
    for i = 1:it
        for j = 1:jt
            count = count+1;
            siback(:,count) = detectorResponseFunction(:);
        end
    end
    lineStr = 'siback=';
    prefix = ' ';
% $$$          for j=1:it*jt;
% $$$          if mod(j,30) == 0
% $$$          fprintf('j = %g\n',j);
% $$$          end
    %Give the initial value of the value holder

```

```

ind = 1;
valHold = siback(ind,1);
KEEP_GOING = 1;
while(KEEP_GOING) %This will loop until the current string
                  % has been written
                  %Okay, I need to find how many values have the same
                  % value as "valHold" in a row

SAME = 1;
count = 1;
while(SAME && ind < ngroup)
    ind = ind+1;
    if(siback(ind,1) == valHold)
        %If yes, then increment ind and count and keep looking
        count = count+1;
    else
        %If no, then kill this round and set it out.
        ind = ind-1;
        SAME = 0;
    end
end
%Okay, so here, I know how many times the "valHold"
% value has been repeated, and I know the place of the
% next value. Let's work the former first.
if(count > 1)
    %If the count is greater than 1, then the repeated
    % syntax needs to be used to reduce the space needed
    % to represent the geometry in the file.
    tmpStr = sprintf('%3ir%-12.5E',count,valHold);
    tmpStr = deblank(tmpStr);
else
    %Then print a simple, single value is there is only
    % one of them.
    tmpStr = sprintf('%12.5E',valHold);
% $$$          fprintf('valHold = %g\n',valHold)
% $$$          fprintf('ind = %3i\n',ind);
% $$$          fprintf('j = %3i\n',j);
% $$$          fprintf('k = %3i\n',k);
% $$$          fprintf('zones(ind,j,k) = %g\n',zones(ind,j,k));
% $$$          pause
end
if ind == ngroup
    %This means that it found the end of the

```

```

    % "string", or line of the x values.
    tmpStr = [tmpStr ';' ];
    %Since we found the end of the "string" we need to
    % get out of the loop, and move onto the next y
    % place and therefore, the next "string".
    KEEP_GOING = 0;
else
    %Since, I am not at the end of the "string," I need
    % pick up the next value to find if it is repeated.
    ind = ind+1;
    valHold = siback(ind,1);
end
%Contatenate the new string (character string) onto the
% line for writting it.
lineStr = [lineStr ' ' tmpStr];
if(length(lineStr) > 68)
    %If the line is greater than 72 characters, than
    % write it to the file and set up the next line.
    fprintf(fid, [lineStr '\n']);
    lineStr = prefix;
end
end
% $$$          fflush(fid);

% $$$          end
% At the end of the line, there will be a partial row that is under
% the 72 character limit, but is a complete row, as it contains the
% rest of the data. This also needs to be written.
if length(lineStr) > length(prefix)
    fprintf(fid, [lineStr '\n']);
end

tmpStr = sprintf('%i', it*jt-1);
fprintf(fid, [prefix tmpStr 'Y1;\n']);
end%End of isotropic logical
end

```

%Alright, you're done, You just need to tell PARTISN.

```
fprintf(fid, ' T\n');
%*****
%*****
% START BLOCK VI
% Edit input
%write the dillimeter lines to separate this block from the others.
fprintf(fid, '\n');
fprintf(fid, '/***** B L O C K VI *****/');
fprintf(fid, '\n');
fprintf(fid, '/PRINTED BY MATLAB FILE "PARTISN_gridStructure.m".\n');
fprintf(fid, '/ PLEASE CONSULT THAT FILE AND THE PARTISN MANUAL FOR MORE DETAILED\n');
fprintf(fid, '/ EXPLANATION OF WHAT THESE VARIABLES ARE\n');

pted = 1; %Do the edits by the fine mesh? 0/1 = no/yes
zned = 0; %Do the edits by the zone? 0/1 = no/yes

fprintf(fid, 'pted= %i\n', pted);
fprintf(fid, 'zned= %i\n', zned);

% $$$ fprintf(fid, 'pted=1 prplted=0 edoutf=1\n');
% $$$ fprintf(fid, 'edxs="heat" resdnt=1\n');

%Alright, you're done, You just need to tell PARTISN.

fprintf(fid, ' T\n');

% $$$ fflush(fid)
fclose(fid);
```



# Appendix E



moder /Use the binary form of the ENDF libraries since the DTFR module needs them in binary

20 -21

reconr

```
-21 -32/ %Unit number of the ENDF Library (copied to "tape21"), Unit number of the PENDF output file
'Testing RECONR PENDF write' / %Written at the top of the PENDF file
1 1 0/ %CARD 3: %***** Material Hydrogen, ncards, number of user energy points of interest
0.001 300.0/ %CARD 4: %fractional reconstruction tolerance, temperature (K)
'1-H-1 Hydrogen' / %CARD 5: %description of card
6 1 0/ %CARD 3: %***** Material Carbon, ncards, number of user energy points of interest
0.001 300.0/ %CARD 4: %fractional reconstruction tolerance, temperature (K)
'6-C-12 Carbon ' / %CARD 5: %description of card
7 1 0/ %CARD 3: %***** Material Nitrogen, ncards, number of user energy points of interest
0.001 300.0/ %CARD 4: %fractional reconstruction tolerance, temperature (K)
'7-N-14 Nitrogen Gas' / %CARD 5: %description of card
8 1 0/ %CARD 3: %***** Material Oxygen, ncards, number of user energy points of interest
0.001 300.0/ %CARD 4: %fractional reconstruction tolerance, temperature (K)
'8-O-16 Oxygen Gas' / %CARD 5: %description of card
13 1 0/ %CARD 3: %***** Material Aluminum, ncards, number of user energy points of interest
0.001 300.0/ %CARD 4: %fractional reconstruction tolerance, temperature (K)
'13-Al-27 Aluminm' / %CARD 5: %description of card
18 1 0/ %CARD 3: %***** Material Argon, ncards, number of user energy points of interest
0.001 300.0/ %CARD 4: %fractional reconstruction tolerance, temperature (K)
'18-Ar-40 Argon Gas' / %CARD 5: %description of card
53 1 0/ %CARD 3: %***** Material Iodine, ncards, number of user energy points of interest
0.001 300.0/ %CARD 4: %fractional reconstruction tolerance, temperature (K)
'53-I-127 Iodine' / %CARD 5: %description of card
55 1 0/ %CARD 3: %***** Material Cesium, ncards, number of user energy points of interest
0.001 300.0/ %CARD 4: %fractional reconstruction tolerance, temperature (K)
'55-Cs-133 Cesium' / %CARD 5: %description of card
0/
```

gamnr

```
-21 -32 0 -33/ %CARD1: ENDF Library unit number, PENDF unit number (from RECONR), I don't know, output GENDF unit number
1 1 1 5 1/ %CARD2: Starting with Hydrogen (H), User Defined Group Structure, Read in Weighting Function, P5 Legendre order, maximum print
option
```

```
'8 Group photon interaction library P5' / %CARD3: title
```

8

```
2.0000E+03 2.2000E+04 3.0000E+04 4.0000E+04 5.4000E+04 6.2000E+04 7.0000E+04 9.0000E+04 1.2500E+05
0.0000E+00 0.0000E+00 0.0 0.0 0.0 1.0 124.0
124.0 1.0
2.7440E+03 0.0000E+00 3.9819E+03 0.0000E+00 4.9698E+03 0.0000E+00
1.9577E+03 0.0000E+00 6.9456E+03 0.0000E+00 7.9335E+03 0.0000E+00
0.9214E+03 0.0000E+00 9.9093E+03 0.0000E+00 1.0897E+04 0.0000E+00
.1885E+04 0.0000E+00 1.2873E+04 0.0000E+00 1.3861E+04 0.0000E+00
.4849E+04 0.0000E+00 1.5837E+04 0.0000E+00 1.6825E+04 1.4175E-09
.7812E+04 5.7231E-08 1.8800E+04 2.1200E-07 1.9788E+04 7.0732E-06
.0776E+04 3.8945E-05 2.1764E+04 9.8001E-05 2.2752E+04 2.1879E-04
.3740E+04 4.8692E-04 2.4728E+04 8.9016E-04 2.5716E+04 1.5538E-03
```

www.mharc.com

2.6704E+04 2.4464E-03 2.7692E+04 3.4656E-03 2.8679E+04 4.9004E-03  
 2.9667E+04 6.6314E-02 3.0655E+04 8.1885E-03 3.1643E+04 9.7394E-03  
 3.2631E+04 1.1377E-02 3.3619E+04 1.3267E-02 3.4607E+04 1.4699E-02  
 3.5595E+04 1.7068E-02 3.6583E+04 1.8320E-02 3.7571E+04 1.9081E-02  
 3.8558E+04 2.0241E-02 3.9546E+04 2.1235E-02 4.0534E+04 2.2284E-02  
 4.1522E+04 2.3467E-02 4.2510E+04 2.3781E-02 4.3498E+04 1.9964E-02  
 4.4486E+04 2.3822E-02 4.5474E+04 2.4711E-02 4.6462E+04 2.3319E-02  
 4.7450E+04 2.3876E-02 4.8438E+04 2.5703E-02 4.9425E+04 2.4472E-02  
 5.0413E+04 2.3224E-02 5.1401E+04 2.3063E-02 5.2389E+04 2.1897E-02  
 5.3442E+04 2.2261E-02 5.4429E+04 2.2371E-02 5.5353E+04 2.2489E-02  
 5.6341E+04 2.2212E-02 5.7329E+04 2.1590E-02 5.8317E+04 2.8597E-02  
 5.9304E+04 3.2284E-02 6.0292E+04 1.6145E-02 6.1393E+04 1.5234E-02  
 6.2381E+04 1.4178E-02 6.3256E+04 1.4186E-02 6.4244E+04 1.4554E-02  
 6.5232E+04 1.3665E-02 6.6220E+04 1.3596E-02 6.7208E+04 1.7097E-02  
 6.8196E+04 1.1301E-02 6.9345E+04 1.2300E-02 7.0333E+04 9.5161E-03  
 7.1159E+04 9.0050E-03 7.2147E+04 9.5811E-03 7.3135E+04 8.7177E-03  
 7.4123E+04 8.1092E-03 7.5111E+04 7.7057E-03 7.6099E+04 8.0621E-03  
 7.7087E+04 7.7817E-03 7.8075E+04 7.1380E-03 7.9062E+04 7.1757E-03  
 8.0050E+04 7.0599E-03 8.1038E+04 6.8217E-03 8.2026E+04 6.3301E-03  
 8.3014E+04 6.1338E-03 8.4002E+04 6.0060E-03 8.4990E+04 5.4889E-03  
 8.5978E+04 5.0769E-03 8.6966E+04 5.0197E-03 8.7954E+04 4.9474E-03  
 8.8942E+04 4.4953E-03 8.9929E+04 4.2061E-03 9.0917E+04 4.3558E-03  
 9.1905E+04 3.9863E-03 9.2893E+04 3.6959E-03 9.3881E+04 3.6652E-03  
 9.4869E+04 3.3637E-03 9.5857E+04 3.2564E-03 9.6845E+04 3.4038E-03  
 9.7833E+04 3.0617E-03 9.8821E+04 2.7847E-03 9.9808E+04 2.9368E-03  
 1.0080E+05 2.4353E-03 1.0178E+05 2.4698E-03 1.0277E+05 2.4678E-03  
 1.0376E+05 2.1314E-03 1.0475E+05 2.2067E-03 1.0574E+05 1.8768E-03  
 1.0672E+05 1.8733E-03 1.0771E+05 1.7371E-03 1.0870E+05 1.6866E-03  
 1.0969E+05 1.4769E-03 1.1068E+05 1.2380E-03 1.1166E+05 1.1926E-03  
 1.1265E+05 8.7867E-04 1.1364E+05 9.0361E-04 1.1463E+05 7.7145E-04  
 1.1561E+05 7.2838E-04 1.1660E+05 7.3520E-04 1.1759E+05 7.7024E-04  
 1.1858E+05 5.1693E-04 1.1957E+05 4.2325E-04 1.2055E+05 3.5048E-04  
 1.2154E+05 2.4807E-04 1.2253E+05 1.9516E-04 1.2352E+05 1.3143E-04  
 1.2451E+05 1.0612E-06 /  
 -1/ %CARD6: Use all interaction processes  
 6/ %CARD7: Now process the Carbon (N)  
 -1/ %CARD6: Use all interaction processes  
 7/ %CARD7: Now process the Nitrogen (N)  
 -1/ %CARD6: Use all interaction processes  
 8/ %CARD7: Now process the Oxygen (O)  
 1/ %CARD6: Use all interaction processes  
 3/ %CARD7: Now process the Aluminum (Al)  
 1/ %CARD6: Use all interaction processes  
 8/ %CARD7: Now process the Argon (Ar)  
 1/ %CARD6: Use all interaction processes  
 3/ %CARD7: Now process the Iodine (I)  
 1/ %CARD6: Use all interaction processes  
 5/ %CARD7: Now process the Cesium (Cs)  
 1/ %CARD6: Use all interaction processes

```

dtfr
-33 34 0 0/ %CARD 1: Read in the GENDF tape (Tape33), output ASCII DTF format Tape 34, PENDF tape number for point plots, Tape number for
plot to the plotr module
1 0 0/ %CARD 2: Print Full, don't write a plot (0), Edit control is outside the DTFR module (if desired)
6 8 3 4 11 0 0/ %CARD 3: Legendre Order+1 (The number of tables), # of gamma groups, Position of Total Cross-section, Position of in-
group scattering cross-section, Table length Desired (ng+iptotl), ***NO EDITS***
0 0/ %CARD 7 (Gamma Data - NOT USED): The number of tables, # of Gamma Groups
'Hyd' 1 1 0.0/ %CARD 8: Hollerith identifier for Hydrogen, MAT(Gamma data) for Hydrogen (ENDF format)
'CrB' 6 1 0.0/ %CARD 8: Hollerith identifier for Carbon, MAT(Gamma data) for Carbon (ENDF format)
'Nit' 7 1 0.0/ %CARD 8: Hollerith identifier for Nitrogen, MAT(Gamma data) for Nitrogen (ENDF format)
'Oxy' 8 1 0.0/ %CARD 8: Hollerith identifier for Oxygen, MAT(Gamma data) for Oxygen (ENDF format)
'Alu' 13 1 0.0/ %CARD 8: Hollerith identifier for Aluminum, MAT(Gamma data) for Aluminum (ENDF format)
'Arg' 18 1 0.0/ %CARD 8: Hollerith identifier for Argon, MAT(Gamma data) for Argon (ENDF format)
'Iod' 53 1 0.0/ %CARD 8: Hollerith identifier for Iodine, MAT(Gamma data) for Iodine (ENDF format)
'Ces' 55 1 0.0/ %CARD 8: Hollerith identifier for Cesium, MAT(Gamma data) for Cesium (ENDF format)
0/

```

```

stop
*****

```

# Appendix F

## DICOM

patient\_003\_3p0mm

-7.50, 2.70, 4.0, 19.0, -109.5, -102.3

0.3, 0.3, 0.3

55

AIR700ICRU

109, 0.000100, 0.083000, 1.000000

lung

366, 0.083000, 0.323335, 1.000000

Mix386

517, 0.323335, 0.450000, 1.000000

Mix513

628, 0.450000, 0.576665, 1.000000

Mix640

739, 0.576665, 0.703335, 1.000000

Mix766

850, 0.703335, 0.830000, 1.000000

Mix893

918, 0.830000, 0.906665, 1.000000

lipid

934, 0.906665, 0.925000, 1.000000

adipose3

943, 0.925000, 0.935000, 1.000000

breast33

952, 0.935000, 0.945000, 1.000000

adipose2

961, 0.945000, 0.955000, 1.000000

breast50

970, 0.955000, 0.965000, 1.000000

adipose1

980, 0.965000, 0.976250, 1.000000

Mix982

991, 0.976250, 0.988750, 1.000000

Mix995

1000, 0.988750, 1.001250, 1.000000

Mix1007

1014, 1.001250, 1.013750, 1.000000

sftTissueICRU44Female

1025, 1.013750, 1.025000, 1.000000

lymph

1035, 1.025000, 1.035000, 1.000000

lungCongested

1045, 1.035000, 1.045000, 1.000000

muscleAdult

1060, 1.045000, 1.060000, 1.000000

eyeLens

1085, 1.060000, 1.085000, 1.000000

skCartilage

1110, 1.085000, 1.110000, 1.000000

Mix1120

1130, 1.110000, 1.130000, 1.000000

Mix1140

1150, 1.130000, 1.150000, 1.000000

Mix1160

1179, 1.150000, 1.179000, 1.000000

Mix1198

1207, 1.179000, 1.207000, 1.000000

Mix1216

1225, 1.207000, 1.225000, 1.000000

Mix1234

1243, 1.225000, 1.243000, 1.000000

Mix1252

1261, 1.243000, 1.261000, 1.000000

skFemur10yo

1280, 1.261000, 1.280000, 1.000000

skSacrumMale

1300, 1.280000, 1.300000, 1.000000

Mix1310  
1320, 1.300000, 1.320000, 1.000000  
skVertebralD6  
1345, 1.320000, 1.345000, 1.000000  
Mix1360  
1375, 1.345000, 1.375000, 1.000000  
skSacrumFemale  
1400, 1.375000, 1.400000, 1.000000  
skRib2  
1415, 1.400000, 1.415000, 1.000000  
skVertebralC4  
1440, 1.415000, 1.440000, 1.000000  
skHumerus  
1475, 1.440000, 1.475000, 1.000000  
Mix1490  
1505, 1.475000, 1.505000, 1.000000  
skRib10  
1531, 1.505000, 1.531250, 1.000000  
Mix1542  
1554, 1.531250, 1.553750, 1.000000  
Mix1565  
1576, 1.553750, 1.576250, 1.000000  
Mix1587  
1599, 1.576250, 1.598750, 1.000000  
skCranium  
1622, 1.598750, 1.621650, 1.000000  
Mix1633  
1645, 1.621650, 1.645000, 1.000000  
Mix1656  
1668, 1.645000, 1.668350, 1.000000  
skMandible  
1695, 1.668350, 1.695000, 1.000000  
skCortical1yo  
1730, 1.695000, 1.730000, 1.000000  
skCortical5yo  
1770, 1.730000, 1.770000, 1.000000  
skCortical10yo  
1810, 1.770000, 1.810000, 1.000000  
skCortical15yo  
1820, 1.810000, 1.875000, 1.000000  
skCortical  
2000, 1.875000, 2.500000, 1.000000  
TI  
5000, 2.500000, 5.000000, 1.000000  
FE  
10000, 5.000000, 10.000000, 1.000000  
AU  
20000, 10.000000, 20.000000, 1.000000

# Appendix G

```

Dimitrios Body Phantom
13
reg# n_comp med      ino. of regions
      1 1 1, 0, Extern trans_no n_int Intern
      2 1 2, 1, 1, 1, 2,
      3 1 3, 1, 10, 3,4,5,6,7,8,9,10,11,12,
      4 1 3, 2, 1, 0,
      5 1 15, 2, 1, 0,
      6 1 5, 2, 1, 0,
      7 1 16, 2, 1, 0,
      8 1 8, 2, 1, 0,
      9 1 4, 2, 1, 0,
     10 1 7, 2, 1, 0,
     11 1 3, 2, 1, 0,
     12 1 3, 2, 1, 0,
     13 1 5, 1, 2, 0,
reg# comp# geom      axis      comb_op
      1, 1, 2, 3, 1,
      2, 1, 2, 3, 1,
      3, 1, 2, 3, 1,
      4, 1, 2, 3, 1,
      5, 1, 2, 3, 1,
      6, 1, 2, 3, 1,
      7, 1, 2, 3, 1,
      8, 1, 2, 3, 1,
      9, 1, 2, 3, 1,
     10, 1, 2, 3, 1,
     11, 1, 2, 3, 1,
     12, 1, 2, 3, 1,
     13, 1, 6, 3, 1,

```

```

      1, 1.3000E+04, 1.3000E+04, 1.1000E+05, 0.0000E+00, 0.0000E+00, 0.0000E+00,
      2, 1, 180.0000000, 130.0000000, 0.25000E+03, 0.0000E+00, 0.0000E+00, 0.0000E+00,
      3, 1, 20.00000000, 25.00000000, 0.24000E+03, 100.0000000, 0.0000E+00, 0.0000E+00,
      4, 1, 20.00000000, 25.00000000, 0.23500E+03, -100.0000000, 0.0000E+00, 0.0000E+00,
      5, 1, 16.00000000, 16.00000000, 0.23000E+03, 0.00000000, -54.0000E+00, 0.0000E+00,
      6, 1, 16.00000000, 16.00000000, 0.23000E+03, 0.00000000, 54.0000E+00, 0.0000E+00,
      7, 1, 16.00000000, 16.00000000, 0.23000E+03, 31.200E+00, 23.000E+00, 0.0000E+00,
      8, 1, 16.00000000, 16.00000000, 0.23000E+03, -31.200E+00, 23.000E+00, 0.0000E+00,
      9, 1, 16.00000000, 16.00000000, 0.23000E+03, 31.200E+00, -23.000E+00, 0.0000E+00,
     10, 1, 16.00000000, 16.00000000, 0.23000E+03, -31.200E+00, -23.000E+00, 0.0000E+00,
     11, 1, 8.000000000, 50.00000000, 0.23000E+03, -65.0000E+00, -20.000E+00, 0.0000E+00,
     12, 1, 8.000000000, 50.00000000, 0.23000E+03, 65.0000E+00, -20.000E+00, 0.0000E+00,
     13, 1, 0.4800E+02, 0.3500E+02, 0.25000E+03, 0.0000E+00, 0.0000E+00, 0.0000E+00,
r_comp:com offset in reg frame
!x: 180 y:130

```

```

trans# ang_reg      z_x      z_y      z_z      r_reg
      1, 0.0000, 0.0000E+00, 0.0000E+00, 0.1000E+01, 0.000000000E+00, 0.000000000E+00, 0.000000000E+00
      2, 0.0000, 0.0000E+00, 0.0000E+00, 0.1000E+01, 0.000000000E+00, -0.850000000E+03, 0.000000000E+00

```



```

../dlc146/xsect_air.dat
../dlc146/xsect_liqwat.dat
../ct/x_skcortical.dat
../ct/x_adipose2.dat
../ct/x_muscleAdult.dat
../ct/x_lipid.dat
../ct/x_breast50.dat
../dlc146/x_lucite.dat
../dlc146/xsect_pb.dat
../dlc146/xsect_al.dat
../dlc146/xsect_CsI.dat
../dlc146/xsect_air.dat
../Ndlc146/x_MoLy.dat
../Ndlc146/x_Gd202S.dat
../dlc146/x_prostate.dat
../ct/x_adipose3.dat

../dlc146/aff_air.dat
../dlc146/aff_liqwat.dat
../ct/aff_skcortical.dat
../ct/aff_adipose2.dat
../ct/aff_muscleAdult.dat
../ct/aff_lipid.dat
../ct/aff_breast50.dat
../dlc146/a_lucite.dat
../dlc146/aff_pb.dat
../dlc146/aff_al.dat
../dlc146/aff_CsI.dat
../dlc146/aff_air.dat
../Ndlc146/a_MoLy.dat
../Ndlc146/a_Gd202S.dat
../dlc146/aff_prostate.dat
../ct/aff_adipose3.dat

/data/CAX_spect_125kVp.txt
1      !(x,y,z),medium, region number,critical radius
-60.0  3    -40.0  0.0  1  1  0.5
15      3
1
0.0000E+00,-1.0000E+03, 0.0000E+00, 1, 0, 1 !0.0128205128205128
0.2505E+00, 0.2505E+00, 2.8000E+00, !svol(1:3) describing all sources
0.2485E+00, 0.2485E+00, 2.7960E+00, !needed for cyl shell detector
2, 5000000, 0.00005 !Pri_score_type (1=det; 2=stochas; 3=MC.), max iteration, max fx dev
12
1 !incl coherent scattering
1 !all collisions forced if bounded medium
1 !simulate all orders of coll? (1 = Yes)
1 !order of coll simulated if not all
0 !tabulate dose by region (0=No, 1=Yes)
0, 100 !dump sd values of =1, interval bewt/dumps
1 !spec_prim_mesh: 0 = default; 1 = user specified
60, 20, 10 !int mesh: n_thet_cap, n_rad_cap, n_len_cap (geoms = 11)
60, 20, 30 !int mesh: n_thet_sh, n_rad_sh, n_len_sh (geoms = 11)
60, 60, 20, 1 !num_phi, num_thet, num_len, num_rad (volume geoms .ne. 11)
3294796, 2, 591529675 !nhist, (primary = 1, scatter = 2, dose =3), random_num_seed
3 !Random No. generator: 1 = VAX_RAND; 2 = RAND2
0.05 2.5 3000.0
160, 160, 100 !nx_cell, ny_cell, nz_cell
,1,1
-180.0000, 180.0000 !min_x,max_x co-ordinates of planes bounding
-130.0000, 130.0000 !min_y,max_y scoring matrix (score_type = 11 or 12)
-125.0000, 125.0000 !min_z,max_z
$$_3 ! $_3 = key for the Compton input data (incl_at_binding = 5)
fortnew.txt compton.txt ! input file for DDCS and output file (for s/r_init_c_broadening)
0 1 5000000 10.0 !itest,med_test,n_test,e_test(kev) for DDCS and MC comparison
$$_5 !$_4: Brachytherapy, $_5: CBCT, $_6: FBCT
40, 1, 30 !nx_proj, ny_proj, nz_proj

```



```

Full Fan Detector Plate Placement
-198.6560, 198.6560, xdet_proj_max, xdet_proj_max detector boundaries (in mm) at zero angle
500.0000, 500.6000, !ydet_proj_min, ydet_proj_max
-148.9920, 148.9920, !zdet_proj_min, zdet_proj_max
Half Fan Detector Plate Placement
-50.6560, 346.6560, !xdet_proj_min, xdet_proj_max detector boundaries (in mm) at zero angle
500.0000, 500.6000, !ydet_proj_min, ydet_proj_max
-148.9920, 148.9920, !zdet_proj_min, zdet_proj_max

Cone Beam Bow Tie Filter
2, 1, 0.4800E+02, 0.3500E+03, 0.0000E+00, 0.0000E+00, 0.0000E+00, 0.0000E+00,
0, './input/BTr.txt', 2 !Bow-tie filter: on=1,off=0. If on,BT file name follows
Cone Beam Detector Plate
1, 0.6, 11 !detector plate l=yes, 0=no, thickness in mm, # of material
Cone Beam Fan angular extent
1, 0.00, 0.00 !The number of image detector modules, Fan angle in the neg x-direction, Fan angle in the positive x-direction
Cone Beam Spectrum Data
./data/CAX_spect_125kVp.txt !data/Xray120.txt
Cone Beam Source Placement
0.0000E+00, -1.0000E+03, 0.0000E+00, 1, 0, 1 !0.0128205128205128
Cone Beam Bowtie filter transformation
2, 0.0000, 0.0000E+00, 0.0000E+00, 0.1000E+01, 0.00000000E+00, -0.85000000E+03, 0.00000000E+00

*****
*****
Fan Beam field size in iso-plane
-358.2655, 358.2655 !X-dimensions of field in the iso-plane (left-right)
0.0000 0.0000 !Y-placement of field in the iso-plane (anterior-posterior)
-23.9554, 30.2482 !Z-dimensions of field in the iso-plane (superior-inferior)

Fan Beam Detector Module
16, 1, 4 !nx_proj, ny_proj, nz_proj
-10.8160, 10.4640 !xdet_proj_min, xdet_proj_max detector boundaries (in mm) at zero angle
538.4480, 539.8480 !ydet_proj_min, ydet_proj_max
-21.8500, 21.8500 !zdet_proj_min, zdet_proj_max

Fan Beam Bow Tie Filter
2, 1, 1.0425E+02, 0.1360E+03, 0.1050E+02, 0.0000E+00, 0.0000E+00, 0.0000E+00,
0, './input/BT_josh_BB.txt', 2 !Bow-tie filter: on=1,off=0. If on,BT file name follows
Fan Beam Detector Plate
1, 1.4, 14 !detector plate l=yes, 0=no, thickness in mm, # of material
Fan Beam Fan angular extent
1, 27.2781, 27.2781 !The number of image detector modules, Fan angle in the neg x-direction, Fan angle in the positive x-direction
Fan Beam Spectrum Data
./data/xray_Njosh.txt !data/Xray120.txt
Fan Beam Source Placement
0.0000E+00, -0.6450E+03, 0.0000E+00, 1, 0, 1 !0.0128205128205128
Fan Beam Bowtie filter transformation

```

```
2, 0.0000, 0.0000E+00, 0.0000E+00, 0.1000E+01, 0.000000000E+00, -0.45986194E+03, 0.000000000E+00
9.01754E+13 0 !Total Photon Number, Compound Poisson Noise: 1=yes, 0=no, 1=Photons 2=Air_kerma,
504288 0 !Total Photon Number, Compound Poisson Noise: 1=yes, 0=no, 1=Photons 2=Air_kerma,
```



# Vita

Andrew Joseph Sampson was born on July 9<sup>th</sup>, 1982 in Vancouver, WA and is an American citizen. He graduated from Mountain View High School, Vancouver, WA in 2000. From there, he served a two year mission to Melbourne, Australia from September 2001 to August 2003 for The Church of Jesus Christ of Latter-day Saints. Upon returning home, he married his sweetheart, Candace Joy Davis, for time and all eternity in the Portland, OR LDS temple on November 7<sup>th</sup>, 2003. He currently has five children and resides in San Antonio, TX.

## *Education*

- PhD                    **Virginia Commonwealth University (CAMPEP Accredited)**, Medical Physics, May 2013
- B.S.                    **Brigham Young University**, Physics with Math minor, 2007

## *Fellowships, Awards and Other Accomplishments*

- 2011                    Successfully passed Part 1 of the ABR Radiological Physics certification exam
- 2007 – Current            Graduate Research Assistantship, VCU
- 2006                    E. Rodney Nilson Signature Scholarship, BYU
- 2006                    Questar Corporation Scholarship

### *Professional Organization Memberships*

- 2007 American Association of Physicists in Medicine (Student Member)

### *Dissertation Topic*

Title: *Increasing Efficiency of Monte Carlo Patient-Specific Brachytherapy Dose Calculations and Cone-Beam Computed Tomography Scatter Projections through Principled Variance Reduction*

1. Developed and implemented methods to reduce calculation time for accurate Monte Carlo dose calculations for brachytherapy. By applying novel variance reduction techniques, a 50 fold efficiency improvement was gained above and beyond that for the prior optimized Monte Carlo simulation. This permits accurate dose calculations for low-energy brachytherapy sources in a clinical timeframe and reveals common errors of up to 20% within the CTV. On standard computing hardware, dose is computed in 17 seconds
2. Developed and implemented a hybrid radiation transport technique that uses an *a priori* outcome estimate obtained through deterministic methods to bias the forward transport of scattered photons for cone-beam computed tomography Monte Carlo simulation. The accurate scatter estimate can be used to improve reconstruction of clinical cone-beam CT images.

### *Skills*

- Computer Skills FORTRAN IV-95, Matlab/Octave, linux OS, LaTeX, hardware, C/C++, JAVA, and OpenMP parallelization
- Other Experimental design fabrication and machining.

### *Presentations*

1. **Andrew Sampson** and Jeffrey Williamson, "Efficient High Resolution Brachytherapy Dose Computation using Low Spatial-resolution Correlated-sampling Monte Carlo," *American Association of Physicists in Medicine Annual Meeting, 2011, Vancouver, BC.*
2. **Andrew Sampson** and Jeffrey Williamson, "Efficient Low Spatial-resolution Correlated-sampling Monte Carlo for High Resolution Brachytherapy Dose Computation," *Virginia Commonwealth University, Department of Radiation Oncology Spring Research Conference, 2011.*

3. **Andrew Sampson**, Yi Le, Dorin Todor, and Jeffrey Williamson, "Using Correlated Sampling to Accelerate CT-Based Monte Carlo Dose Calculations for Brachytherapy Treatment Planning," *World Congress on Medical Physics and Biomedical engineering, Munich, Germany, 2009.*  
(Presented by Jeffrey Williamson)
4. **Andrew Sampson**, Yi Le, Dorin Todor, and Jeffrey Williamson, "A Fast Correlated-sampling Monte Carlo Engine for Brachytherapy Treatment Planning," *AAPM Mid-Atlantic Chapter Annual Meeting, College Park, MC, 2009.*

#### *Publications*

1. **Andrew Sampson**, Yi Le, and Jeffrey Williamson, "Fast patient-specific Monte Carlo brachytherapy dose calculations via the correlated sampling variance reduction technique," *Medical Physics* **39** 1058 (2012)
2. N. D. Mukhopadhyay, **A. J. Sampson**, D. Deniz, G. Alm Carlsson, J. Williamson, A. Malusek, "Estimating statistical uncertainty of Monte Carlo efficiency-gain in the context of a correlated sampling Monte Carlo code for brachytherapy treatment planning with non-normal dose distribution," *Applied Radiation and Isotopes, Article in Press.*
3. **A. Sampson**, Y. Le, D. Todor, and J. Williamson, "Using Correlated Sampling to Accelerate CT-Based Monte Carlo Dose Calculations for Brachytherapy Treatment Planning," *IFMBE Proceedings* **25/1**, 311 (2009)
4. R. L. Spencer, J. Krogel, J Palmer, A. Payne, **A. Sampson**, W. Somers, and C. Woods, "Modeling the gas flow upstream and in the sampling nozzle of the inductively coupled plasma mass spectrometer via the Direct Simulation Monte Carlo algorithm," *Spectrochimica Acta Part B: Atomic Spectroscopy* **64** 215 (2009)

